The Ionic Drone: A plasma-assisted UAV without moving control surfaces

Final Report - Draft

AE3200 Design Synthesis Exercise

Group 16 – June 26, 2023

Archisman Acharya	5298563	Tudor Bejan	5265460
Louis Bruninx	5227690	Daniels Gorovojs	5312450
Anton Lang	5110467	Mick Resink	5307511
Onno Schreurs	5004535	Simon Stenger	5056098
Jasper Tillie	5063388	Giannis Vardanikas	5241103

Delft University of Technology

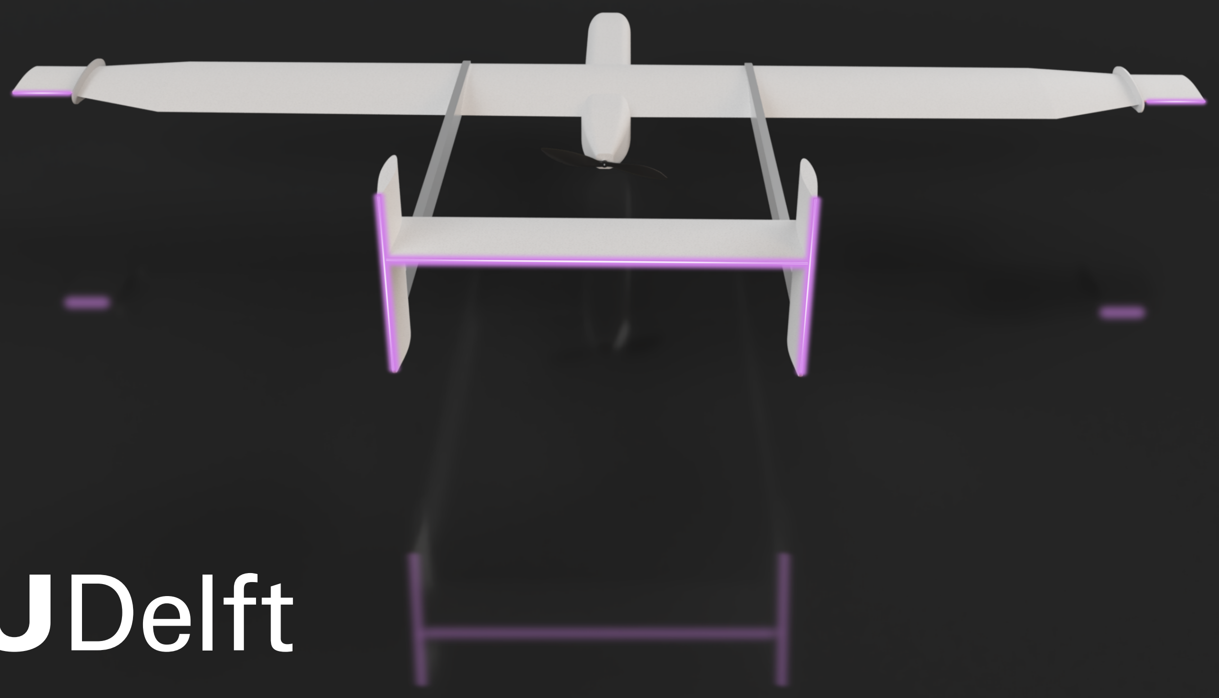

TU Delft

Executive Summary

The use of plasma actuators for active flow control presents an interesting option for the design of an aircraft. Plasma-actuated systems boast the opportunities of having facilitated maintenance, increased operational efficiency, and a decreased noise profile, with minimal impact on general performance. Yet, due to the novelty of the technology, the exact implementation of a 100% plasma-controlled drone is yet to be done. Group 16 was tasked with designing an unmanned aerial vehicle (UAV) which omits conventional mechanically-actuated control surfaces, and instead uses plasma actuators. This report explores the various technical and non-technical design facets of the Plasma-actuated Unmanned Light Surveillance and Eco-friendly Drone (PULSE Drone). Due to the inherent novelty in the design stages, this paper aims to explain the current PULSE Drone design and its approach such that it becomes a benchmark for future development. From the depth of explanations, this paper becomes a relevant source for future projects aiming to incorporate plasma actuators. A render of the final design during operations can be seen in Figure 1.

Figure 1: Final Render of the P.U.L.S.E. Drone

Mission Profile

As part of the project, a mission had to be specified which brought out the advantages that plasma technologies offer. This meant that in addition to assessing the viability of substituting control surfaces for current common UAV missions, market gaps were found which are uniquely accessible through plasma actuators. After trading off 21 mission profiles, it was selected to design a silent drone which can map noise and perform surveillance for noise-sensitive areas. Three possible payloads were selected for this mission depending on the customer's needs. The design includes an array of random incidence microphones for noise mapping, one targeted free field microphone and a noise camera for noise source identification.

After selecting the mission profile, the Coepelduynen nature reserve, Katwijk aan Zee, Noordwijk, and the Kennemerland-Zuid nature reserve were selected as sample mission locations. These areas offer a unique opportunity to compare noise maps between a touristic town (Katwijk aan Zee) and a traditional town (Noordwijk), while the nature reserves provide suitable conditions for the mission's endurance and range requirements. All legal regulations were adhered to during the design, setting limits on parameters such as flight altitude, wingspan and mass. From computational fluid dynamic analysis, the noise produced by the drone was found to be 56dB, which after propagating 55m to the ground results in 22dB. The drone is designed to stay within the limits of the open category of certification, meaning minimal certification procedures and bureaucracy have to be followed for the future development of the P.U.L.S.E. Drone.

To minimise the noise profile of the drone during measurements, it was chosen to turn off the propulsion such that the drone is in a pure glide state during measurements. After gliding the length of the measurement area, the drone will re-circle while climbing and subsequently re-enter the glide and measurement phase. This cycle is repeated 20 times.

Performance

From the mission profile, specifications on the performance of the drone could be made. A cruising flight speed of $15.1\,\mathrm{m/s}$ was selected due to being the optimal velocity such that the lift-drag ratio of the UAV is maximised. After the first two iterations, a lift-to-drag ratio was estimated using CFD. Additionally, this velocity results in

a Re_{MAC} of 315,000 which is reported as an acceptable value for plasma performance [1]. Additionally, this flight speed ensures a 3.4 m/s margin above the minimum flight velocity such that wind gusts of the reference areas can be endured. Similarly, conservative roll and pitch requirements were derived based on the mission profile, reported as 5.85 deg/s^2 and 10.1 deg/s^2, respectively. No yaw requirement was able to be set due to the limited scope of the paper.

Moreover, as the last step of the current iteration, a CFD analysis was performed in order to provide a more accurate estimate of the lift-to-drag ratio. A time-averaged method solution indicates the current lift-to-drag ratio achieved in nominal operations can be closer to the region of 15. Another simulation employing a transient method was used to estimate the sound intensity of the drone during gliding conditions. Within the noise-reduction scope of a mission, the preliminary estimated value in the vicinity of the P.U.L.S.E Drone is 56 dB. Furthermore, it was determined that at the height of 55 m, which is the minimum height the drone will operate at, the perceived sound intensity on the ground is 22 dB, approximately the sound intensity of leaves rustling.

Plasma Actuation System

The plasma control system is based on circulation control around a NACA642015 with a blunt trailing edge of radius 3.5 % chord length. Using the blunt trailing edge, the Kutta condition cannot be enforced and thus plasma actuators are able to shift the stagnation points. This change varies the circulation and thus the lift of the airfoil. Alternating current (AC) dielectric barrier discharge (DBD) plasma actuators will be placed in a three-electrode (two embedded ground electrodes and a single exposed powered electrode) configuration symmetric about the chord such that bidirectional control can be achieved. In this configuration, the electrodes shall be made of copper, with a PET polycarbonate layer used as a dielectric and trailing edge structure. The actuation of the system is controlled through a high-voltage high-frequency electrical signal generated by a Minipuls 0.1 lightweight high-voltage generator. The signal is further modulated and distributed to the plasma actuators through a set of relays.

Due to the inherent novelty of such a design, the feasibility had to be verified. This was done by the method of wind-tunnel testing in the TU Delft M tunnel. The set-up measured the resultant forces when varying angles of attack and various actuation parameters for a total of 260 tested configurations. The tests yielded a maximum change in lift coefficient ΔC_l of 0.07. For the sake of conservative estimations, a ΔC_l value of 0.05 was taken for the design of the control surfaces. The plasma control section yielded the largest number of recommendations for further study, due to the limited scope of the experiments conducted within the Project P.U.L.S.E.D. timeframe. These recommendations varied from improvements in design parameters to experimentation and optimisation techniques.

Wing design

The wing design was completed in two independent sections, namely the lifting section and the control section of the wing. From the plasma actuation section, the angle of attack was set at 2.4 degrees and a chord length of 0.169 m such that the local Reynolds number remains at 210,000. Based on the roll acceleration, this resulted in a span of 0.17m for the plasma actuators per side. A representation of the planform can be seen in Figure 2

For the lifting section of the wing, the airfoil was selected from a trade-off procedure of 50 viable options. The selected airfoil for the lifting section of the main wing was the MH115, which proved to obtain the best lift drag performance as desired by the mission profile. The dimensions of the lifting section were determined by optimising the overall lift distribution for ellipticity. This optimisation iterated designs for various dimensions and twist rates. Additionally, an iterative correction factor for three-dimensional effects from XFLR5. To minimise the aerodynamic effects of the change of geometry between the lifting and control sections of the wing, a plate was designed to limit cross flow and effects caused by pressure differences between the sections. The final geometry with dimensions, angles and airfoil selection is shown in Figure 2 using green, blue and orange, respectively. This surface has a total area of 0.76 m^2 and an aspect ratio of 12.

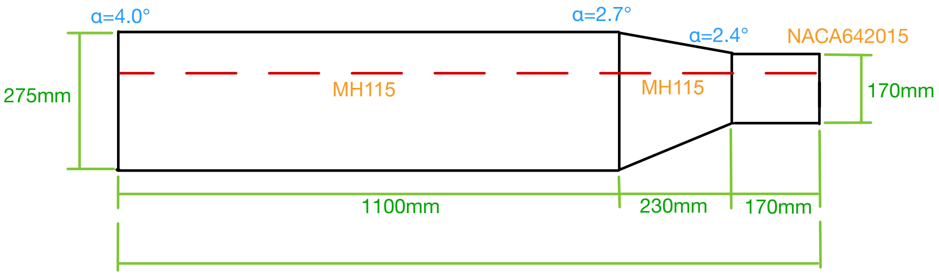

Figure 2: Final platform dimensions. The schematic is drawn to scale

The wing structure was designed to withstand the lift and drag force and the torsional moment due to the pitching moment around the aerodynamic centre and due to the loads transferred from the empennage to the wing. For this, a trapezoidal aluminium wing box that scales with the size of the local chord of the wing was designed. To this, the wing ribs made of balsa wood will be adhered. The wing skin also made of balsa wood will be adhered to the flanges of the ribs

Fuselage Design

The fuselage is designed with a semi-monocoque structure. The layout contains 4 L stringers on the corners of the fuselage, along with six formers. The design also considers features such as access holes and a wing box that enables the aircraft's modularity. The chosen configuration demonstrates it has the potential to meet the customer's needs. The main structural components are analysed under multiple flight phases and failure modes, such as stress concentrations and stringer crippling, for which the results indicate positive results. The design decisions made led to four access holes, two of them being ”cut” in the fuselage cross-section direction and the other two on its surface.

Empennage Design

The design of the empennage considered two main paradigms, aiming to ensure both static stability and control authority during manoeuvres. Two configurations were considered preliminarily, a box tail and an H-tail, with the box-tail concept being discarded due to higher complexity and added structural mass due to worse aerodynamic performance as a consequence of bi-wing interactions. The NACA642015 rounded trailing edge airfoil is considered for both the horizontal and vertical stabilisers and a plasma control section is designated on the horizontal stabiliser. The horizontal stabiliser dimensions were limited by stability, thus it has an integrated section for the plasma actuators on approximately one-third of its span. The final horizontal stabiliser span resulted to be 0.732m, on a rectangular planform with a chord length of 0.169m. The horizontal stabiliser is inclined at an effective angle of -2.4 degrees as determined to be optimal from the plasma actuation section.

Two vertical stabilisers are considered for the H-tail configuration and are sized based on a heuristic approach. The destabilising lateral effects of the fuselage, propulsion group and effective dihedral are quantified and the vertical stabiliser was sized to directly counter-act these effects. Finally, two vertical stabilisers of 0.366m span each are used. The chord length is the same as for the horizontal stabiliser to reduce structural complexity.

Finally, the empennage layout is constructed to mitigate propeller wake interactions with the horizontal stabiliser over an angle of attack range that allows the optimal performance and predictability of the NACA642015 aerofoil to be reached.

The structure for the empennage was made using a similar design approach to that of the wing. Since the loads on the wing structure were relatively low and thus the wing structure dimensions were based on manufacturing constraints. It was expected that this would also be the case for the empennage since its loads are several orders of magnitude lower than those of the wing. Therefore a structure was designed limited by manufacturing constraints. It was post-facto analysed that this structure can indeed withstand its internal loads.

Stability and Control

For proper functioning of the P.U.L.S.E. Drone, static and dynamic stability should be ensured while maintaining adequate controllability. The static stability was analysed in the empennage design to size the horizontal and vertical tails. Dynamic stability, both longitudinal and lateral, was analysed by linearising, simplifying and transforming the equations of motion for steady symmetric flight. This led to a system of equations from which the eigenvalues could be determined. OpenVSP was used to find the stability derivatives which were used to populate the system of equations. The eigenvalues were found and plotted which resulted in all eigenmotions being in the negative real region, meaning they are stable, except for the spiral motion. This motion was slightly unstable which can be easily corrected by the pilot or the control system, therefore it was concluded that this system is stable. This is acceptable within industry standards.

This analysis however did use several assumptions which should be kept in mind. The equations of motion were simplified and linearised around a certain flight condition. This means that they are capable of approximating the results for a certain flight condition with only slight variations in the parameters. Besides this, the stability derivatives were obtained using OpenVSP which also uses a linear model. This results in an analysis which is only valid for the assumed conditions and can not be used to evaluate extreme behaviour of the UAV nor any behaviour in a region with separated flow.

The control system was split up into three sections. The *Drone Operator*, which is the pilot either directly controlling the UAV or inputting the mission profile to be used by the autopilot. The second section is the *Autopilot - GNC loop* section. This section involves the navigation, guidance, control, control allocation and data fusion aspects of the control system. The last section is the *Physical System*. This involves the sensors, the UAV state-space system and the plasma actuators. The high-level architecture for the entire system was constructed and prepared for future design. As a more detailed design for the entire system was unfeasible given the project's time frame, the pitch control system was designed and tuned (to be included in the final report) to demonstrate the general functioning.

Several assumptions and simplifications were made which should be accounted for during later design phases. Any time delay was ignored when constructing the Simulink model. Besides this, the disturbances and noise inputs have been randomly selected. These should be revised to more accurately represent reality. Additionally, all the different sections should be completely worked out to create a fully functional simulation which can then be visualised and tested by connecting a joystick and using the FlightGear flight simulator.

Propulsion

The propulsion subsystem of the P.U.L.S.E. Drone is specifically designed for use during the climbing phase of the flight. During the gliding phase, in addition to turning the motor off, the propellers are folded inwards to minimise the wake drag. This folding motion is controlled actively using a simple switch. The sizing of the propulsion system is based on the assumption of a continuous cruise flight profile, rather than the cyclic motion done in reality. This assumption is valid because it places greater demands on endurance. After careful consideration, the final propeller-motor combination chosen is a 12-inch folding pusher propeller paired with the SunnySky X3520 V3 motor. This combination has a thrust capability that exceeds twice the requirement for the climbing stage, making it a non-limiting factor. Additionally, the rotation speed was selected at 7200 rpm such that the power consumption of the propeller is minimised for the 15.1 m/s cruise velocity.

Avionics

The design of the avionics system is largely conventional and not significantly affected by the plasma system. Thus for each component, a commercial off-the-shelf option has been selected which allows precise budgeting for important things such as power, mass and cost. Due to requirements from the customer and other subsystems, three primary required sub-subsystems have been identified. These are the telecommunications system, the flight controller and additional sensors.

First, a tradeoff has been performed for the telecommunications system, as there are a large number of options available on the market at vastly different price points and capabilities. The main relevant requirements are a range of 10 km, GPS telemetry, and a live navigation video feed. In this trade-off, three concepts were traded off which all fulfil these requirements. The selected configuration features a 900 Mhz direct RC Radio Link for control commands and telemetry. An additional higher latency LTE link is included as well for video, very long-range commands, and payload internet connectivity purposes. This configuration has been selected mainly due to cost advantages at similar capabilities to more expensive commercial direct video links.

For the flight controller, as it is a mission-critical component and reliability is essential, the well-established and reputable Pixhawk 6X flight controller has been selected. This allows the execution of popular open-source autopilot options such as Ardupilot and PX4 which are capable and extensive software packages that allow a large degree of customization and capabilities. This is done such that external autopilot options remain possible for aspects of the control system which are not produced in-house. The autopilot already includes many sensors such as redundant IMUs, temperature sensors, and barometers. However, four additional required sensors have been identified, a Pitot Tube, Video Camera, GPS and a Compass for which suitable components were selected.

Finally, a detailed electrical diagram indicating to which ports the components connect and what data is communicated between them has been created. This also includes interfaces with other subsystems such as the plasma control system.

Electrical power system

A preliminary tradeoff opted for a battery-electric power system rather than hydrogen which resulted in the system being relatively simple. This system consists of two primary components: The battery, and a power distribution board.

First, the battery has been selected. For this, various battery chemistries have been compared. This resulted in the conventional Lithium-ion (Li-Ion) and Lithium-polymer (Li-Po) chemistries being considered viable options. As the power requirement is relatively low at around 2 kW and on UAV the energy density is paramount, a 6S 22 Ah Li-Ion battery with a $250\,\frac{\text{Wh}}{\text{kg}}$ energy density has been selected. The selected battery has a capacity of 488 Wh and is thus sufficient for a two-hour flight time including a 20% margin.

The power management board is the PM03D by the same manufacturer as the Pixhawk6X flight controller. It measures battery voltage and current flow and reports these numbers to the flight controller. This helps in estimating the remaining capacity and thus the remaining flight time. Additionally, it provides efficient switching converters for 12 V and 5 V to provide power to the payload and avionics.

Landing

The parachute system was selected to be the landing mechanism. The advantages of this include landing in small required landing areas as well as considerable safety advantages during the mapping of sound in urbanised areas since relatively safe landings can be conducted should a system failure occur.

For the parachute design, a ready-made system rated for a 10 kg UAV by the company FruityChutes has been selected. This is one of the only complete fixed-wing complete parachute systems available commercially. The results in a descent speed of around $4.5\,\mathrm{m/s}$.

This descent speed has been identified as too high to be absorbed by the structure during landing impacts. Thus the design of an airbag has been conducted that reduces the landing acceleration to the maximum load factor the UAV is designed for during normal operation. This eliminates the need for any additional structural considerations resulting from the ground impact. This airbag consists of a ripstop nylon skin which is inflated by a fan during descent. With appropriate sizing of the orifice, this can result in relatively low landing accelerations reducing the likelihood of damage during impact.

Ground support systems

The ground support system consists of two major components, notably the UAV launcher and ground station. and the telemetry station.

The UAV launching mechanism was chosen to be a launch catapult. This was chosen since it requires no high-lift devices and it minimises take-off clearance requirements. There are two major classes available for catapults, pneumatic and elastic. The advantage of elastic launchers is lower price and transportation weight while having a lower launch mass capability. The latter disadvantage was deemed acceptable for the P.U.L.S.E. Drone and thus, the ElevonX Scorpion was selected as the launcher suitable for the mass of the Drone. As the launcher has a launch energy of 1 kJ, the launcher can accelerate the UAV to around 16 km which comfortably clears the stall speed.

The ground station can be subdivided into two smaller subsystems, the control station and the telemetry station. For the former, it was decided a remote control with gimbals was sufficient to allow the pilot direct control of the plane. A laptop can be used as a telemetry and video monitoring station. The laptop can connect to the UAV both over LTE and over the telemetry radio which is also included under the avionics descriptions. Both options allow for sending commands and receiving telemetry, however, only the LTE option allows viewing of the navigation video.

Operations and Logistics

To aid in the project development and to familiarize stakeholders with the operational profile of the drone, the operations and logistics of the project have been defined. The elements of operation include the plasma UAV itself, the operator, the ground control station, the launcher, the environment where all of the measurements are taking place, the charging station, the navigation system and finally the transportation. All of these components have to work in harmony for the mission to take place successfully.

The project entails the production of two prototypes. Due to the limited budget of the project, TU Delft facilities will be used for the bulk of the manufacturing processes. Storage of the UAV will also be done in TU Delft facilities. Large batteries must the stored in battery-safe boxes so that the fire hazard is reduced. For the transportation of the UAV to the target mission area, public roads will be used. The modular design of the P.U.L.S.E. Drone facilitates transportation along with ensuring easy assembly and disassembly.

Regarding the end-on-life logistics, the method of disposition of the P.U.L.S.E. Drone must ensure the minimum sustainability requirements. This will be further elaborated in the following section

Sustainability

An important consideration throughout the design process is the sustainability of the project. This does not only cover the sustainability of the final product but also the economic, operational and social sustainability. The first step for this is to define a school of thought that allows the implementation of sustainable principles. Circular Economy proposes an economy that works with closed material loops. A product is created, used, reused and repaired before it is finally recycled. This reduces the overall waste of a mission. However, this is just a general idea that has to be converted into a specific analysis for the particular project. The sustainability aspects of this project have been split into different phases: The conceptual phase, the production phase (using lean manufacturing), the testing phase, the operational phase and the end-of-life phase. Sustainability must be maintained in all of these phases for the whole project to be environmentally friendly.

Contents

Nomenclature

Abbreviations

Abbreviation	Definition
AC	Alternating Current
AoA	Angle of Attack
BER	Bit Error Rate
BVLOS	Beyond Visual Line of Sight
CFD	Computational Fluid Dynamics
CNC	Computer Numerical Control
CoG	Centre of Gravity
COTS	Commercial Off-The-Shelf
DSE	Design Synthesis Exercise
DATCOM	DATa COMpendium
DBD	Dielectric Barrier Discharge
EASA	European Union Aviation Safety Agency
EM	Electromagnetic
EMP	Electromagnetic Pulse
EPS	Electrical Power System
FEM	Finite Element Method
GCS	Ground Control Station
IMU	Inertial Measurement Unit
LNVL	Air Traffic Control Agency of the Netherlands
MAC	Mean Aerodynamic Chord
MCI	Material Circularity Index
MPS	Mitigated Probability Score
MR	Mitigated Risk
MSS	Mitigated Severity Score
MTOW	Maximum Take-Off Weight
MMOI	Mass Moment of Inertia
OOP	Object Oriented Programming
STOL	Short Take Off and Landing
SWOT	Strengths, Weaknesses, Opportunities and Threats
TRL	Technological Readiness Level
UAS	Unmanned Aerial System
UAV	Unmanned Aerial Vehicle
VALID	Verifiable, Attainable, Logical, Integral and Definitive
VLOS	Visual Line of Sight
VnV	Verification and Validation

Symbols

Symbol	Definition	Unit
d	Interline path distance	m
h	Altitude	m
C_L	Lift coefficient	-
C_D	Drag coefficient	-
w	Measurement area width	m
l	Measurement area length	m
r	Turn radius	m
l_{climb}	Turn horizontal distance	m
R	Range	km
F_A	Force on the aileron	N
S_A	Surface area of one aileron	m^2
$\Delta C_{L/l}$	Change in lift coefficient	-
b_w	Lifting wing span	m
I_{SAT}	Saturation current	A
$I_{B,min}$	Minimum base current	A
$I_{B,act}$	Actual base current flowing	A
β	DC Current Gain	-
σ	Normal stress	MPa
τ	Shear stress	MPa

1 Introduction

As part of the Design Synthesis Exercise in Spring 2023, Group 16 has been assigned the task of designing a plasma-assisted Unmanned Aerial Vehicle (UAV) without moving control surfaces. Plasma actuators exploit the energy transfer into the boundary layer caused by a high-voltage AC signal between two electrodes separated by a dielectric, causing the affected flow to accelerate tangentially to the wall. It is theorised that a smart arrangement of such actuators can completely remove the need for moving control surfaces.

Incorporating plasma actuators in UAVs offers numerous advantages, including enhanced control, reduced design and maintenance complexity, improved aerodynamic efficiency and lower noise emissions. These benefits make plasma-actuated aerial vehicles a desirable and elegant solution to facilitate aircraft operations, lower operational costs, and reduce emissions as well as noise pollution drastically. The latter, especially, is a recognised problem in the Netherlands and increases the operational complexity significantly in large airports such as Schiphol [2]. While plasma-actuated aircraft could reduce or eliminate these issues, no aircraft exploiting the advantages of plasma actuation are operational and commercially available. That gap is to be filled by the designs made by Group 16 as part of the DSE 2023 with a fully plasma-actuated unmanned aerial vehicle, the PULSE drone.

This report documents the detailed design process and choices behind the development of the plasma-assisted UAV, starting with a detailed market analysis in Chapter 2. Before starting any design process, it is important to understand the existing market, in addition to possible gaps to be filled with novel technology. Based on this, an exemplary mission can be defined for the UAV. While the designed aircraft is not limited to the noise measurement mission from Chapter 3, it has been optimised for this case and the required performance. As a last step before the technical design process can be started, a detailed overview of the required time and resource allocation is detrimental and heavily aids the design process. For this purpose, a series of systems engineering tools were utilised throughout the project which is documented in Chapter 5.

The technical design starts with the division of subsystems and their interfaces in Chapter 6, which is concluded by initial sizing and followed by performance analysis. Based on the previously performed initial sizing, as well as the mission profile from Chapter 3, the UAV's required performance could be characterised further in Chapter 7. In Chapter 8, the different possibilities for plasma actuators were explored and traded off. Furthermore, this chapter investigates the required high-voltage system, as well as the wind tunnel experiments performed to characterise the UAV's response to different control inputs. The following chapters concern the aerodynamic and structural design of the UAV, where Chapter 9 addresses the design of the wing, Chapter 10 deals with the design of the fuselage, and Chapter 11 elaborates the design of the horizontal and vertical tail. Chapter 12 contains the analysis done to investigate the UAV's stability characteristics and the control system needed to meet the set requirements. This is followed by Chapter 13, which concerns the design and sizing of the chosen propulsion system. Chapter 14 documents the electronics required to control the UAV and communicate its state to the operators at all times, as well as any other avionics. Due to their close relation, the avionics are succeeded by the electrical power system in Chapter 15. The technical section of the report is concluded by Chapter 16, describing the landing and take-off systems of PULSE, as well as Chapter 17, which summarises the entire system and integrates the subsystem solutions presented in preceding chapters.

Chapter 18 gives an overview of the different budgets and how resources have been allocated. This is followed by the concept of operations in Chapter 19 and Chapter 20 outlining the design philosophy and procedure with respect to their environmental impact. Lastly, Chapter 21 documents the employed verification and validation techniques, before the report culminates in a conclusion including a series of recommendations for future design improvements.

2 Market Analysis

Design projects such as this are justified by the needs of a customer and the prospect of establishing the product in a specific market. For this, a market analysis needs to be performed to assess the market factors that will affect the product's success. This analysis is thus broken down into a number of factors, overviewing the market gaps, the competitors and the stakeholders

2.1. Industry Overview and Market Definition

For a plasma actuator-controlled fixed-wing UAV, the involved industries can be divided into two phases. Firstly, in the short term, the UAV is primarily a research aircraft focused on the development and testing of plasma actuator technologies. As such, it would be a part of the research & development part of the aerospace industry. Research and development of new aerospace technologies constitute a sizeable part of the global aerospace market. In 2022, Airbus and Boeing, two of the largest aerospace companies, spent a combined total \$ 6.4 bln. on R&D projects [3, 4]. Moreover, there are numerous companies specialising solely in the development of novel technologies, with companies like Electrofluid Systems working on plasma actuator aircraft specifically [5]. Moreover, several universities and institutes have invested in aerospace development projects.

Secondly, once the underlying actuator technologies are developed and tested, the project enters the larger UAV market. According to external analysis, the global drone market was valued at \$ 26.2 bln. in 2022 [6] and \$ 33.9 bln. in 2023 [7]. Out of that, approximately 21% of the market share, or \$ 7.1 bln. constitutes of fixed-wing UAVs [7]. The market is expected to grow at approximately 20% per year [6, 7].

2.2. Market Gaps Overview

To establish the advantages the use of plasma actuators can have over other, more conventional flight control solutions, an analysis of the market gaps is done. The identified gaps in the market are not quantified in terms of resources or possible applications for the final product, but rather to the use of plasma control actuators over mechanical actuators. Thus, the gaps are identified with regard to the operational cost of the aircraft due to fuel consumption, the maintenance costs of conventional actuators and use in highly energised flight[1].

In recent developments, studies have been performed on the suppression of flow separation and the reduction of aerodynamic noise by making use of plasma actuators. Furthermore, studies have shown applications regarding the control of acoustic oscillatory flows could serve as an outcome for increasing lift efficiency. [8] The aforementioned studies have been done on independent systems or simplified flow models although the use of plasma actuators in an integrated aerospace system is still to be done. This implies that a technical gap exists in the field of plasma actuators since their validity for actual application has limited proof. If the use of plasma actuators is actually proven to be more efficient than conventional moving control surfaces, or if they can be used in aircraft vortex drag reduction, this would open up a market gap in energy-efficient solutions.

The use of plasma actuators instead of high lift surfaces has been proven to reduce drag, and in the works of C. He, a reduction of as much as 27% was reported[9]. Further advantages of plasma actuators are stated in the works of F.O. Thomas, A. Kozlov, and T.C. Corke [10]. Opposed to conventional solutions, installing plasma actuators flush with the wing surface implies higher aerodynamic efficiency, subsequently leading to the overall energy efficiency of the aircraft. The flush installation also prevents added drag by control mechanisms and makes the system less vulnerable. According to the works of T. Corke and B. Mertz, plasma actuators can be mounted directly on the wing, removing the hinge gap present in conventional hinged control surfaces, resulting in a reduction of as much as 10% in wing drag [11]. In the future, advances can be made in further reducing drag by reducing skin friction drag through virtual-wall oscillations. [12] The prospect of reducing drag during flight can have implications for better fuel efficiency, which means that the use of plasma actuators can solely account for a significant change in aircraft operational costs.

Furthermore, plasma actuators have a smaller response time than mechanical actuators, leading to better control performance. Since these types of actuators are powered by electrical current, the low-rise time of the discharge currents (in the range of 10ms to ns [13]) leads to a low response time for control.

A final advantage of plasma actuators compared to mechanical flow is their simplicity. Due to their simplicity, they are inexpensive and easier to maintain. Apart from that they can be implemented on a really small scale raising possibility to treat them as body point forces reducing simulation and computational costs.

These advantages of using plasma actuators translate into potential covers for a number of market gaps which are shown in Table 2.1. Note, each market gap is given a unique identifier and rationale

2.3. Competitors Overview

In order for the final product to be useful, it needs to meet or exceed the performance of other products aimed at a similar market. Therefore, these competitors are listed below with key specifications. Given the market as defined in the previous sections, possible competitors have been split into two groups: Plasma-actuated UAVs

---

[1] This gap mainly refers to high-speed flight, where the effectiveness of conventional control surfaces is hindered.

Table 2.1: Market Gaps Overview

Market Gap ID	Market Gap	Rationale
MG-01	Decreasing maintenance cost	Less parts and easier inspection
MG-02	Increasing fuel efficiency	Less drag produced
MG-03	Noise reduction	Acoustic oscillatory flow control
MG-04	Better response time of the aircraft	Instantaneous Electrical current control

and conventional UAVs, as there is a significant difference in the technology readiness level between these two.

2.3.1. Conventional UAVs

In this section, some UAVs with similar wingspan, payload capacity, and endurance are shown. The following list gives an overview of the most relevant competitors from different application areas and companies. They are also depicted in Figure 2.1.

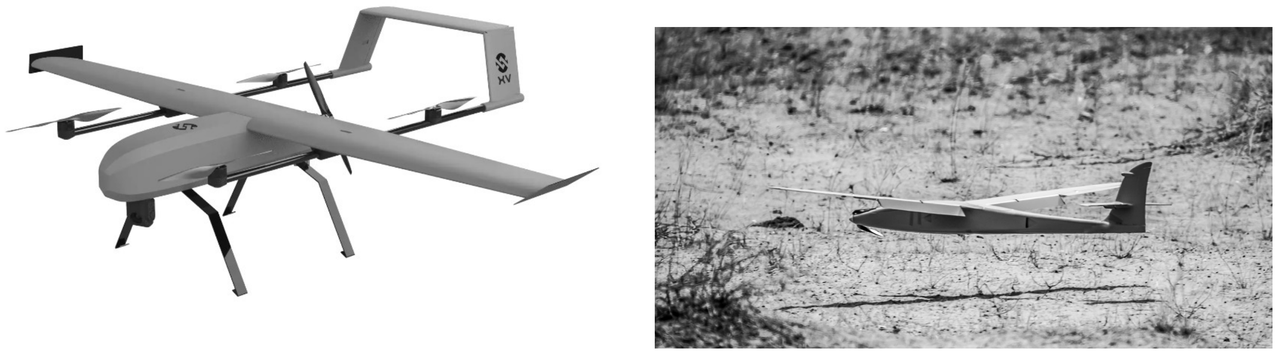

(a) XV UAV by Plymouth Rock

(b) Strix 300 UAV by EOS-Technology

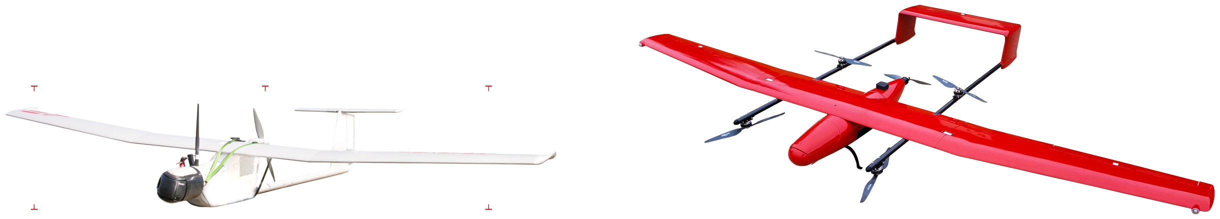

(c) AR4 UAV by Tekever

(d) E400 UAV by Event 38

Figure 2.1: Competitive Non-plasma actuated UAVs

- The **Albatross** UAV by Up-Caelivia is an electric-powered fixed-wing aircraft. It features a boom-mounted inverted V-tail fixed-wing and has a wingspan of 3 m. The UAV has a payload capacity of 2 kg to 4.4 kg, an endurance of approximately 4 h, and a range of 100 km depending on battery size and payload. It can land and take off from a runway with its landing gear. [14]
- The **Penguin C** by Edge Autonomy is a gas-powered boom-mounted invert V-tail fixed-wing aircraft with a wingspan of 3.3 m. It has an endurance of over 20 h and a communications range of up to180 km. The UAV takes off using a pneumatic catapult mechanism and lands using a parachute and airbag system. [15]
- The **XV** UAV developed by Plymouth Rock Technologies features four horizontal rotors, allowing for VTOL. In nominal operations, it utilizes a rear propeller and a main wing with a span of 2.95 m, resulting in an endurance of 3 h and a range of 50 km assuming a payload of 2.5 kg. [16]
- The **Strix 300** by EOS-Technology is an electric cruciform tail fixed-wing aircraft with a wingspan of 2.99 m. It has a maximum payload of 1 kg and an endurance of 3 h to 4 h. The UAV can be launched by hand and landed using off-road landing. [17]
- The **Bramor C4EYE** by C-Astral is an electric blended wing body aircraft with a rear propeller and winglets. It has a wingspan of 2.30 m and can carry a payload between 0.6 kg to 1.0 kg at an endurance of 3.5 h and

a range of 40 km. The UAV takes off using a pneumatic catapult mechanism and lands by deploying a parachute in a 30 m by 30 metre zone. [18].

- The **Black swift S2** by Black Swift Technologies is an electric powered with a high-wing configuration. It has a boom-mounted V-tail and a wing span of 3 m. The UAV has a payload capacity of 2.3 kg, an endurance of approximately 1.5 h, and a nominal range of 92 km. [19]
- The **AR4** developed by Takever Technologies features a T-tail and an electric rear propeller with a high wing configuration. It has a wingspan of 2.1 m and can carry a payload of 1.0 kg. Launched by hand, it deploys a parachute to land and has a range of 20 km, paired with an endurance of 2 h. The aircraft is hand-launched and can be landed by either belly landings or parachutes. [20]
- The **E400** by Event38 is an fully electric VTOL aircraft. The plane has an inverted, high boom tail and a wingspan of 3 m. It has a payload capacity of 1.3 kg, an endurance of approximately 1.5 h. [21]

2.3.2. Plasma-actuated UAVs

As plasma actuation is a brand-new technology very few competitors can be found in this company. Plasma actuators are still mostly used in research and have not been properly commercialised as of spring 2023, which is why these should not necessarily be regarded as competition. Nevertheless, existing demonstrators and prototypes are listed below.

- For the European Plasmaero project [22], the Technical University of Darmstadt designed a plasma-actuated prototype using DBD actuators for active flow control. This UAV has a wingspan of 2.38 m and a flight mass of approximately 10 kg. Fault-free operations have been demonstrated with a series of different actuators and airfoils, attaining Reynolds numbers between 300,000 and 600,000. [1]
- As part of their research on Dielectric Barrier Discharge (DBD) actuators, Satoshi Sekimoto et al. [23] retrofitted a **Voltantex RC Ranger EX** [24] with leading-edge DBD actuators in order to investigate the impact on stall performance. While this aeroplane does not use plasma actuators to replace control surfaces, it still demonstrates some advantages of plasma actuation.
- In January 2023 Aurora Flight Sciences, a subsidiary of Boeing has been tasked with the full-scale design of the CRANE X aeroplane designed by DARPA. This is a highly militarised project resulting in very little information available. [25]
- The Berlin-based company Electrofluidsystems advertises multiple plasma-actuated UAVs, for instance, the **H2PlasmaFalcon 1.66**. This is a blended wing body aircraft using liquid hydrogen and a fuel cell to provide thrust. It has a wingspan of 1.66 m and can carry a payload of 4.4 kg [5]. It should be noted that Electrofluidsystems seems like an extremely small company and has barely shown any activity since 2018. It is therefore assumed that the company is not active in the market anymore.

From this analysis, it can clearly be seen that no commercial plasma-actuated UAVs exist so far. However, various electric UAVs exist that can be regarded as direct competitors and should be used to determine the baseline functionality and performance of the plasma-actuated UAV that is to be designed.

2.4. Target Market Analysis

A target market analysis is done in order to determine if plasma-actuated UAVs are a viable business idea. A market definition was given in section 2.1. This section gives an overview of where the product would fit in this market and how it can fit in.

UAVs are currently being used for agricultural [26], military [27], construction [28], logistical [29], surveillance [30] [31], rescue [27] [31] [29] [32], maintenance applications [31], they are also used to access remote areas. The design requirements range per market and can be split up into two main design types, one focuses on manoeuvrability and the other on endurance.

Rescue operations, logistic operations and operations that explore inaccessible areas have UAV designs that focus on manoeuvrability due to the nature of their task. Quadcopters are often used for these over fixed-wing UAVs due to their superior manoeuvrability characteristics. It is safe to assume that these applications will not be the target markets for this product, since innovations in plasma actuators will most likely not affect the performance of quadcopters. Some operations including maintenance require UAVs to hover which again is only possible using quadcopters and hence is not taken into consideration.

Endurance applications namely, agricultural, military and surveillance applications, will benefit from the enhanced aerodynamic performance since operational costs will decrease. for these applications, fixed-wing aircraft trump quadcopters due to their innate longer range and endurance.

Moreover, if significant advancements are observed in the capabilities of UAVs, the potential for this technology to revolutionize the commercial aviation sector is considerable. By incorporating a hybrid system that merges traditional moving control surfaces with plasma actuators, large airliners can benefit from enhanced aerodynamic performance, resulting in reduced operational costs.

2.5. Market SWOT Diagram

From the market analysis performed in this chapter, a number of strengths and weaknesses can be identified. These are visualized for both internal and external factors in Figure 2.2.

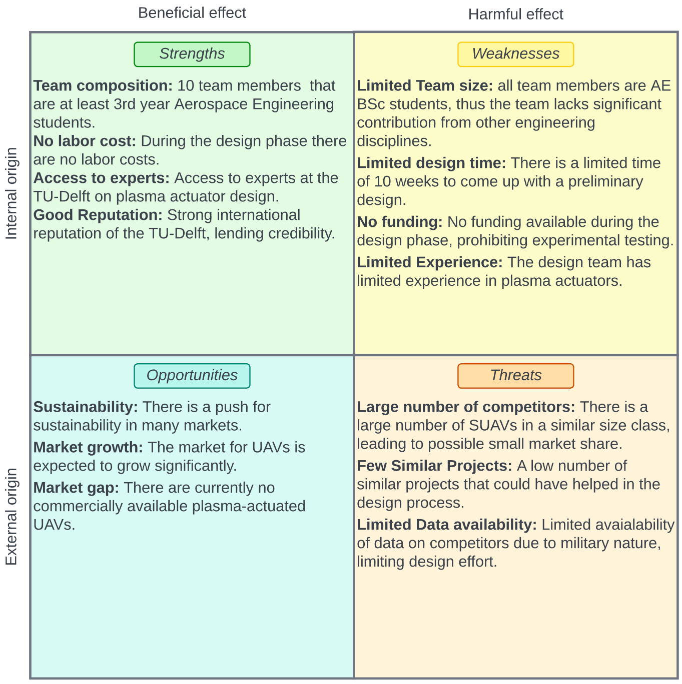

	Beneficial effect	Harmful effect
Internal origin	*Strengths* **Team composition:** 10 team members that are at least 3rd year Aerospace Engineering students. **No labor cost:** During the design phase there are no labor costs. **Access to experts:** Access to experts at the TU-Delft on plasma actuator design. **Good Reputation:** Strong international reputation of the TU-Delft, lending credibility.	*Weaknesses* **Limited Team size:** all team members are AE BSc students, thus the team lacks significant contribution from other engineering disciplines. **Limited design time:** There is a limited time of 10 weeks to come up with a preliminary design. **No funding:** No funding available during the design phase, prohibiting experimental testing. **Limited Experience:** The design team has limited experience in plasma actuators.
External origin	*Opportunities* **Sustainability:** There is a push for sustainability in many markets. **Market growth:** The market for UAVs is expected to grow significantly. **Market gap:** There are currently no commercially available plasma-actuated UAVs.	*Threats* **Large number of competitors:** There is a large number of SUAVs in a similar size class, leading to possible small market share. **Few Similar Projects:** A low number of similar projects that could have helped in the design process. **Limited Data availability:** Limited avaialability of data on competitors due to military nature, limiting design effort.

Figure 2.2: A SWOT diagram for the Ionic Drone market analysis.

3 Mission Profile

A clear and well-defined mission statement acts as a compass, providing a sense of direction and purpose to all stakeholders involved. It serves as the guiding force that directs the entire endeavour, ensuring that all aspects of the project are aligned with its ultimate purpose and objectives. Without a mission that is well-defined, comprehensive, and precise, it becomes increasingly difficult to finalize relevant requirements that will effectively support and enhance the project's mission. In this chapter, we discuss the mission profile and the corresponding flight plan of the PULSE built.

3.1. Mission

The initial requirements of the customer led to the Mission Objective Statement:

The product must be a light, live-time tracking UAV designed for research, which utilises plasma actuators as its sole control system, achieving better performance than similar competitors.

However, the lack of a specific mission profile did not allow for the identification of competitors and the generation of system requirements. As such, based on the previously performed market analysis, a list of missions with commercial potential was identified and compiled into 21 options: *Aerial photography, Wildfire inspection, Wildlife monitoring, Noise pollution mapping, Orography, Atmospheric monitoring, Package delivery, Jail patrolling, Border Patrolling, Light intensity surveying, Infrastructure inspection, Meteorology, Stealth surveillance, Area damage inspection, Agriculture field monitoring, Air pollution monitoring, Inspection of volcanic activities, Searching for survivors, Military target identification and definition, Attack drone, and Aircraft Maintenance.*

The 21 identified missions were categorized into different applications, including military, private, civilian, and scientific. After conducting a trade-off analysis [33], the chosen mission was silent noise mapping in urban areas. This selection is considered favourable because the propulsion group is one of the primary contributors to aircraft noise. By transitioning to glide flight during noise measurements, potential errors caused by sound interference from the propulsion system can be minimized.

To find the optimal location intended for the mission, an analysis was performed on the surrounding regions on Delft based on: proximity to nature reserves, proximity to regulated airspace and applicability of the scientific scope of the mission. To assess the proximity to regulated airspace, the Air Traffic Control Agency of the Netherlands (LVNL) was consulted and a map was used to determine the optimal area of interest[34].

Based on this, four target locations were selected. Two of them are nature reserves(Coepelduynen, Kennemerland) whereas the other two are small towns(Katwijk aan Zee, Noordwijk). These locations were decided to be optimal as Katwijk is a small touristic town compared to Noordwijk which is a larger town thus their noise footprint might differ, and moreover, the area of the natural reserves can be optimally covered under the specified range requirements.

Using Google Maps and online available sources[35], a preliminary characterisation of the area of interest was done in terms of its geography and limiting mission factors. The overview of each of the four selected regions is provided in Table 3.1.

Table 3.1: Mission location profile

Location	**Katwijk aan Zee**	**Coepelduynen**	**Noordwijk**	**Kennermerland**
Elevation $[m]$	2/11	5/25	3/25	6/14
Min. altitude $[m]$	51	With margin above min. elevation	40	With margin above min. elevation
Max. altitude $[m]$	131	145	145	134
Perimeter $[km]$	9.0	9.0	8.0	9.2
Area $[km^2]$	3.2	1.8	4.4	3.2
Flora	N/A	Short vegetation	N/A	Short vegetation
Fauna	N/A	Birds	N/A	Large grazers
Regulations	Flying above-uninvolved people	Permit for flying above nature reserves	Flying above uninvolved people	Permit for flying above nature reserves

Flight profile: Assuming a rectangular measurement area, two coverage patterns are possible: The Boustrophedon path[36] and Zamboni pattern[37], both of which can be seen in Figure 3.1. The green rectangle indicates the measurement area and the inter-line distance is given as d, which is a function of the on-board payload and required measurement resolution. The aircraft performs a gliding flight over the measurement area, beginning at altitude h_{max} and exiting the measurement area at altitude h_{min}. Subsequently, the aircraft performs a climbing turn, changing its heading by $180°$ and climbing from h_{min} to h_{max}. Measurement area width is limited by the aircraft's glide ratio, while overall range determines measurement area length. The UAV shall be designed to perform both coverage patterns.

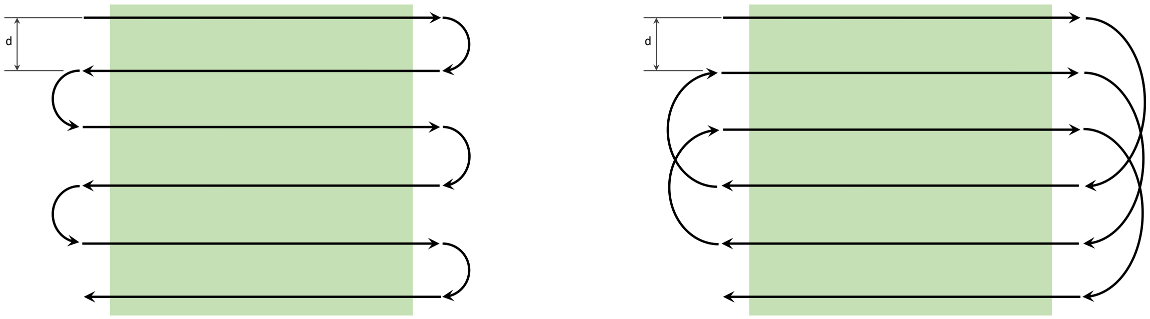

(a) Boustrophedon flight pattern

(b) Zamboni flight pattern

Figure 3.1: Area coverage flight patterns

Performance requirements can be derived from the flight patterns, namely, minimum turn radius, maximum climb angle, glide ratio and overall range. To estimate these parameters, the following assumptions are made:

- The measurement area is assumed to be 900 m × 1000 m (length×width), approximately equal to the urban area of Katwijk.
- The unpowered gliding flight happens along the width of the measurement area, i.e., 900 m
- As the nature reserves do not have any spatial resolution limitations, the houses in Katwijk and Noordwijk were taken into consideration. The minimum distance between streets is about 50m. This gives a value of the spatial resolution and hence a maximum radius of the turn requirement.
- Post the gliding phase, a powered climbing turn is performed. Here it is assumed that the required thrust is produced as soon as the propellers are powered up.
- It is assumed that the velocity remains constant, for both the gliding and the climbing turning phase.

- The operational ceiling for the mission is set at 120 meters, while the lower limit for operation is defined at 55 meters. This is because the highest building in Katwijk stands at approximately 50 meters. Therefore, for this particular mission, we can utilize an altitude of 65 meters.

Given equal mission parameters, by visual inspection, it can be concluded that a Boustrophedon pattern is more demanding towards turn and climb performance, while the overall range requirement is determined by the Zamboni flight path. The glide ratio, or C_L/C_D is equal for both patterns and is given by Equation 3.1. The height difference is taken from the most limiting area, i.e., Katwijk aan Zee.

$$Glide\ Ratio = \frac{C_L}{C_D} = \frac{w}{h_{max} - h_{min}} = 13.84 \tag{3.1}$$

The range requirement was initially given by the customer to be 10km. But, with the mission profile slected, a new range is calculated and turns out to be about 20km. The rest of the performance parameters can be found in chapter 7.

3.2. Payload Selection

Considering the mission objective, noise mapping requires specific identification of noise sources in flight, together with an assessment of the general and specific noise levels. This introduces three possible payload solutions: an array of random incidence microphones for noise identification, one targeted free field microphone for noise assessment of a specific source and a noise camera both for the loudest noise source identification in real-time. The sound level measurements also need to be labelled in terms of altitude and position to establish the spatial distribution of the noise sources. The altitude can be established using a barometric altitude sensor, and the location can be obtained using the Ground Positioning System (GPS).

4 Technical Risk Management

4.1. Risk Identification & Assessment

In order to carefully carry out a technical risk assessment, all possible risks need to be identified. A list of all identified risks including their explanation is provided below. Furthermore, severity (S) and probability (P) scores are assigned to each risk according to Table 4.1.

Table 4.1: Risk assessment score allocation

Severity	Score	Probability	Score
Negligible	1	Very low	1
Marginal	2	Low	2
Critical	3	Moderate	3
Catastrophic	4	High	4
		Very high	5

A breakdown structure was set up in order to prevent overlapping risks. All risks include an identifier corresponding to the categories given in the breakdown structure and detailed subsystem risks have been identified.

- **RSK-SUP-01: Increased production costs. S = 3, P = 4**
  An increase in production costs can lead to either design trade-offs, an unfeasible design or unsatisfied cost requirements. Production costs are usually larger than material costs. Despite the small time span of the project, inflation is of topical importance and should be considered.
- **RSK-SUP-02: Material unavailability. S = 2, P = 4**
  This will lead to production delays, or the need to revise the design, affecting the schedule. Furthermore, it might lead to cost requirements not being met. Material costs are usually smaller than production costs. Despite the small time span of the project, inflation is of topical importance and should be considered.
- **RSK-SUP-03: Test facility unavailability. S = 2, P = 2**
  This can affect system or subsystem testing, verification, or validation for flight. Such a case mainly affects scheduling requirements, which would not be significant in this project's case. When aiming for an aircraft in the 'open' category only small test facilities are needed.

- **RSK-SUP-04: Production delays. S = 2, P = 2**
  This can lead to missed deadlines. Such a case mainly affects scheduling requirements, which do not pose great significance to the DSE project. Not a common thing for technical parts, in particular when low in rarity.
- **RSK-SUP-05: Increased shipping costs. S = 2, P = 1**
  This could occur when product origin changes. An increase in shipping costs is highly unlikely since they are mostly preset before ordering.
- **RSK-SUP-06: Shipping damage. S = 2, P = 2**
  This can lead to production delays. Such a case mainly affects scheduling requirements or may slightly increase costs which would not be significant in this project's case. The probability is low, as high-value parts are handled carefully when designated shipping is used.
- **RSK-SUP-07: Shipping delays. S = 2, P = 3**
  This can lead to production delays. Such a case mainly affects scheduling requirements, which would not be significant in this project's case. With the world currently experiencing a transportation crisis this is likely to happen for some of the materials/products.
- **RSK-REG-01: Mandatory pre-flight inspection. S = 3, P = 1**
  This results in more man hours needed subsequently increasing operation costs. The probability of regulations changing in the small time span of the project is small.
- **RSK-REG-02: Flight height requirement decrease. S = 3, P = 1**
  This could lead to a change in design, payload decisions and considerable alterations in the design. The probability of regulations changing in the small time span of the project is small.
- **RSK-REG-03: Mass requirement decrease. S = 4, P = 1**
  This drastically changes the design since weight is a driving factor in the design process. The probability of regulations changing in the small time span of the project is small.
- **RSK-STA-01: Customer requirement change. S = 4, P = 1**
  These can lead to design revisions, affecting the schedule. Most strict top-level requirements are set by the customer increasing the severity of this risk. However, the probability of this happening is low.
- **RSK-STA-02: Locals disturbance. S = 1, P = 1**
  Test flights may cause local disturbances to nearby households or companies. Since the aircraft is designed to be relatively quiet the probability is low.
- **RSK-STA-03: Local authorities disturbance. S = 2, P = 1**
  Local airport or test facility regulations may be violated with their respective consequences. Informing about regulations beforehand ensures a low probability of this happening.
- **RSK-STA-04: Customer requirement not met. S = 4, P = 2**
  To be decided with the customer if the requirement is a killer requirement. Violating a killer requirement would pose a great threat to the design outcome.
- **RSK-STA-05: Aircraft not profitable. S = 3, P = 1**
  To be decided with the customer if profitability is a killer requirement. This makes it not interesting for the commercial sector. Since drones are in high demand nowadays, such an innovative design will have a lot of potential buyers.
- **RSK-STA-06: Over-restraining requirements. S = 3, P = 3**
  This prevents the development of a feasible design solution. This prevents reaching an optimal design, decreasing technical performance. The high amount of stakeholders results in many stakeholder requirements. Without identifying killer requirements this thus is likely to happen.
- **RSK-DES-01: Low confidence intervals for VnV. S = 2, P = 3**
  This can result in poorly validated models, which might lead to wrong design decisions. Small design margins introduce a probability that the product will not achieve the desired technical performance. The probability is quite high, as the author's team lacks experience.
- **RSK-DES-02: Coding errors. S = 4, P = 3**
  This may result in overall false values. A coding error can lead to the failure of the design and/or mission, similar to calculation errors. Coding will most probably be a human process raising the chance of errors.
- **RSK-DES-03: Calculation errors. S = 4, P = 1**
  This may result in overall false values. A calculation error can lead to the failure of the design and/or mission. Calculations will mostly be done by computers decreasing the probability of errors.
- **RSK-DES-04: Autopilot catastrophic flaw. S = 4, P = 1**
  Control of the aircraft will be lost. Since no pilot is controlling the aircraft during most flight phases, a total failure of the autopilot most likely leads to a crash. The likelihood is reduced due to thorough verification.
- **RSK-DES-05: Autopilot partial flaw. S = 3, P = 2**
  See RSK-DES-04. Less severity, higher likelihood.

- **RSK-DES-06: Operating system crash. S = 4, P = 1**
  The aircraft will be unable to control its subsystems causing catastrophic problems. The probability of software experiencing this is low.
- **RSK-DES-07: Considerable signal error (sent to subsystems). S = 3, P = 1**
  This will decrease subsystem performance considerably. Due to wired connections between subsystems, this is unlikely to happen.
- **RSK-DES-08: Higher-than-expected autopilot model errors. S = 2, P = 2**
  The performance of the autopilot is partly violated resulting in errors in control input. Not too likely to happen since assumptions are rare in this regard.
- **RSK-DES-09: Plasma actuators operation modelling error. S = 3, P = 1**
  Plasma actuator control will be tested with simulations. Modelling errors could eventually result in insufficient plasma performance.
- **RSK-DES-10: Landing causes higher stress than estimated. S = 1, P = 1**
  This is a structural design flaw. It could damage the system, but only while landing at the base. Therefore severity is low.
- **RSK-DES-11: Wires not designed for the actual weather conditions. S = 4, P = 1**
  This is a design flaw in the electrical subsystem. This could result in (partial) failure of the electrical system. The mission area is known so this is unlikely to happen.
- **RSK-DES-12: Degradation of power source is underestimated. S = 1, P = 1**
  This is a design flaw resulting in considerable power reduction over time. Degradation is a slow process so severity is low. Since conventional power sources are used degradation time is well-known.
- **RSK-DES-13: Faulty GPS algorithm. S = 4, P = 1**
  Receiving wrong positioning information. Due to the high reliability of GPS systems, this is highly unlikely, although the severity will be high.
- **RSK-DES-14: Velocity calculation undesirably inaccurate. S = 2, P = 2**
  An avionics failure refers to either the instrumentation or the responsible software failing. This event has a marginal effect on the aircraft's performance and its probability is low.
- **RSK-DES-15: Unexpected interference between propeller and plasma. S = 3, P = 2**
  The interaction of plasma with fast-moving surfaces such as a propeller is barely investigated. This could cause a critical failure with a low probability since there is no apparent reason that this would happen.
- **RSK-DES-16: Catastrophic vibration mode. S = 4, P = 1**
  This event accounts for the case when a catastrophic mode is not predicted by the simulation software used. This could lead to a catastrophic failure but has a low probability as such a major effect is easily detectable by simulations.
- **RSK-DES-17: Stress concentrations underestimated. S = 3, P = 1**
  The stress concentrations being underestimated during the design phase could cause a critical failure, making mission success questionable. It has a low probability due to the advanced calculation and modelling techniques used.
- **RSK-DES-18: Measurement algorithm introduces unwanted errors. S = 2, P = 2**
  The UAV's instrumentation provides measurements with higher errors than expected. Such an event has marginal severity and a low probability due to the robustness of the algorithms that utilise these values.
- **RSK-DES-19: TRL of plasma actuators. S = 4, P = 3**
  The use of plasma actuators for control might prove inefficient. In the case this technological gap cannot be covered, the mission goal would be partially violated, resulting in catastrophic failure. The probability of this cannot be precisely assessed, as literature shows potential for covering this technological gap.
- **RSK-SCH-01: Delay of own product. S = 2, P = 3**
  These relate to the improper management of the schedule, leading to delays, or missed deadlines. Such a case mainly affects scheduling requirements, which would not be significant in this project's case. During a ten-week project with ten team members and several external parties, this is common to occur.
- **RSK-IND-01: Chemical contamination. S = 3, P = 1**
  Chemical contamination of the area can interfere with the aircraft's functions and subsystems, possibly jeopardising the completion of the mission. Such a probability, however, is low in the Netherlands.
- **RSK-IND-02: Explosion. S = 4, P = 1**
  A similar event as RSK-IND.01, but related to explosion events. Its severity is higher, as explosions can severely damage the structure and aerodynamics of the UAV.
- **RSK-IND-03: Radiation contamination. S = 4, P = 1**
  Similar to RSK-IND-02, but the radiation would mainly affect electronics, causing multiple bit-flips and possibly damaging electronics.

- **RSK-INF-01: Take-off site unavailable. S = 4, P = 2**
  In case the area of interest is relatively remote, it is probable that the take-odd locations are limited and potentially unavailable. The severity of such an event is critical, as it can easily render take-off impossible. The probability is low because the prerequisites for the setup of launch systems are so low that it is rare to have no take-off sites available.
- **RSK-INF-02: Roadworks. S = 2, P = 3**
  Roadworks would impede the access of the transportation vehicle to the area of interest. Its severity is relatively low as detours can be found, but the probability is high in a modern country.
- **RSK-PER-01: Shooting at the drone. S = 4, P = 1**
  Dependent on the mission attacks on the drone need to be considered. Due to the missions being performed in the Netherlands, this is highly unlikely.
- **RSK-PER-02: Collision with other aircraft. S = 4, P = 1**
  This will result in catastrophic failure of the whole system. Collisions are rare due to the small dimensions of the UAV.
- **RSK-AIR-01: Software running errors. S = 3, P = 2**
  Undermines the validity of the flight control subsystem output, however, flight control software is widely available.
- **RSK-AIR-02: Plasma actuator burning. S = 3, P = 3**
  Local heating may occur in plasma actuators resulting in damage to subsystems. Local melting/burning can partially peril a subsystem function.
- **RSK-AIR-03: deploy failure. S = 2, P = 2**
  Aircraft will not be able to land using its primary landing system. A belly landing should therefore probably be performed increasing damage chances.
- **RSK-AIR-04: short circuit. S = 4, P = 3**
  Short circuit directly results in the loss of electrical subsystems. Such an event can lead to the failure of the aircraft's electrical systems, losing control and crashing itself. Could develop in the electrical system and power systems making them likely to occur.
- **RSK-AIR-05: Electrical Power loss. S = 4, P = 2**
  This results in the loss of all electrical systems and subsequently total failure of the aircraft.
- **RSK-AIR-06: ground station signal loss. S = 1, P = 2**
  Loss of input from the ground station. The aircraft autopilot is still functioning lowering system impact.
- **RSK-AIR-07: GPS signal loss. S = 1, P = 1**
  Loss of aircraft positioning. Since aircraft will remain in the visual line of sight this is easily dealt with.
- **RSK-AIR-08: Propeller failure. S = 2, P = 2**
  The loss of propulsion results in the immediate initiation of the landing procedure. Aircraft needs to be
- **RSK-AIR-09: Engine failure. S = 2, P = 2**
  Such an event could temporarily render the completion of the mission impossible, but can easily be flown again by replacing the broken component. For such a conventional design, the possibility is low.
- **RSK-AIR-10: Hole formation. S = 3, P = 2**
  This endangers the subsystems' structural integrity and protection. A hole can severely decrease the performance of the aircraft in aerodynamics, structures, controls, etc. This only occurs in the long run and is unlikely for materials used in similar aircraft.
- **RSK-AIR-11: Crack development & propagation. S = 4, P = 2**
  This endangers the structural integrity and protection of subsystems. A crack, if left untreated, can cause complete structural failure of the aircraft. This only occurs in the long run and is unlikely for materials used in similar aircraft.
- **RSK-AIR-12: Corrosion. S = 4, P = 2**
  This endangers subsystems' structural integrity and protection. Corrosion mainly affects the structure, undermining its rigidity. It can lead to complete failure if left untreated. This only occurs in the long run and is unlikely for materials used in similar aircraft.
- **RSK-AIR-13: Flutter. S = 4, P = 2**
  This can lead to resonance, which in turn might lead to structural failure. It takes place in aerodynamic surfaces, the failures of which lead to complete mission failure most of the time. Unlikely to happen for well-designed aircraft, slightly higher for an inexperienced design group.
- **RSK-AIR-14: Noise. S = 4, P = 1**
  This can lead to resonance, which in turn might lead to structural failure. This kind of vibration can cause failure of structural components. Less likely to happen than flutter.

- **RSK-AIR-15: Buffet. S = 4, P = 1**
  This can lead to structural failure or impede stability for a short period. This kind of vibration can cause failure of structural components. Less likely to happen than flutter.
- **RSK-AIR-16: (Payload) Data link loss. S = 1, P = 4**
  No communication is possible or there is not enough bit-rate available for all the data, losing important payload data if not saved. This is considered not unlikely to occur. However, data storage is cheap and live data is not essential thus severity is considered low.
- **RSK-AIR-17: (Payload) Instrument over-saturation. S = 1, P = 4**
  This results in payload data loss. This can easily happen with overexposure of the camera, but the severity is low since the settings can be adjusted and no damage is caused.
- **RSK-AIR-18: (Payload) Detachment. S = 4, P = 1**
  This results in material loss and the inability to continue measurements. However, it is unlikely for this to happen since the payload will be housed internally. The severity would be very high.
- **RSK-LAU-01: Launch to the ground. S = 2, P = 2**
  Direct launch into the ground and thus immediate crash. This can happen if the launcher fails to impart adequate velocity and it launches below the stall speed.
- **RSK-LAU-02: Launch system failure. S = 1, P = 2**
  The launch catapult might fail to launch the aircraft. This is considered unlikely since the catapult will be a relatively simple system since it is expected to be an elastic catapult. The severity is low since the UAV is unlikely to be damaged if it does not leave the launcher.
- **RSK-LAN-01: Landing structural failure. S = 2, P = 3**
  Since the parachute will not decelerate the aircraft to zero velocities. However, the damage is not likely to be significant since the speeds are low.
- **RSK-GRO-01: Aircraft signal loss (ground station). S = 2, P = 4**
  Control input for aircraft from the ground station can become unattainable. This is considered possible, but not high severity since the aircraft is expected to have a return to home mode.
- **RSK-WEA-01: Excessive Rain. S = 3, P = 4**
  If not waterproof this can damage the aircraft subsystems. Assuming the aircraft is not waterproof this could damage electrical subsystems and impede the effectiveness of plasma actuators. Rain is very likely to occur in the testing environment.
- **RSK-WEA-02: Hail. S = 2, P = 2**
  Hailstones can inflict structural damage, or affect other subsystems sensible to shocks. Due to the hailstone's large relative size compared to the drone, it can cause significant structural damage. Testing is done during summer time making hailstone unlikely to occur.
- **RSK-WEA-03: Frost. S = 2, P = 1**
  Considerable increase in drag and reduction of lift.
- **RSK-WEA-04: Lightning. S = 4, P = 1**
  A lightning strike can impede telecommunications, inflict structural damage, or affect power generation. High electrical discharges can completely destroy onboard and ground electronic equipment. Lightning hitting the aircraft is unlikely but will result in catastrophic damage.
- **RSK-WEA-05: Solar storm. S = 3, P = 1**
  This can affect all electronic components on board the aircraft, from the flight controller to the payload. Electromagnetic pulses can cause bit-flips and other damage, the impact of which varies based on the hard/software domain affected. Severe natural occurrences are unlikely, and artificial causes are also rare.
- **RSK-WEA-06: Cosmic rays. S = 3, P = 1**
  This can affect all electronic components on board the aircraft, from the flight controller to the payload. Cosmic rays can cause bit flips, the impact of which varies based on the hard/software domain affected.
- **RSK-WEA-07: Severe wind gusts. S = 3, P = 2**
  These can affect the stability of the aircraft. An unexpected wind gust can also break aerodynamic surfaces. Wind gusts are generally a common event, but the probability of them causing a complete failure is very low.
- **RSK-FLO-01: Bird strike. S = 4, P = 1**
  This most likely results in catastrophic failure, otherwise damage will be significant. This can lead to catastrophic failure but is considered very unlikely.
- **RSK-FLO-02: Tree collision. S = 3, P = 2**
  This most likely results in catastrophic failure, otherwise damage will be significant.

- **RSK-URB-01: Building collision. S = 4, P = 1**
  This most likely results in catastrophic failure, otherwise damage will be significant. However, buildings are easily visible and can be avoided.
- **RSK-URB-02: Wire collision. S = 4, P = 3**
  This most likely results in catastrophic failure, otherwise damage will be significant. This is considered more likely than a building collision since wires can be difficult to spot.

A total of 76 technical risks were identified and assessed that could form a threat to the technical design. Although being high in number this amount can be justified since the risks can be easily mitigated by little mitigation measurements. The breakdown structure also serves as a helping hand for keeping a risk overview.

4.2. Risk Map and Mitigation

In order to gain a general overview of the characteristics of the mission risks, a so-called risk map can be constructed based on the risk assessment done in section 4.1. By characterising its severity and probability at once, every risk can be quantified by its risk score which is defined as in Equation 4.1.

$$Risk\ score = Severity\ score \cdot Probability\ score \tag{4.1}$$

The risk score and the risk map indicate the priority of the risks and help identify the risks which pose the highest threat to the mission and thus require mitigation measurements.

Pre-Mitigation Risk Map

A first assessment is done before any mitigation measures are applied. The risk map associated with the initial risks is presented in Table 4.2.

Table 4.2: Risk map before mitigation

Severity of the event		Probability of Event 1	2	3	4	5
	4	RSK-REG-03 RSK-STA-01 RSK-DES-03 RSK-DES-04 RSK-DES-06 RSK-DES-11 RSK-DES-13 RSK-DES-16 RSK-IND-02 RSK-IND-03 RSK-PER-01 RSK-PER-02 RSK-AIR-14 RSK-AIR-15 RSK-AIR-18 RSK-WEA-04 RSK-FLO-01 RSK-URB-01	RSK-STA-04 RSK-INF-01 RSK-AIR-05 RSK-AIR-11 RSK-AIR-12	RSK-DES-02 RSK-DES-19 RSK-AIR-04 RSK-URB-02		
	3	RSK-REG-01 RSK-REG-02 RSK-STA-05 RSK-DES-09 RSK-DES-17 RSK-IND-01 RSK-WEA-06 RSK-DES-07	RSK-DES-05 RSK-DES-15 RSK-AIR-01 RSK-AIR-10 RSK-WEA-07 RSK-FLO-02	RSK-STA-06	RSK-SUP-01 RSK-WEA-01	
	2	RSK-SUP-05 RSK-STA-03 RSK-WEA-03 RSK-WEA-05	RSK-SUP.-03 RS-SUP-04 RSK-SUP-06 RSK-DES-08 RSK-DES-14 RSK-DES-18 RSK-AIR-08 RSK-AIR-09 RSK-LAU-01 RSK-WEA-02	RSK-SUP-07 RSK-DES-01 RSK-SCH-01 RSK-INF-02 RSK-LAN-01	RSK-SUP-02 RSK-GRO-01	
	1	RSK-STA-02 RSK-DES-10 RSK-DES-12 RSK-AIR-07	RSK-AIR-06 RSK-LAU-02		RSK-AIR-16 RSK-AIR-17	

Table 4.3: Risk map after mitigation

Severity of the event		Probability of Event 1	2	3	4	5
	4	RSK-REG-03 RSK-STA-01 RSK-DES-03 RSK-DES-04 RSK-DES-06 RSK-DES-11 RSK-DES-13 RSK-DES-16 RSK-IND-02 RSK-IND-03 RSK-PER-01 RSK-PER-02 RSK-AIR-14 RSK-AIR-15 RSK-AIR-18 RSK-WEA-04 RSK-AIR-11 RSK-AIR-12 RSK-STA-04 RSK-INF-01	RSK-DES-02 RSK-AIR-04 RSK-URB-02			
	3	RSK-REG-01 RSK-REG-02 RSK-STA-05 RSK-DES-09 RSK-IND-01 RSK-WEA-06 RSK-WEA-07 RSK-AIR-10 RSK-FLO-01 RSK-URB-01 RSK-AIR-01 RSK-FLO-02 RSK-DES-07	RSK-DES-05 RSK-DES-15 RSK-DES-19 RSK-WEA-01 RSK-STA-06 RSK-AIR-05			
	2	RSK-SUP-05 RSK-STA-03 RSK-WEA-03 RSK-WEA-05 RSK-DES-17	RSK-SUP-03 RSK-SUP-04 RSK-DES-08 RSK-DES-14 RSK-DES-18 RSK-AIR-08 RSK-AIR-09 RSK-LAU-01 RSK-WEA-02	RSK-SUP-07 RS-.DES-01 RSK-SCH-01 RSK-INF-02	RSK-SUP-01 RSK-SUP-02 RSK-GRO-01	
	1	RSK-STA-02 RSK-DES-10 RSK-DES-12 RSK-AIR-07	RSK-AIR-06 RSK-LAU-02 RSK-SUP-06 RSK-LAN-01		RSK-AIR-16 RSK-AIR-17	

Mitigation Procedures

In order to handle the most severe risks the following mitigation procedures are implemented:

- **MIT-1 Budget margins increase** Increasing budget margins allows for more design freedom.
- **MIT-2 Weather forecast** Using an advanced weather forecast system before a flight can decrease damage due to bad weather.

- **MIT-3 Ensure material endurance** Using a stainless material that does not fail easily under structural shocks such as projectiles and landing impact.
- **MIT-4 Code verification and validation** Verifying and validating codes and software reduces the chance of mistakes made
- **MIT-5 Closed electrical circuit** Protecting the electrical circuit by encapsulating it prevents short circuits.
- **MIT-6 Flight location mapping** This includes studying flight locations beforehand in order to prevent collisions with nearby obstacles.
- **MIT-7 Killer requirement monitoring** Throughout the design process requirements should be closely monitored in order to identify requirements that turn into killer requirements. These then need to be discussed with stakeholders.
- **MIT-8 Test flight planning** Test flights should be planned well in advance and should not rely on single days but rather on bigger time spans in order to prevent take-off site unavailability.
- **MIT-9 Subsystem redundancy** Assuring redundancy for more likely-to-fail subsystems ensures the continuity of subsystem functions.
- **MIT-10 Plasma actuator assistance** The TRL of plasma actuators can be assessed and design iterations can be performed. Given the existing applications of plasma actuators, further literature research and collaboration with other research parties can prevent the failure of plasma technology in this project.

The mitigation measurements mainly focus on mitigating the most severe risks. However, the mitigation procedures are not risk-specific, thus each procedure can cover more risks and decrease the probability, and/or the severity of the corresponding risk.

Table 4.2 entails the complete overview of the associated risks, their initial severity and probability scores, the corresponding mitigation procedures and their Mitigated Severity Score (MSS), Mitigated Probability Score (MPS) and Mitigated Risk (MR) are depicted.

Post-Mitigation Risk Map

Each mitigated risk is depicted in Table 4.3. As shown, no risks fall within the non-tolerated risk zone resulting in a successful mitigation process.

4.3. Contingency Plan

In order to address the situation in case one of the risks shall occur, the contingency plan aims to provide solutions and procedures to mitigate and contain the effect of the risk. The main focus is on risks that remain at levels higher or equal to 8 after mitigation. For each risk, the carried-out actions are stated.

- **RSK-SUP-01: Increased production costs** A design iteration must be conducted upon which cheaper manufacturing methods are imposed.
- **RSK-SUP-02: Material unavailability** Similar to RSK-SUP-01, an iteration has to be done, in which cheaper materials are considered.
- **RSK-DES-02: Coding errors** An investigation of the code in multiple levels would be required to locate the error. This includes system, integration and unit tests in this specific order so that the error is located efficiently.
- **RSK-AIR-04: Short circuit** Hardware inspection is required, so that the point of failure is located. Subsequently, depending on the nature of the flaw, additional protection needs to be added or the architecture needs to be redesigned.
- **RSK-URB-02: Wire collision** Investigation of the sensors, navigation and ranging algorithms would be required. The hardware components could be tested similarly to RSK-AIR-04, while software can be tested in a way similar to RSK-DES-02.
- **RSK-STA-06: Over-restraining requirements** Discussion with responsible stakeholders to relax particular requirements.
- **RSK-GRO-01: Aircraft signal loss (ground station)** An investigation of the mission is suggested to find the reason why it failed and attempt to fix it. The focus should be on the communication subsystem for apparent reasons.

4.4. SWOT Analysis

To aid and complement technical risk assessment, the analysis of major strengths, weaknesses, opportunities and threats of the technical aspects of the UAV has been revised based on the updated mission profile and risk management. The SWOT analysis is compiled in Figure 4.1. It must be noted that the SWOT diagram is expected to change as the drone is developed from concept to final design.

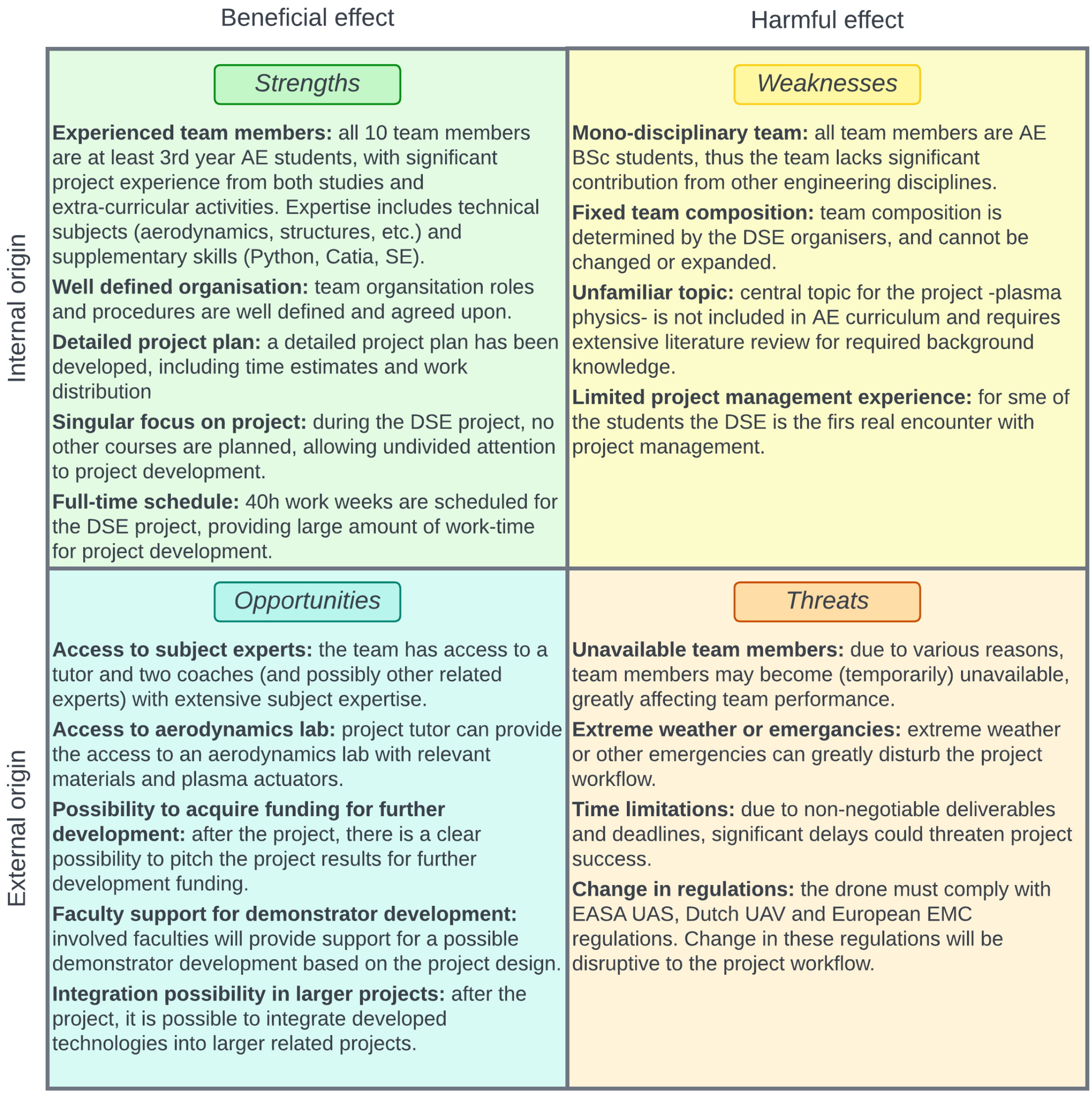

Beneficial effect

Harmful effect

Internal origin

Strengths

Experienced team members: all 10 team members are at least 3rd year AE students, with significant project experience from both studies and extra-curricular activities. Expertise includes technical subjects (aerodynamics, structures, etc.) and supplementary skills (Python, Catia, SE).

Well defined organisation: team organsitation roles and procedures are well defined and agreed upon.

Detailed project plan: a detailed project plan has been developed, including time estimates and work distribution

Singular focus on project: during the DSE project, no other courses are planned, allowing undivided attention to project development.

Full-time schedule: 40h work weeks are scheduled for the DSE project, providing large amount of work-time for project development.

Weaknesses

Mono-disciplinary team: all team members are AE BSc students, thus the team lacks significant contribution from other engineering disciplines.

Fixed team composition: team composition is determined by the DSE organisers, and cannot be changed or expanded.

Unfamiliar topic: central topic for the project -plasma physics- is not included in AE curriculum and requires extensive literature review for required background knowledge.

Limited project management experience: for sme of the students the DSE is the firs real encounter with project management.

External origin

Opportunities

Access to subject experts: the team has access to a tutor and two coaches (and possibly other related experts) with extensive subject expertise.

Access to aerodynamics lab: project tutor can provide the access to an aerodynamics lab with relevant materials and plasma actuators.

Possibility to acquire funding for further development: after the project, there is a clear possibility to pitch the project results for further development funding.

Faculty support for demonstrator development: involved faculties will provide support for a possible demonstrator development based on the project design.

Integration possibility in larger projects: after the project, it is possible to integrate developed technologies into larger related projects.

Threats

Unavailable team members: due to various reasons, team members may become (temporarily) unavailable, greatly affecting team performance.

Extreme weather or emergancies: extreme weather or other emergencies can greatly disturb the project workflow.

Time limitations: due to non-negotiable deliverables and deadlines, significant delays could threaten project success.

Change in regulations: the drone must comply with EASA UAS, Dutch UAV and European EMC regulations. Change in these regulations will be disruptive to the project workflow.

Figure 4.1: Revised Technical SWOT Diagram

5 Project Management

Creating a detailed plan of how the design should work is crucial for achieving high-quality results. In this chapter, the processes that the product should execute and the steps that can be followed after the DSE are discussed. section 5.1 describes how the design accomplishes its mission. On the other hand, section 5.2 gives an overview of the expected design activities after the DSE ends.

5.1. Functional Diagrams

Systems are characterised by their actions. In industry nomenclature, the actions of a system are named functions, and each function can have multiple levels of complexity. To capture all of these levels, a Functional Flow Block Diagram (FFBD) and a Functional Breakdown Structure (FBS) are created.

The first step in defining the FFBD is defining its highest-level flow. Level zero is defined as ”Perform Mission”. The related level 1 functions and the level 0 function are given in Figure 5.1.

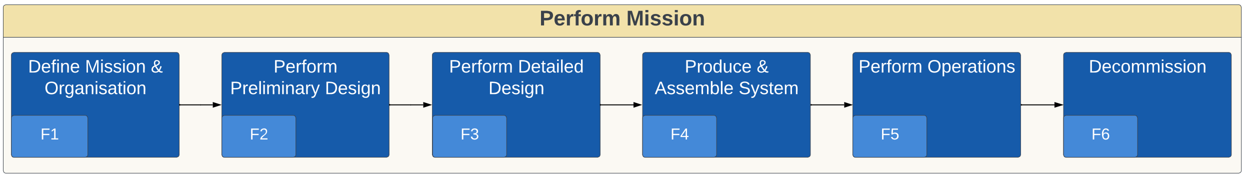

Figure 5.1: General Flow of Functional Flow Block Diagram

The FFBD seen in Figure 5.2 where the flow of functions, as denoted by the arrows, is 3 levels deep relative to the overall goal of ”Perform Mission”. Note that ”F5.3.4: Recover System” is in two locations at the flow, once in ”F5.3: Manage Emergencies” and once in ”F5.8: Perform Landing”. This was done since the recovery process in the two flow cases is the same, thus the same function can be re-used.

Figure 5.3 depicts the FBS of the mission. The functions are taken from the FFBD, and certain functions are broken down one more level to have a relative depth of 4 to the ”Perform Mission” Function. Note again that the aforementioned ”F5.3.4: Recover System” function is only listed as a sub-function of ”F5.3: Manage Emergencies”

5.2. Post-DSE Activities

When looking at the project as a whole, the DSE corresponds only to the conceptual and possibly the preliminary design phase. This means that a plan must be made, to indicate which activities should be followed, for the project to develop properly. Two tools are used, the Project Design and Development Logic, shown in Figure 5.4 and the Project Gantt Chart, shown in Figure 5.5. The former provides tasks in a flowchart, showing sequential, parallel and iterative relations between them. The latter shows the same tasks with respect to a time frame, enabling the scheduling of specific activities.

A common and crucial term in the figures is the Minimum Viable Product (MVP). This refers to the design approach of delivering a product with minimum features, receiving feedback from the customer, and iterating the design[1]. Since the customer of the project is currently one person, this allows the easy implementation of this design approach.

---

[1] agilealliance.org

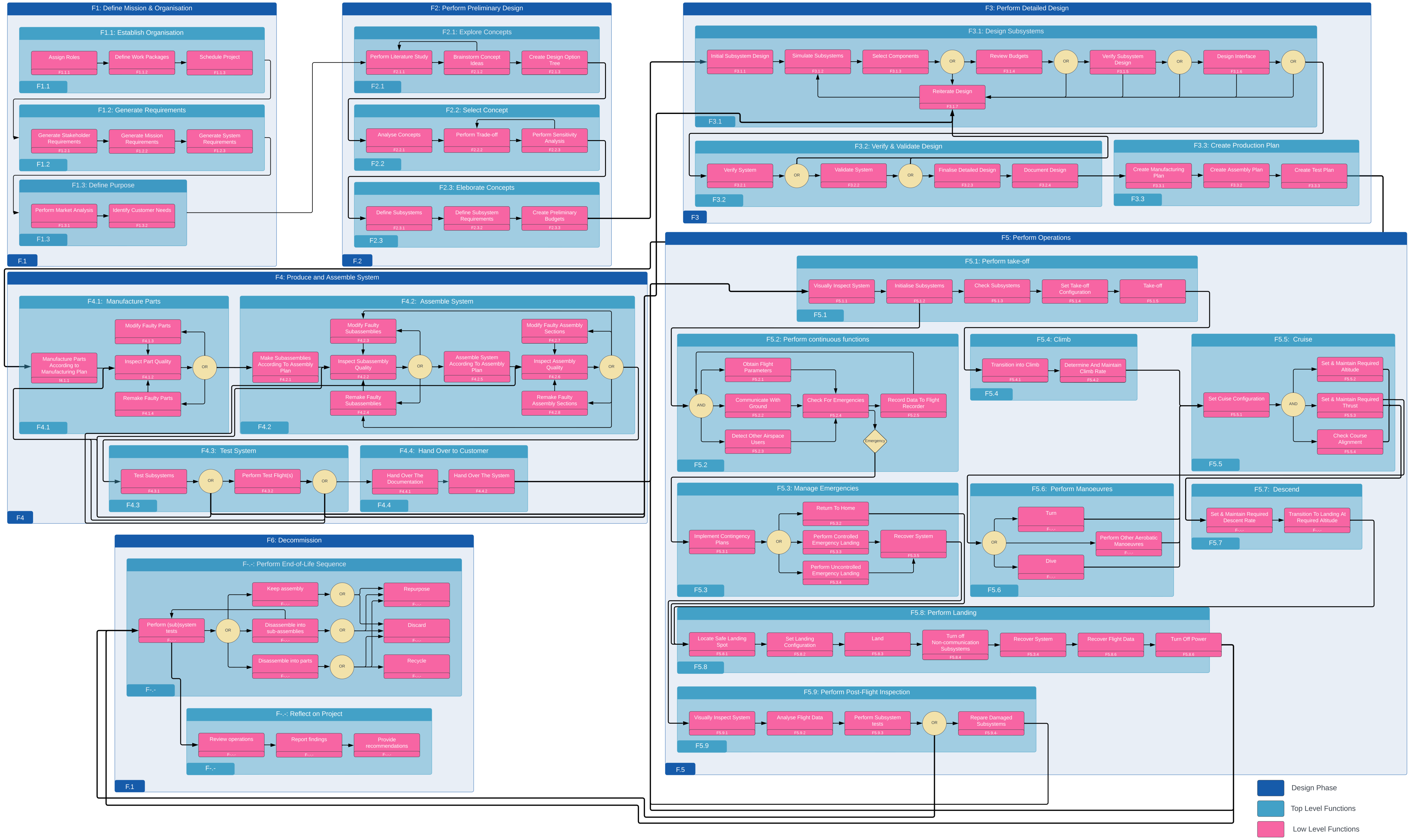

Figure 5.2: "Perform Mission" FFBD

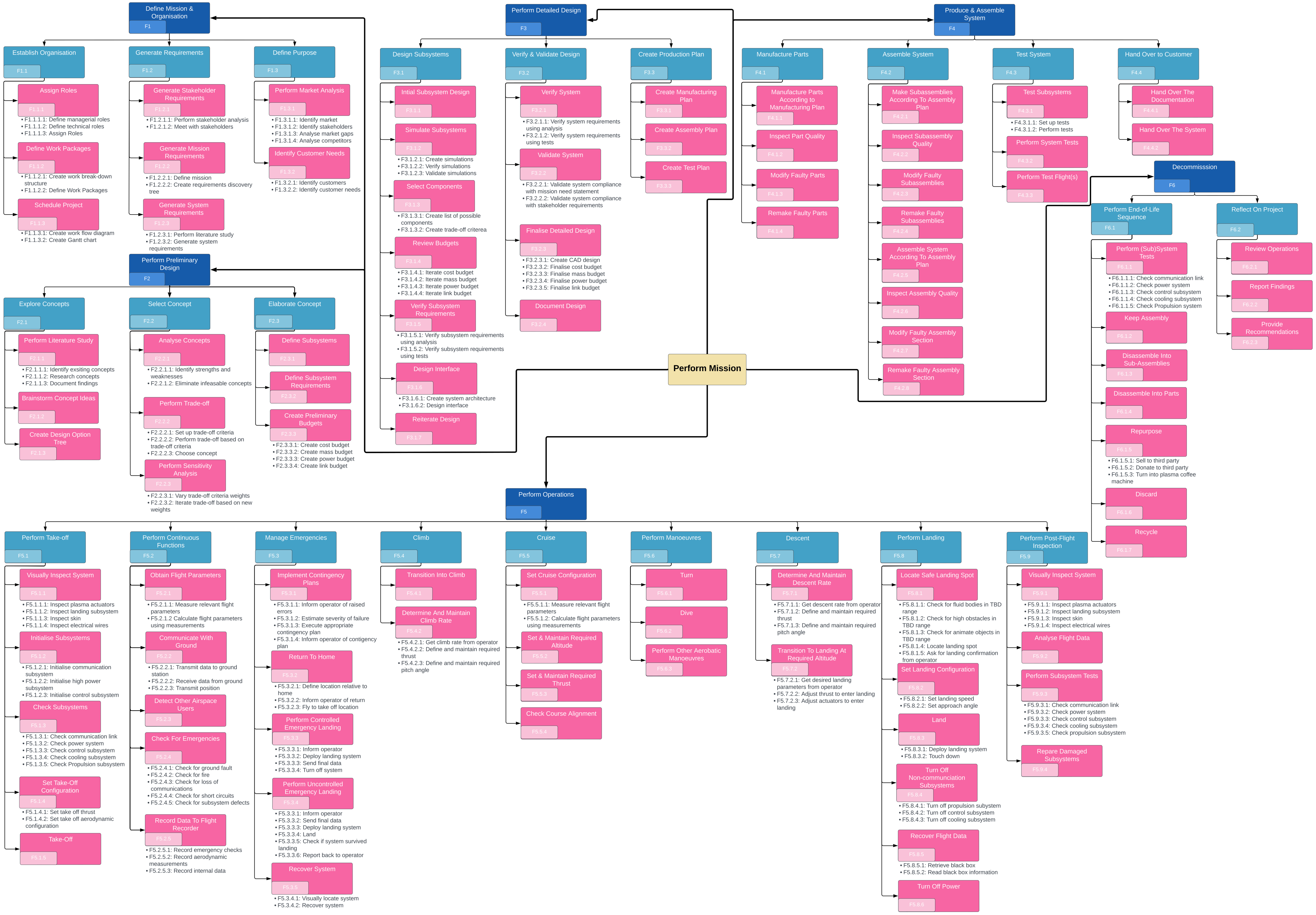

Figure 5.3: "Perform Mission" FBS

Figure 5.4: Project Design and Development Logic

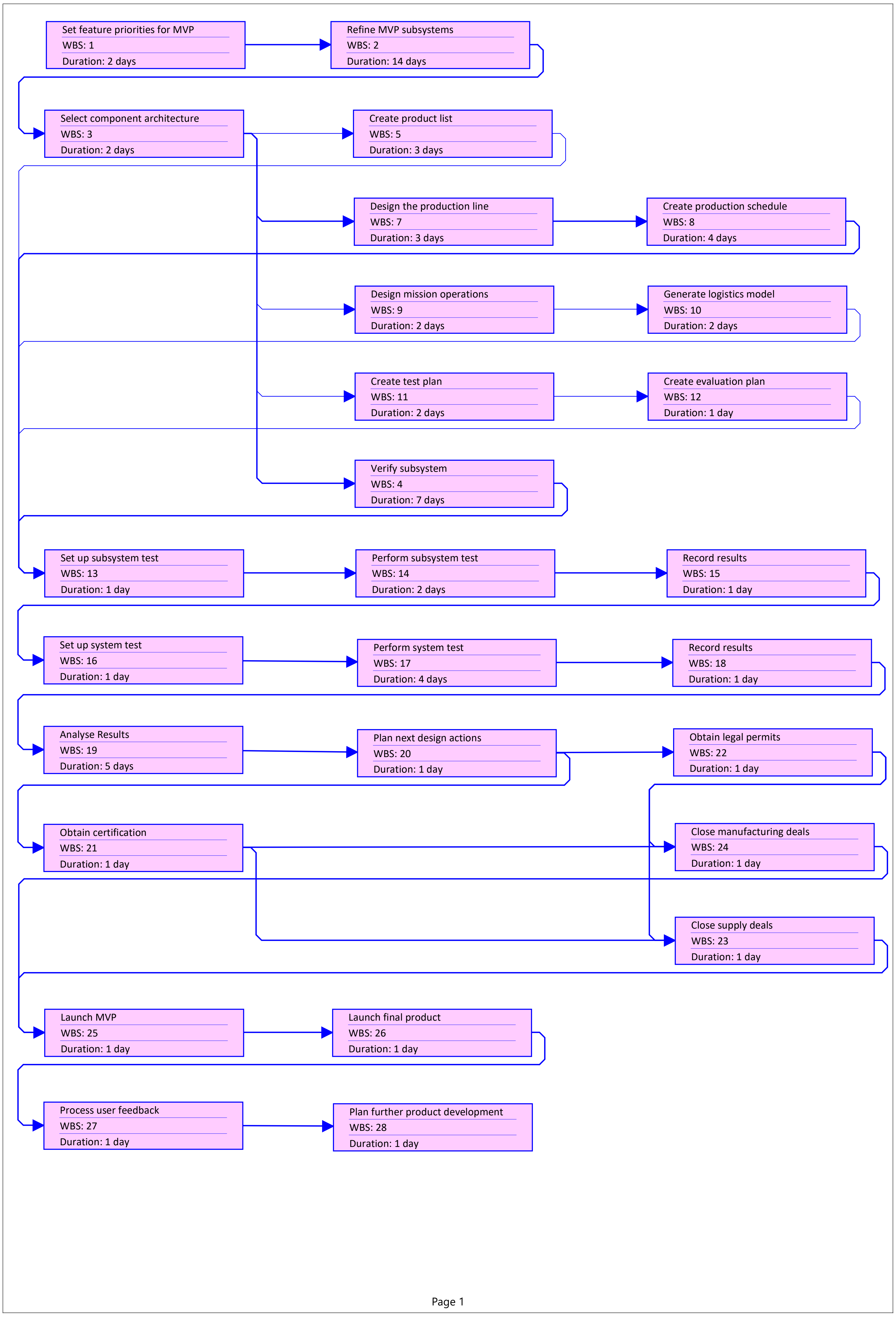

Figure 5.5: Project Gantt Chart

ID	WBS	ⓘ	Task Name	Duration	Start	Finish	Predecessors	Resource Names
1	1		Set feature priorities for MVP	2 days	Wed 21/06/23	Thu 22/06/23		
2	2		Refine MVP subsyster	14 days	Fri 23/06/23	Wed 12/07/2	1	
3	3		Select component architecture	2 days	Thu 13/07/23	Fri 14/07/23	2	
4	4		Verify subsystem	7 days	Mon 17/07/2	Tue 25/07/2	3	
5	5		Create product list	3 days	Mon 17/07/2	Wed 19/07/2	3	
6	7		Design the production line	3 days	Mon 17/07/23	Wed 19/07/23	3	
7	8		Create production schedule	4 days	Thu 20/07/23	Tue 25/07/23	6	
8	9		Design mission operations	2 days	Mon 17/07/23	Tue 18/07/23	3	
9	10		Generate logistics model	2 days	Wed 19/07/23	Thu 20/07/23	8	
10	11		Create test plan	2 days	Mon 17/07/2	Tue 18/07/2	3	
11	12		Create evaluation pla	1 day	Wed 19/07/2	Wed 19/07/2	10	
12	13		Set up subsystem tes	1 day	Wed 26/07/2	Wed 26/07/2	4,5,7,11,9	
13	14		Perform subsystem te	2 days	Thu 27/07/2	Fri 28/07/23	12	
14	15		Record results	1 day	Mon 31/07/2	Mon 31/07/2	13	
15	16		Set up system test	1 day	Tue 01/08/2	Tue 01/08/2	14	
16	17		Perform system test	4 days	Wed 02/08/2	Mon 07/08/2	15	
17	18		Record results	1 day	Tue 08/08/2	Tue 08/08/2	16	
18	19		Analyse Results	5 days	Wed 09/08/2	Tue 15/08/2	17	
19	20		Plan next design actic	1 day	Wed 16/08/2	Wed 16/08/2	18	
20	21		Obtain certification	1 day	Thu 17/08/2	Thu 17/08/2	19	
21	22		Obtain legal permits	1 day	Thu 17/08/2	Thu 17/08/2	19	
22	23		Close supply deals	1 day	Fri 18/08/23	Fri 18/08/23	20,21	
23	24		Close manufacturing deals	1 day	Fri 18/08/23	Fri 18/08/23	20,21	
24	25		Launch MVP	1 day	Mon 21/08/2	Mon 21/08/2	22,23	
25	26		Launch final product	1 day	Tue 22/08/2	Tue 22/08/2	24	
26	27		Process user feedbac	1 day	Wed 23/08/2	Wed 23/08/2	25	
27	28		Plan further product development	1 day	Thu 24/08/23	Thu 24/08/23	26	

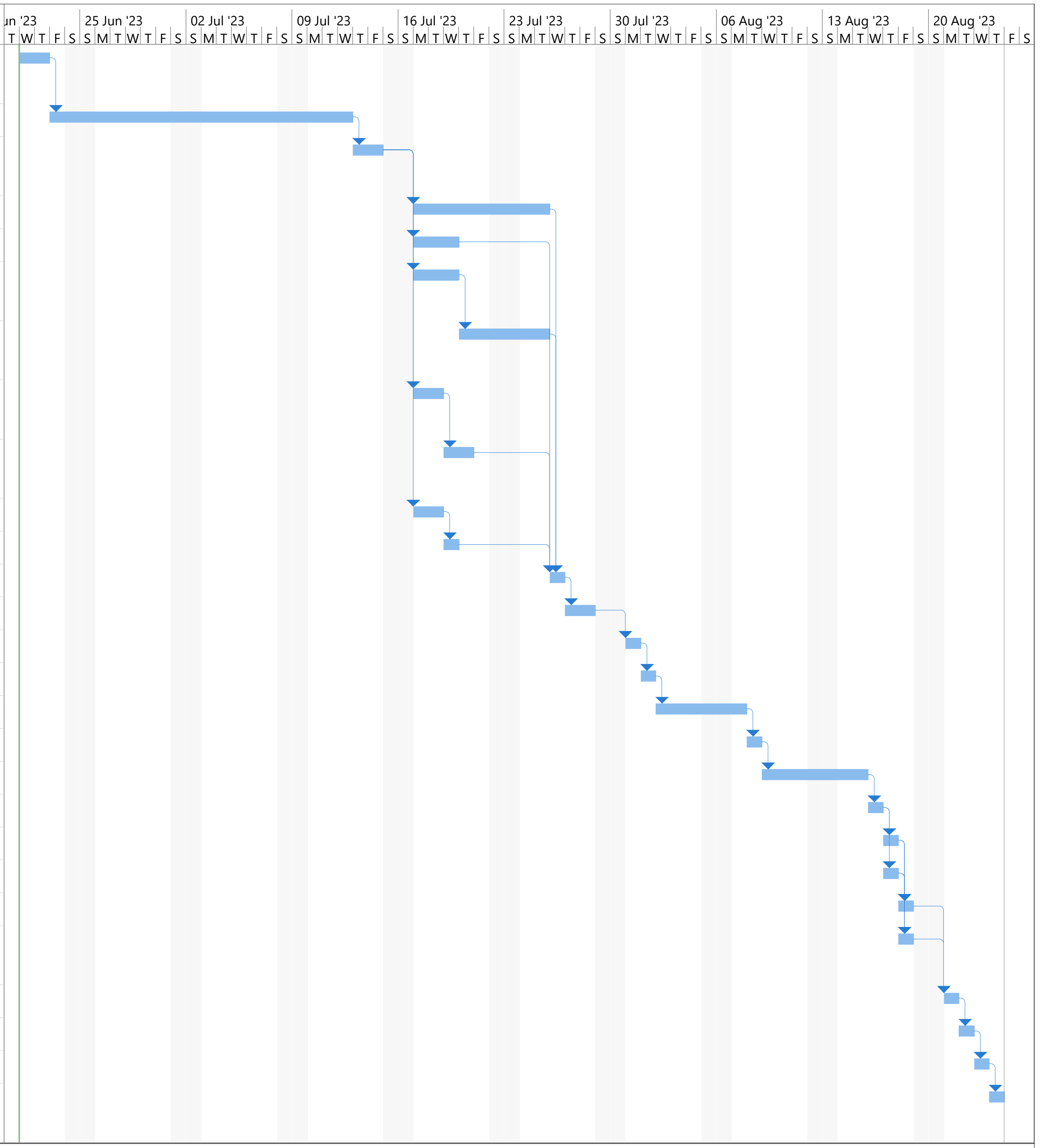

Project: POSTDSE
Date: Wed 21/06/23

Task	▬	Project Summary	┌─┐	Manual Task	▬	Start-only	[	Deadline	⬇
Split	┅	Inactive Task	▭	Duration-only	▬	Finish-only	]	Progress	─
Milestone	◆	Inactive Milestone	◇	Manual Summary Rollup	▬	External Tasks	▬	Manual Progress	─
Summary	┌─┐	Inactive Summary	┌─┐	Manual Summary	┌─┐	External Milestone	◆		

6 Design Methodology

This chapter covers the initial steps taken towards the detailed design of the PULSE UAV. The system is broken down into subsystems and their interfaces are visualised using an N2 chart. This process helps in designing the subsystems and defining the subsystem requirements. Furthermore, the initial sizing of the aircraft is done in terms of class I estimations, providing baseline values for mass, aerodynamic performance and mission profile.

6.1. Conceptual Trade-Off Results

In order to follow the design path from conceptual to preliminary to final design, the results of concept trade-offs will form the starting point of Phase D. Conceptual design, or Phase C provided the main direction of the design process, with possible solutions to the system requirements being offered. Five design option categories were defined, pertaining to the structural layout, the engine configuration, the power source, the take-off and the landing systems.

Individual solutions were found within each design category with the help of a Design Option Tree and a design space was defined by constraining which solutions can work independently of their category and which are coupled with solutions from other categories. Within each design category, a trade-off was performed to determine the optimal solution. Thus, each of the solutions was assessed based on different criteria. Each criterion was assigned a weight depending on the relative importance of fulfilling the system requirements and each possible solution was assigned a score. The trade-offs were analysed under small perturbations in the scoring, in the form of a sensitivity analysis, in order to eliminate any bias. Within the structural layout category, five solutions were identified, but finally, the winning solution was chosen for its reduced complexity, technology readiness level and ease of design for both stability and controllability. An engine configuration compatible with this structural layout was chosen, considering integration challenges and interference with the payload space. Safety, sustainability and technology readiness levels were considered for the energy system and two possible solutions were traded off. Take-off solutions varied from hand launches to conventional take-offs, with launch reliability, effect on the airframe and complexity being the most important considered aspects. The landing solution was chosen based on its low complexity and on the fact that the mission profile did not impose any requirements on landing.

Finally, the five trade-offs of the conceptual design concluded that an appropriate integrated solution would be a battery-powered single-pusher platform with a high-mounted wing and aft-placed twin-boom horizontal stabiliser. For reference, the structural layout of the traded-off concept is present in Figure 6.1.

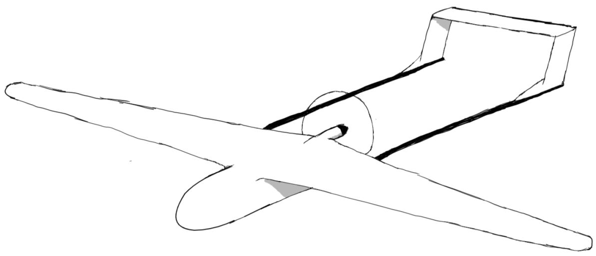

Figure 6.1: Structural configuration of the conceptual design solution

6.2. Subsystem Breakdown

The system is broken down into subsystems which allows more minor, but more specialised teams to design. These subsystems work together to make up the UAV and provide the essential functions it has to fulfil. In Table 6.1, the final subsystems of the UAV are stated, along with a brief description and abbreviation for future reference. The extent of the relationship between these subsystems is presented in section 6.3.

Table 6.1: Subsystem breakdown for The Ionic Drone

Subsystems	Description	Abbr.
Aerodynamics	The wing and empennage shape and sizing	
Structures	The physical structure of the UAV that provides the structural integrity.	STR
Electrical Power System	The electrical power storage system of the aircraft.	EPS
Plasma Control System	The plasma actuators that control the aircraft. Includes the high voltage generation system.	PCS
Payload	The payload of the aircraft.	PAY
Propulsion	The propulsion system. Includes the propeller, electric motor, and ESC.	PRP
Avionics	Avionics equipment on the UAV such as sensors (pitot-tube, IMU, GPS, humidity, etc.), flight computer and the transceiver.	AVC
Launch System	The external (catapult) launcher for the UAV.	ELS
Landing System	The landing system of the UAV (parachute).	LND
Ground Station	The system which sends and recieved commands and data.	GSS

6.3. Subsystem Integration and N2 Chart

An N2 chart was created to define the interfaces between the subsystems defined in Table 6.1 and certain functions. The boxes are coloured pink or purple, respectively, based on their classification. Ten subsystems and two functions are identified, corresponding to the breakdown in Table 6.1 and to the powered and gliding phases of the mission. The distinction between gliding and powered flight is necessary since the payload and propulsive systems will be alternatively operated due to the mission profile. The N2 Chart aids in the generation of the subsystem requirements, thus the abbreviations for the subsystems are included in the chart. Note that these abbreviations do not exist for the functions. The final results are shown in Figure 6.2

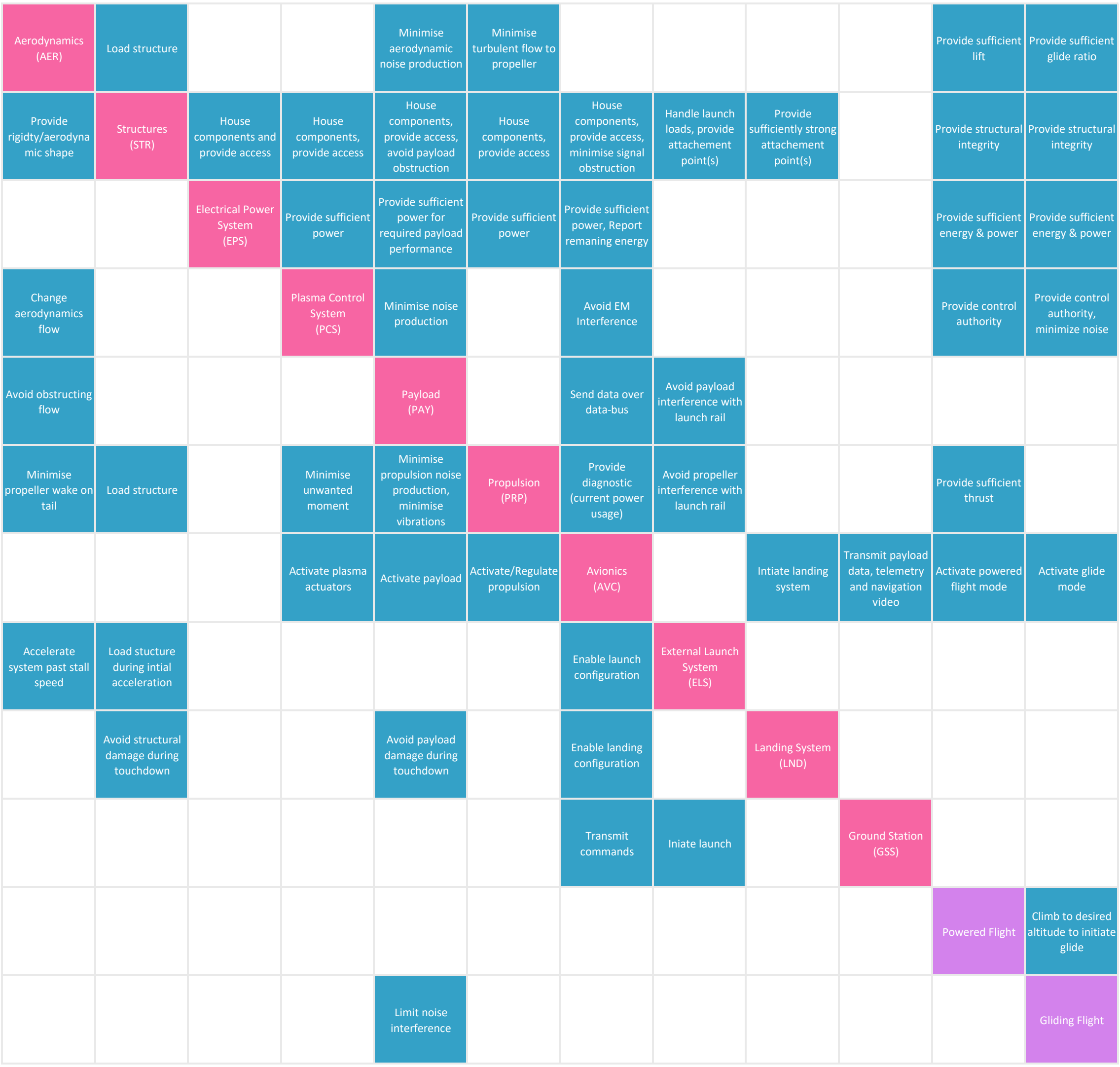

Aerodynamics (AER)	Load structure			Minimise aerodynamic noise production	Minimise turbulent flow to propeller					Provide sufficient lift	Provide sufficient glide ratio
Provide rigidty/aerodynamic shape	Structures (STR)	House components and provide access	House components, provide access	House components, provide access, avoid payload obstruction	House components, provide access	House components, provide access, minimise signal obstruction	Handle launch loads, provide attachement point(s)	Provide sufficiently strong attachement point(s)		Provide structural integrity	Provide structural integrity
		Electrical Power System (EPS)	Provide sufficient power	Provide sufficient power for required payload performance	Provide sufficient power	Provide sufficient power, Report remaning energy				Provide sufficient energy & power	Provide sufficient energy & power
Change aerodynamics flow			Plasma Control System (PCS)	Minimise noise production		Avoid EM Interference				Provide control authority	Provide control authority, minimize noise
Avoid obstructing flow				Payload (PAY)		Send data over data-bus	Avoid payload interference with launch rail				
Minimise propeller wake on tail	Load structure		Minimise unwanted moment	Minimise propulsion noise production, minimise vibrations	Propulsion (PRP)	Provide diagnostic (current power usage)	Avoid propeller interference with launch rail			Provide sufficient thrust	
			Activate plasma actuators	Activate payload	Activate/Regulate propulsion	Avionics (AVC)		Intiate landing system	Transmit payload data, telemetry and navigation video	Activate powered flight mode	Activate glide mode
Accelerate system past stall speed	Load sructure during intial acceleration					Enable launch configuration	External Launch System (ELS)				
	Avoid structural damage during touchdown			Avoid payload damage during touchdown		Enable landing configuration		Landing System (LND)			
						Transmit commands	Iniate launch		Ground Station (GSS)		
										Powered Flight	Climb to desired altitude to initiate glide
				Limit noise interference							Gliding Flight

Figure 6.2: N2 Diagram

6.4. Initial sizing

Beginning with the initial budget, the class I weight estimation method was chosen. Initially, a set of subsystem mass values was selected, and based on these values, the required energy and mass budgets were calculated. This procedure was then iterated to determine the final mass of the drone. Generally, the gravitational acceleration g_0 is considered to be equal to 9.81N/m^2, which has a conservative effect on all design iterations. Standard atmospheric conditions at sea level are considered, as the maximum change in altitude is negligible from a density point of view. This assumption has a slightly non-conservative effect. Both of these assumptions are used throughout the conceptual, preliminary and final design.

Assumptions

Table 6.2 gives a list of assumptions that were made during the initial sizing process. Most of the assumptions made were

Table 6.2: Weight Estimation Assumptions

Code	Assumption	Rationale
ASS-PRE-01	The battery density is 170Wh/kg	140-200Wh/kg [38]
ASS-PRE-02	Propeller Efficiency is 80%	Typically 85%, but lowered to have a conservative effect
ASS-PRE-03	Battery Efficiency is 80%	Typically 90%, but lowered to have a conservative effect
ASS-PRE-04	Avionics Mass is 655 g	10% of MTOW, Taken from Baseline Report [39]

ASS-PRE-05	Velocity is taken to be $12\,\mathrm{m/s}$	Compared to competitors
ASS-PRE-06	Plasma Actuator Mass is 588	9% of MTOW, Taken from Baseline Report [39]. Does not change as wing span remains the same
ASS-PRE-07	Oswald Efficiency Factor is 0.7	0.95 for elliptical wing [40], but conservative assumption
ASS-PRE-08	Airfoil Assumption	NACA 23018 were chosen as thick airfoils are more efficient at low speeds. This is subject to change
ASS-PRE-09	C_{D0} Assumption	A 30% margin is applied to the C$_{D0}$ of the chosen airfoil to take into consideration the fuselage. [41]
ASS-PRE-10	Wingspan Assumed to be $2.4\,\mathrm{m}$	Taken from literature [42]
ASS-PRE-11	Initial Mass Assumption	Taken from literature [42]
ASS-PRE-12	Two-term drag polar equation	Simple version of three-term drag polar deemed sufficient for preliminary design
ASS-PRE-13	Linear power mass relation for of propulsion system relation of $m_{PRP} = 0.3542 \cdot P_{req_{climb}} - 0.8421$	Taken from a linear relation found in the literature [43]
ASS-PRE-14	Battery sized only for cruise endurance (m_{EPS} only depends on $E_{req_{cruise}}$)	Negligible duration of the initial climb, and flight profile is not known from mission profile yet
ASS-PRE-15	Negligible difference of C_l and V for climb and cruise conditions	Minor differences were seen when calculated, thus the different conditions are not considered preliminarily. The more constraining (cruise) condition was taken
ASS-PRE-16	10% Power margin	Taken from Baseline report [39], considered to be enough to account for fluctuations of conditions
ASS-PRE-17	10% Energy margin	Taken from Baseline report [39], considered to be enough to encapsulate the actuators and avionic energy usage
ASS-PRE-18	Structure mass is 35% of total mass	Taken from literature [44]

Initial Values

Table 6.3 provides the initial values of the inputs considered for sizing the drone. During the preliminary sizing, the NACA 23018 airfoil was initially chosen, although it may be subject to change in the detailed design phase. The span efficiency factor calculated from $C_{L,cruise}$ was determined to be 0.7. While the design team acknowledges that this value is lower than the expected span efficiency factor, it will be utilized for a conservative design approach and to account for the presence of the fuselage.

Table 6.3: Initial Values

Parameter	Value	Rationale
m_{PAY}[kg]	1	REQ-CUS-06
u_{dens} [Wh/kg]	170	ASS-PRE-01
Propeller Efficiency [-]	0.8	ASS-PRE-02
Battery Efficiency [-]	0.8	ASS-PRE-03
Wing Span [m]	2.4	ASS-PRE-10
m_{AVC} [kg]	0.655	ASS-PRE-04
m_PCS[kg]	0.588	ASS-PRE-06
E [hrs]	2	REQ-CUS-04
V [m/s]	12	ASS-PRE-05
C_{D0} [-]	0.03	ASS-PRE-09
$C_{Lcruise}$ [-]	1.1	From NACA 23018 data
Total Mass [kg]	6.555	ASS-PRE-11
Rate of Climb [m/s]	2.8	SYS-PER-01
Oswald Efficiency Factor [-]	0.7	ASS-PRE-07

Calculated Values and Iteration

Following the selection and assumptions for the initial values, preliminary calculations and an iterative loop can be established to get initial mass, power and energy budgets. A summary of the interrelations between the initial, intermediate and final values is shown in Figure 6.3 and depicted by dark blue, light blue and pink, respectively.

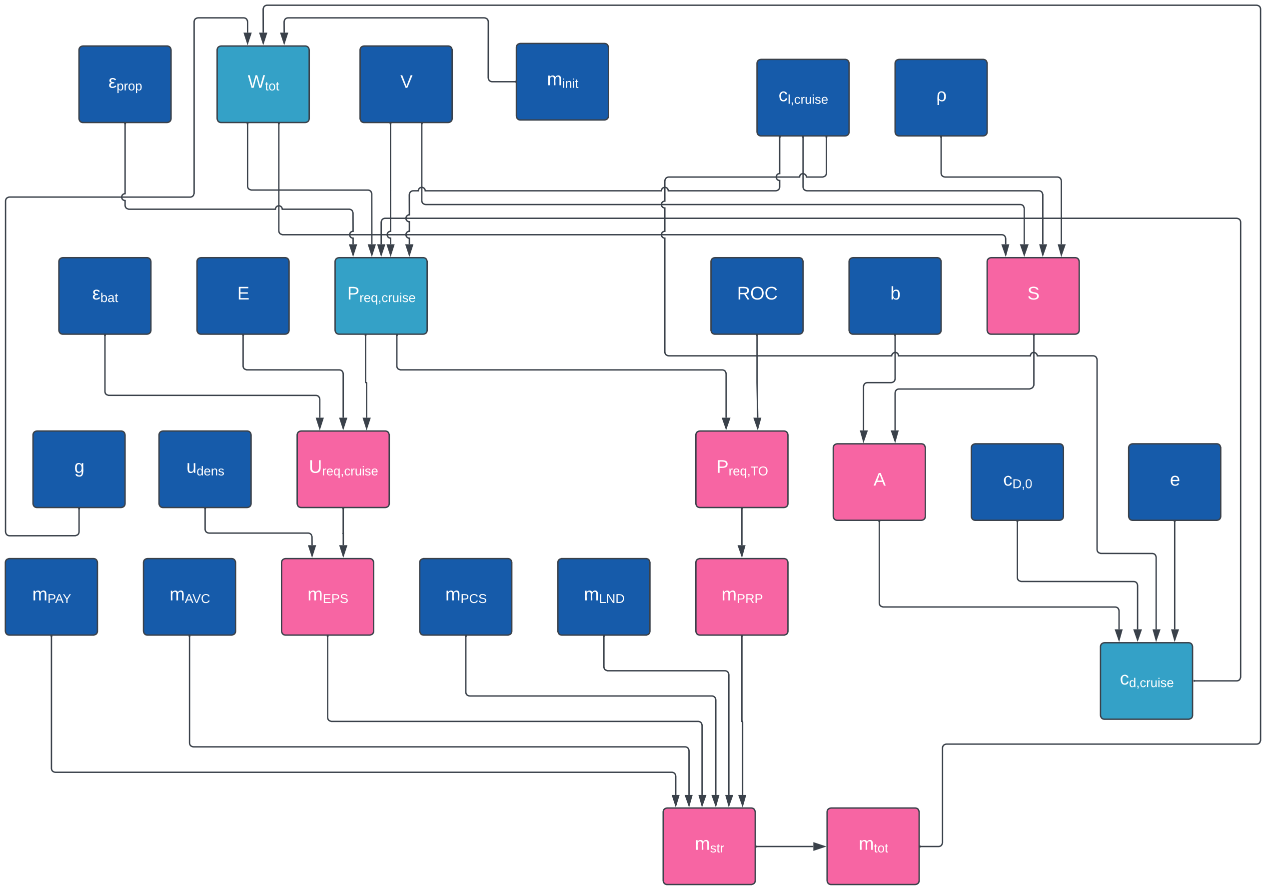

Figure 6.3: Class 1 design iteration

Following this iteration loop, the following values seen in Table 6.4 were found (excluding the values shown in the initial input values). Note that the initial mass is included in both tables, with the more recent version being the 5.9kg value.

Table 6.4: Converged preliminary design iteration values

Variables	Description	Value
m_{TOT}	Total mass [kg]	5.9
m_{EPS}	Mass of electronic power system [kg]	1.0
m_{PRP}	Mass of propulsion system [kg]	0.10
m_{STR}	Mass of structural system[kg]	2.1
$E_{req,cruise}$	Energy required for 2h cruise [Wh]	170
$P_{req,climb}$	Power required for climb [W]	290
S	Wing planform area [m^2]	0.60
A	Wing Aspect ratio [-]	9.6

7 Performance

This chapter describes the performance aspect of the drone. It starts off with the S-V diagram, then moves onto the roll requirements, pitch requirements and finally the yaw requirements. It must be noted that the increase in lift is achieved by increasing the thrust and not by changing the aeroplane's angle of attack. This increase in thrust increases the velocity which in turn increases lift. This is done because trimming an aircraft is comparatively more complicated.

7.1. Performance requirements

The relevant subsystem requirements for this chapter are shown in Table 7.1. Note that these subsystem requirements come from the performance and aerodynamics departments. Compliance with these requirements is assessed at the end of the nine-week design period during the DSE.

Table 7.1: Performance Requirements

Requirement ID	Requirement	Verification	Compliance
SUB-PER-01	The system shall be able to operate in windspeeds up to 3.4 m/s.	Analysis	**PASS**
SUB-PER-02	The system shall be able to climb at a rate of at least 2.8 m/s	Analysis	**PASS**
SUB-PER-03	The system shall be able to perform a 180-degree horizontal turn within a lateral distance of 50m	Test	**PENDING**
SUB-AER-01	The system shall have a glide ratio of at least 14	Analysis	**PENDING**

7.2. S-V Diagram

To determine the general aircraft parameters, velocity and wing surface area, a design space was defined and a point was taken. This served as an initial idea for the further development of the preliminary design. Note that the velocity and surface area are detailed further in chapter 9.

1. **PER-SVD-01:** The mass of the aircraft is 7.68 kg. This is calculated from the mass of the conceptual design in the midterm report with a 20% margin. [33]
2. **PER-SVD-02:** The aircraft parameters will be sized for cruise conditions. In reality, the mission will have more gliding and climbing states than cruise however for simplicity and the small difference between the different conditions, cruise condition is assumed.
3. **PER-SVD-03:** The zero-lift drag coefficient of the entire aircraft is 1.3 times larger than the zero-lift drag coefficient of the aerofoil. [41]
4. **PER-SVD-04:** The Reynolds number limit for plasma efficiency is 450,000. This value is taken as the average value Friedrichs [1].
5. **PER-SVD-05:** No wing twist is assumed at this stage due to the additional complexity it brings to the system. This assumption is removed in subsection 9.4.1.

The relations are shown below, note that equations 7.1 and 7.2 are derived from cruise conditions at optimal range and endurance conditions. Meanwhile, equations 7.3 and 7.4 are inequality equations which serve as boundaries for the design space.

$$V^4 S = \frac{4W^2}{c_{D0}\rho^2\pi b^2 e} \tag{7.1}$$

$$V^4 S = \frac{4W^2}{3c_{D0}\rho^2\pi b^2 e} \tag{7.2}$$

$$VS > \frac{Re_{limit}\mu b}{\rho} \tag{7.3}$$

$$V < 1.3\sqrt{\frac{W}{S}\frac{2}{\rho}\frac{1}{c_{l,max}}} + V_{wind} \tag{7.4}$$

Note that certain values are assumed from requirements, notably b was defined as 3 m to allow for a 5 cm margin, and V_{wind} as 3.4 m/s as was specified from SUB-AER-01. [33] The resultant graph can be seen in Figure 7.1 where the white space is the possible design space.

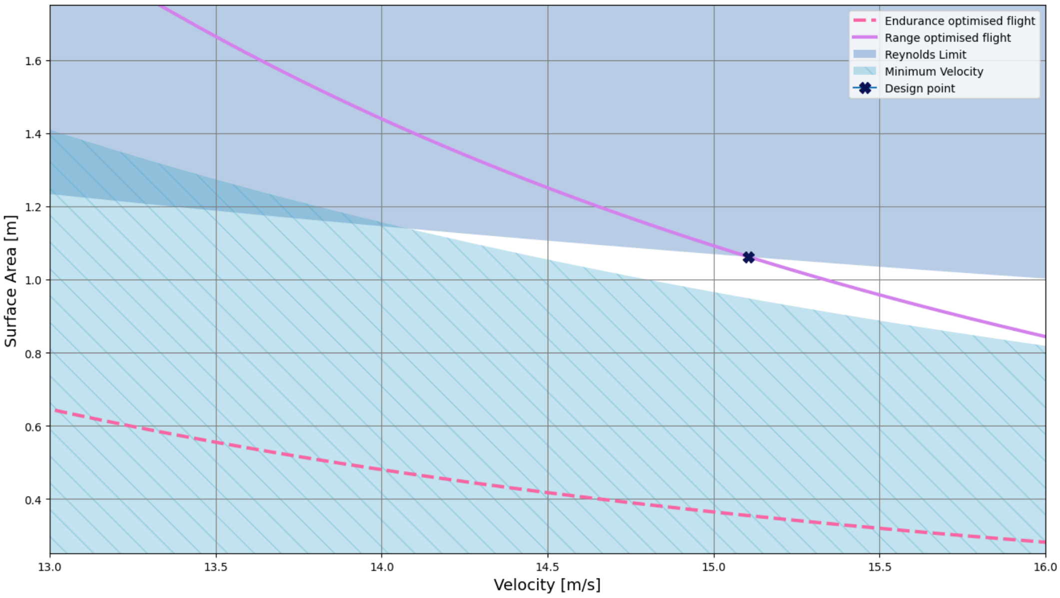

Figure 7.1: Surface area in relation to Velocity diagram

From the figure, it can be seen that it was decided to optimise for range. This coincides with optimising the performance for the highest L/D ratio, which is an important parameter. Furthermore, it was decided to stay on the Reynolds limit boundary due to having larger margins with the stall boundary. Therefore, the risk of entering the minimum velocity boundary region after removing PER-SVD-02 is minimised. Thus, the intermediate preliminary design surface area and velocity were decided to be $1.1\,\mathrm{m}^2$ and $15.1\,\mathrm{m/s}$. Note that these values will be further iterated on in subsection 9.4.1 and subsection 9.6.3, respectively.

7.3. Maneuverability Requirements

In preparation for sizing control surfaces, pitch, roll and yaw moments should be defined. These definitions come directly as a result of the mission performance. The assumptions made for this section are the following.

1. **PER-ROT-01:** Motions are considered two dimensional. This comes from the fact that the pitch and roll motions can be sequential and thus do not interfere with each other and are decoupled. Considering a motion with couples pitching up and rolling is considered outside the scope of the current state of the report. Additionally, since the flight time is not a driving requirement, the time penalty of performing the manoeuvres sequentially is not harmful to the success of the mission.
2. **PER-ROT-02:** The angles of attack of all surfaces remain constant during the motions. This is used for the calculations such that geometric parameters of the aircraft are not included as a variable. This assumes the dimensions of the aircraft relative to the motion are minimal.
3. **PER-ROT-03:** Thrust variations are accurate and instantaneous. This relates to the variations in thrust throughout the roll motion such that the motion remains a 2-dimensional motion (see PER-ROT-01). For the pitching motion, this leads to full thrust being delivered after engine ignition. This assumption is made since the spin-up time is a function of the engine choice and is thus not known at this stage.
4. **PER-ROT-04:** Neutral stability in the axis of intended rotation. This assumption leads to more simple equations of motion. This was done since the stability depends on various (currently) undetermined parameters.

   no moment produced by the propeller

7.3.1. Roll Acceleration

To determine the required roll acceleration, the limiting case was determined to be during the climbing phase, where the aircraft performs a 540° turn before starting the glide phase as determined in section 3.1. Note that turning motion occurs as a horizontal banked turn in accordance with **PER-ROT-01**.

The simulation uses a Newton method iterative process to determine the minimum required roll acceleration to complete the motion. This means that the effects of the initialisation value are calculated through a time-discretised model, and the difference between the real and desired turn distance is used to scale the next iteration of the roll acceleration estimate. This cycle continues until an accuracy of 10 cm is achieved. Note that the time discretised model is needed due to the velocity and centripetal force being a function of roll angle and thus changes over time.

The result of this system is one where the roll rate increases linearly until the half-point of the turn is reached before decreasing the roll rate such that it straightens out by the end of the turn. A visualisation of the flight path can be seen in Figure 7.2.

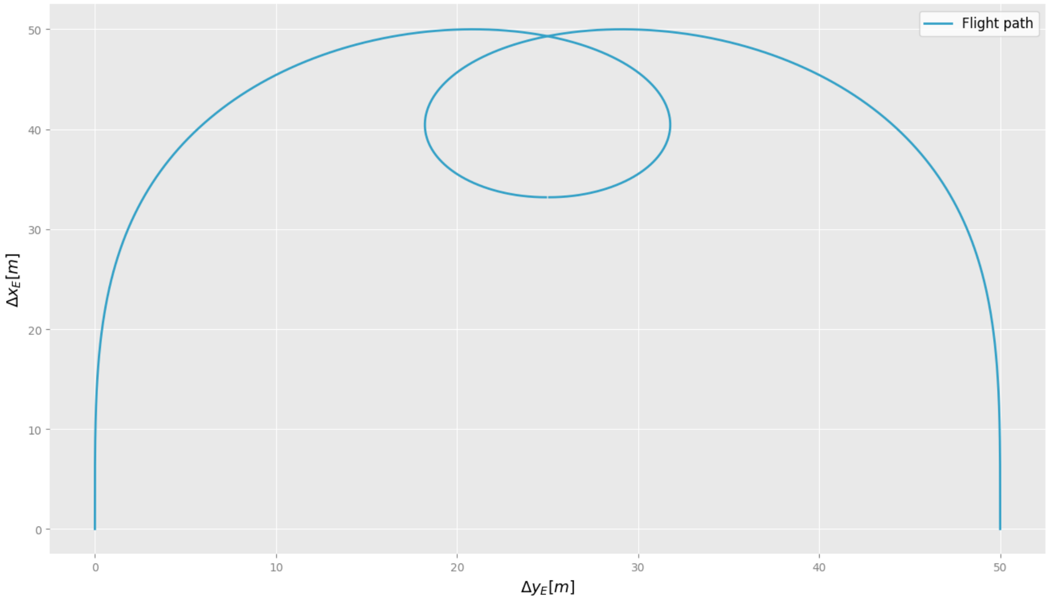

Figure 7.2: Flight path in earth reference frame for 540° turn with continuous roll acceleration

The values for this motion are shown in the Table 7.4. The maximum roll acceleration will be the parameter which is used for the aileron sizing. The maximum roll rate will be used to verify and if needed iterate on **AER-AIL-06** from subsection 9.3.1 and **PER-ROT-02**. The roll angle is used to calculate the load factor which is calculated to help verify the motion is below the maximum load factor 3.75. Lastly, the time discretisation is reported for repeatability.

Table 7.2: Roll Motion parameters

Parameter	Value	Unit
Roll acceleration	2.22	$[deg/s^2]$
Maximum roll rate	11.9	$[deg/s]$
Maximum roll angle	32.0	$[deg]$
Maximum load factor	1.59	$[-]$
Time discretisation	0.001	$[s]$

7.3.2. Pitch Acceleration

The limiting pitching motion was determined to be the transition between the glide and climb phases. The transition between the stages is performed through increasing the airspeed, where the additional lift causes centripetal acceleration. The pitch acceleration is derived from this through **PER-ROT-02** such that the pitch of the aircraft leads to the angle of attack being constant. For simplicity of the problem, as assumed by **PER-ROT-03**, the increase in airspeed is from applying the thrust required to climb at the end of the gliding stage. A visualisation of the flight path is shown in Figure 7.3.

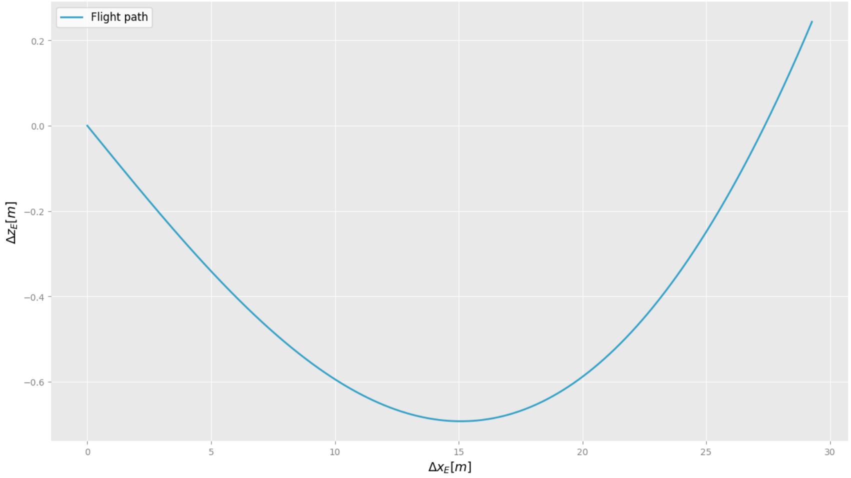

Figure 7.3: Flight path in earth reference frame during pitch motion transitioning between glide and climb

A summary of the parameters for the motion in Figure 7.3 are shown in Figure 7.3. In this table, the pitch acceleration will be used for the horizontal tail sizing for control. The maximum pitch rate is used to calculate the maximum load factor, to verify that it is below the value specified in the load factor requirements, thus verifying the assumption **PER-ROT-03**. Lastly, the time discretisation is displayed to allow for reproducible results.

Table 7.3: Pitch Motion parameters

Parameter	Value	Unit
Pitch acceleration	10.1	$[deg/s^2]$
Maximum pitch rate	10.3	$[deg/s]$
Maximum load factor	1.29	$[-]$
Time discretisation	0.001	$[s]$

7.3.3. Yaw Acceleration

When attempting to define a yaw acceleration requirement, at the current stage in design with the mission, no requirement can be defined. This is due to the fact that yaw is used for crosswind landings and as a coupled effect due to roll.

Due to the mission, there are no cross-wind landings since landings occur with a parachute and landing bag. Therefore no requirement can be set from this.

Regarding deriving a yaw acceleration requirement as a coupled effect of the roll, for preliminary design, it is assumed that the moment produced by the vertical stabiliser during the roll will be minimal. This can be justified when qualitatively investigating the induced velocity on a twin tail. Due to the offset of each tail from the Y axis of the plane, the induced angle of attack during roll is less than the single vertical tail counterpart. Furthermore, due to the selection of the plasma aerofoil, the $c_{l,alpha}$ value is lower than conventional aerofoils and thus the coupled motion is less than for conventional aircraft. To further analyse this phenomenon in a qualitative form, other geometries of the drone have to be well defined, thus it is not possible to define it at the current stage of design, yet will have to be done during iteration. This means the vertical stabiliser will be sized from the stability condition.

7.4. Design Iteration

7.4.1. Roll Acceleration

For the iteration of the performance models, the main improvement made was including roll damping in the roll motion model. This was done since the roll acceleration was relatively small at $2.22\,\mathrm{deg/s^2}$, whereas the roll rate was $11.9\,\mathrm{deg/s}$. Therefore it was thought and calculated that the resultant roll-damping moment was non-negligible.

The roll-damping of the two is an effect of the angle of attack differential between the two half-spans of the wings. The effect of roll rate on roll-damping is presented in Figure 7.4 for the main wing.

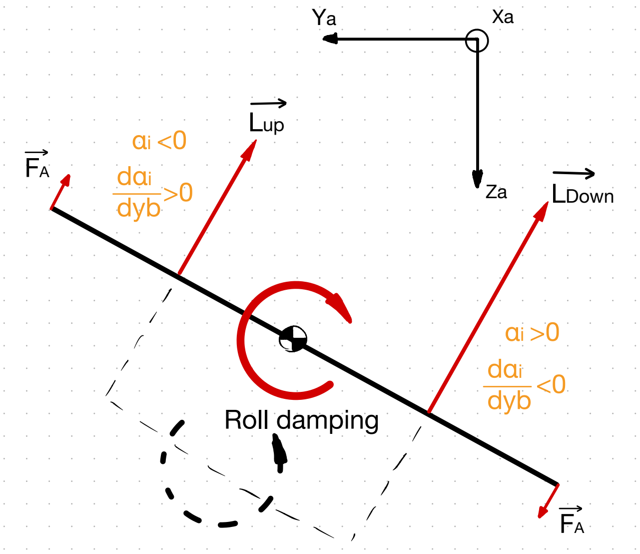

Figure 7.4: Schematic of the restoring effect of roll

In this case, the roll induces a velocity perpendicular to the wing along the span, which has the effect of modifying the local angle of attack at each span-wise section. The induced angle of attack can be calculated assuming the induced angle is small by using Equation 7.5.

$$\alpha_i = \frac{\dot{\phi} y}{V_\infty} \tag{7.5}$$

The effects of the induced angle are to increase the effective angle of attack of the 'downwards-going' wing and reduce it for the 'upwards-going' one. The total effects can be quantified by assuming the local lift at an infinitesimally small slither of span can be represented by Equation 7.6.

$$dL = \frac{1}{2}\rho V_\infty^2 C_L(y) dS \tag{7.6}$$

Moreover, the surface of the small span slither is equal to $c(y) \cdot dy$, where $c(y)$ represents the chord as a function of span-wise location and dy is the width of the span slither. This small lift quantity acting at a y location along the halfspan will induce a small moment $dL \cdot y$. Finally, using $C_L(y) = C_{L_0}(y) + C_{L_\alpha}\alpha_i$ and Equation 7.6, the total moment contribution of one wing can be expressed by the integral in Equation 7.7.

$$M_{U/D} = \int_{-\frac{b}{2}/0}^{0/\frac{b}{2}} \int_{-\frac{b}{2}/0}^{0/\frac{b}{2}} \frac{1}{2}\rho V_\infty^2 c(y)(C_{L_0}(y) + C_{L_\alpha}\frac{\dot{\phi} y}{V_\infty}) y dy^2 \tag{7.7}$$

The moments on each wing are slightly different in magnitude and thus induce a resultant moment acting in the counterclockwise direction. The term $C_{L_0}(y)$ represents the local lift coefficient during level flight and is expressed as a function of y to suggest that the lift correction factor discussed in subsection 9.6.3 is already included. A similar analysis can be performed to determine the roll counteracting moment induced by the horizontal stabiliser.

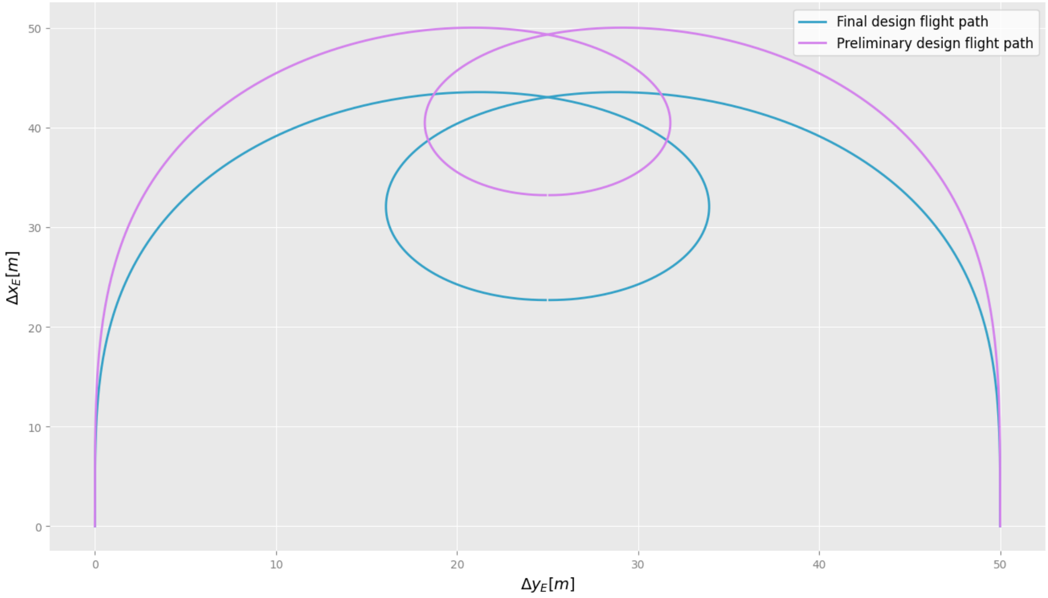

Figure 7.5: Rolling Flight path of preliminary design versus final design

Table 7.4: Roll Motion parameters

Parameter	**Old Value**	**New value**	**Unit**
Roll acceleration	2.22	5.85	$[deg/s^2]$
Maximum roll rate	11.9	4.75	$[deg/s]$
Maximum roll angle	32.0	21.6	$[deg]$
Maximum load factor	1.59	1.59	$[-]$
Maximum roll damping acceleration	0	5.85	$[deg/s^2]$
Time discretisation	0.001	0.001	$[s]$

The addition of this roll damping moment would have an effect on the flight path during turning, as seen in Figure 7.5. The new flight path set new requirements on roll rate and acceleration which will further constraining the design of the ailerons in section 9.6. The final roll requirements are presented in Table 7.4.

7.4.2. Pitch Acceleration

No changes are made to the approach with which the pitch requirements are determined. Conceptually, one recommendation can be made such that a ramp-up function is implemented for the thrust. Compared to the preliminary design case, due to the new lift-to-drag performance of $L/D = 19$ identified in Table 13.3 and a more accurate estimation of the mass of the system and aerodynamic performance of the horizontal stabiliser (lift gradients determined from wind tunnel experiment results presented in Figure 8.19), a new pitch acceleration requirement is determined. The final pitch manoeuvre requirements are presented in Table 7.5.

Table 7.5: Pitch Motion Parameters

Parameter	**Old Value**	**New Value**	**Unit**
Pitch acceleration	10.3	9.0	$[deg/s^2]$
Maximum pitch rate	10.1	9.1	$[deg/s]$
Maximum load factor	1.29	1.26	$[-]$
Time discretisation	0.001	0.001	$[s]$

8 Plasma Actuation System

A major and unique aspect of the P.U.L.S.E. Drone is control of the aircraft attitude angles - roll, pitch and yaw - solely by plasma actuators. The design and implementation of plasma actuators for the purpose of aircraft control is covered by the plasma actuation system and is presented in detail in this chapter.

Plasma actuation system design begins with subsystem requirements identification presented in section 8.1. Subsequently, the actuation method is selected in two phases - preliminary selection in section 8.2 and detailed trade-off in section 8.3. Afterwards, simulation, sizing and detailed design of the selected method are discussed in section 8.4, whilst section 8.5 explores plasma actuator control signal generation circuits. Design choices and budgets are then compiled in section 8.7. The method viability is validated with a wind tunnel test, whose setup, procedure and results are discussed in section 8.6. Lastly, future design steps and recommendations are outlined in section 8.8.

8.1. Plasma Actuation System Requirements

This section discusses the essential criteria that the plasma system must meet in order to ensure the controllability of the UAV. Many of these requirements have been derived from the control system prerequisites, while others have been established based on the limitations imposed by the UAV's electronics. A comprehensive tabular compilation of all the design requirements can be found Table 8.1. It must be noted that no performance requirements are made towards the plasma actuation system, and the required control moments shall be achieved by wing and empennage control section scaling in their respective chapters. Nevertheless, method performance shall be considered when selecting actuation methods to ensure an achievable overall design.

Table 8.1: Plasma Actuation System Requirements

Req. ID	Requirement	Verification	Rationale
SUB-PCS-01	Plasma actuation system shall not damage aerodynamic surfaces	Analysis	Damage to aerodynamic surfaces would impede performance and in the long term lead to system failure.
SUB-PCS-02	Plasma actuation system shall generate maximum noise of 50 dB	Testing	Must not be more than 30dB once it propagates to the ground. With margin must be 50dB, at a height of 10m it would be 30dB on the ground.
SUB-PCS-03	Plasma actuation system shall use a maximum of 90 W of power	Analysis	Maximum power that can be provided by Minipulse 0.1
SUB-PCS-04	Plasma actuation system shall have a durability of 2 hr under a duty cycle of 80 %	Testing	2hr is the mission length, and is such is the minium durability requirement of all subsystems.
SUB-PCS-05	Plasma actuation system will weigh less than 720 grams	Inspection	Based on 1.2 margins over preliminary sizing

8.2. Preliminary Control Method Selection

During Phase C, a literature study was conducted on existing methods of using plasma actuators to exert control moments on an aircraft [33]. In total, fifteen methods were identified, including two concepts conceived by the authors, instead of based on existing literature: flow channelling in a slotted aerofoil and aerodynamic features in plasma-controlled separation.

For each method described, two performance parameters were estimated or taken from literature directly, i.e., ΔC_l and ΔC_d (for differential drag application), as well as unique advantages and disadvantages of each method. These considerations are compiled in Table 8.2. Both performance parameters for all actuation methods could not be devised from the literature. Unknown parameters will be treated as being too low to provide sufficient aircraft control. At this stage of the selection, maximum available performance parameters shall be used, regardless of whether those values are achievable at the to-be-flown flight conditions.

In the end, based on this compilation and discussion within the design team and with the tutor, four methods are identified that shall be considered further for the UAV control method - 6:partial flow separation control, 13:aerodynamic features within separation region, 14:airflow channels within the aerofoil and 15:Rounded TE circulation control. These methods offer medium-to-high performance without significantly limiting flight parameters or design options. Method 14 specifically is considered despite lacking literature sources for the potential of providing attitude control without inflicting high lift and drag penalties, which is characteristic of separation control methods.

Table 8.2: Plasma Actuation Method Selection

#	Method	ΔC_l	ΔC_d	Advantages	Disadvantages
1	Virtual plasma flap [45]	0.05	-	Easy to implement, low noise, low impact on aerodynamics	Low power efficiency
2	DD Flow deceleration	-	-	Easy to implement, low noise, low impact on aerodynamics	Low power efficiency
3	Virtual Gurney flap [46, 47]	0.02	-	Easy to implement, low noise, low impact on aerodynamics	Low power efficiency
4	Plasma thrust vectoring[1][48]	-	-	Theoretically high moments can be achieved	Extremely high power consumption / High force thrusters are heavy
5	Flow reattachment over complete aerofoil[2][49]	0.6	-0.15	Well documented performance	High drag penalty / Applicable at stall AoA / separation generates noise
6	Flow reattachment over aerofoil trailing edge [50]	0.4	-0.1	Well documented performance	Medium drag penalty / Requires specialised sub-optimal aerofoils/separation generates noise
7	LE vortex breakdown delay [51]	-	-	Actuation increases overall flight efficiency	Applicable only at high AoA / applicable only to high sweep delta wings/results not proven
8	Differential skin drag reduction [52, 53]	-	0.004	Good efficiency parameters - actuation increases overall efficiency	Skin drag reduction either very low or ineffective
9	Induced separation for DD	-0.6	0.15	High difference in drag can be achieved	High lift penalty/separation generates noise
10	Induced transition for DD [54, 55]	-	0.004		Only applies if the flow is initially laminar
11	Wingtip vortex control [56]	0.02	-	Easy to implement, low noise	Actuation force fixed / not applicable to the empennage
12	Hysteresis branch transition [57]	0.5	0.2	Low energy consumption - activation only for transition	Only applies at close to stall AoA
13	Aerodynamic features in separation [50]	>0.4	>0.1	Combination of documented actuation methods and increased performance	Medium drag penalty / hard to estimate performance
14	Flow channelling in slotted aerofoil	?	?	Low drag penalty / relatively quiet	No literature for this approach, hard to estimate performance
15	Rounded TE circulation control [58]	0.1	0.04	Low drag penalty / can be actuated both ways / well documented	Significantly decreased performance at medium-high Re numbers

8.3. Plasma Control Method Trade-off

This section talks about the trade-off of the selected plasma control method. Firstly, the selection criteria and the corresponding weights are chosen with a rationale. Next, the actual trade-off is performed and the section ends with a sensitivity analysis to check if the trade-off is valid.

8.3.1. Trade-off Criteria

Five criteria are central to plasma control method selection were identified, namely, performance, efficiency, source availability in literature, compliance with mission requirements and design feasibility. A description of what these criteria cover, as well as assigned weights and justifications, are compiled in Table 8.3.

---

[1] Thrust values of 0.1 N to 10 N can be achieved, ΔC_l and $\Delta C - d$ are not applicable to this method

[2] Performance values estimated at stall conditions

Table 8.3: Mission trade-off criteria weights and rationale

Criterion	Weight(%)	Weight rationale
Performance	25	Performance criterion describes the effectiveness of the method for the purposes of aircraft control. Since none of the considered methods utilises differential drag for moment generation, performance can be mostly described by a single parameter, namely, change in lift coefficient ΔC_l. Since the focus of this project is exploring whether plasma actuators are suitable for aerodynamic control, plasma control method performance is given a high weight.
Efficiency	10	Efficiency in this trade-off concerns the impact of chosen control method on overall UAV efficiency. This impact is mostly the result of an increase in drag or a decrease in lift from the specific method. However, since plasma actuation sections will constitute a small part of the overall UAV wetted area, the efficiency criterion is assigned a low weight.
Literature Availability	10	This criterion describes the number and applicability of existing sources in the literature. A larger amount of scientific sources provide more data that can be used in design and model verification, therefore increasing confidence in the design choices. The literature criterion is given a low weight since the difference in required engineering effort due to literature availability is deemed low.
Compliance with Mission Requirements	30	During phase C [33], a specific mission was determined, namely, noise mapping in urban and rural areas. As a result, additional mission requirements were devised, such as a limit on generated noise. Since non-compliance with these requirements would either invalidate the design or require extensive revision of the mission profile, compliance with mission requirements is weighted the highest.
Design Feasibility	25	Design feasibility criterion describes whether the specific control method can be designed to sufficient detail given the time and resource limitation of the DSE project. Methods that need analysis of larger design parameter space score lower. Due to the strict limitations of the DSE format, this criterion is given a high weight.

8.3.2. Trade-Off

After carefully selecting the criteria and assigning weights to each of them, the trade-off process was carried out. The designs that were chosen for comparison and trade-off were as follows: Plasma Separation Control, Plasma Separation Control with Flaps, Slotted Aerofoil, and Kutta Circulation. Each design was evaluated and assigned a score on a scale of 1 to 4, with 4 representing the best performance.

Next, a weighted summation was calculated by multiplying each design's score by its corresponding weight and summing up the results. This calculation took into account the importance of each criterion as determined by the assigned weights.

Ultimately, based on the weighted summation scores, the winner of the trade-off was determined. A summary table of the trade-off can be found in Table 8.4

Table 8.4: Plasma actuation system Trade-Off

Criteria	Performance	Efficiency	Literature Availability	Compliance with Mission Requirements	Design Feasibility	Total
Weight	25%	10%	10%	30%	25%	100%
Plasma Separation Control	3	2	2	2	3	2.50
Plasma Separation Control + flap	4	1	1	2	2	2.30
Slotted aerofoil	2	4	1	2	1	1.85
Kutta circulation	1	2	3	3	4	2.65

8.3.3. Sensitivity Analysis

To ensure that the criterion weight chosen was valid and did not majorly influence the final result, a sensitivity analysis was conducted.

For the analysis, one by one, each of the criteria was given a change in weight. To balance it out, the weight is distributed between the rest of the criteria based on their weights.

The sensitivity analysis results are summarized in Table 8.5. In this table, the first row shows the weight change for each criterion. Ranks were assigned to each design configuration, with 1 indicating the best option. The ranks were then totalled and presented in the table. Therefore, the design with the lowest total rank performed the best.

Table 8.5: Plasma Sensitivity Analysis

Design/Weight Change	**Plasma Separation Control**	**Plasma Separation Control + Flap**	**Slotted Aerofoil**	**Kutta Circulation**
+30%	9	15	20	6
+20%	10	15	20	5
+10%	10	15	20	5
-10%	10	15	20	5
-20%	10	15	20	5
-30%	10	15	20	5

Based on the information provided in the table, Design 4, Kutta Circulation, consistently performs the best across various changes in weights, except for a 30% increase scenario where it comes in second place. In that specific case, the Plasma Separation Control design emerges as the top performer.

The results of the sensitivity analysis support the validity of the trade-off made, confirming that the chosen design, Kutta Circulation, is indeed the best option.

8.4. Plasma-actuated Circulation Control Method Design

In this section, the selected plasma actuation method - circulation control over aerofoil with a rounded trailing edge - is designed in more detail. While the specific approach of modifying trailing edge stagnation point to increase aerofoil circulation is covered in literature both numerically [59] and experimentally [58], these sources do not explore the effects of varying geometry (aerofoil shape, TE radius, etc) on the method effectiveness. Moreover, no sources were found that analyse the possibility of inducing negative ΔC_l (decreasing lift), which is required for symmetric control of the aircraft. As such, it was decided to size aerofoil parameters for circulation control using computational fluid dynamics (CFD) simulations. Firstly, the aerodynamic effect of DBD plasma actuators is discussed in subsection 8.4.1 and modelled in subsection 8.4.2. Subsequently, the rounded trailing edge aerofoil for circulation control is simulated in subsection 8.4.3. Lastly, other parameters, such as plasma actuator materials, is determined in subsection 8.4.4.

8.4.1. Dielectric Barrier Discharge Plasma Actuator

The selected circulation control method utilises an AC dielectric barrier discharge plasma actuator to generate body force on the air around the trailing edge. This type of actuator uses a high voltage, high frequency alternating current between an exposed and a hidden electrode, with an insulating layer in between. A portion of the air above the embedded electrode is then ionised by the generated electric field. The neutral air is affected by momentum transfer from collisions between ionised and neutral particles [60]. A schematic of conventional

DBD plasma actuators is presented in Figure 8.1. While most actuators use two electrodes, multi-electrode DBD actuators are also possible, depending on the application.

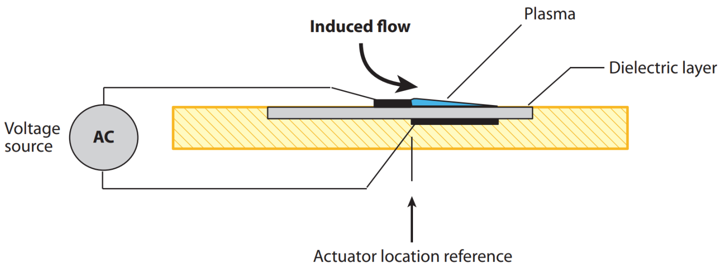

Figure 8.1: Schematic of dielectric barrier discharge plasma actuators. Courtesy of Thomas C. Corke et al. [60]

8.4.2. Modelling of Aerodynamic Effects of Plasma Actuators

To accurately simulate plasma-actuated circulation control, firstly the effects of plasma actuators themselves have to be replicated. For this and further CFD simulations, Ansys Fluent software is used. While Fluent can simulate airflow in nominal plasma-off cases with reasonably high accuracy, the effect of DBD plasma actuators on aerofoil aerodynamics is significantly more difficult to replicate.

A number of models of plasma actuators have been developed in the last few decades, the most well-known of which are numerical Shyy's [61] and Suzen's [62] models, as well as empirical Dörr and Kloker model [63]. While reasonably accurate, these models are deemed too complicated to implement into the Ansys simulation software. Instead, to roughly approximate the effects of plasma actuators, a small portion of the surface, similar in dimensions to DBD electrodes, is defined in the simulation as a no-slip moving wall boundary layer. Firstly, the parameters used to set up the simulation are briefly described, and subsequent results are compared with experimental data from existing literature.

CFD Simulation Parameters

To determine a relation between plasma actuator parameters and respective moving wall boundary conditions, a rudimentary simulation of a flat plate in quiescent air is defined. The simulation domain is a rectangle $1\,\text{m}\times0.3\,\text{m}$ in dimensions $(length \times width)$. The left edge is defined as zero velocity inlet, while the boundary conditions on both the top and right surfaces are pressure outlets. The bottom surface, representing a flat plate, is respectively defined with a no-slip wall boundary condition. A 10 mm section of the plate located at $x = 0.3$ m from the inlet is instead defined as a no-slip moving wall, thus approximating velocity induced by plasma actuators. The moving wall is assumed to be geometrically equivalent to the embedded electrode of plasma actuators over which plasma is produced.

Results and Comparison with Experimental Data

Moving wall boundary condition section results in a wall jet over the flat plate, presented in Figure 8.2. By visual inspection, the simulated wall jets are closely similar to jets generated by plasma actuators, shown in Figure 8.3.

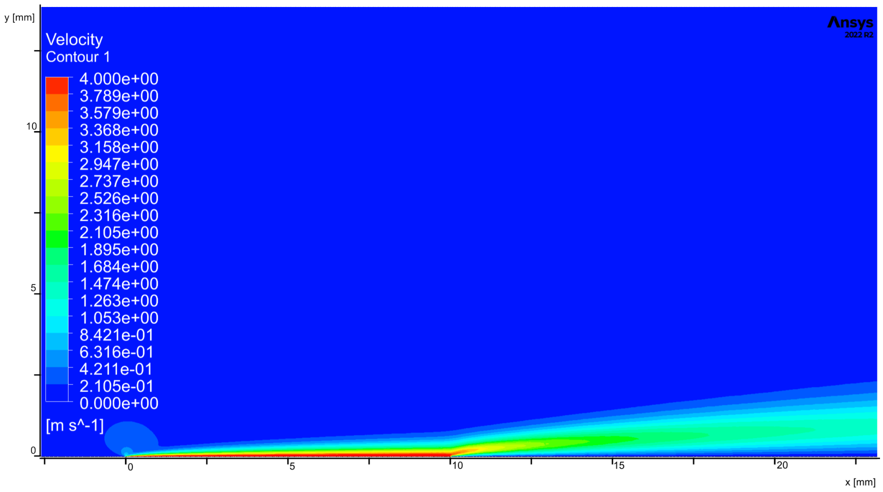

Figure 8.2: Jet generated by moving wall boundary condition section over flat plate

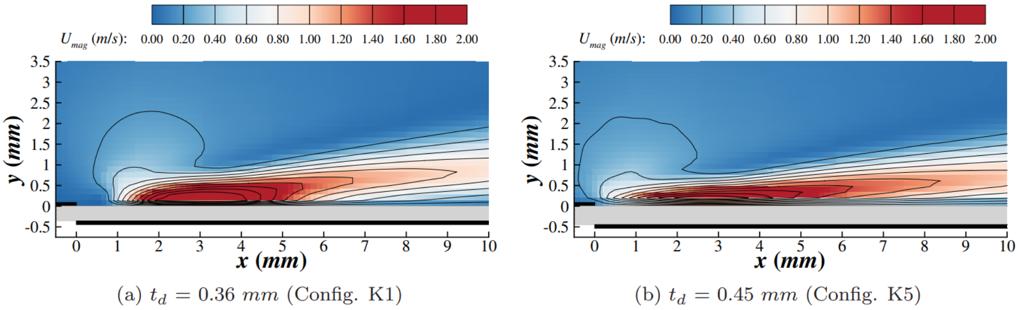

(a) $t_d = 0.36\ mm$ (Config. K1) (b) $t_d = 0.45\ mm$ (Config. K5)

Figure 8.3: Jet generated by DBD plasma actuators over flat plate, courtesy of J. P. Murphy and P. Lavoie [64]

For a quantitative comparison between the moving wall model and experimental results in the literature, profiles of velocity components in the x direction are analysed. Since it is clear that the velocity profile over the moving wall itself shall be greatly different from that over the plasma actuator, the velocity profiles are analysed at a point 5 mm downstream of the moving wall, or 15 mm downstream of the exposed electrode edge in case of plasma actuators. Since the moving wall width is 10 mm, these locations are equivalent for both simulations and experiments. The velocity profiles of moving wall simulations for different moving wall velocities are displayed in Figure 8.4. To facilitate comparison with experimental data, both velocity component u and height y are normalised according to Equation 8.1 and Equation 8.2, respectively. y^* specifically is determined by normalising against height at which velocity is equal to half the maximum value, taking the highest of those two points. The normalised velocity profiles are subsequently plotted alongside experimental data from [64] in Figure 8.5. It can be seen that, firstly, normalised velocity profiles of simulations and the experiment are similar in shape, indicating similar jet behaviour downstream of the moving wall section/plasma actuator. Secondly, normalised profiles for different moving wall velocities exhibit very little variation between each other in the considered range. This behaviour is somewhat replicated by plasma actuators, whose normalised velocity profiles do not differ greatly at different voltages [64].

$$u^* = \frac{u}{u_{max}} \quad (8.1) \qquad y^* = \frac{y}{y_{u=0.5u_{max}}} \quad (8.2)$$

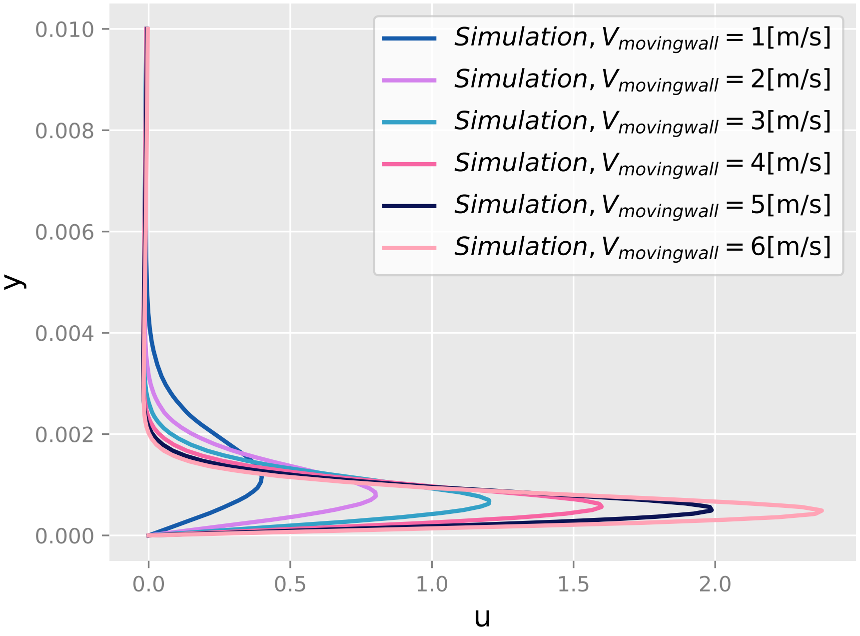

Figure 8.4: Velocity profiles of moving wall section for different moving wall velocities at $x = 15$ mm downstream of moving wall velocity section start.

In order to relate the moving wall velocity to the performance of existing plasma actuators, a momentum coefficient c_μ is derived from the simulation data. c_μ is a parameter commonly used to characterise the performance of DBD plasma actuators, blown jets and similar devices, and is given by Equation 8.3, where J is

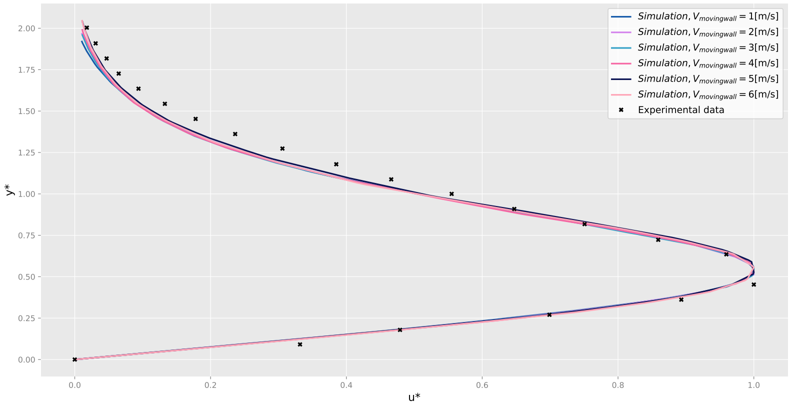

Figure 8.5: Normalised velocity profiles compared to experimental data from [64].

the momentum produced by the actuation method in quiescent conditions, calculated using Equation 8.4. For the moving wall simulations, J is calculated numerically from the velocity profile at the downstream edge of the moving wall section, since that is the point at which imparted momentum is maximal and losses due to viscous forces and dissipation minimal. A relation between imparted jet momentum and moving wall velocity in quiescent air is presented in Figure 8.6a. This relation is subsequently used in conjunction with experimental jet momentum to peak-to-peak voltage relation retrieved from [65] and shown in Figure 8.6b to determine equivalent moving wall velocity. In section 8.5, it is determined that the maximum peak-to-peak voltage of 12 kV and frequency of 10 kHz achievable by the selected hardware. Since there is no data available for this point, a jet momentum of $V_{pp} = 14$ kV and $f = 2$ kHz is used to determine equivalent moving wall velocity of $6.6\,\mathrm{m/s}$. While this value might not be representative of the specific actuator parameters in the final design, it is close enough to allow the use of computational fluid dynamics simulations for aerofoil geometry sizing.

$$c_\mu = \frac{J}{q_\infty c} \tag{8.3}$$

$$J = \int_0^\infty \rho u^2 dy \tag{8.4}$$

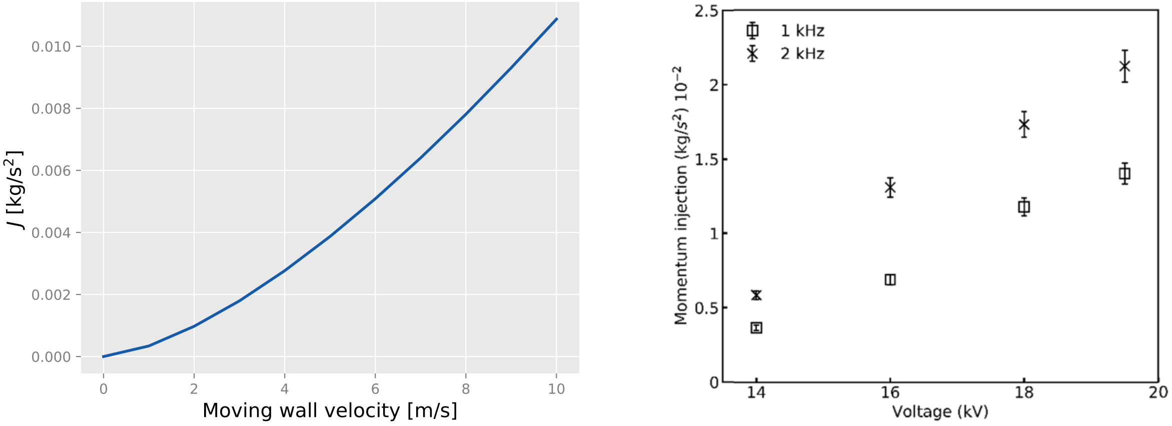

(a) Jet momentum against moving wall velocity

(b) Jet momentum against applied voltage at different actuation frequencies, courtesy of A. Tang et al. [65]

Figure 8.6: Jet momentum plots as functions of actuator input parameters

8.4.3. Simulation of Plasma Circulation Control

Using the moving wall boundary layer approach to replicate the effects of DBD plasma actuators, the circulation control over a rounded trailing edge aerofoil was simulated to estimate the effects of geometry, most importantly trailing edge radius, on the overall method performance. Similar to flat plate simulations in subsection 8.4.2, a two-dimensional CFD simulation was set up in Ansys Fluent software. First, the defined geometry and boundary conditions are described, before the results and subsequent analysis and discussion is presented.

CFD Geometry and Boundary Conditions

For the purposes of later validation, the same aerofoil that was used in experiments in [58] is used in the simulation, namely, NACA642-015A. The trailing edge radius is defined parametrically, while a 10 mm section on that curve representing a plasma actuator is defined so that the midpoint of that section is at a $45°$ angle against the chord. The angle of attack is additionally also defined parametrically so that it can easily be changed for a range of simulations. The chord length is set at 169.2 mm, equal to the aileron chord length as determined in subsection 9.3.1, and the coordinate system is defined from the leading edge of the aerofoil, with x-direction facing towards the trailing edge and y-direction being upwards.

A rectangular domain is defined around the aerofoil: the inlet is located at $x_{inlet} = -2$ m, and a pressure outlet is placed at $x_{oulet} = 5$ m. Horizontal no-slip walls were defined on both top and bottom horizontal surfaces, at $y_{wall} = \pm 2$ m. Inlet velocity is set to the cruise speed, 15.1 m/s.

CFD Results, Analysis

Initially, the nominal plasma-off case was simulated to verify geometry and boundary conditions. The wake generated by the rounded trailing edge, shown in Figure 8.7a, matches closely to experimental PIV measurements from [58], shown in Figure 8.7b, except the fact that simulated wake vortices are more elongated, reaching to $1.07c$ in simulations and 1.02 in experiments.

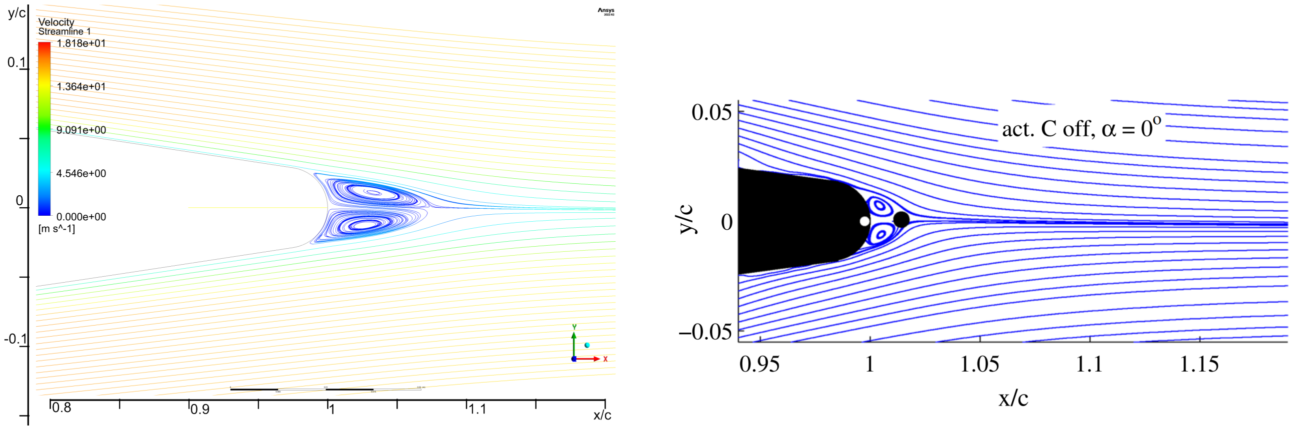

(a) CFD simulation of rounded TE wake

(b) Streamlines derived from PIV measurements of rounded TE wake, courtesy of M. Kotsonis et al. [58]

Figure 8.7: Simulation and experimental result of the wake generated by a rounded TE aerofoil at $\alpha = 0°$ in nominal plasma-OFF case.

Afterwards, the plasma actuator section is set to a rotating moving wall, with a wall velocity of 6.6 m/s. The effect on flow streamlines is presented in Figure 8.8a, where it can be seen that the moving wall slightly enlarges the bottom, counterclockwise rotating vortex aft of the trailing edge. While this is largely in agreement with experimental results of equivalent configuration from [58], shown in Figure 8.8b, the increase in C_l found in [58] could not be replicated. M. Kotsonis et al. [58] reports ΔC_l values of 0.03-0.04 for equivalent conditions of V_∞ and α, while ΔC_l of only 0.0028 was achieved by the simulation, increasing to 0.0056 for a moving wall velocity of 20 m/s.

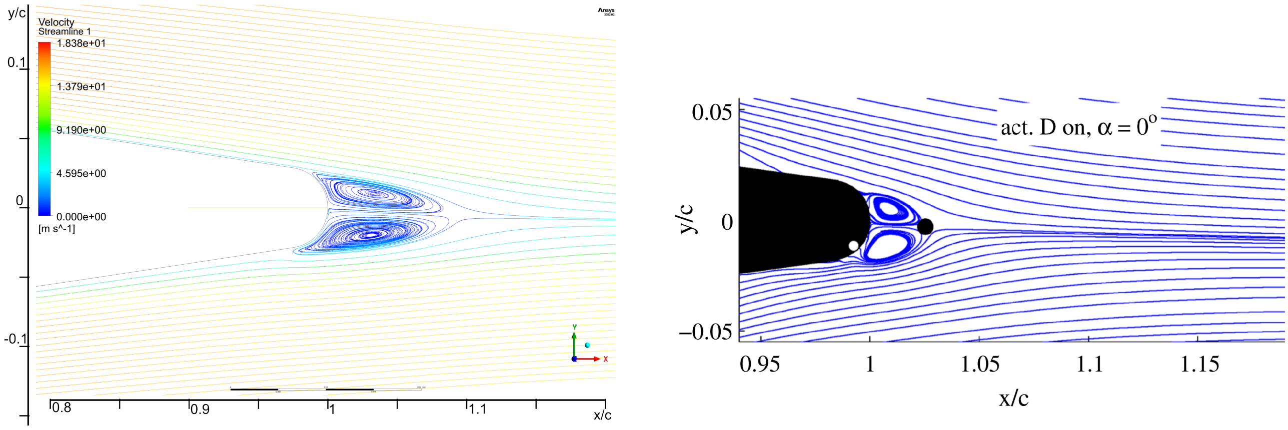

(a) CFD simulation of rounded TE wake, moving wall velocity = $5.6\,\mathrm{m/s}$

(b) Streamlines derived from PIV measurements of rounded TE wake with plasma ON, courtesy of M. Kotsonis et al. [58]

Figure 8.8: Simulation and experimental result of the wake generated by a rounded TE aerofoil at $\alpha = 0°$ in plasma-ON case

.

It has been reported in the literature that numerical simulation of circulation control, with results being sensitive to numerical parameters, chosen turbulence models and solution methods[66]. The effect of turbulence models on the simulated ΔC_l is explored and compiled in Table 8.6. While non-negligible differences between the models can be observed, with a maximum deviation from the mean value of 43% (Transition SST model), the turbulence models themselves do not fully explain the large differences between simulations and experiments. The moving wall section location and mesh definition were varied as well, with minimal (less than 10%) effects on the simulated ΔC_l.

Table 8.6: Simulated ΔC_l for different turbulence models

Turbulence model	ΔC_l
k-ω	0.0028
Spalarat-Allmaras	0.0029
k-ϵ	0.0024
Transition k-kl-ω	0.0018
Transition SST	0.0013
Reynolds Stress	0.0026

A potential explanation for the high discrepancy between simulation and experimental results from literature might lay within the limitations of approximating DBD plasma actuators as a moving wall. Moving wall sizing performed in subsection 8.4.2 was based purely on downstream effects, and it is clear that the locally moving wall and DBD plasma actuator behave very differently. It is unclear what role local boundary layer effects play in aerofoil circulation control.

To summarise, the computational fluid dynamics analysis performed in this section failed to provide data that can be used for circulation aerofoil sizing. As such, a more thorough analysis of CFD methodology and implementation, effects of different turbulence models, mesh refining, boundary conditions etc. must be performed. However, such an approach is deemed too costly with regard to time and resources and falls outside the scope of a DSE project. Instead, circulation aerofoil geometry shall be based on available literature about similar designs and related phenomena in subsection 8.4.4.

8.4.4. Plasma Actuator Design Parameters

This subsection talks about the various design parameters that influence the effect of plasma on the aerofoil. These parameters are namely the aerofoil geometry, material of the electrode and its geometry and the material of the dielectric and its geometry

Aerofoil Geometry

To limit the uncertainty about aerofoil shape effects on circulation control performance, it is decided to use aerofoil geometries already considered in simulations and previous research, namely, NACA642-015A symmetric aerofoil used in experiments by M. Katsonis et al. [58]. The trailing edge is assumed to be a constant radius circle tangent to both sides of the aerofoil.

Due to the overall inability of the used simulation model to consistently replicate the effects of plasma actuators on circulation control, the CFD simulation could not be used to size the trailing edge radius. In existing sources concerning plasma-actuated circulation control over aerofoils, the radius of the trailing edge is rarely mentioned, let alone its effect on the method performance discussed. As such, due to limited time and resources at this stage, the TE radius is sized based on a related but phenomenologically different method of circulation control, namely, a blown jet over a rounded trailing edge. According to [67], an optimal TE radius to chord ratio r/c lies between $2\% - 5\%$. For the control aerofoils of the UAV, the median of this range, $r/c = 3.5\%$ shall be used. The control section aerofoil geometry is shown in Figure 8.9.

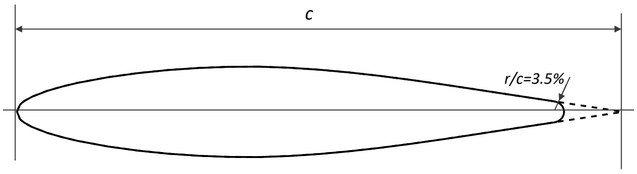

Figure 8.9: Control section aerofoil geometry

Electrode Material and Geometry

To ensure symmetric control of roll, pitch and yaw, the plasma actuators are designed to allow circulation control in both directions. For this purpose, each actuator shall consist of a single exposed electrode placed at the trailing edge and two grounded embedded electrodes placed under the surface of the aerofoil symmetrically against the chord. The embedded electrodes can be connected or disconnected from the electrical ground, offering controlled actuation in both directions. From experimental data presented in [58], it is seen that an optimal location of the exposed/embedded electrode interface for a wide range of angles of attack is at $45°$ against the chord. As such, the exposed electrode covers a $90°$ arc of the rounded trailing edge. This leads to the exposed electrode length being defined by the chord length as Equation 8.5. Meanwhile, the width of the embedded electrode is governed solely by the generated plasma, i.e., the covered electrodes must be strictly wider than the plasma so as not to limit the performance of the actuator [68]. It is reported in [68] that performance of $V_{pp} = 12\,\text{kV}$ plasma actuators approaches an asymptote at $\approx 15\,\text{mm}$ embedded electrode width. To ensure appropriate margins and allow the usage of more powerful power supplies down the line, the embedded electrode width is $l_{embedded\,electrode} = 20\,\text{mm}$.

$$l_{exposed\,electrode} = 0.035c\frac{\pi}{2} \tag{8.5}$$

Copper is reported to be a highly durable electrode material for the purposes of plasma generation [69], and as such shall be used for both exposed and embedded electrodes. The thickness of electrodes on the performance of the DBD actuators is reportedly small [70], and it is decided that the electrodes shall have the same thickness as in circulation control wind tunnel experiment in [58], that is, $t_{el} = 60\,\mu\text{m}$, in order to further limit uncertainty that electrode thickness has both on method performance and nominal case aerodynamics.

Dielectric Material and Geometry

Polycarbonate, specifically PET, is chosen as the dielectric material. This way the dielectric material shall act as the trailing edge structure as well, similarly to the experimental aerofoil used in [58]. The setup in [58] used a dielectric thickness of $3\,\text{mm}$, with actuation peak-to-peak voltage of up to $35\,\text{kV}$. Given that peak-to-peak voltage available on the UAV is limited by the hardware to $V_{pp} = 12\,\text{kV}$, as described in section 8.5, a dielectric thickness of $t_d = 2\,\text{mm}$ is deemed sufficient to prohibit dielectric breakdown and offer sufficient durability[3]. The final TE design geometry, together with top-level electrical connections, is presented in Figure 8.10

---

[3] From discussions with M. Kotsonis, the PET dielectric used in [58] provided exceptional actuator durability.

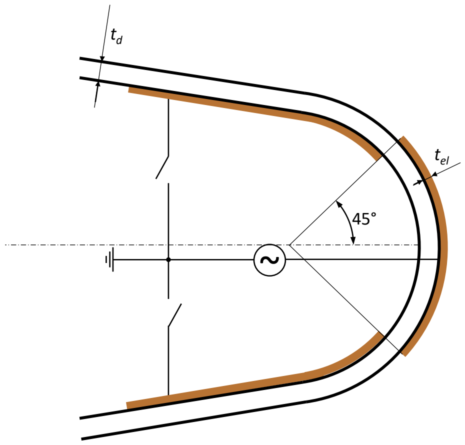

Figure 8.10: Rounded trailing edge with three electrode DBD plasma actuator for circulation control

8.5. Plasma Actuator Electrical Control Signal

The required control signal can be seen in Figure 8.11. The peak voltage V_p is generally in the range of 1.4 kV-20 kV kilo-volts and depends on the dielectric thickness [71]. The base frequency is usually in the order of several kilo-hertz and the burst frequency is in the order of several hertz to hundreds of hertz [72].

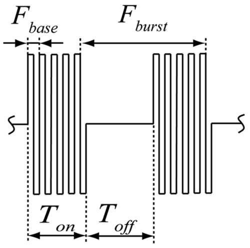

Figure 8.11: Required burst modulated control signal for the plasma actuator [73]

8.5.1. Available HV Generators

As described in the previous section, the system required high-voltage AC bursts in the order of kilo-volts. As it will be a component of a UAV, the weight must be kept low. As experience and knowledge in electrical design is limited, a ready-designed option is required.

The only commercial off-the-shelf solution that could be identified is the Minipuls 0.1 [74] originally designed for [72] and now available for a price of 2000€. Additionally, in literature a number of papers detailing the design of lightweight DBD-plasma power supplies are available. These can be split into two main categories: H-bridge and transformer [73, 75], and solid-state multistage power supplies [71, 76].

In this stage of the design, due to availability and the readily available data on weight and power consumption, the Minipuls 0.1 is chosen which has been used in demonstrator projects previously [1, 72]. It has an input voltage of 15 V-35 V and a base frequency of 5 kHz-20 kHz. It allows tuning of the burst frequency, output power, and duty cycle via onboard trimmers or an analogue control signal [74].

8.5.2. High-Voltage System Layout

There are six control surfaces in total which have to be individually controllable. These are aileron left, aileron right, elevator up, elevator down, rudder left, and rudder right. Furthermore, there are three groups of plasma actuators, of which the members are never turned on simultaneously, these are the ailerons, elevator and rudder.

There were two main options considered for the control layout. Firstly, as seen in Figure 8.12, a single HV-Generator generates a continuous AC-Signal and each plasma actuator's burst frequency and duty cycle are individually controlled by a relay. In this case, relays are considered appropriate since the burst frequencies will be in the order of a few hertz, and the switching speed of the relay is 1 ms [77]. And, as this is a high voltage signal, solid-state switch solutions have poor availability and high cost and are thus avoided. Secondly, as seen in Figure 8.12, a separate HV-Generator for each control surface group, aileron, rudder, and elevator. As each control group contains 2 plasma actuators, relays are still necessary.

As the Minipuls 0.1 has a considerable price of 2000€, which would amount to 12000€ for two UAVs in the case of layout 2, it is considered not possible within the budget of 30000€. Therefore, in this phase of design, layout 1 is used. The Minipuls 0.1 allows for a total actuator length of 90 cm which is well within the total length of the plasma actuator groups [74]. The Minipus 0.1 allows a maximum power consumption of 30 W. Throughout the flight, the power consumption is conservatively assumed to be at 75% of that, leading to an energy budget of 45 W h.

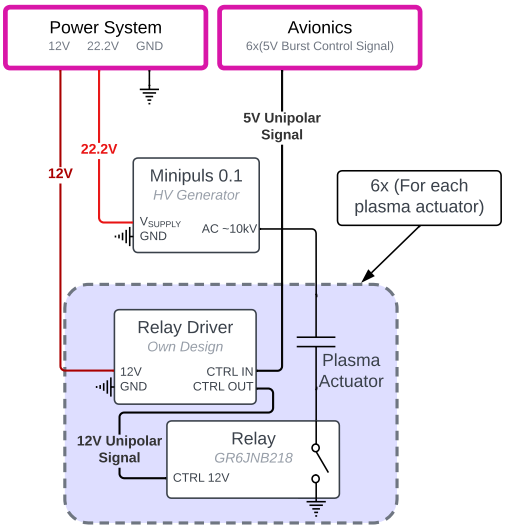

Figure 8.12: Proposed Layout 1 for the Plasma HV system

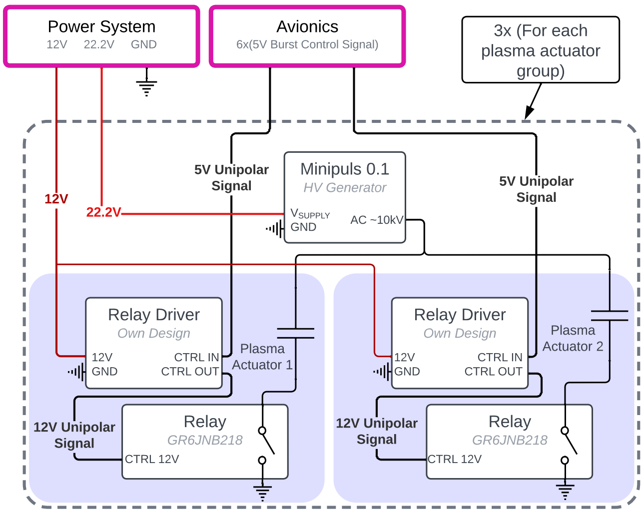

Figure 8.13: Proposed Layout 2 for the Plasma HV system

8.5.3. Plasma burst frequency relay driver

The selected plasma control signal relays require a 12 V control signal. However, the IO outputs of the Pixhawk 6X are at 5 V and are not optimized to deal with the inductive loads of the relay. Additionally, the GR6JNB218 Relay datasheet recommends a Diode for the listed activation times on the order of 1 ms [77]. Therefore a relay drive circuit is designed. The general layout can be seen in Figure 8.14. The base resistor R_B must be low enough to ensure that the actual base current $I_{B,act}$ is larger than the minimum required base current $I_{B,min}$ [78].

The 2N4401 [79] NPN transistor is chosen as the base transistor, providing and can handle the I_{SAT} which is calculated from Equation 8.6 to be 32 mA [77]. This is the current that flows through the relay during the on-state. From this, the DC current gain β is required, which is 90 at the given amperage for the chosen 2N4401 [79]. Then, $I_{B,min} = 0.34$ mA using Equation 8.7. In Equation 8.8 using V_B as 0.7 Volts for silicon diodes, R_B is determined to be 7.7 kΩ or lower. Using a margin of 20% 6 kΩ is chosen. This results in a power consumption of about 2 mW and is thus considered negligible.

$$I_{SAT} = \frac{V_s}{R_{relay}} \quad (8.6) \qquad I_{B,min} = \frac{I_{SAT}}{\beta} \quad (8.7) \qquad I_{B,act} = \frac{V_o - V_B}{R_B} \quad (8.8)$$

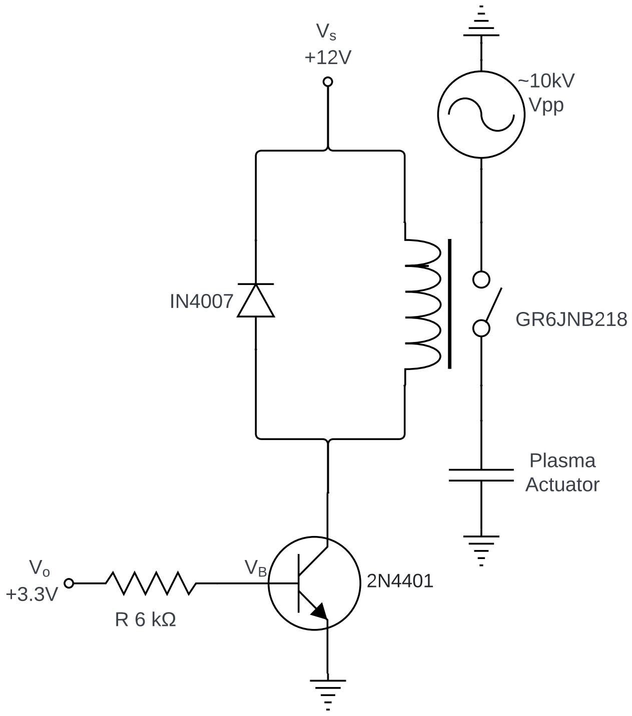

Figure 8.14: Relay Drive Circuit showing the selected components

8.6. Wind Tunnel Experiment

As plasma actuation is a relatively new technology, no reliable models predicting its impact on the aerodynamic performance of a plasma-actuated aerofoil are available. Furthermore, little experimental data has been gathered documenting the response to variations in the applicable control variables. Therefore, a series of wind tunnel experiments were performed in order to investigate the effects of the various control variables on the aerodynamic characteristics of an aerofoil. The wind experimental setup, the testing method and the gathered results are summarised in this section. Additionally, the results will be picked up again in chapter 12, as they are relevant for the actuator model used in the control system, as well as the control derivatives used by the state-space model employed to simulate the UAV.

8.6.1. Test Setup

The experiment was performed in the M-tunnel at TU Delft's Low-speed Wind Tunnel Laboratory. A sample wing was constructed using 3D printers. The wing was printed in different sections which were later on glued together. The trailing edge was replaced by a groove. This allowed for last-minute printing of the trailing edge to increase flexibility. In the final assembly, a 3D-printed trailing edge was fitted in the groove finalising the wing. The CAD file can be seen in Figure 8.15a and Figure 8.15b. Figure 8.15c shows the printed model with the trailing edge and the plasma actuator attached. As used in the design of the PULSE drone, the tested model has a NACA642-015A aerofoil with a chord length of 152 mm and a trailing edge radius of 5.9 mm.

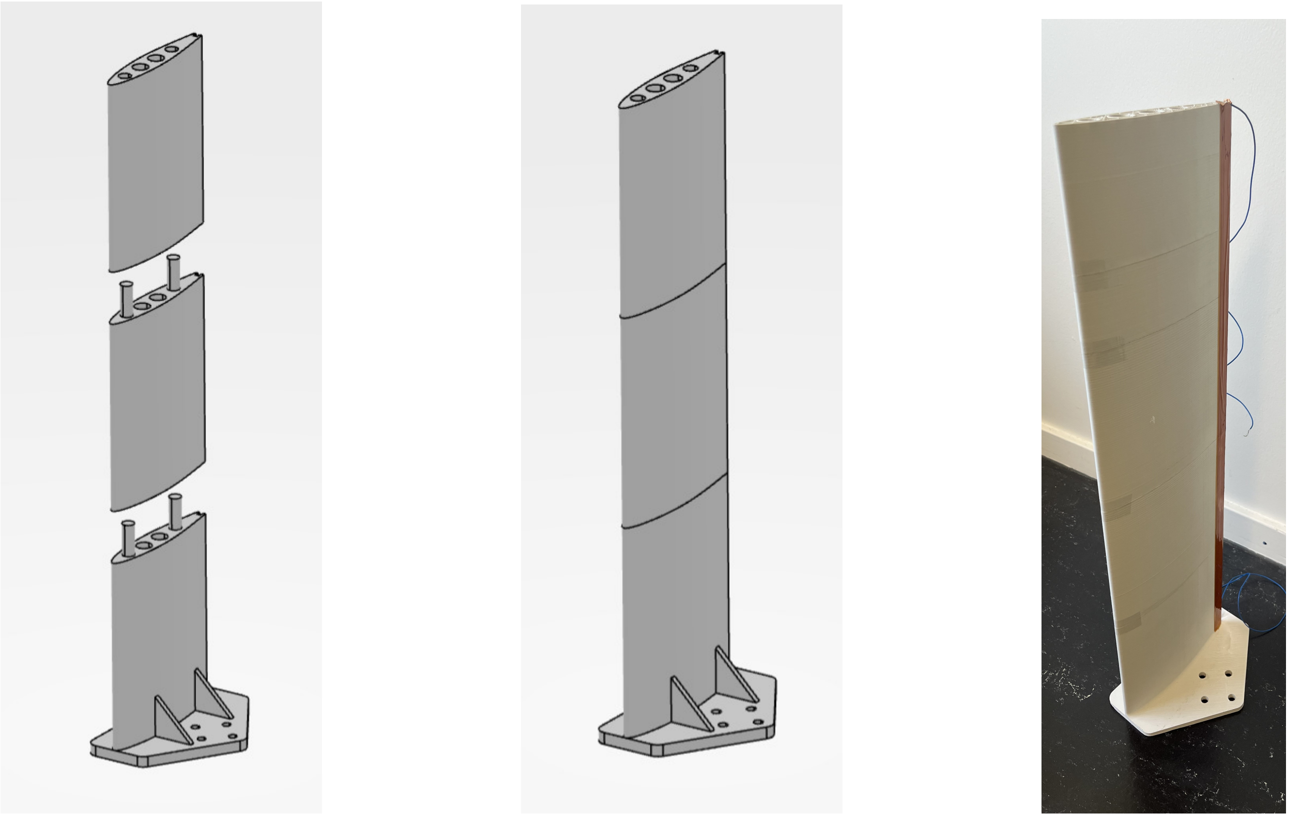
(a) Expanded CAD view of test wing **(b)** Assembled CAD view of test wing **(c)** Printed test wing

Figure 8.15: Overview of test wing development

As all control surfaces have exactly the same dimensions, the results of the wind tunnel tests are directly applicable to the designed UAV. The model has a length of 54 cm while the M-tunnel has a test section of 40 cm height. It is therefore assumed that no 3D effects occur and the measured results are of a purely 2-dimensional nature.

As specified in chapter 3, the entire mission is flown around a velocity of $15\,\frac{\mathrm{m}}{\mathrm{s}}$, resulting in all experiments being performed at this airspeed. Even though the angle of attack is also hardly varied during the mission, it is varied in the experiment due to the fact that different control surfaces sit at different angles of attack. In addition to α, four plasma control variables were considered for iteration during the experiment: The peak-to-peak voltage V_{pp}, the carrier frequency f_{car}, the burst frequency f_{burst} and the duty cycle dc. However, due to design limitations caused by the power system of the actual UAV, V_{pp} and f_{car} were not varied during the experiment as they will also not be varied on the actual UAV. For this experiment the carrier frequency was fixed at 2000 Hz and the peak-to-peak voltage was fixed at either zero, for the plasma-off case, or 12 kV, for the plasma-on case. Since ΔC_l is known to increase with voltage [58], the highest peak-to-peak voltage that can be delivered by the power system of the drone was chosen.

This left three parameters to be varied, resulting in three different test series. In Test Series 1, the focus was put on varying alpha, with f_{burst} and dc set at a few reference values. Test Series 2 focuses on varying the burst frequency with a set of reference values for the other variables. Test Series 3 saw large variations in the duty cycle while keeping the other control variable in rather small rages. A summarised version of the resulting test matrix is given in Table 8.7, where it should be noted that all possible variations in this table were run, including all cases in the first series also being run with the plasma actuators off. In total, this resulted in a total of 264 measurements.

Table 8.7: Overview of performed tests

Test Series 1	α [deg]	f_{burst} [Hz]	dc [-]
	-8, -5, -2, 0, 2, 5, 8, 10, 12	10, 50, 200	0.1, 0.5, 1
Test Series 2	α [deg]	f_{burst} [Hz]	dc [-]
	-2, 0, 2, 5, 8	2, 5, 10, 20, 50, 100	0.1, 0.5, 1
Test Series 3	α [deg]	f_{burst} [Hz]	dc [-]
	-2, 0, 2, 5, 8	10, 50, 200	0.1, 0.3, 0.5, 0.7, 1

For each measurement, the normal and axial forces experienced by the aerofoil were measured by a force balance system for a total of 15 seconds at a frequency of 6250 Hz. The force balance system uses strain gauges to measure the forces, and it should be mentioned that significant interference due to the high voltage signals used to actuate the plasma actuators was observed. However, as each measurement is averaged out over the 15 seconds of measurement time, it is assumed that the experienced interference cancels out due to its oscillatory nature.

The final test setup can be seen in Figure 8.16a. While testing the plasma can be visualised by turning of the lights. A picture of the plasma actuator during one of the tests can be seen in Figure 8.16b.

(a) Test setup **(b)** Picture during test

Figure 8.16: Pictures from wind tunnel test

8.6.2. Processing of Test Data

Each measurement results in a `.tmds` file containing approximately 90,000 force measurements done over the 15 seconds of measurement time. These were read using a MATLAB script from the manufacturer of the force balance measurement system and the useful information was extracted for all files obtained during the test using a different MATLAB script. The 90,000 force measurements were averaged out. Two normal force components were obtained, which were added to get the total normal force. One axial force component was obtained directly from the averaging. The results were saved in an excel file which could be used later on to process the data and analyse the results in Python.

Once the excel file was created, the results were read into a `pandas.Dataframe()` in Python and concatenated with the test matrix. The axial and normal forces are converted into lift, drag and moment, as well as being normalised based on aerodynamic specifications of the test model and the flow environment, such as chord length, surface area or density. The created Python file then splits the normalised data by test series and plots all aerodynamic coefficients against the variable of interest, for instance against α for Test Series 1. Additionally, the ΔC_l is computed and plotted for Test Series 1.

As the main goal of the wind tunnel experiment is to find an actuator model for the PULSE drone, each test series is then interpolated using the `scipy` library and the derivatives of each aerodynamic coefficient with respect to all control variables, so α, f_{burst} and dc are computed.

8.6.3. Results & Discussion

The experiment's main goal was to understand the effect of plasma actuators and gather enough data to predict the required changes in the control variables to achieve the desired change in aerodynamic forces. The first result of the experiment is displayed in Figure 8.17a with the corresponding legend in Figure 8.17b.

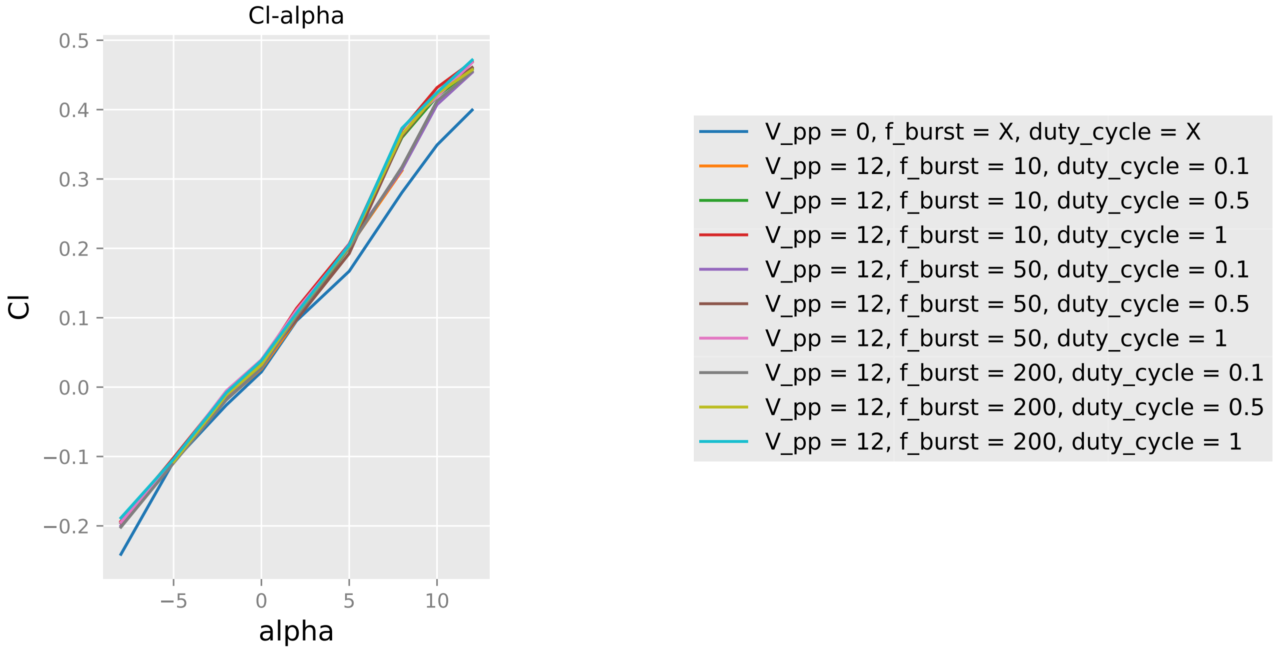

(a) Lift coefficient vs angle of attack

(b) Legend

Figure 8.17: Results lift coefficient vs angle of attack

It can be observed that when the plasma actuators are active there is a clear increase in lift. This shows that the plasma actuators have the desired effect of increasing lift. However, it can also be observed that the overall values that were achieved for the lift coefficient are rather low. When comparing these with data for the same aerofoil from aerofoil Tools [80]. It can be noted that significantly lower C_l values were obtained in the wind tunnel test. Dr Leo Veldhuis was contacted who proposed several reasons for this anomaly. The M-tunnel that was used to perform the measurements is a 40cm by 40cm open-section wind tunnel. The wing used for the test had a span of 54cm which means that part of the wing was outside the direct flow of the wind tunnel. This effectively reduces the surface area of the wing that was impacted by the flow meaning that the values for the coefficients reported in Figure 8.17a are lower than the values that were actually obtained for the parts of the wing in direct flow. Besides this, the effective angle of attack experienced by the wing can be heavily affected by the open-section wind tunnel. The effect can reduce the angle of attack by a factor of 3 according to Dr Leo Veldhuis. This could be a viable explanation for the low C_l values as the effective angles of attack were significantly lower resulting in less lift being produced.

To find the severity of the impact on the effective angle of attack a comparison can be made between the measurement data and data available from aerofoil Tools for the NACA642015 aerofoil used [80]. From the $C_l - \alpha$ graph obtained from aerofoil Tools the amount of lift that should have been generated by the tested wing during the test can be calculated using the test parameters and Equation 8.9. Do note that the $C_l - \alpha$ graph represents the lift coefficient for this aerofoil with a sharp trailing edge. However, the aerofoil used on the UAV uses a rounded trailing edge, which is known to decrease the lift generated. For now, it is assumed that this has a minor impact but it should be checked in later iterations.

$$L = \frac{C_l \cdot \rho \cdot V^2 \cdot S}{2} \tag{8.9}$$

The lift obtained by theory compared with the lift obtained during the test can be seen in Figure 8.18a. Based on Dr Leo Veldhuis' recommendation, the alpha values of the test were scaled to fit with the theoretical values. The result of this scaling can be seen in Figure 8.18b. The correction factor that led to this fit is 0.3.

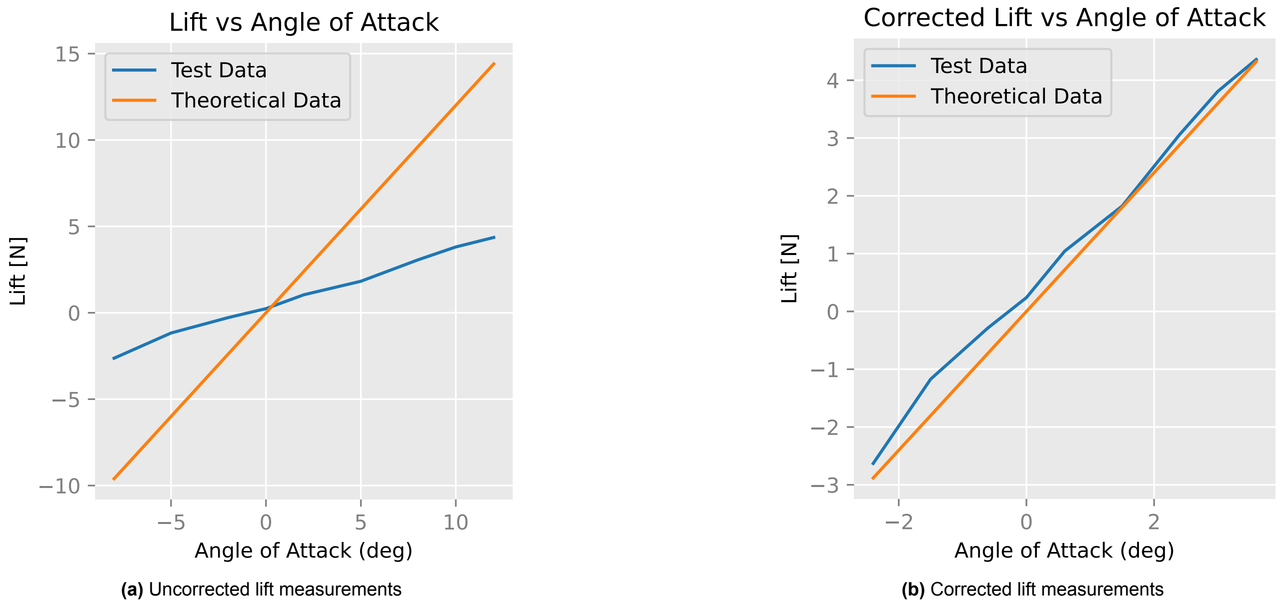

(a) Uncorrected lift measurements

(b) Corrected lift measurements

Figure 8.18: Lift measurement angle of attack corrections

After applying this correction factor, the remaining plots can also be modified to show the corrected angle of attack. Test Series 1 varies alpha over a wide range while only slightly varying the burst frequency and the duty cycle. Therefore, Test Series 1 resulted in the aerodynamic coefficients being plotted against alpha as can be seen in Figure 8.19. From the lift coefficient versus alpha curve the change in lift coefficient versus alpha can be obtained which is given in Figure 8.20a. The different lines present in the plots can be linked to the different test cases through the legend present in Figure 8.20b. Test Series 2 resulted in plots displaying the aerodynamic coefficients as a function of the burst frequencies. This plot and the corresponding legend are given in Figure 8.21 and Figure 8.22 respectively. Figure 8.23 shows the plots corresponding to Test Series 3. The aerodynamic coefficients are varied as a function of the duty cycle. The legend for this plot is given in Figure 8.24.

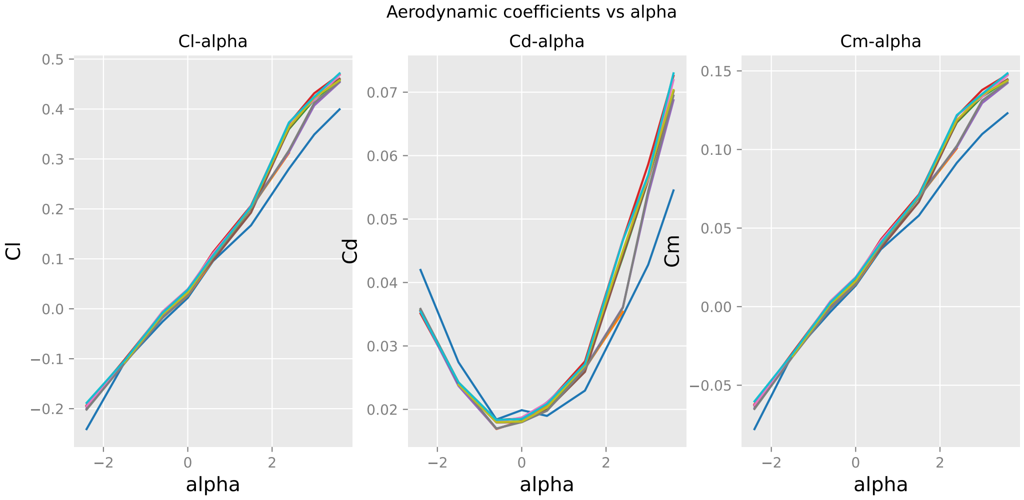

Figure 8.19: Aerodynamic coefficients versus angle of attack

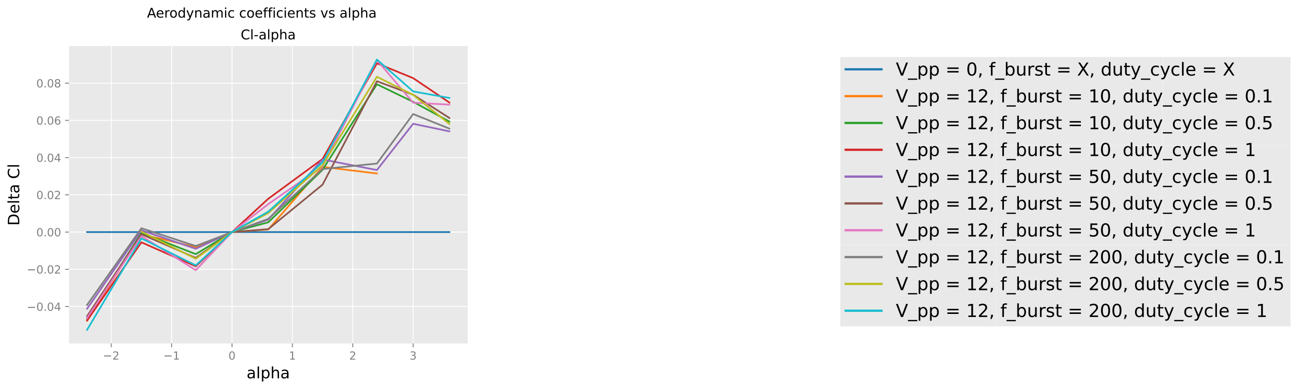

(a) Increase in lift coefficient versus angle of attack

(b) Test Series 1 legend

Figure 8.20: Results Test Series 1

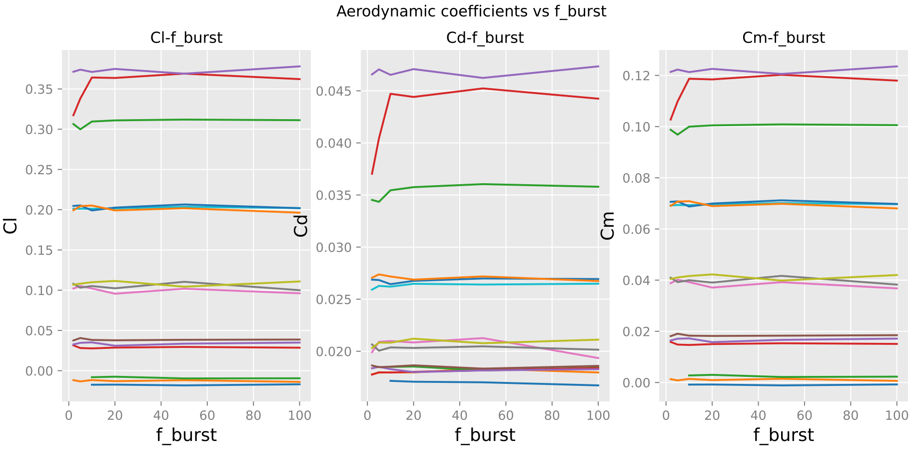

Figure 8.21: Aerodynamic coefficients versus burst frequency

Figure 8.22: Test Series 2 legend

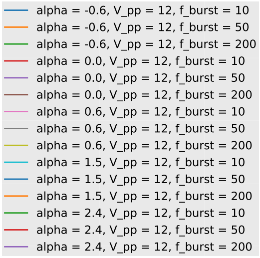

Figure 8.24: Test Series 3 legend

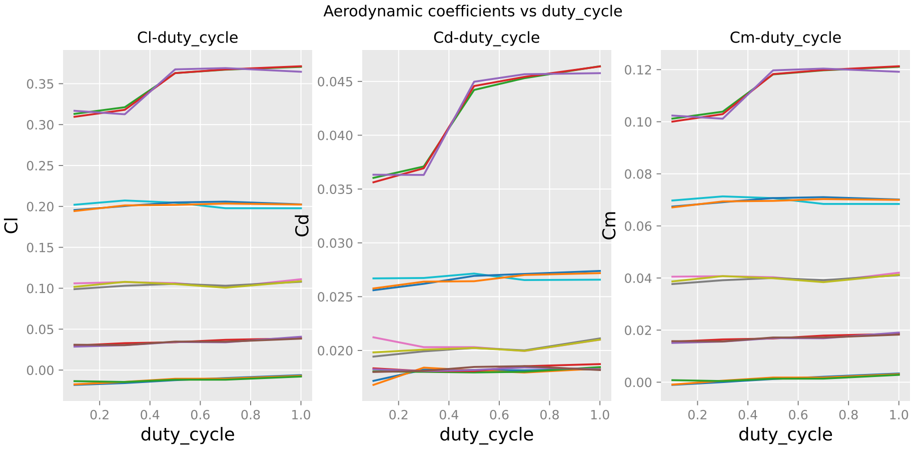

Figure 8.23: Aerodynamic coefficients versus duty cycle

From these plots several observations can be made. From Figure 8.19 it can be seen that due to the increase in lift created by the plasma actuators, there is also an increase in drag and moment around the quarter-chord point. The drag increase is due to an increase in lift-induced drag as the lift increased when the plasma actuator was turned on. The moment was calculated by multiplying the lift force with the moment arm which explains why this graph is a scaled version of the $C_l - \alpha$ plot.

Figure 8.21 shows that when varying the burst frequency, all parameters remain nearly constant. This indicates that f_{burst} has a very low influence on the increase in lift generated by the plasma actuators. Because of this effect and because of hardware limitations explained in section 8.5 a very low burst frequency in the order of a few Hertz is chosen.

In Figure 8.23 it can be seen that the duty cycle has a very low influence on the increase in lift for most angles of attack. This can be observed by the very low gradient of the plotted lines. However, for $\alpha = 2.4$ a significant gradient can be observed. This indicates that in this region the plasma actuator influence can be controlled using the duty cycle, thus the duty cycle could be used as a control variable. Nevertheless, it should be noted that in this configuration there would be a significant region in which there is no control authority which would impose several issues.

Overall, this test showed that it is possible to obtain a significant increase in lift when using plasma actuators. Besides this, it indicated that changing the burst frequency has a very minor effect on the increase in lift. However, increasing the duty cycle has been shown to increase the lift generated by the plasma actuator at a certain angle of attack range. Due to the post-processing angle of attack corrections for open-section wind tunnels that had to be performed, only a small range of angles of attack was tested. The effect of the duty cycle for larger ranges of alpha should be investigated further to expand on the research done so far.

8.7. Plasma Actuation System Preliminary Design Results

This section compiles the results of the plasma actuation system preliminary design. Roll, pitch and yaw control is achieved by changing circulation over a rounded trailing edge aerofoil. Since there is no sharp trailing edge to enforce the Kutta condition, the location of the rear stagnation point and by extension lift generated by the aerofoil can be modified by plasma actuators. A modified NACA642-015A aerofoil is chosen for the control sections, with a trailing edge radius to chord ratio $r/c = 3.5\%$. To provide symmetric control, each plasma actuator consists of three electrodes - a single exposed electrode mounted on the symmetry axis and two embedded grounded electrodes on both sides of the aerofoil. Exposed electrode width is defined by the section chord, while embedded electrodes are 20 mm in width. All electrodes are made from 60 µm thick copper tapes, while 2 mm thick PET acts as both dielectric and the TE structure. The circulation aerofoil is shown in Figure 8.9

and a detailed TE geometry overview is presented in Figure 8.10.

An electrical system was designed to provide plasma actuators with sufficient power and control signals. Namely, Layout 1, shown in Figure 8.12, is used. A mass, power, energy and cost budget of the plasma actuation system is presented in Table 8.8. It must be noted that actuators and cables are not given power and energy values, since their power is provided by the Minipuls 0.1 HW generator.

Lastly, an overview of plasma actuation system compliance to subsystem requirements is presented in Table 8.9

Table 8.8: Plasma actuation system mass, power, energy and cost budgets

Component	Function	Mass [g]	Power [W]	Energy [W h]	Cost [€]
Copper + Dielectric	Ailerons	0.15	-	-	170
Copper + Dielectric	Elevators	0.075	-	-	85
Copper + Dielectric	Rudder	0.04	-	-	45
Belden Wire Cable 8890 002100	HV Wire	0.125	-	-	81
Minipuls 0.1	HV Generator	0.34	30	45	2148
DAR70575-HR	HV Relay	0.144	0.19	0.38	254.7
Other Components	PCB, Diodes, etc.	0.015	0.10	0.20	40
Total		0.889	30.29	45.58	2823.7

Table 8.9: Plasma Actuation System Compliance Matrix

Requirement ID	**Requirement**	**Verification**	**Compliance**
SUB-PCS-01	Plasma actuation system shall not damage aerodynamic surfaces	Testing	**PASS**
SUB-PCS-02	Plasma actuation system shall generate maximum noise of 50 dB	Testing	**PENDING**
SUB-PCS-03	Plasma actuation system shall use a maximum of 90 W of power	Analysis	**PASS**
SUB-PCS-04	Plasma actuation system shall have a durability of 2 hr under a duty cycle of 80 %	Testing	**PASS**
SUB-PCS-05	Plasma actuation system will weigh less than 720 grams	Inspection	**PENDING**

8.8. Further Design and Recommendations

In this chapter, the research and design process for the plasma actuation system was presented, which ultimately resulted in using DBD plasma actuators at the aerofoil trailing edge for circulation control. The work presented in this chapter included preliminary method selection and trade-off, modelling of DBD plasma actuators and aerofoil circulation control in CFD simulations, geometry sizing and concept validation by a wind tunnel test. Nevertheless, several recommendations towards further design are made, that could not be implemented in the scope of a DSE project. These recommendations are instead compiled in this section.

Method Design and Simulation

Firstly, it is suggested that a more complete numerical model is implemented for the optimisation of control aerofoil geometry. Since the moving wall approach for replicating the aerodynamic effects of DBD plasma actuators did not succeed in simulating circulation control, the implementation of existing numerical plasma actuator models within CFD software is recommended. Common DBD plasma actuator models are Shyy's [61], Suzen's [62] and Dörr and Kloker [63] models. An analysis of the governing equations and model performance should be performed to determine which model is best suited for simulating plasma-actuated flow circulation control.

Moreover, circulation control computational fluid dynamics are reportedly sensitive to the turbulence model chosen [66]. To ensure reliable simulation results, the different turbulence models, their governing equations and validation methods, as well as possible modifications/corrections should be investigated for meaningful and accurate results. Additionally, a more extensive mesh sensitivity analysis should be conducted.

A sophisticated CFD simulation, if properly verified and validated, can subsequently be used for the control section aerofoil geometry optimisation. Three main geometry parameters are identified for which numerical optimisation is recommended, given below. All optimisation results should subsequently be validated in a wind tunnel test.

- **Aerofoil shape:** In this paper, NACA642-015A aerofoil is considered for all control section aerofoils, since for this aerofoil experimental data is available in literature [58]. However, it is expected that by modifying aerofoil shape and therefore pressure distributions, flow behaviour at the trailing edge can be fine-tuned to favourably affect plasma actuator performance. Moreover, asymmetric aerofoils should also be considered for control sections, especially for roll control. Doing so could increase nominal plasma-OFF performance, as well as minimise three-dimensional effects at the interface between different aerofoils.
- **Trailing edge shape:** For the sake of simplicity and management of limited time and resources, only circular trailing edges tangent to the aerofoil contour were regarded in this work. Alternative trailing edge geometries, such as elliptical, parabolic, etc., are possible and could be implemented for increased performance or controllability over a wider range of flight or electrical input parameters.
- **Trailing edge radius:** Due to the unsuccessful implementation of CFD simulations for circulation control and limited literature, the trailing edge radius is taken from an adjacent yet different control method, namely, blown Coandă jets over rounded trailing edges. It is expected that increasing the TE radius is a trade-off between achieving increased ΔC_l and decreasing the aerodynamic performance of the aerofoil.

For the purposes of circulation, only single AC-DBD actuators were considered. However, in the past decades, a number of variations and combinations of actuator configurations have been developed. These include multiple DBD actuator arrays[81], sliding discharge DBD actuators[82], and nanosecond pulse DBD actuators[83], among others. Each of them offers its individual advantages and disadvantages, and it is recommended that their applicability for flow circulation control be investigated for increased performance and controllability.

Control Signal Generation

For the generation of the high-voltage high-current, a commercially available Minipuls 0.1 HV generator is used. While it offers substantial performance at a relatively low weight, the voltage is limited to 12 kV peak-to-peak. Moreover, the transformer cascade used in the Minipuls still accounts for non-negligible mass addition, and the cost of Minipuls limits the amount that can be used in the UAV. As such, exploring alternative ways of supplying the required AC signal to the actuators is recommended, possibly designing specialised generators in-house. One notable transformer-less method is using solid-state MOSFETs [84], which is capable of achieving higher efficiencies than conventional transformer cascades.

Wind Tunnel Testing

The circulation control method viability was validated by a wind tunnel experiment. The experiment was conducted in the TU Delft M Tunnel, which has an open-section setup. As such, several recommendations are made to account for the aerodynamic effects associated with open-section tunnels.

First, angle of attack correction is required to account for the jet deflection by the aerofoil. A number of correction equations are available in the literature, depending on the wind tunnel parameters. Alternatively, the effective angle of attack can be determined by matching experimental data with known $C_l - \alpha$ curves, as was done in this paper. However, to correctly capture the aerodynamic effects of a rounded trailing edge, the reference $C_l - \alpha$ curve should be from a modified aerofoil as well, for which $C_l - \alpha$ curves are rarely available, and lifting line theory used in simple aerofoil analysis tools is not applicable. It is strongly recommended that angle of attack corrections are applied in reverse to the range of desirable angles of attack before finalising the test matrix.

In comparison, closed-section wind tunnel experiments would allow more accurate measurements of plasma-actuated circulation control in two dimensions and are as such preferred over open-section tunnels.

Moreover, it is suggested to greatly expand the test measurement series so that a wide array of actuator design parameters can be validated. Major aspects to be tested in wind tunnel measurements are given below:

- **Different TE geometries:** Validation of the trailing edge design is recommended due to difficulties encountered in CFD simulation. Depending on manufacturing techniques, the aerofoil can be made in such a way as to allow for interchangeable trailing edges.
- **Different plasma actuator configurations:** Different plasma actuator configurations, such as multi-DBD arrays or sliding discharge DBD actuators, are increasingly more complex to simulate numerically. As such, their viability for aerofoil circulation control is best determined through wind tunnel test series.
- **Local velocity fields:** Experiments performed as part of this work consisted solely of force balance measurements. While such an instrument provides generated lift and drag that can subsequently be used for actuator performance determination, local aerodynamic behaviour around the TE is not captured. For this purpose, it is recommended that velocity fields near the TE plasma actuator are measured through

particle image velocimetry (PIV) or similar techniques. Such an experiment would provide insight into the local effects and might aid in actuator design and optimisation.

- **Atmospheric effects:** Performance of plasma actuators is reportedly dependant on atmospheric effects such as temperature or moisture [85]. If possible, measurement and control of atmospheric parameters within the tunnel are suggested, so that they can be correlated to the mission environment.
- **Noise:** While the use of plasma actuators is expected to reduce noise generated by the UAV aerodynamic elements, during the wind tunnel test it was observed that a distinct high-frequency sound was produced by the plasma actuator itself. While not confirmed by measurements, it is assumed that the sound corresponds to the actuator carrier frequency. Due to the mission focus on silent flight, measurements of the actuator sound intensity and frequency spectrum are recommended, and subsequently that data could be used for measurement filtering or, possibly, active noise cancelling. It must be noted that such measurements require silent room facilities instead of a wind tunnel.

9 Wing Design

The wing is the main lifting body of the aircraft, thus particular attention is required during the design, both aerodynamically and structurally. This chapter starts with selecting and designing aerodynamic elements such as aerofoil and ailerons. Next, the aerodynamic integration is discussed considering 3D effects. Lastly, the required structure is designed.

9.1. Wing Design Requirements

The relevant subsystem requirements for the wing design are summarised in this section under Table 9.1. Since this is a multidisciplinary aspect of the design, the subsystem requirements pertain to several departments. Note that the compliance in the fourth column pertains to the final design compliance with the verification.

Table 9.1: Wing Design Requirements

Requirement ID	Requirement	Verification	Compliance
SUB-AER-01	The system shall have a glide ratio of at least 14	Analysis	PENDING
SUB-PCS-09	The system shall have no moving control surfaces.	Inspection	PASS
SUB-PCS-11	The system shall provide roll control authority.	Analysis	PENDING
SUB-STR-01	The structure shall support a wing loading of 52.1 N/m^2	Analysis	PASS
SUB-STR-03	The structure shall support a wing loading of 52.1 N/m^2	Analysis	PASS
SUB-STR-04	The wing shall be detachable.	Inspect	PASS
SUB-STR-05	The wing itself shall be modular such that it fits inside 387x468x1818 mm when non-operable.	Inspect	PASS
SUB-STR-12	The structure shall not deform plastically during landing	Analysis	PASS
SUB-STR-19	The structure shall not fail under maximum loads of 3.75 and -1.5	Analysis	PASS
SUB-STR-20	The structure shall not fail under ultimate load factors.	Analysis	PASS

9.2. Aerofoil Selection

The aerofoil selection occurred in three steps. Firstly, a collection of 50 aerofoils were taken from past successful missions, literature and personal knowledge of aerofoils. From this, the selection was reduced with an initial trade-off (not shown) and the six best-performing aerofoils were explored in more detail. Lastly, a sensitivity analysis was performed on the results.

9.2.1. Detailed Trade-off

As mentioned previously, the best six performing aerofoils from the 50 initial aerofoils were chosen to be investigated and traded further. The trade-off criteria were selected with the respective weights and justifications given in Table 9.2. After collecting the data for each aerofoil a score of 1-4 relative to each other was given. The results can be seen below in Table 9.3.

Table 9.2: Aerofoil Tradeoff Criteria weights and rationale

Criterion	**Weight(%)**	**Weight rationale**
c_l, max	25	This parameter dictates the stall speed of the aircraft and thus the cruise speed as well. Plasma has larger effects at lower cruise velocities due to the relative momentum the plasma actuator can impart on the flow. Due to this reason, a high weight was allocated.
$(l/d)_{max}$	25	As explained in section 3.1, a large portion of the flight will be an unpowered glide. While this is purely a measure of the theoretical peak l/d ratio, it serves to measure the potential of the aerofoils. Thus the maximum potential lift-drag ratio of the aerofoil is an important parameter.
$(l/d)_{cruise}$	15	The justification of this parameter is similar to that of $(l/d)_{max}$. However, this takes into account the angle of attack that the aircraft will fly at (from the mass found during conceptual design)[33]. Thus it serves to be more of an indication of the expected l/d ratio. This is not weighted as much as the other important parameters due to the uncertainty of this value.
$(l/d)_{deflection}$	10	This parameter measures the largest drop in l/d ratio at 5° either side of the peak l/d angle. This parameter was chosen due to being a measure of the sensitivity of the system to deflections in the angle of attack. A small drop in l/d leads to the reliability of glide performance.
c_m	10	The moment coefficient is a parameter which will impact the design, however, the weight is relatively low due to the fact it is not a driving design parameter. It can be compensated for with careful design of the empennage.
c_{d0}	5	This parameter largely impacts the overall drag of the drone due to the plot. However, the low weight was attributed due to the fact that the drag can be compensated for with the propulsion system and the low accuracy of the drag model used.
Stall Characteristic	5	The stall characteristic is a qualitative measure of the lift curve response to deviations in the angle of attack. This was due to the operations being in a coastal area where wind velocities and thus angle of attacks can vary. This was given a low weight due to the relatively low accuracy of separation models used for the source data.
Linearity	5	The linearity qualitatively measures the linearity of the data. This parameter was considered for two reasons. Firstly for simplicity of working with the data, since iterations of the aerofoil can be linearised. This was given a low weight due to being an inconvenience rather than a driving design parameter.

Table 9.3: Final aerofoil Tradeoff

Criteria	C_l,max	l/d max	l/d cruise	l/d drop 5deg	Cm	Cd0	Stall	Linearity	Total
Weight	25%	25%	15%	10%	10%	5%	5%	5%	100%
MH115	3	3	4	4	1	3	2	4	3.05
MH114	4	3	2	4	1	1	3	2	2.85
Goe 532	3	1	1	3	3	1	4	4	2.20
NACA 4412	2	1	3	2	3	3	4	2	2.15
A18	1	2	3	1	2	3	1	2	1.80
E176	1	2	4	1	4	4	1	2	2.20

9.2.2. Sensitivity Analysis

After the trade-off was performed, a sensitivity analysis was performed on the results to evaluate the effect of the criterion weight on the outcome of the trade-off result. For this, each of the criterion weights were adjusted by -30% to 30% in increments of 10% and the change was dispersed among the other weights based on the proportion of their original weights. Table 9.4 displays the sum of the positions of each aerofoil for the weight change of each parameter. Thus the lower the number, the better the aerofoil performed.

Table 9.4: Aerofoil Sensitivity Analysis

Design/Weight Change	MH115	MH114	Goe 532	NACA 4412	A18	E176
30%	8	16	29	38	48	29
20%	8	16	29	38	48	29
10%	8	16	28	40	48	28
-10%	8	16	28	40	48	28
-20%	8	16	29	38	48	29
-30%	8	16	29	37	48	30

From Table 9.4, it is clear to see that the MH115 aerofoil performed above all other aerofoils. Furthermore, the MH114 also constantly performs well to achieve second best across all weight changes. Both aerofoils are actually propeller aerofoils, which have similar properties that match the profile of this mission. Particularly the high performance in l/d-related criteria. The drawback of propeller aerofoils is clearly seen at the moment coefficient. The implication of this to the plasma drone design is minimal since the team expects that the limiting factor for the horizontal stabiliser will be control authority rather than stability. This is to say that the area of plasma actuators needed for the control authority is expected to be larger and thus more constricting than the area needed for stability to counteract the main wing moment. Thus the chosen aerofoil for the preliminary design is the MH115, with its implications being further explored in section 11.5.

9.3. Aileron Design

Following a usual aircraft configuration, the wing planform will contain two ailerons close to the wing tips for roll control. By being conversely actuated, ailerons produce moment disequilibrium resulting in the aircraft rolling about its longitudinal axis. While in conventional aircraft ailerons are moving surfaces which physically alter the local camber of the wing section, the author's drone will make use of changing the Kutta condition location to produce a local increase in the lift to set the aircraft rolling.

The requirements imposed for rolling are derived from flight performance requirements and are identified in the form of a rotational acceleration requirement of $2.22\frac{rad}{s^2}$ around the y-axis of the aircraft.

9.3.1. Sizing the Plasma Aileron

For the preliminary design of the roll control actuators, the problem was simplified to a great extent, by means of the following assumptions and modelling choices:

1. **AER-AIL-01:** The restoring effects of the lift distribution on the wing and horizontal stabiliser are not considered. This has a non-conservative effect since in reality, the actuators need to be sized to counteract this restoring moment as well.
2. **AER-AIL-02:** The actuation force is concentrated at a point at the end of the main wing. This has a conservative effect since the moment arm of the actuation force will be slightly smaller than in reality, resulting in a conservative estimation of the actuation force.

3. **AER-AIL-03:** The roll manoeuvre is performed at a constant angle of attack. Due to the varied efficacy of plasma actuators at different angles of attack, the effect is case-specific and cannot be determined at this stage whether it is conservative or not. For simplicity, it will be assumed that the ailerons are inclined with respect to the free stream at their optimum angle (see subsection 8.6.3 or the works of Kotsonis M. et al. [58]).
4. **AER-AIL-04:** Both positive and negative ΔC_L values are equal in magnitude at the optimal angle of attack. This implies a symmetrical behaviour of the aerofoil when it is inclined at the optimal angle of attack for the plasma actuators.
5. **AER-AIL-05:** The aircraft is considered to be in a state of pure roll. The force equilibrium is only considered for the two opposing actuation forces. The effects of these assumptions will be considered under section 7.4.
6. **AER-AIL-06:** The roll-induced angle of attack at the wing tips is negligible. The effects of these assumptions will be considered under section 7.4.
7. **AER-AIL-07:** The ailerons are going to be placed at the end of the wing tips.
8. **AER-AIL-08:** Three-dimensional flow effects do not affect the wing tips. This is a non-conservative assumption, as wing tip vortices will sway the optimal operation of the ailerons.
9. **AER-AIL-09:** The effects of the plasma actuators on the local lift distribution are optimal.
10. **AER-AIL-10:** Reynolds number matching ensures the applicability of the experimental data gathered by Kotsonis M. et al [58] to the ailerons. This restricts the chord length of the aileron sections to 169mm.
11. **AER-AIL-11:** The effects of the step change in aerofoil from the wing tip to the aileron are minimised.

The problem was initialised by drawing the simplified FBD of the problem and applying Newton's Second Law for Rotation. The simplified FBD is shown in Figure 9.1. Only the forces affecting the roll manoeuvre are displayed.

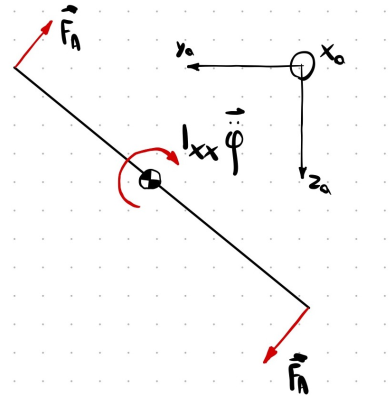

Figure 9.1: Free body diagram of the drone during the simplified roll manoeuvre.

Considering the sum of moments about the centre of gravity, the relation can be expressed by Equation 9.1.

$$I_{yy}\ddot{\phi} = F_A \cdot \frac{b_w}{2} + F_A \cdot \frac{b_w}{2} = F_A \cdot b_w \tag{9.1}$$

The force on the actuator can be expressed as in Equation 9.2, considering that it is a consequence of the local circulation increase due to plasma actuation.

$$F_A = \frac{1}{2}\rho V^2 S_A \Delta C_L \tag{9.2}$$

In reality, the ΔC_L term considers the three-dimensional effects near the wing tip, although, for preliminary sizing purposes, this is replaced by the two-dimensional ΔC_l. The three-dimensional effects are ignored as per AER-AIL-07. Including this assumption, Equation 9.1 and Equation 9.2 can be rearranged into Equation 9.3, in order to determine the surface of one aileron.

$$S_A = \frac{2 I_{xx}\ddot{\phi}}{\rho V^2 \Delta C_l b_w} \tag{9.3}$$

Equation 9.3 presents the idealised equation used to determine the total surface area of one aileron. To account for the non-conservative assumptions, a safety factor of 1.5 is used to ensure the ailerons will ensure control authority. Extending the surface area by a factor of 1.5 assumes that the ΔC_L can be modulated such

Table 9.5: Aileron sizing and performance parameters

Parameter	Value	Unit
Aerofoil	NACA642015	$[-]$
Safety factor	1.5	$[-]$
Surface area (with SF)	2x1.5E-2	$[m^2]$
Chord length	0.169	$[m]$
Aileron span	0.089	$[m]$
$\alpha_{aileron}$	8	$[°]$
ΔC_l	0.01	$[-]$

that an acceleration lower than the maximum attainable acceleration is possible.
The analysis of this simplified case resulted in the final aileron parameters listed in Table 9.5.

Until this juncture, the aileron is sized to satisfy the roll requirements under specific conditions. A concluding remark on preliminary aileron design entails a reflection on the validity of the assumptions and their consequences. The main restraint of this reckoning lies in AER-AIL-03 and AER-AIL-08, which limit the validity of the design in a real context. To address AER-AIL-03, during the design process, it was mistakenly considered that an 8$[°]$ angle of attack of the aileron will serve optimally, although the fact that both positive and negative lift is needed for the roll was neglected. Thus, the current design assumes a one-direction roll manoeuvre with limited ability to roll in the opposite direction. This will be addressed in the detailed design of the aileron in subsection 9.4.1. The relevancy of wing tip three-dimensional effects due to the step change in the wing's section geometry will be addressed in subsection 9.3.2, where mitigation of cross-flow interaction between the wing tip and the aileron will be addressed.

9.3.2. Aileron Integration

The current section addresses the solution for mitigating cross-flow at the location where the wing tip and aileron conjoin. This solution follows a number of design choices, done for decoupling the wing tip from the aileron and to simplify the structural integration of the aileron.

Due to the lack of literature on the subject of the integration of different wing geometries, two approaches were defined by the author with the help of outside resources. The first approach will treat the problem of interaction from the point of view of mitigating consequences of viscous effects, while the second will treat the issue of cross-flow from an inviscid perspective. In both cases, it was concluded that cross-flow will be a consequence of pressure differentials between the surface of the wing tip and the aileron surface. In the current scope of the dividing plate, the pressure differentials are to be mitigated both on the pressure and suction sides of the two geometries.

The pressure differential between the two surfaces can be visualised in the form of pressure distribution graphs in Figure 9.2.

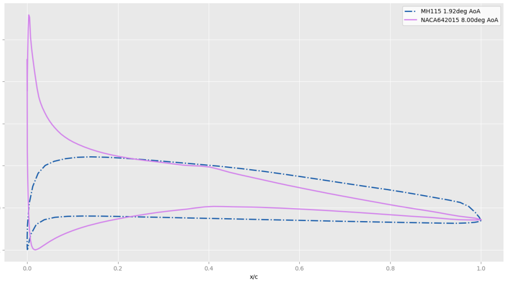

Figure 9.2: The pressure distributions on the MH115 and NACA642015 aerofoils at the wing tip and aileron angle of attack

The pressure distributions presented in Figure 9.2 were obtained using XFLR5 Type 1 analysis at Re=210000. This entails that the analysis is done at a constant velocity at the specified angle of attack using a Vortex Panel Method[1]. A pressure differential can be visualised in Figure 9.2 anywhere the dashed and full lines do not intersect. This means that at a specific chord-wise location the pressure distribution of the MH115 differs from the one of the NACA642015 and fluid will tend to flow from the large to the low-pressure zone.

---

[1] The validity of the pressure coefficient estimation cannot be directly quantified, although a qualitative validation has been performed by Mathieu Scherrer and is presented in the XFLR5 documentation

Boundary Layer Fence Concept

The first approach to counteract the pressure differential followed an idealised situation, neglecting 3D effects. Due to the problem's geometry, it was determined that the bounds of the plate will be determined by the upper surface of the MH115 and the lower surface of the NACA642015. This condition can be visualised in Figure 9.3, where the two aerofoils are represented at their inclination in the airpath reference frame. It is clear that the pressure differentials will need to be counteracted at the top surface of the MH115 and at the bottom surface of the NACA642015. As well, the bottom of the MH115 and the top of the NACA642015 will interact due to pressure differences, although these effects are not considered, as the region will be covered and different sizes would provide the same form drag.

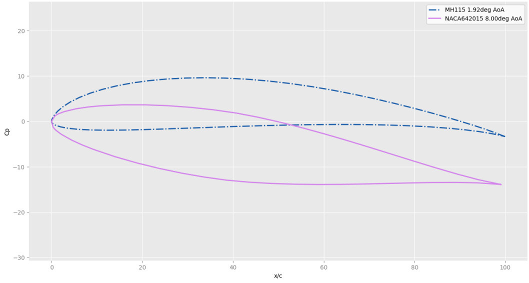

Figure 9.3: Footprint of the aerofoils at the wingtip-aileron conjunction.

In order to decrease the form drag introduced by the dividing plate to a minimum, the initial approach targeted the pressure differential only over the location where it occurred. Considering viscous effects, a boundary layer forms along each surface encountering free stream flow in which flow velocity is retarded and the pressure does not vary vertically[86]. This means that the pressure differential at the top surface would occur due to the low pressure in the boundary layer of the MH115 and the free stream pressure on the bottom side correspondingly. This suggested that a dividing plate extending the exact height as the boundary layer thickness on top of the MH115 and on the bottom of the NACA642015 would block the pressure differential at a minimum cost of form drag.

This approach was built on the assumption that three-dimensional effects would not affect the pressure distribution. As such, the 'boundary layer approach' was conceptually validated upon consultation with an outside party[2]. Similar methods have also been employed in old Soviet aircraft[3] and were known as 'boundary layer fences' or 'wing fences'[4].

Preliminary Aileron Fence

With the help of Dr Leo Veldhuis, the problem was deemed to be more complex than initially expected, mostly due to the lack of research in three-dimensional cross-flow behaviour. The authors were recommended to take on a heuristic approach and estimate the optimal divider size by trial and error. Such an approach can be validated in two ways, either by CFD analysis or by a wind tunnel experiment. Due to resource constraints, neither of these approaches was deemed feasible. It is recommended, however, that the effects are first studied using the former of the two validating approaches and the latter be used for quantification of the effects purposes. For preliminary purposes, the dividing plate was sized by considering a 2cm normal extension to the footprint set by the two aerofoils. The design can be visualised in Figure 9.4, where a top view of the divider plate is shown. The footprint of the aerofoils is shown for reference.

---

[2] The boundary layer method was approved by Ir. Joris Melkert and PhD candidate Alessandro Porcarelli at the TU Delft Aerospace Engineering Faculty.

[3] www.wikipedia.org (accessed on 10-06-2023)

[4] Finally, at the suggestion of Ir. Joris Melkert, Dr Leo Veldhuis was contacted to shed light on the boundary layer approach. His insight proved that the cross-flow and interactions between the two different geometries will not be governed by two-dimensional viscous effects, but rather by three-dimensional inviscid vortices.

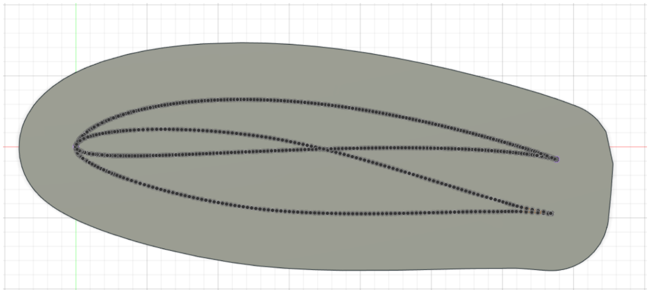

Figure 9.4: Divider plate top-view.

The dimensions of the divider plate presented in Figure 9.4 will be addressed further in Table 9.6.3.

9.4. Consideration of three dimensional Effects

After the aileron dimensions are defined, the lifting planform of the wing can be iterated. The aim of the iteration is to adjust local twists and chords such that the final lift distribution of the wing section resembles and elliptical lift distribution with high fidelity. This is done numerically, by minimising the residual sum of squares method between the obtained lift distribution and the corresponding elliptical one. These values were only iterated for the lifting section since the aim for the wing's control (plasma) section was to keep variables as constant as possible such that performance is predictable and easy to use. The goal of this section is to optimise the elliptical distribution of the wing such that the lift-drag ratio is also maximised. The assumptions used for this section are explained below.

1. **AER-TDE-01:** 3D correctional factors remain constant for different platforms. This assumption was made such that the 3D effects could easily be integrated into the optimisation code. The magnitude of the effect of this assumption is unknown however is used for the preliminary design and will be removed in further iterations. The methodology for this assumption is further explained in subsection 9.4.1
2. **AER-TDE-02:** Negligible aerodynamic interaction between lifting and control sections of the wing. This assumption is made to simplify the problem for the purpose of preliminary iterations. Additionally, this is done since the interactions are not quantifiable at the level of detail of this iteration. However, the goal of the aileron fence is to minimise the effects of the interaction between the surfaces. This assumption is non-conservative with respect to the total lift produced.
3. **AER-TDE-03:** Negligible aerodynamic interactions between the lifting surface and fuselage. This assumption is made to simplify the problem for the purpose of preliminary iterations. Additionally, this is done since the interactions are not quantifiable at the level of detail of this iteration. The assumption is non-conservative with respect to the total lift produced
4. **AER-TDE-04:** Negligible aileron fence plate. This assumption was made to not include the lift forces from the plate. This effect of this assumption is low due to the thin nature of the divider plate, in addition to being a constant discrepancy for all the iterations.
5. **AER-TDE-05:** Rigid structure. This assumption is made to simplify the problem for the purpose of iteration. This assumption is conservative with respect to the lift produced since the moment produced will decrease the local angle of attack along the span. The magnitude of the effect of this assumption is unknown.
6. **AER-TDE-06:** The optimal configuration has a total wingspan of 3 m. This assumption is made since it would result in higher lift-drag ratios due to reducing the impact of 3D effects.

9.4.1. Three dimensional effects approximation method

To account for 3D effects factors, a correction factor polynomial was created which relates the 2D lift to 3D effect. Despite not being perfectly accurate, by defining the 3D effects polynomial the iteration process would include considerations for 3D effects which was deemed more time efficient and reliable than considering it later. This was also done in accordance with AER-TDE-01.

The lift distribution was gotten from a model of a NACA642015 airfoil with 0.169 m chord length, 1.5 m wingspan and 8 degrees angle of attack, inserted into XFLR5. The geometric parameters were taken from Table 9.6.3, extrapolated for the semi-wing span, this is justified by the fact that these parameters were believed to mimic the wingtips conditions best. XFLR5 with the 3D panel method was chosen as the simulation method due to simplicity and familiarity. From the resultant lift fraction distribution, a sixth-order polynomial correctional factor was created. The polynomial is displayed as Equation 9.4. Note that the y variable is the position along the span.

$$CF = -6.4621y^6 + 27.265y^5 - 44.064y^4 33.828y^3 - 12.495y^2 + 1.9321y + 0.9162 \tag{9.4}$$

The equation is shown in relation to the data points in Figure 9.5. It should be remarked that this is only valid for total wingspans of $3\,\mathrm{m}$, which was assumed as part of AER-TDE-06.

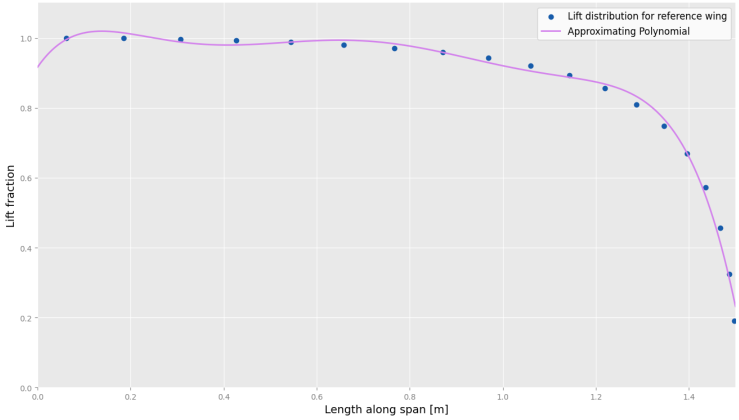

Figure 9.5: 3D correctional factor polynomial

9.4.2. Design Approach

Three possible lifting planform configurations were considered, each developed as a result of analysing the shortcomings of the previous iteration. The differences between the planforms are strictly for the lifting (non-plasma) sections since the ailerons were sized independently in subsection 9.3.1. Each configuration varies in complexity and computational cost as explained below. Note that the possibility of an elliptical planform was excluded due to manufacturing constraints.

- **Tapered, linear twist lifting section:** This was the first approach which was explored since it was the continuation of the conceptual design planform. From this optimisation, the resultant lift distribution varied noticeably from the elliptical distribution. Another minor issue was that the optimisation resulted in a root angle of -0.5° and a lifting-planform tip angle of 1.1°. Thus resulting in a positive twist, which is unfavourable since it results in a less mass optimal result. Upon further investigation, the positive twist was attributed to the fact that a simple (no twist) taper results in a linear reduction of twist, therefore, the program attempted to correct this effect by increasing the angle of attack near the tip of the lifting planform section. The mass optimisation is clearly not ideal for mass due to the system trying to minimise c_l at the root. Note that usually twist is done to delay stall at the control surfaces, however since that section is separated through a divider plate, the interference between the respective sections is minimal[5].
- **Tapered, Quadratic twist of lifting section:** As an attempt to mitigate the previous result, an approach was undertaken with a quadratic varying twist along the wing. Despite adding an additional degree of freedom to the system, this was done in an attempt to increase the efficiency of the root section since there is an additional degree of freedom for the local twist along the chord. Additionally, this approach aimed to match the elliptical distribution better. The results from this code resulted in a very close match of the elliptical distribution at the expense of worsening the positive twist result similar to the previous configuration, in this configuration the angles changed from -4° at the root to -1.16° at the tip of the lifting surface. Additionally, a new adverse effect occurred, where the root chord increased from 0.4 (from the previous approach) to 1.2m. This new value was also deemed unacceptable since the fuselage dimension for the preliminary design was 0.7m as determined in section 10.3. Lastly, from a manufacturing standpoint, a quadratic twist may be complicated to implement and thus unfavourable.
- **Constant chord section with an additional tapered section, linear twist:** To tackle issues of the previous configuration. It was thought to add a constant chord section at the root before tapering. This was done since the elliptical distribution varies minimally near the root. This solution seemed to solve the previous problems without introducing additional complexities. Note that the additional degree of freedom with respect to the first configuration remained.

To help visualise the planform and define relevant variables, Figure 9.6 was created. In the figure, the dimensions, angles, airfoils and aerodynamic centre have been depicted with green, blue, orange and red colours, respectively.

---

[5] This approach was suggested during a personal discussion with Dr Leo Veldhuis, in which the issue was treated from a vortex mitigation perspective.

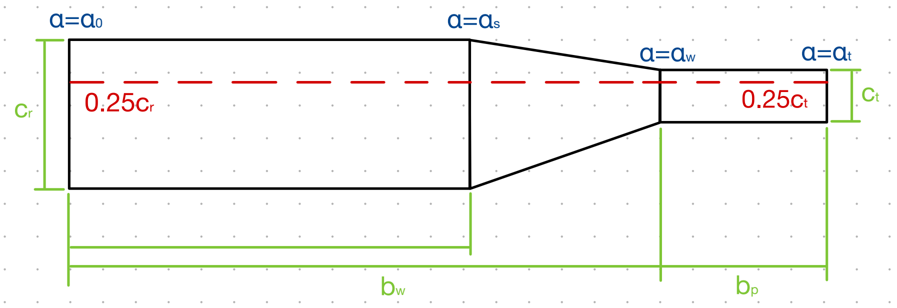

Figure 9.6: Wing parameter definitions

All the parameters regarding the plasma section of the airfoil have been well defined in subsection 9.3.1. Thus, b_w can be determined using the total wing span requirement. Additionally, no sweep was included since the flight profile was far out of the transonic/sonic regime, and the centre of mass could be adjusted through the positioning of the fuselage with respect to the wing. The quarter chord length indicates the positioning of the aerodynamic centre, which for simplicity was chosen to be kept at a constant position with respect to the fuselage.

All other parameters remain undefined. However, the problem would be over-constrained if they were simply to be iterated for. The twist parameter was chosen to relate α_s and α_w as functions of the spanwise position and α_0. Lastly, the lift of the wing was a constraint which could be used to define one of the degrees of freedom. This was done by calculating the integral of lift along the lifting section span and equating it to the total required lift minus the lift the control (plasma) section produces. Note this equation considers the changing lift due to varying chord lengths and angles of attack, and not the 3D effects. The derived equation is shown below.

$$\phi = \frac{6b_w \frac{L-L_{plasma}}{\rho V^2 c_{L\alpha}} - 6c_r(\alpha_0 - \alpha_{L=0})b_w^2 - 3(\alpha_0 - \alpha_{L=0})(c_t - c_r)(b_w^2 - b_s^2)}{3c_r b_w^3 + 2(c_t - c_r)(b_w^3 - b_s^3)} \tag{9.5}$$

Due to Equation 9.5, the free variables that remain are α_0, c_r, and b_s. For the optimisation algorithm, a fixed step input discretisation of $1\,°$, $0.1\,$m, $0.1\,$m was chosen, respectively. Using this initial input, the system would calculate the effectiveness of the lift distribution by the method of sum of residual squared. Subsequently, it would perform the same operations for variations of the input parameters of $\pm\,0.25\,°$, $0.025\,$m, and $0.025\,$m, respectively. If one of these variations was found to perform better than the initial guess, the system would perform the same variations at the new point. This operation was done for a maximum of three steps in any direction. The maximum number of three steps was implemented to limit computational time since on the fourth step in a direction would result in being at the same initial guess of another node. This means that two nodes would be converging at the same point rendering one of them redundant, thus imposing the maximum step limit would significantly reduce computation time.

9.4.3. Results

The resultant lift distribution for the preliminary design is shown in Figure 9.7. The distribution is compared to the conceptual design planform (updated for the preliminary mass value to compare their ellipticity).

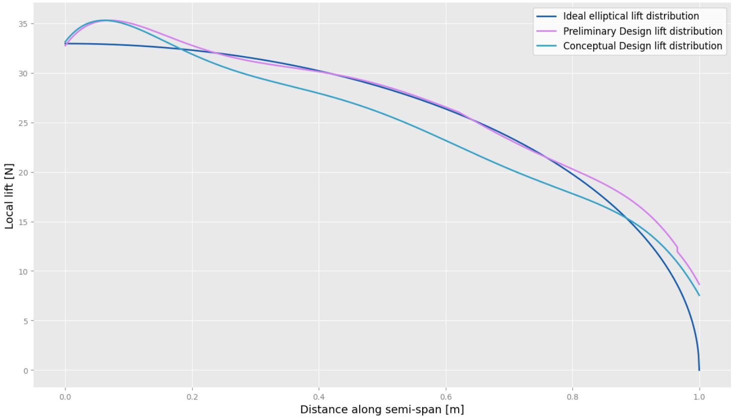

Figure 9.7: Ideal, preliminary and conceptual design lift distributions

When relating the two curves, it can be seen that the preliminary design matches the elliptical distribution better than the conceptual design, with an exception at the root section and tip section. The root section difference is caused by Runge's phenomenon affecting the accuracy of the 3D effects polynomial close to the root boundary, whereas the tip section difference is due to the fixed profile of the control section. One recommendation for reducing the error close to the root is to discretise the root section of the wing with more control points in the XFLR5 analysis. This was fixed during the iteration process explained in subsection 9.6.3. The conceptual and preliminary design tip sections do not match since the conceptual design lacked control surfaces.

A summary of the variables for the preliminary design lift distribution seen in Figure 9.7 is shown in Table 9.6. Note that the control surface-related variables are repeated in this table for completeness, with the values for those parameters having been determined in subsection 9.3.1.

Table 9.6: Planform sizing

Parameter	Value	Unit
b_s	0.9	$[m]$
b_w	1.41	$[m]$
c_r	0.2	$[m]$
α_0	6	$[deg]$
α_s	3.23	$[deg]$
α_w	1.68	$[deg]$
twist rate	3.08	$[deg/m]$
c_t (repeated)	0.169	$[m]$
b_p (repeated)	0.089	$[m]$
α_t (repeated)	8	$[deg]$

9.5. Structural Design

The functionality of the wing structure is to endure loads produced during all aircraft operations and transfer them to the fuselage. This section discusses all aspects that were connected to designing such a structure for the mission at hand.

9.5.1. Subsystem Requirements

In order to drive the design of the fuselage structure, subsystem requirements are generated. This is done by investigating which system requirements affect the particular subsystem and then making them specific to it. section 9.1 illustrates the structure subsystem requirements, listing their ID, its title and a proposed validation method.

9.5.2. Assumptions

All assumptions are based on the collective experience of the group and serve to simplify the design process. They are stated in the following list.

- **STR-WS-01:** The drag force experienced by the wing does not play a critical role in designing the wing structure.
- **STR-WS-02:** The distributed weight force does not play a critical role in designing the wing structure.
- **STR-WS-03:** The skin of the wing does not carry any of the internal loads.

The structural integrity of a wing can be achieved with many different layouts. An analytical model can be made to analyse these layouts and to figure out which of these will be the most weight-efficient option, but this is not feasible due to the time constraint of the project. Therefore all feasible design options will be listed together with their pros and cons after which one option from these will be chosen in a group discussion and analysed.

Normal and shear stresses due to lift force, bending moment, and torsional moment will be analysed in the first design iteration. The analysis will be performed using an idealised structure with zero-thickness skin and point area booms. The boom areas will be sized using the maximum internal bending moment derived from the aerodynamic analysis done in XFLR5. Next, the minimum thickness of the aerofoil skin and structural elements will be determined by calculating the maximum internal shear flow caused by the internal shear force and torsional moment. For the first iteration it is assumed that the internal shear force is only due to the lift force (**STR-WS-01**) and the internal torsional moment is only due to the lift force and pitch moment around the aerodynamic centre. The stresses will be calculated with the loads at cruise conditions multiplied by a maximum load factor of 3.8 [6]. After the stresses are calculated the specific shape of the structural elements will be chosen.

The type of layout chosen would heavily rely on the type of internal loads in the wing. The MH115 aerofoil chosen in chapter 9 had the structural downside that it has a larger pitch moment coefficient than standard wing airfoils, due to the fact that it officially is a propeller aerofoil. Due to this open sectioned layouts were discarded because of their poor resistance to torsion. A wing box structure with two spars was chosen due to its efficient resistance to torsion and its good resistance against normal forces. One spar is placed at 0.25c and the second is placed at 0.65c.

The idealisation of the wing box with its applied forces can be seen in Figure 9.8a. In this idealisation all the normal forces are carried by the point area booms and all the shear forces are carried by the zero-thickness skin. The shear force (V_y) was translated to the symmetry axis to make the analysis easier, this is shown in Figure 9.8b. Due to this translation, the torsion (T) increases by V_y multiplied by the translated distance. Using the preliminary wing design, forces and moments experienced by the wing could be obtained in XFLR5. These moments and forces were processed using Python and led to the internal loading diagrams seen in Figure 9.9. To keep the stress calculations simple all boom point areas are assumed to be equal. This leads to a product moment of inertia (I_{xy}) of zero. This reduces the normal stress equation to Equation 9.6. This also causes the shear stress analysis to be a special case in which the formula for the shear flow in the vertical walls can be reduced to Equation 9.7. The shear flow due to torsion can be calculated using Equation 9.8 in which the shear flow flows in the same direction as the torsion.

$$\sigma = \frac{M_x \cdot z}{I_{xx}} \quad (9.6) \qquad q_v = \frac{V_z}{2 \cdot 0.07c} \quad (9.7) \qquad q_t = \frac{T}{2A_m} \quad (9.8)$$

Aluminium alloys and polymers like carbon fibre are both good materials to use for structural elements in aircraft due to their high specific strength. Aluminium 2024-T4 will be chosen over carbon fibre since the design needs to be modular (**SUB-STR-05**). Aluminium spars have the property to be clamped or bolted tight to other components. Carbon fibre although very strong in the plane had a hard time resisting the out of plane loads that occur during clamping and bolting. The design is made so much that the skin and the ribs do not carry any load. Therefore, these can be made from very light material.

After running the program with a specified boom area of $15mm^2$ per boom the maximum normal stress stays under 70% of the yield stress. The booms are therefore over-designed for normal stress. Running the program for the shear stress results in a necessary vertical spar thickness of $0.02mm$ for aluminium which is well below the manufacturing limit for aluminium sheets. Aluminium sheets can be manufactured for a reasonable cost until at minimum $0.31mm$ thick [7]. However, this comes at the cost of being very sensitive to damage. After taking this into account together with the manufacturability of the eventual spar it was decided that the spars will be c-stringers with a uniform thickness of $1mm$ and flange widths of $15mm$ that are manufactured by bending an aluminium sheet. This way they are over-designed for bending, torsion and shear. The necessary horizontal skin thickness is $0.06mm$ for aluminium, which again is not manufacturable. The code was again run but this time with balsa wood as the material. This led to a necessary wall thickness of $3mm$ at the root of the wing. The weight of using aluminium and balsa reinforcements were compared and eventually, the balsa reinforcement was chosen due to its lighter weight. The ribs and skin do not carry any load and therefore a very lightweight

---

[6] www.eaa.org (accessed on 11-06-2023)

[7] This value was suggested by Ir. J. Sinke as the minimal sheet thickness that can be produced at a reasonable cost.

and easily producible material can be used for the ribs and the skin. For this balsa wood was chosen [8]. All parameters are summarized in Table 9.7

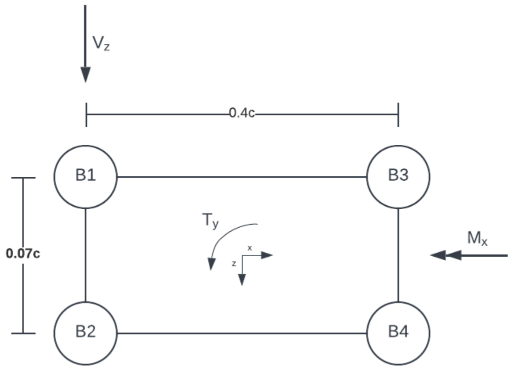

(a) Idealisation of the wing box with the applied forces.

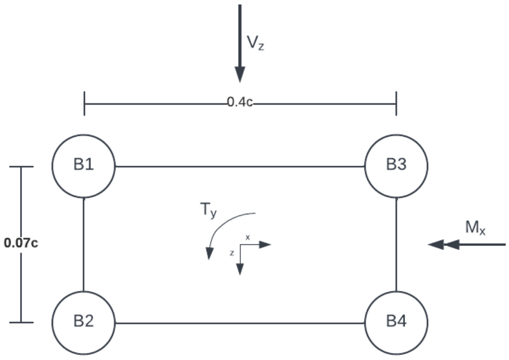

(b) Idealisation of the wing box with the applied forces with the shear force translated to the symmetry axis.

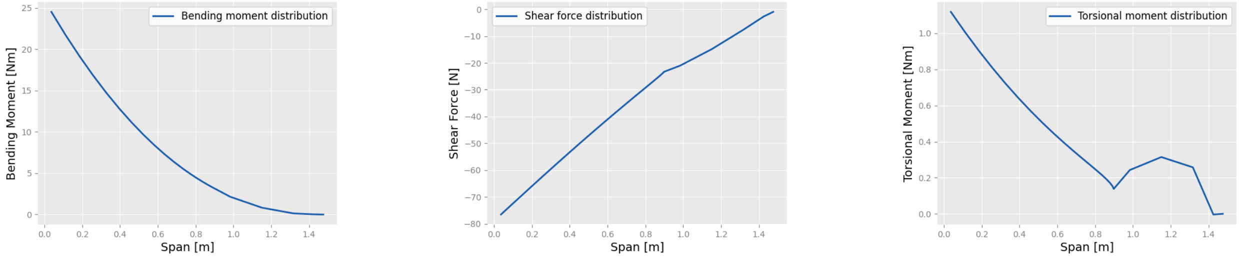

(a) The internal bending moment over the half-span of the wing.

(b) The internal shear force over the half-span of the wing.

(c) The internal torsional moment over the half-span of the wing

Figure 9.9: Graphs of the internal forces and moments in the wing.

9.5.3. Manufacturing

In this section, a more rigid argumentation will be formed regarding manufacturing decisions made in the design process. The web thickness of the spar is over-designed for the loads it carries, it was however made this thick so that it would be easily manufacturable. Now each spar can be made out of one metal sheet by bending it 90 degrees twice. The wing itself does not need to be modular. Therefore the flanges of the ribs can adhere to the flanges of the spar using an adhesive. The same can be done for attaching the wing skin to the rib flanges. Holes need to be drilled in the flanges of the spars where it sticks out of the root of the wing so that they can be bolted to the wing box.

9.6. Design iteration

The iteration of the wing design revolved mainly around improving the models used for the aileron design and three-dimensional effects. Due to the resultant changes in the planform, the supporting structure had to be iterated as well. This iteration stage also considered the updated mass and inertia from the end of the preliminary design stage, as stated in Equation 11.7.

9.6.1. Aileron Design Iteration

Due to high aspect ratio requirements dictated by gliding flight, the span of the wing needed to be maximised with respect to its surface area. This imposed that both the ailerons and the main wing should not go over a span of 3m as per legal requirements. Optimising the aileron thus proved a delicate problem, which was carried out in parallel with the wing design.

Compared to the preliminary design, the final design of the ailerons added a higher level of complexity, mainly by removing some of the assumptions and obtaining more accurate values of roll requirements and I_{xx}.

First of all, **AER-AIL-01** was removed completely, by considering the roll-damping effects of the horizontal stabiliser and main wing. These effects are quantified in the performance requirements in Table 7.4 and thus

---

[8] Balsa was chosen seen as many group members had prior experience with building model airplanes out of this material.

Table 9.7: Wing structure parameters

Parameter	Value	Unit
Spar flange width	15	$[mm]$
Spar web height	0.07c	$[mm]$
Spar thickness	1	$[mm]$
reinforcement thickness	3	$[mm]$
reinforcement span	1400	$[mm]$
Aerofoil skin thickness	1	$[mm]$
Maximum internal bending moment	24520	$[Nmm]$
Maximum internal shear force	76.582	$[N]$
Maximum internal torsional moment	9951	$[Nmm]$
σ_{max}	221.8	$[MPa]$
τ_{vmax}	27.3	$[MPa]$
τ_{hmax}	4.8	$[MPa]$
σ_{y-Al}	324	$[MPa]$
τ_{Al}	283	$[MPa]$
τ_{Balsa}	5	$[MPa]$

the sizing method for the ailerons does not change.

Secondly, AER-AIL-04 has been validated through wind tunnel experimental data in chapter 8. Considering the graphs in Figure 8.20a, the maximum angle of -2.4° was considered as both a negative and positive change in lift coefficient is viable at this angle of attack. The change in lift coefficient ΔC_L considered for the final design is 0.05 and corresponds to the -2.4° angle of attack.

Moreover, **AER-AIL-07** has been fully acclimatised as a design choice, with the final aileron design considering the control surfaces mounted at the tips of the main wing. **AER-AIL-09** is no longer an assumption, but rather a design choice, suggested by the experimental wind tunnel data. **AER-AIL-11** is no longer an assumption, as the availability of experimental wind tunnel data validates the use of a 169mm chord.

However, one shortcoming of this configuration occurs at the integration of the wing tips with the aileron. Due to the twist angle of both the aileron and wing tip, larger pressure gradients occur than for the preliminary design. One recommendation for mitigating this effect is constraining the wing tip twist angle to be such that the local lift coefficient matches the lift coefficient of the aileron.

Table 9.8: Final aileron sizing and performance parameters

Parameter	Old Value	New Value	Unit
Aerofoil	NACA642015	NACA642015	$[-]$
Safety factor	1.5	1.25	$[-]$
Surface area (with SF)	2x1.5E-2	2x2.9E-2	$[m^2]$
Chord length	0.169	0.169	$[m]$
Aileron span	0.089	0.17	$[m]$
$\alpha_{aileron}$	8	2.4	$[^\circ]$
ΔC_l	0.01	0.05	$[-]$

The new aileron parameters are presented in Table 9.8. The aileron final design has one major shortcoming, which was not quantified within the scope of the current project: the efficacy of ailerons placed at the wing tips under three-dimensional effects. This shortcoming is only treated conceptually and two recommendations arise. First of all, the obvious solution is to move the ailerons at a different span-wise location further away from the tips. This would entail redesigning the entire lifting platform and within the author's design project, the choice of placing ailerons at the wing tips is quantified in **AER-AIL-07**. Furthermore, placing the ailerons at a different span-wise location would reduce the effective moment arm of the aileron force, which under the current technology readiness level of plasma actuators can be a limiting factor[9]. The second recommendation to mitigate three-dimensional effects close to the wing tip is to include winglets.

9.6.2. Final Interplate

The interplate dividing the aileron from the wing tip was redesigned to account for the new geometry. Due to the problem's novelty, the design was not further optimised. The new geometry is presented in Figure 9.10.

---

[9] During a wind tunnel experiment, the author proved the use of DBD plasma actuators on a NACA642015 wing, which resulted in lift coefficient increments as high as 0.08.

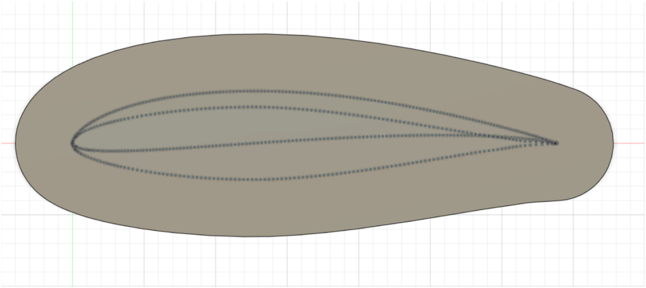

Figure 9.10: Final divider plate top view

9.6.3. Three-Dimensional effects iteration

This section is closely related to section 9.4. From this section, the main improvements revolved around improvements in the three-dimensional effect model, thus removing **AER-TDE-01**. Contrary to what was done for the preliminary model, the 3D model was iterated. This means that every iteration was run in conjunction with an XFLR5 simulation from which the correctional factor polynomial was found.

Another improvement of the model was noticed from Equation 9.4, which was not an even function, despite lift being symmetric about the Y axis of the plot. To improve this, an approach was taken that used both sides of the lift distribution to interpolate a function. The updated function used for the final iteration can be seen in Equation 9.9, with the resultant plot seen in Figure 9.11.

$$P^n(y) = CF = -0.0169y^6 - 0.1924y^4 + 0.0622y^2 + 0.9891 \tag{9.9}$$

Note the $P^n(y)$ notation used in Equation 9.9. The n notation superscript is used to state the order of the polynomial. Thus the integral of $P^n(y)$ is $P^{n+1}(y)$, as explained below in Equation 9.10. This concept and notation are used for Equation 9.11.

$$P^{n+1}(y) = CF = -\frac{0.0169y^7}{7} - \frac{0.1924y^5}{5} + \frac{0.0622y^3}{3} + 0.9891y \tag{9.10}$$

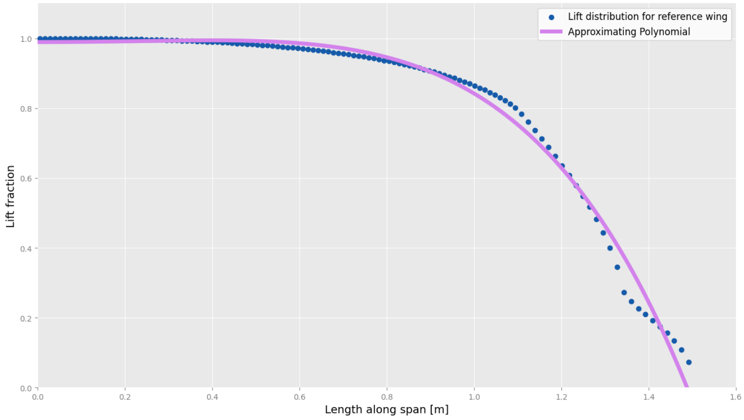

Figure 9.11: Updated 3D correctional factor polynomial

From this plot, it can be seen that the characteristic "bump" of Figure 9.5 near the root section of the wing was removed which was a noticeable error in the Figure 9.7.

Another improvement from the platform iterating process was that the model simply iterated to be close to the elliptical distribution, with minimal consideration of the amount of lift the wing produces in reality (with 3D effects specific to the wing). To ensure the wing produced sufficient lift, a condition was set such that the program would avoid converging towards planforms which did not produce sufficient lift. Additionally, using the equation for 3D effect factor, the equation of Equation 9.5 was adjusted to ensure the lift produced by the twist rate ensures vertical equilibrium. This means to include the polynomial shown in Equation 9.9 within the integral, the results are shown in Equation 9.11.

$$\phi = \frac{\frac{L-L_{plasma}}{\rho V^2 c_{L\alpha}} b_w + (\alpha_{L=0} - \alpha_t)\left[c_r b_w P^{n+1}(b_w) + (c_t - c_r)\left[P^{n+2}(b_w) - P^{n+2}(b_s)\right]\right]}{c_r b_w^2 P^{n+1}(b_w) - c_r b_w P^{n+2}(b_w) + b_w(c_t - c_r)\left[P^{n+2}(b_w) - P^{n+2}(b_s)\right] - (c_t - c_r)\left[P^{n+3}(b_w) - P^{n+3}(b_s)\right]} \tag{9.11}$$

Comparing Equation 9.5 to the newer Equation 9.11, it can be seen that the latter considers the tip angle of attack as an input rather than the former which considered the root angle as an input. This was done to minimise the geometrical change between the different sections of the wing, such that the effect of **AER-TDE-02** is minimised. The equation can be verified by relating it to Equation 9.5 setting $P^n(y)$ equal to 1, and the resultant equation matches Equation 9.5 which was previously verified.

The resultant lift distribution is shown in Figure 9.12. It is plotted alongside the preliminary and conceptual design lift distributions.

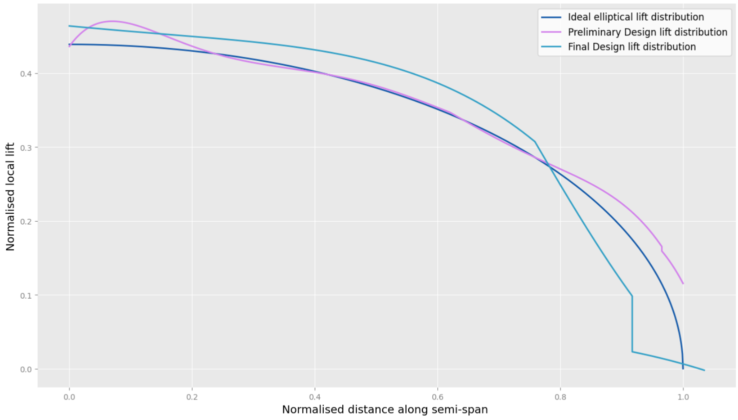

Figure 9.12: Lift distribution of platform for detailed design wing

When comparing the lift distributions, it can be seen that the updated correctional factor removes the "bump" from the root section of the wing. However, it seems to be a worse overall match. This is attributed to the requirement of the angles of attack of the lifting wing and controlling wing. Additionally, the confidence in the final design result is significantly higher due to the significant improvements to the model made in this section. The resultant parameters are summarised in table Table 9.9.

Table 9.9: iterated planform sizing

Parameter	Old value	New value	Unit
S	0.578	0.760	$[m^2]$
AR	15.6	11.8	$[-]$
b_s	0.9	1.1	$[m]$
b_w	1.41	1.33	$[m]$
c_r	0.2	0.275	$[m]$
α_0	6.0	4.0	$[°]$
α_s	3.23	2.7	$[°]$
α_w	1.68	2.4	$[°]$
twist rate	3.08	2.7	$[°/m]$
c_t (repeated)	0.169	0.169	$[m]$
b_p (repeated)	0.089	0.17	$[m]$
α_t (repeated)	8	2.4	$[°]$

Despite the improvements of the models made in this iteration, there are certain shortcomings which can further be improved. Aside from improving the accuracy of the models by removing assumptions **AER-TDE-02**, **AER-TDE-03**, and **AER-TDE-04**, two concrete suggestions are made below which are believed to have a larger impact on the design.

Firstly, an improvement in approach could be to ensure that the lifting and control section match lift coefficients at their connection side. This would minimise the aerodynamic interaction between the surfaces due to having similar downwash according to lifting line theory[86]. This is believed to have a larger importance on the design than the structural/geometric interaction of the components which the final design currently optimises for.[10].

Another point of improvement would be to include the effect of 3D effects on the aileron design, particularly the efficiency of the ailerons. Two methods were thought of to consider this, one which aims to mitigate the effects and one which attempts to quantify the effects.

Reflecting on the former solution of the two, although it is stipulated that a match in lift coefficient would reduce the cross-flow effects, one even more efficient method would be to gradually change the geometry of the wing from the MH115 section to the rounded trailing edge NACA641015 section. This approach was suggested also by Dr Leo Veldhuis and a suitable approach is to designate a small portion of the wing span for the lofting geometry.

Mitigating 3D effects could be done using a design with winglets. Traditionally used to reduce induced drag when operating below the crossover velocity, winglets could both improve the lift distribution of the main wing by essentially increasing its aspect ratio and mitigate the same effects that alter the efficiency of the ailerons. A design approach suggested by M.D. Maughmer of Pennsylvania State University can be used to design winglets[87]. Secondly, applying the correctional factor to the aileron δc_l would be a straightforward solution, albeit potentially inaccurate since there is limited literature on the effects of 3D flow over plasma actuators. To solve this, experiments could take place such that a design can be optimised based on a static correctional factor similar to the approach for the planform design for the conceptual design.

Before concluding the aerodynamic design of the wing, two matters must be addressed. Firstly, it can be noted that compared to the preliminary design, the final design wing has a larger surface area for the same span. This is an effect of the increased mass of the system, as the wing needs to produce larger amounts of lift compared to the preliminary wing. The side effect of this increase in surface area is a decrease in aspect ratio from 15.6 to 11.8, which would suggest a reduction in the aerodynamic performance of the wing. In reality, the aerodynamic performance of the wing is quantified through aspect ratio and twist, thus their cumulative effect is a measure of the aerodynamic performance. With regard to the differences between the preliminary and final design, a final reference is made to Figure 9.12, which accentuates the big discrepancy between the two designs close to the root and the large lift gradient from 0.75 to 0.9 of the final design. Thus, it must be noted that both designs have specific advantages and disadvantages and that both represent an intermediary step in the design process. Concluding on the discrepancies between the two designs, one recommendation is made to improve aspects of the second iteration. As the wing tip twist angle is constrained in the final design by the twist angle of the aileron, but it does not produce the desired effect, as can be observed by the steep deviation from the elliptical lift distribution, it is recommended that other boundary conditions for the wing twist distribution are explored. One example would entail trading off the efficiency of the Kutta condition control method by increasing the twist angle slightly such that close to the tip, the lift distribution matched the elliptical one closer.

9.6.4. Structural Iteration

There were three reasons the first design needed to be iterated. First off, errors were identified in the code during verification that underestimated the internal torque of the wing. Secondly, When modelling the wing box and the ribs in CATIA it was found that the horizontal webs of the wing box did not physically fit inside the airfoil. Lastly, the new planform discussed in Table 9.6.3 has a new load distribution which the wing needs to be able to withstand. Due to the physical constraint, the skin of the horizontal web of the wing box needs to be thinner. The current material, balsa, cannot take the new shear loads at its current size let alone when the skin is made thinner. Therefore the material will need to be changed to the same aluminium alloy used for the vertical spars. Adjusting the code for this new layout resulted in a trapezoidal wing box with the parameters shown in Table 9.10. This design change led to a decrease in wing group weight.

The structure of the wing complies with all the requirements that have been set during the conceptual phase of the design and the final weight is also in line with the predictions made using the Raymer method [40]. It was assumed that the wing box will not fail under buckling due to the low loads and stresses in the system and therefore this was not analysed. Further design iterations will need to look into these more complex loading cases. The wing box can be further optimised after this analysis is performed such that the weight can be decreased.

---

[10] Dr Leo Veldhuis also suggested that the change in geometry can occur gradually. To design conservatively for this case, a marginal portion of the wing span can be dedicated for lofting the MH115 section to the NACA642015 rounded trailing edge section.

Table 9.10: Iterated wing structure parameters

Parameter	Value	Unit
Front spar height	0.085c	$[-]$
Aft Spar web height	0.045c	$[-]$
skin thickness	0.5	$[mm]$
	1400	$[mm]$
Aerofoil skin thickness	1	$[mm]$
Maximum internal bending moment	26903	$[Nmm]$
Maximum internal shear force	123	$[N]$
Maximum internal torsional moment	58380	$[Nmm]$
σ_{max}	67.99	$[MPa]$
τ_{max}	123	$[MPa]$
σ_{y-Al}	324	$[MPa]$
τ_{Al}	283	$[MPa]$
Wing weight	1.03	kg

10 Fuselage Design

The fuselage of the aircraft requires detailed attention during this design phase, as it is the component that houses the majority of the subsystems. The chapter starts by stating the requirements that affect the specific design. Then the assumptions used during the design process are listed and explained. The preliminary, as well as final design iterations, are analysed in the respective sections, while recommendations for the continuation of the design are provided in the last section.

10.1. Requirements

The design of every subsystem is guided and restricted with requirements. The requirments that affect the fuselage structure are illustrated in Table 10.1.

Table 10.1: Fuselage structure requirements

Requirement ID	Requirement	Verification	Compliance
SUB-STR-02	The structure shall provide simple access to all subsystems and parts.	Inspect	PASS
SUB-STR-03	The structure shall be at least 80 percent recyclable by mass.	Analysis/Test	PASS
SUB-STR-04	The wing shall be detachable.	Analysis/Inspect	PASS
SUB-STR-06	The structure shall provide room such that all subsystems can be housed	Inspect	PASS
SUB-STR-07	The structure shall provide a mechanism to mount the payload subsystem.	Inspect	PASS
SUB-STR-10	The structure shall not interfere electromagnetically with the communication signals	Test	PENDING
SUB-STR-12	The structure shall not deform plastically during landing	Analysis/Test	PASS
SUB-STR-13	The structure shall not deform plastically during take-off.	Analysis/Test	PASS
SUB-STR-14	The structure shall prevent the system's components from failing structurally.	Analysis/Test	PENDING
SUB-STR-15	The structure shall not fail at an ambient temperature between 2.5 and 23 Celsius.	Analysis/Demonstration	PENDING
SUB-STR-16	The structure shall not fail at an internal temperature between 0 and 35 Celsius.	Analysis/Demonstration	PENDING
SUB-STR-17	The structure shall operate at an ambient humidity range between 70 and 86 percent.	Demonstration	PENDING

SUB-STR-19	The structure shall not fail under maximum loads of 3.75 and -1.5	Demonstration	PASS
SUB-STR-20	The structure shall not fail under ultimate load factors.	Demonstration	PENDING

10.2. Assumptions

For an approach of progressive detail, multiple assumptions need to be initially made. This can help with simplifying calculations, providing values that can be used for further iterations. In this section, the assumptions are listed and discussed. Their verification is further explained in chapter 21.

- **STR-FD-01:** The shape of the fuselage is rectangular cuboid, with the smallest surface facing the flow. This is a conservative assumption used to simplify external load calculations.
- **STR-FD-02:** The fuselage generates no lift. Particularly, the wing is assumed to make all of the required lift.
- **STR-FD-03:** The drag of the fuselage acts as a force uniformly distributed on its front surface, pointing in the axial direction.
- **STR-FD-04:** The aerodynamic effect of the front surface of the fuselage resembles that of a cube. In this way, its drag coefficient can be estimated.
- **STR-FD-05:** The launch and parachute deployment loads act as point forces on the half-span of the fuselage, in the axial direction. As the calculation of the actual loads requires simulation, such an assumption is made for the first design stages.
- **STR-FD-06:** The thrust of the aircraft acts in the axial direction, on the centerline of the fuselage. In later design stages, the moment introduced from the moment arm that the thrust actually has must be considered.
- **STR-FD-07:** The drag of the wing acts on the fuselage as a point force in the axial direction.
- **STR-FD-08:** The lift of the wing acts on the fuselage as a force, distributed in a span equal to the root chord of the main wing, pointing vertically to the fuselage. Such an estimation resembles a wingbox-like structure.
- **STR-FD-09:** The cushion force during landing is uniformly distributed along the length of the fuselage and points in the direction normal to it.
- **STR-FD-10:** The booms/stiffeners of the fuselage take all normal loads. Such an approximation opts to simplify internal loading calculations.
- **STR-FD-11:** The skin of the fuselage takes all shear loads. Such an approximation opts to simplify internal loading calculations.
- **STR-FD-12:** Shear flow is generated only on the components parallel to the shear force direction.
- **STR-FD-12:** The loading condition of the holes resembles that of an infinite panel. This assumption is used in the stress concentration analysis of the holes of subsection 10.4.1.

The shape assumptions, STR-FD-01 and STR-FD-04, were made to simplify the geometrical analysis of the structure, making the internal load analysis easier. The inaccuracies introduced are mainly related to the performance in bending and the drag calculation. A more detailed analytical or numerical analysis could reduce possible errors. However, only actual testing will show if the design actually holds.

The majority of the external load assumptions lead to results that are non-conservative, as the force distributions are not uniform but concentrated. Thus, margins must be imposed on the distributions to take these effects into account. Regarding point load assumptions, conservative results are provided as stress is lower in real loading scenarios.

Assumptions STR-FD-10 and STR-FD-11 give conservative results since normally the stiffeners and the skin share the loads together. In a later design stage, the performance of both structural components in shear and normal loading should be investigated. Such an evaluation of components under combined loads can be done using analytical tools like Mohr's circle.

10.3. Preliminary Design

The preliminary design of the fuselage determines the overall layout of its structure. It contains the load distribution, configuration selection, the design iteration loop and the discussion of the results.

10.3.1. Load distribution

In order to investigate how the fuselage structure performs under stress, the external loading applied to it needs to be analysed first. In particular, normal, shear and bending load distributions are generated for four loading cases. These are launch, cruise under the maximum load factors, parachute deployment and landing. For each case, different forces and force distributions are estimated using equations related to assumptions STR-FD-01 to STR-FD-09. The loads considered are shown in Table 10.2, whereas the corresponding loading cases and related assumptions are given in Equation 11.7.

Table 10.2: Fuselage external loads list and corresponding loading type

ID	Loading	Type
LD-01	Fuselage weight	Distribution
LD-02	Wing lift	Distribution
LD-03	Wing-tail weight	Distribution
LD-04	Fuselage drag	Point force
LD-05	Wing drag	Point force
LD-06	Launch load	Point force
LD-07	Parachute deployment	Point force
LD-08	Landing cushion	Distribution

Table 10.3: Fuselage loading cases, loads applied and related assumptions

Case	Loading	Assumptions
Cruise	LD-01, LD-02, LD-03, LD-04, LD-05	STR-FD-01, STR-FD-02, STR-FD-03, STR-FD-04, STR-FD-06, STR-FD-07, STR-FD-08
Launch	Cruise loads, LD-06	Cruise assumptions, STR-FD-05
Deployment	Cruise loads, LD-07	Cruise assumptions, STR-FD-05
Landing	Cruise loads, LD-08	Cruise assumptions, STR-FD-09

Based on the loading information in Table 10.2 and Table 10.3, equations can be set up to quantify the loads. The last important step for the determination of the internal loads is the way the loads are applied. For the clarification of this process, diagrams can be made, such as the one shown in Figure 10.1.

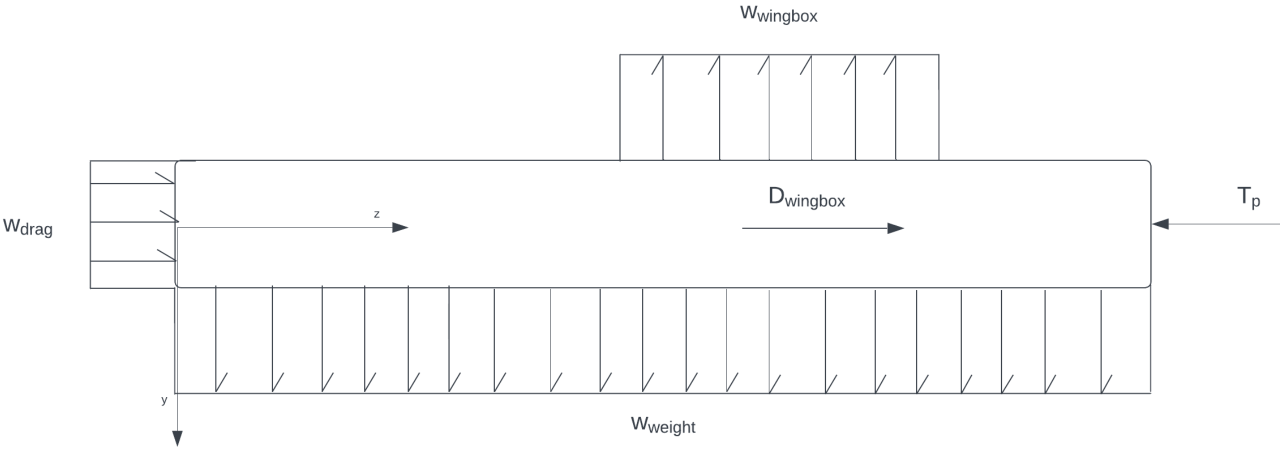

Figure 10.1: Fuselage loading case during cruise

$w_{wingbox}$ stands for the load of lift and weight of the wing and tail, distributed over the wingbox of the structure. w_{Weight} represents the weight distribution of the fuselage, $D_{wingbox}$ is the drag of the main wing, w_{drag} is the drag distribution of the fuselage and T_p is the thrust, The illustrated example corresponds to the cruise loading case. The shape and distributions follow the assumptions shown in Table 10.3. Using this model and the equations characterising the forces, the internal loading diagrams can be generated, which are used as inputs in subsection 10.3.3.

10.3.2. Configuration Selection

The guiding factor to determine the structural configuration is the arrangement of the aircraft's subsystems in their housing space. Their placement is done taking into account drag minimisation and payload functionality. To minimise drag, they were placed in a manner so that the cross-section is minimized. The payload is placed in the bottom surface of the fuselage, in order to point to the ground and make efficient measurements during nominal operations. The layout of this internal configuration is shown in Figure 17.3.

The main subsystem components are directly labelled for reference. As shown, the most suitable cross-sectional shape is rectangular. Such a shape is definitely suboptimal regarding the aerodynamic performance of the fuselage, but the preliminary structural analysis is fully based on it. The current dimensions of the internal configuration are shown in Table 10.4.

Table 10.4: Initial fuselage internal layout dimensions

Parameter	Value	Unit
Length	0.7	m
Height	0.15	m
Width	0.15	m

Having obtained a fuselage shape, the structural components can be determined. In order to save mass, the aerodynamic skin is designed to contribute to the aircraft's structural integrity, apart from reducing drag. However, the usage of structural skin only is risky since it is prone to buckling and impacts, events which undermine its structural integrity. Thus, the critical structural component must be some kind of stiffener. In order to maximise useful housing space, 4 L stringers are chosen, which are placed on the corners of the fuselage.

10.3.3. Design Iteration Loop

An iteration loop has been designed for the sizing of the skin and the stringers. For the analysis of this method, a discussion of the models used is needed. Specifically, structural idealisations with progressive detail are performed.

Structural approximation models are taught in Structural Analysis courses and are used to simplify early design phases. The first one used is called the basic boom structural idealisation and assumes that the structure is comprised only of circular booms. In this case, the booms are placed in points that resemble the corners of the fuselage cross-section, as illustrated in Figure 10.2.

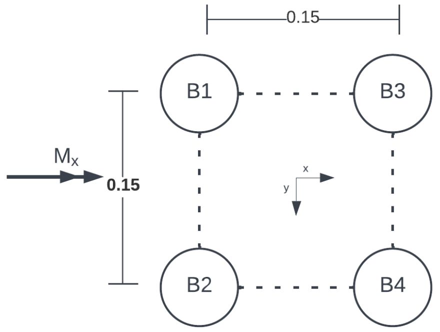

Figure 10.2: Basic boom structural idealisation model. In this case, the only components that contribute structurally are the indicated circular booms, B1, B2, B3 and B4. Only bending M_x and normal loads are considered.

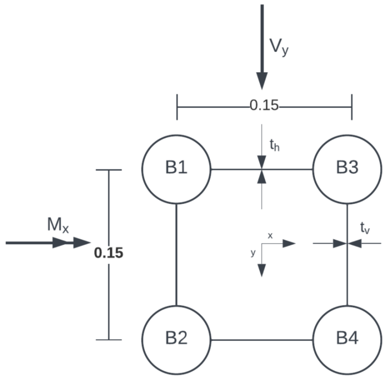

Figure 10.3: Refined boom structural idealisation model. Apart from the indicated circular booms, B1, B2, B3 and B4, the skin with thicknesses t_h and t_v is considered. Bending M_x, shear V_y and normal loads are taken into account.

In such a case, the booms are assumed to be all equal in cross-sectional area, as the shape is symmetric with respect to the x and y axes. Since there is no skin to carry shear loads, only bending and normal loads are considered.

The second, and more detailed, model is the refined boom structural idealisation. Skin is now introduced, with different thicknesses for the horizontal (t_h) and vertical (t_v) components. The complete set of loads is taken into account, as shown in Figure 10.3.

Based on these two approximations, the fuselage's main structural components can be sized. In particular, boom areas $B1$, $B2$, $B3$, $B4$, as well as, horizontal and vertical skin thicknesses t_h and t_v are estimated. An overview of this algorithm is shown in Figure 10.4.

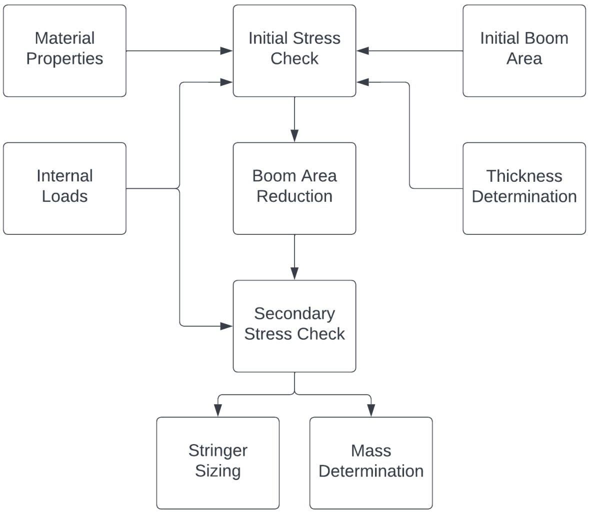

Figure 10.4: Fuselage iteration loop

The loop uses material properties, the internal loading, discussed in subsection 10.3.1, an initial boom area estimation and a skin thickness estimation as inputs. Using the basic boom idealisation model, stress checks are executed for the selected material and in case it passes successfully, the boom area is recalculated based on Equation 10.1.

$$B_{new} = B_{old} - B_v - B_h \tag{10.1}$$

Where B_{new} is the new boom area, representing the stringers' structural contribution, and B_{old} is the old one. B_v and B_h are the skin contributions to B_{old}, that are now subtracted from it, as the skin is taken into account in the next iteration step. The skin contribution is calculated using Equation 10.2.

$$B = \frac{t_{skin} b}{6}\left(2 + \frac{\sigma_2}{\sigma_1}\right) \tag{10.2}$$

In Equation 10.2, t_skin stands for the skin thickness, b for the skin width, σ_1 and σ_2 for the stresses on the two booms attached to the skin. For the fuselage's loading case, the normal stress due to bending is equal for the booms attached to each other horizontally and opposite for the booms attached vertically. Thus, the contribution can be specified in Equation 10.3 and Equation 10.4.

$$B_v = \frac{t_v b}{6} \tag{10.3}$$

$$B_h = \frac{t_h b}{2} \tag{10.4}$$

Having obtained reduced boom areas, a secondary stress check is executed using the refined boom structural idealization this time. This is done considering shear using assumptions STR-FD-10, STR-FD-11 and STR-FD-12. If the test passes, the stringers that the booms represent are sized and the structure's total mass is determined.

To size the stringers' shape, their design needs to be constrained. This is done by considering the validity of the idealized boom approximation. Specifically, the cross-sectional area needs to be concentrated close to that one of the circular booms, in order to not alter the inertial properties of the structure. Therefore, it is stated that the stringer's height and width are equal to 4 times the radius of the boom, calculated using Equation 10.5 and Equation 10.6.

$$r = \sqrt{B/\pi} \tag{10.5}$$

$$h_{str} = w_{str} = 4 \cdot r \tag{10.6}$$

Where r stands for the boom radius, while h_{str} and w_{str} stand for the stringer's height and width. Having obtained these values, stringer thickness t_{str} can be determined, using Equation 10.7, which is derived from equating the boom and stringer cross-sectional areas. It should be noted that the stringer is assumed to be thin, thus the thickness variable is negligible when raised to a power.

$$t_{str} = \frac{B}{h_{str} + w_{str}} \tag{10.7}$$

Finally, the mass of the skin and stringers are calculated using the material density and the volume of the component. These relations are shown in Equation 10.8 and Equation 10.9 for the skin and the stringers respectively.

$$m_{skin} = 2 \cdot \rho_{skin} \cdot l \cdot (t_v \cdot h + t_h \cdot w) \tag{10.8}$$

$$m_{stringers} = 4 \cdot \rho_{stringer} \cdot l \cdot (h_{str} \cdot t_{str} + w_{str} \cdot t_{str}) \tag{10.9}$$

The density of the component is indicated with ρ, whereas l, h and w represent the fuselage's length, height and width, specified in Table 10.4.

To actually obtain a design that approaches an optimal solution, the loop must be executed multiple times. This needs to be done for different combinations of the material and dimensions (boom area and skin thicknesses) inputs. After evaluating the results, a preliminary design is selected.

10.3.4. Preliminary Results

Before introducing more structural aspects to the analysis, a series of calculations based on subsection 10.3.3 give unexpected results. Using typical aerospace aluminium alloys as a stringer material input and typical wood products, the iteration loop calculates that the required structure shall have minimum thicknesses that cannot be produced (close to 0.04 mm).

10.4. Final Design

After the first iteration of the fuselage structural design, its structural components and their corresponding effects can be investigated more in detail. The section starts with a discussion of access holes in subsection 10.4.1 and their effect on the fuselage structure. Buckling effects are analysed in subsection 10.4.2. The design of formers is discussed in subsection 10.4.3. Finally, the mass of the fuselage structure is calculated in subsection 10.4.4. The iterated fuselage dimension values that are considered in this section are shown in Table 10.5.

Table 10.5: Iterated fuselage internal layout dimensions

Parameter	Value	Unit
Length	0.95	m
Height	0.12	m
Width	0.12	m

10.4.1. Access Holes

In order to allow for easy maintenance and operations, holes must be placed on specific locations of the fuselage skin. The layout of these holes is shown in Figure 10.5.

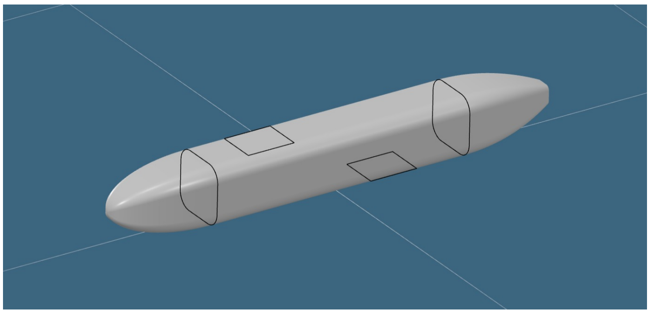

Figure 10.5: Outline of hole placement on the fuselage

In total, 4 holes are created. One is in front of the fuselage, which allows for access to the payload and the battery. It has the shape of the cross-section of the fuselage. On it, the nose cone is bolted. On the other end of the fuselage, there is another hole to enable access to the engine. On it, the tail cone is bolted. Lastly, there are two rectangular holes of 80 mm x 80 mm, one on the upper surface of the fuselage for parachute deployment and one on the bottom, for the landing cushion deployment. These holes are attached to hatches using a joint and are controlled using a servo motor. The nose and tail holes are not in priority, as they are loaded in the transverse direction. The surface holes, on the other hand, are loaded primarily in a uniaxial direction, along the fuselage. Thus, they are the ones investigated. The effect these holes undergo is stress concentration under uniaxial loading. For such a case the parameter of importance is the stress concentration factor, given in Equation 10.10.

$$K_t = \frac{\sigma_{max}}{\sigma} \tag{10.10}$$

σ_{max} stands for the maximum stress found around the hole and σ is the applied overall stress. The stress concentration factor depends on multiple geometrical parameters of the hole and the surrounding structure. For the specific scenario, K_t can be determined using Figure 10.6.

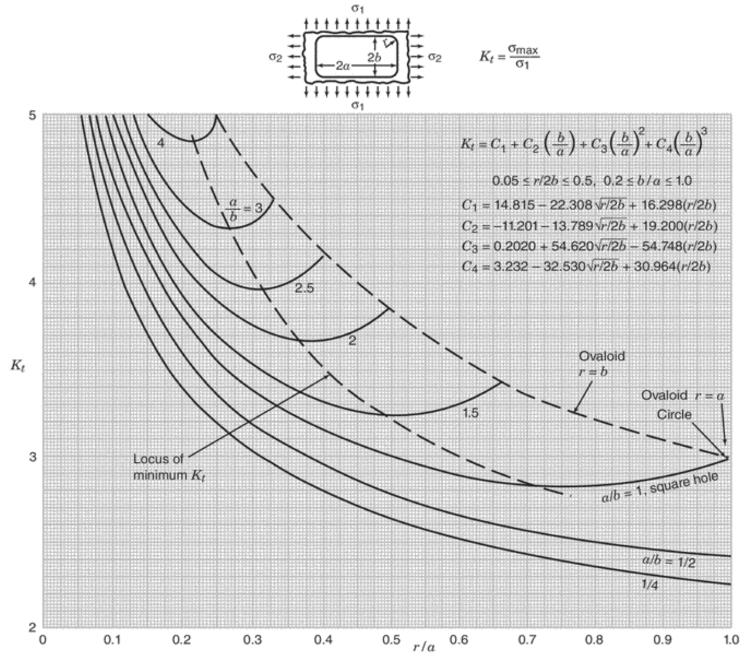

Figure 10.6: Stress concentration factors K_t for a rectangular hole with rounded corners in an infinitely wide thin element: uniaxial tension, σ_2 = 0 [88]

Since rectangular holes by themselves achieve relatively high stress concentration values, a mitigation method must be implemented to reduce structural weight. A common method is the use of bead reinforcement around the hole. Such a feature acts also as an attachment point for the hatch servos and the corresponding hinges. The stress concentration factor for such a case is illustrated in Figure 10.7. It should also be mentioned that such a design is conservative because the attached hatch naturally reduces stress concentration.

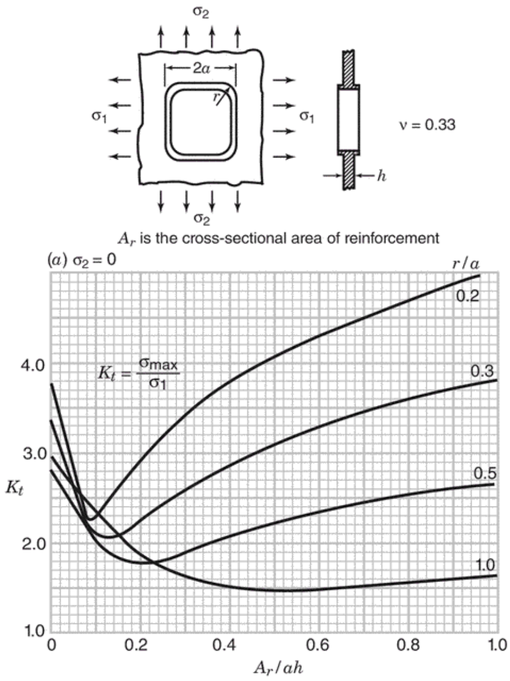

Figure 10.7: Stress concentration factors of round-cornered square holes with bead reinforcement in an infinite panel under uniaxial stress: σ_2 = 0 [88]

For a given configuration, K_t and then σ_{max} are calculated. According to that, the design is sized. Thus, this step must be incorporated in the iteration loop, as shown in Figure 10.8. For the range of dimensions that can be achieved in the current fuselage layout, the K_t is around 2.0.

10.4.2. Buckling

Since the normal load is mainly taken by the stringers, their buckling performance is investigated initially. The buckling mode of stiffeners particularly is called crippling. It describes the event of the stiffener edges buckling, leaving the corners to support the load. To investigate if crippling (its strength indicated as σ_{cc} occurs before the material yields (σ_y), Equation 10.11 is used.

$$\frac{\sigma_{cc}}{\sigma_y} = a \left| \frac{C}{\sigma_y} \frac{\pi^2 E}{12(1-\nu^2)} \left(\frac{t}{b}\right)^2 \right|^{1-n} \tag{10.11}$$

Where a and n are constants equal to 0.8 and 0.6 respectively for aluminium alloys. C is the buckling stress coefficient, equal to 0.425 for this case [89]. E is the material's Young's modulus, ν stands for the Poisson ratio and t for the sheet thickness. Finally, b is the sheet width. Depending on the result of the fraction of Equation 10.11, the failure mode of the stringers changes. This is determined from Equation 10.12.

$$\sigma_{failure} = \begin{cases} \sigma_{cc}, & \text{if } \frac{\sigma_{cc}}{\sigma_y} \leq 1 \\ \frac{\sigma_{cc}}{\sigma_y} \cdot \sigma_y, & \text{if } \frac{\sigma_{cc}}{\sigma_y} > 1 \end{cases} \tag{10.12}$$

Based on these considerations, the design iteration loop can be improved. Its updated flowchart is shown in Figure 10.8.

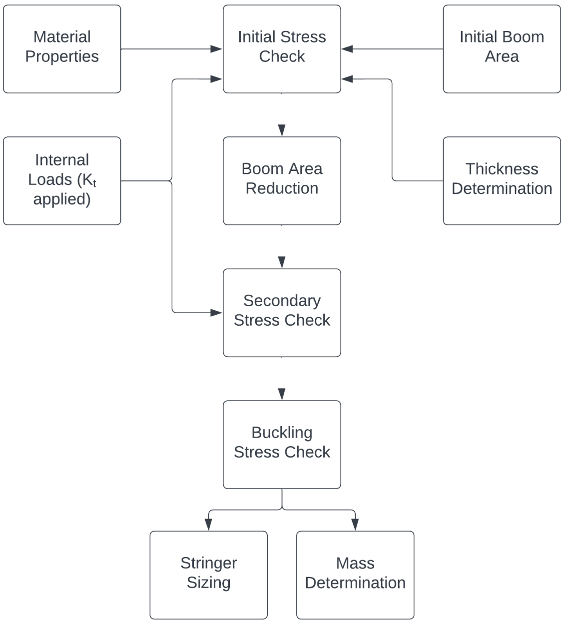

Figure 10.8: Updated fuselage iteration loop

As can be seen, the design consideration have increased. The stress concentration factor K_t due to the holes discussed in subsection 10.4.1 is added. The buckling considerations are implemented in the form of a failure check, after the secondary stress check.

10.4.3. Formers

To retain the shape of the fuselage and prevent certain buckling modes, a dedicated structural component must be added. For the subsystem configuration shown in Figure 17.3, the most suitable element is a hollow rib, also called a former, to allow for the subsystems to pass through. For the given hole configuration, it is decided that 6 formers are used. The layout of the configuration is shown in detail in Figure 10.9.

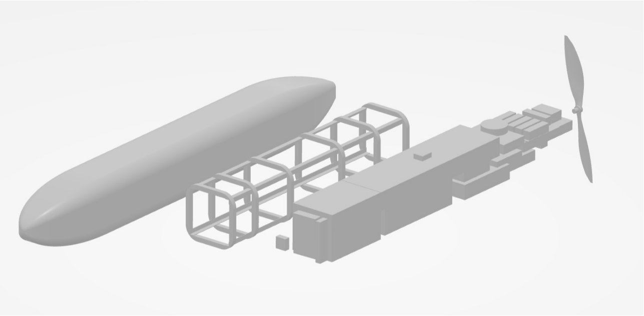

Figure 10.9: The structural components of former design. From left to right: Fuselage skin, formers with stringers and internal components layout.

The dimensions of these components are roughly estimated, as more advanced analytical and numerical tools must be used for their analysis, as discussed in section 10.5. The values are shown in Table 10.6.

Table 10.6: Former design parameters

Parameter	Value	Unit
Width	0.01	m
Thickness	0.01	m

10.4.4. Material Selection & Final Considerations

For the determination of the fuselage structure mass, specific materials must be considered. Two categories are taken into account, wood and aluminum alloys. Wooden materials are used for the skin, as it does not take major loads and mainly provides an aerodynamic shape. American Yellow Poplar Wood [1] is relatively low-weight and recyclable [90]. It has also high shear performance compared to other woods. Aluminium alloy AA2024 [2] is a common fuselage structure material and thus is considered for the stringers and formers [3]. The reference properties derived from the materials are shown in Table 10.7.

Table 10.7: Fuselage material properties

Material	**Density [kg/m3]**	**Tensile strength [MPa]**	**Compressive strength [MPa]**	**Shear strength [MPa]**
Poplar	380	155	38	8.2
AA2024	2780	270	310	276

For the poplar, the tensile and compressive strength values refer to loading that is parallel to its grain, whereas shear refers to an unknown direction. Furthermore, the aluminium alloy is considered to undergo T3 heat treatment, thus making its full material code AA2024-T3. Lastly, it should be mentioned that yielding strength is only considered. For the iterated design discussed, the mass composition is given in Table 10.8.

Table 10.8: Fuselage mass budget

Component	**Volume [cc]**	**Material**	**Density [kg/m3]**	**Mass [kg]**
Skin	456	Poplar	380	0.17
Stringers	76	AA2024	2780	0.21
Formers	288	AA2024	2780	0.80
Total				1.19

Having determined the fuselage design of this stage, the interface between its components must be considered. A first check is conducted by assembling all the components together, as shown in Figure 10.10. A thorough discussion of the interaction between the aircraft subsystems can be found in chapter 17.

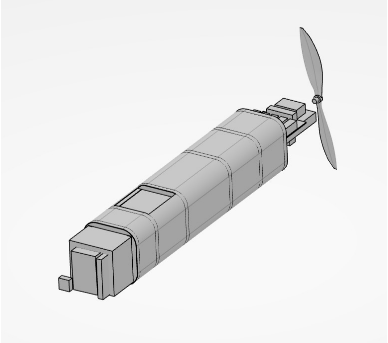

Figure 10.10: Integrated fuselage components

10.5. Further Recommendations

As the structure is a subsystem, the design of which can go very deep, it is expected to go into more detail in future design iterations. The three main categories to which the design can expand are the detail of the analysis, the effects investigated and testing.

As far as analysis depth is concerned, analytical and numerical methods are recommended. Firstly, the former design should be looked upon more in detail, as well as the landing loading case. According to section 16.1, the cushion decelerates the aircraft down to a velocity of $1.3\,\mathrm{m/s}$. The loads introduced by this final impact are not yet considered and most probably require the use of numerical software. A numerical analysis would be useful to the rest of the structural components, as it would increase the level of detail of the investigation and would act as a verification method as well.

Regarding effects that have not been investigated yet, but could affect the design, there are multiple that can be analysed. Examples of major importance would be the analysis of thermal stresses, the wingbox integration, vent holes for cooling, delfection calculations, Electro-magnetic interference (EMI) and other buckling modes (inter-rivet, column, shear buckling etc.).

---

[1] https://www.matweb.com/search/DataSheet.aspx?MatGUID=103514e0d4cb4373925dc4c2cf5d645bckck=1

[2] https://www.matweb.com/search/DataSheet.aspx?MatGUID=781ce4adb30c4d548320b0ab262a5d28

[3] https://www.dierk-raabe.com/aluminium-alloys-for-aerospace-applications/

Lastly, tests can be performed to verify and validate the performance of the subsystem, as well as to quantify the accuracy of the assumptions used. Such activities include destructive tests of specific components and non-destructive tests of the whole integrated structure. The latter is non-destructive as it would cost too much for the information that would be obtained.

11 Empennage Design

An element present in most aircraft configurations, the horizontal and vertical stabilisers, or collectively known as 'the empennage', are required to ensure static stability during cruise flight and, depending on the case enough control authority or damping of eigenmotions. In the scope of the author's work, an empennage was considered for satisfying stability and control requirements starting in Phase B of the project, and the choice of using it was traded-off in Phase C. The current chapter presents the requirements for the empennage design, followed by a discussion on the possible configurations of the horizontal-vertical stabilisers layout, the corresponding steps and assumptions made to design them preliminarily and finally the optimisation was performed on the preliminary design which led to the final design of this subsystem. The reasons for using an empennage will not be addressed in the current report.

11.1. Empennage Requirements

In order to constrain the design of the empennage, the subsystem requirements pertaining to the horizontal and vertical stabilisers are listed in Table 11.1. These requirements have been derived as a further discussion on some of the system requirements. Note that the compliance of these subsystem requirements at the end of the final design are stated in the fourth column.

[H]

Table 11.1: Empennage Requirements

Requirement ID	Requirement	Verification	Compliance
SUB-STB-01	The system shall be statically stable in all flight phases.	Analysis	**PASS**
SUB-PCS-09	The system shall have no moving control surfaces	Inspection	**PASS**
SUB-PCS-10	The system shall provide pitch control authority	Analysis	**PASS**
SUB-PCS-12	The system shall provide yaw control authority	Analysis	**PASS**

The requirements in Table 11.1 relating to control authority are quantified in Table 7.3 in chapter 7, where the required pitch acceleration is determined. The requirements of Table 11.1 are not quantified in the form of performance requirements as performance requirements are not solely achieved by the empennage, but rather relate to the whole system. The two requirements in Table 8.1 relate to the performance of the system during manoeuvres and have been used to constrain and size the empennage. These matters will become evident in section 11.2, section 11.5 and section 11.6.

Due to the novelty of the entire control system, sizing the horizontal problem must be split between sizing for stability or sizing for control. The limiting case will be imposed by the larger needed surface area.

11.2. Tail Configuration and Aerofoil Selection

From the aerodynamicist's point of view, narrowing down the vast design space of possible tail configurations is a task which requires an ample view of the integration of all exterior subsystems of the aircraft. Thus, wake and structural interactions and technology readiness level affect the decision of choosing an appropriate empennage design. As the name suggests, the current design does not consider canard configurations, but only an aft-mounted tail. In Phase C, it was concluded that the horizontal tail shall be boom mounted to the wing-fuselage group.

All tail configurations were considered for control purposes with plasma actuators mounted on the horizontal and vertical surfaces.

In order to limit the 'degrees of freedom' of the problem, a number of design choices were considered. These mostly pertain to the technology readiness level of the plasma actuated concept considered and to interactions with the wake of the main wing and propeller. The following were considered in the choice of a tail configuration:

1. For stability purposes, the horizontal stabiliser shall not sit directly in the wake of the propeller.
2. The ability of the plasma actuated technology to produce both positive and negative ΔC_l values.

Finally, note that the configuration choice has profound implications on sizing the empennage and its early design was heavily dictated by the prospective capabilities of plasma. This is illustrated in the following discussion, which treats the considered tail configurations chronologically, in parallel with the study and design of the plasma actuator models.

Box tail

Following a chronological path, the initial plasma actuator models which posed the most promise for the empennage fulfilling the requirements in Table 11.1 were the 'Plasma Separation Control', 'Plasma Separation Control + Flap' and the 'Slotted Airfoil' concepts. A discussion on their characteristics and their trade-off is present in section 8.3. Following the considerations listed above, the design of a box tail was considered due to two reasons:

1. Two horizontal tail surfaces would allow placement outside of the wake of the propeller.
2. Due to limitations of the plasma actuation methods, a lift gradient could be obtained only in the positive direction, essentially allowing only pitch-up control. This entailed two opposing horizontal surfaces needed for control.
3. Two vertical surfaces are considered for stability purposes due to propeller wake interactions.

The box tail empennage is illustrated in Figure 11.1a.

(a) Artistic representation of the box tail configuration **(b)** Artistic representation of the H-tail

Figure 11.1: Empennage configurations

This configuration posed a number of limitations and an increased level of design complexity. First of all, locally, the four surfaces would act as 'double wings' inducing a high level of interaction between them. Essentially, a reduced lift performance for all four surfaces would occur due to interactions between the parallel ones. These effects were studied and the design of the box tail could be achieved by employing the analysis done by R. Jones et al on biplane wings operating at low Reynolds numbers[91]. Added complexity and higher structural mass than a similar performing conventional configuration rendered the box tail design unfeasible. The choice to discard the box tail design was also aided by proving other feasible plasma actuator solutions. Finally, as it was concluded in section 8.3, the Kutta condition control method would allow producing both positive and negative lift gradients which would, in turn, allow two plasma actuators to be mounted on a single surface, eliminating the need for two horizontal surfaces.

H-tail

Once the box-tail configuration was discarded, a simpler configuration could be explored. The option of an H-tail proved most feasible in terms of aerodynamic efficiency, as a single horizontal planform could be placed outside the wake of the propeller and main wing and at the same time, the vertical stabilisers could be placed as such to limit three-dimensional effects on the horizontal tail. This configuration also decreases the complexity of the empennage, reducing the number of contact points for the booms and failure points where the horizontal and vertical stabilisers join.

The H-tail is illustrated for reference in Figure 11.1b.
Compared to the box tail, the H-tail poses a number of advantages, while keeping the same beneficial effects as the box tail. These advantages pertain to the elimination of the double wing configuration for the horizontal

stabiliser, resulting in better aerodynamic performance. Moreover, the vertical stabilisers, being placed at the ends of the single horizontal stabiliser can act as winglets and reduce induced drag and separation at the tip of the horizontal tail.

11.3. Tail-boom Length Sizing

The required surface of the tail and the required distance from the aerodynamic centre of the main wing are two parameters which are interrelated. To make a justified decision on one of the parameters, two possible approaches were determined, namely optimising the design for mass or for simplification of the aerodynamic design. The latter was the chosen approach, where the length is dictated by the downwash of the main wing propagated onto the horizontal tail. The assumptions are listed below.

- **AER-TBL-01:** Limiting case of an induced angle of 0.5°. This assumption was made as a restricting case, similar to the constraint for the wing box design.
- **AER-TBL-02:** Lifting line theory circulation model. This model was chosen to calculate the induced velocity in the downwash of the main wing. This model was chosen instead of the horseshoe vortex method since it is assumed the size of the horizontal tail is sufficiently small such that the circulation around the main wing remains quasi-constant.
- **AER-TBL-03:** The relative airspeed at the tail is the same as the freestream airspeed. Due to the low induced velocity, the magnitude of the H-tail velocity is the same as the freestream velocity.

To calculate the induced angle at a reference point, the induced velocity at the reference point can be calculated using the Biot-Savart law, as stated in [86]. Then the induced angle can be calculated from the trigonometric from the aerodynamic centre of the induced velocity can be calculated using the Biot-Savart law, stated as Equation 11.1.

$$V_{induced} = \frac{\Gamma_0}{4\pi R} \tag{11.1}$$

The maximum circulation around the wing sections Γ_0 is assumed to have a constant value up to the span of the horizontal stabiliser. This entails that all span-wise locations on the horizontal stabiliser experience the same induced angle. Moreover, the calculation of Γ_0 assumes an elliptical lift distribution, which is estimated in section 9.4. Equation 11.2 is used to determine the value of Γ_0. The lift is considered to be the lift required during nominal operations.

$$\Gamma_0 = \frac{L}{\rho_\infty V_\infty \frac{b}{4}\pi} \tag{11.2}$$

$$\alpha_i \approx \frac{V_i}{V_\infty} \quad [rad] \tag{11.3}$$

The effects of the Biot-Savart law can be visualised in Figure 11.2. The induced angle α_i is set to be constrained at 0.5° for the current design. Using Equation 11.3 can be used to calculate the 'required' induced velocity for an induced angle of 0.5° and the resulting tail-boom length is 1.03m.

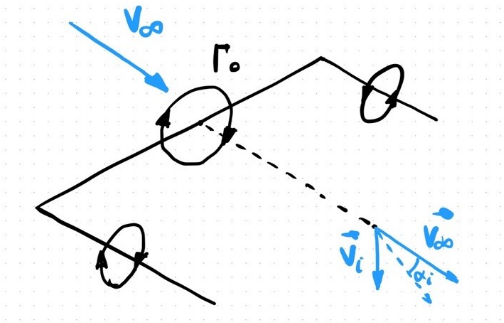

Figure 11.2: Biot-Savart law and tail-boom length sizing

On a final note, although referred to as 'tail-boom' length, l_h refers to a stability parameter and is the distance between the aerodynamic centres of the main wing and the horizontal stabiliser. In reality, the length of the tail boom will vary slightly, according to structural integration.

11.4. Scissor plot

To ensure the P.U.L.S.E. drone is both longitudinally stable and controllable a scissor plot tool was made to design the horizontal tail volume C_h. The formula used to construct the stability line is given in Equation 11.4.

$$C_{h_{stability}} = \frac{S_h l_h}{S\overline{c}} = \frac{\overline{x}_{cg_{range}} - \overline{x}_{ac} + S.M.}{\frac{C_{L_{\alpha_h}}}{C_{L_{\alpha_{A-h}}} \cdot \frac{d\varepsilon}{d\alpha} \cdot \left(\frac{V_h}{V}\right)^2}} \tag{11.4}$$

Besides this, also a control line was constructed using Equation 11.5.

$$C_{h control} = \frac{S_h l_h}{S\overline{c}} = \frac{\overline{x}_{cg_{range}}}{\frac{C_{L_h}}{C_{L_{A-h}}} \cdot \left(\frac{V_h}{V}\right)^2} + \frac{\frac{C_{m_{ac}}}{C_{L_{A-h}}} - \overline{x}_{ac}}{\frac{C_{L_h}}{C_{L_{A-h}}} \cdot \left(\frac{V_h}{V}\right)^2} \tag{11.5}$$

A stability margin of 10% was used to account for any errors that might occur during setting the $\bar{x}_{cg}$ location. This ensures that under small deviations of the centre of mass due to manufacturing or assembly errors the airframe is still stable and controllable. The remaining parameters were estimated based on the approach outlined by Torenbeek[92]. Using these estimations and the formulas a tool was created using Python. The scissor plot was plotted and the centre of gravity range was placed at a random location where the left side was attached to the control line. A slider could be used to move the centre of gravity range to fit perfectly in between the stability and control lines. Once the range is placed correctly the values for the tail volume could be saved with the save button for further use. This tool is visualised in Figure 11.3.

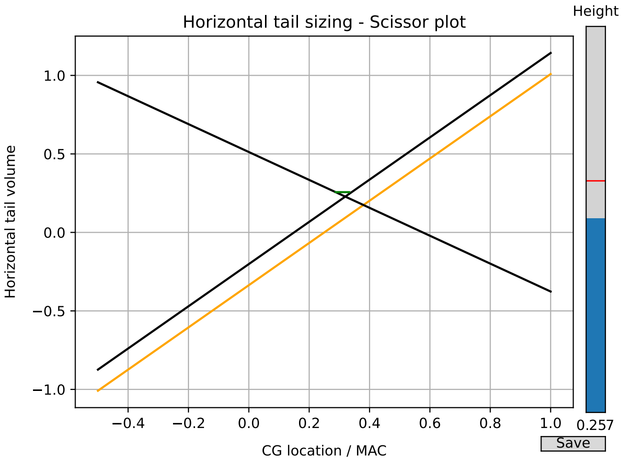

Figure 11.3: Scissor plot tool

As the drone is operated using electrical energy, the location of the centre of mass will not change, as the system does not lose mass. This entails that the $\bar{x}_{cg_{range}}$ is actually a fixed value which needs to satisfy controllability and stability purposes. Thus, the x_{cg} location was chosen to lie at the intersection of the stability and controllability curves defined by Equation 11.4 and Equation 11.5. This resulted in a centre of mass location of 0.31$\bar{c}$, which is used all throughout the preliminary design.

11.5. Horizontal tail sizing

Two approaches were considered to determine the size of the horizontal stabiliser. Firstly, the problem will be treated from a stability point of view, analysing the static stability of the system during 'cruise-like' conditions. Secondly, the horizontal stabiliser was sized from a control authority perspective, considering the Kutta condition control plasma actuation method. The NACA642015 aerofoil is considered for the horizontal stabiliser in both sizing cases.

Sizing for Longitudinal Static Stability

In cruise conditions, the main task of the horizontal stabiliser is to ensure pitch stability. This is considered important as the flight mission of the drone will consist in taking accurate sound measurements during glide.

The problem of longitudinal static stability can be analysed as a simplified case that considers only the lift and moments caused around the wing's aerodynamic centre and the horizontal stabiliser's aerodynamic centre. In order to simplify the design process, a number of assumptions have been made.

The extent of this section is to present the analytical steps taken to obtain the surface area of the horizontal stabiliser. Other dimensions of the horizontal stabiliser such as its span and chord are also addressed.

1. **STB/CTL-HTL-01:** The aerofoils employed for wing and empennage design are thin and are subjects of thin aerofoil theory. This assumption is a reformulation of the linearisation of small angles around 0 and pertains to the change in thickness along the chord. This assumption has been adapted from the works of John D. Anderson Jr.[86, pp. 340-341]. This assumption is mostly true for the MH115, which has a thickness of approximately 11%, while the NACA642015 has a thickness of 15% and thus the validity of this assumption is reduced. This assumption mostly pertains to STB-HTL-02.
2. **STB/CTL-HTL-02:** A consequence of STB/CTL-HTL-01, the location of the aerodynamic centres of the main wing and horizontal stabiliser are considered at 0.25 of their MAC. This is a safe assumption for the NACA642015 wing section, although, for the MH115, the location will be slightly upstream of 0.25 MAC. This assumption has a conservative effect, as the horizontal stabiliser is designed to counteract the moments induced by the wing with a moment arm slightly shorter than in reality.
3. **STB/CTL-HTL-03:** The moment coefficient around the 0.25 MAC point of the NACA642015 is negligible over the intended AoA range. This assumption is validated by simulation data available online[93].
4. **STB/CTL-HTL-04:** Fuselage effects on stability are neglected. This assumption has a non-conservative effect, as fuselages have a negative moment, hence producing destabilising effects.
5. **STB/CTL-HTL-05:** The thrust vector is aligned with the centre of mass of the system. This assumption can eventually be modelled as a design choice, rendering it valid.
6. **STB/CTL-HTL-06:** The aerodynamic performance of the modified NACA642015 airfoil with a rounded trailing edge during plasma-off flight conditions (i.e. cruise) is considered to be identical to the original NACA642015. The effects of this assumption need to be further addressed. The first recommendation for addressing this is correction with wind tunnel experiment data for a trailing edge of a similar radius or employing a more in-depth estimation using numerical methods.
7. **STB/CTL-HTL-07:** The horizontal stabiliser planform is considered rectangular. This is an assumption employed during the calculation and takes the form of a design choice. Therefore it has no effect on the validity of the results.
8. **STB/CTL-HTL-08:** Downwash effects are not considered. This will have the effect of slightly underestimating the surface area needed for stability or the trim angle calculation. This assumption was done to ease the analytical case, albeit its implications are addressed at the end of this section. The ratio V_h/V_∞ is thus considered to be 1.
9. **STB/CTL-HTL-09:** The chord length of the horizontal stabiliser is 0.169m. This is done in order to match the free stream Reynolds number with the Reynolds number reported by Kotsonis M. et al in [58].

The same assumptions apply to the procedure described in the sizing for controllability section. An overview of the forces and moments affecting longitudinal stability is presented in Figure 11.4. For simplicity, only relevant moments and forces are shown. The computation is performed with respect to the air path reference frame.

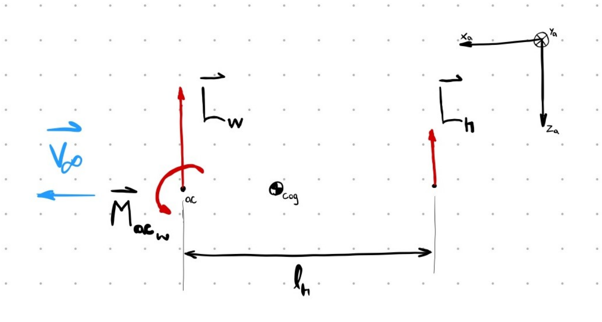

Figure 11.4: Free body diagram during static stability

Thus, it can be observed that in order to ensure moment equilibrium, a force on the horizontal stabiliser is needed to counteract the moments created by the main wing. Summing up moments for stability around the centre of gravity of the system, Equation 11.6 can be obtained.

$$\Sigma M_{ac} + \circlearrowleft: 0 = L_h \cdot [l_h - (x_{cg} - x_{ac})] + M_{ac} - L_w(x_{cg} - x_{ac}) \tag{11.6}$$

Although a straightforward approach, Equation 11.6 posed a great limitation during design. Chronologically, the value of l_h had not been determined when the longitudinal static analysis was performed using this approach, which resulted in an under-defined problem. Thus, both l_h and L_h were two free variables left to be solved by a single equation. Not quite possible. Instead, a second more empirical approach was used initially to help estimate the surface of the horizontal stabiliser.

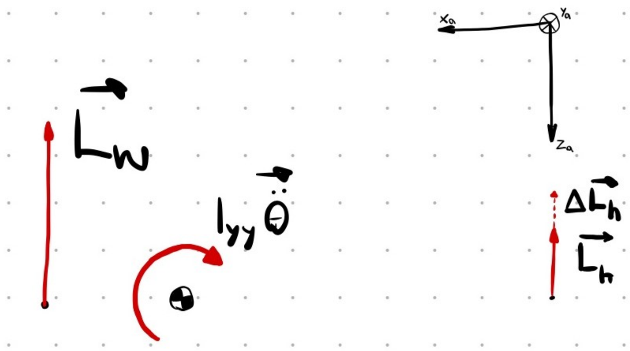

Figure 11.5: Dynamic free body diagram

Referring back to section 11.4, the concept of the 'tail volume' is a quantity describing the relative relevant geometry of the horizontal stabiliser. Re-introducing Equation 11.4, the surface of the horizontal stabiliser can be computed as:

$$S_h = \frac{C_h S \bar{c}}{l_h} \tag{11.7}$$

With l_h previously deduced using the Biot-Savart Law, the surface of the horizontal stabiliser needed for stability can be computed. The resulting horizontal stabiliser surface area S_h needed for stability is 0.028m^2.

This concludes the sizing of the horizontal stabiliser in terms of its surface, but other geometric aspects still remain to be addressed. Returning to Equation 11.6, the initial drawback of not knowing the angle of attack of the horizontal stabiliser is used now to determine its trim angle. Following a backwards approach, the trim angle of the horizontal stabiliser can be determined by rearranging Equation 11.6 into Equation 11.8.

$$\alpha_h = -\frac{C_{m_{ac}} S \bar{c}}{C_{L_{h_\alpha}} S_h l_h} \tag{11.8}$$

Before Equation 11.8 can be used to determine the trim angle, the limiting horizontal tail size must be determined by comparing it with the controllability required surface.

Sizing for Control Authority

During the pitch-up manoeuvre required to switch between gliding and climbing flight at the end of one section measurement, the horizontal control system will need to ensure the required pitch acceleration and pitch rate can be achieved.

Opposed to the stability problem, ensuring control authority during pitching manoeuvres is a dynamic instance in which the required pitch acceleration is reached by firing the plasma actuators on the horizontal stabiliser and momentarily increasing its lift. Thus, the main point of interest in the scope of a pitch-up manoeuvre is a change in the lift coefficient of the NACA642015 rounded trailing edge airfoil. The maximum pitching acceleration determined in chapter 7 and presented in Table 7.3 is used as the limiting case.

Based on the same assumptions as the sizing for stability, the problem of determining the surface area required to ensure control authority using the Kutta condition control method of flow actuation could be simplified. The FBD of the problem in its dynamic form is presented in Figure 11.5.

It must be noted that between the static problem presented Figure 11.4 and Figure 11.5, the only difference is assumed by the instantaneous increase in lift performance of the NACA642015 rounder trailing edge aerofoil which results in a ΔL_h increase in lift of the horizontal stabiliser. During this small time interval, it is assumed that no other change in velocity or angle of attack occurs, such as no increase in aerodynamic moment or lift of the main wing exists. The effect of the ΔL_h in the lift is to induce a pitch acceleration $\ddot{\theta}$ around the centre of mass. The relation between ΔL_h and the inertia term $I_{yy}\ddot{\theta}$ is presented in Equation 11.9.

$$\Sigma M + \circlearrowright : I_{yy}\ddot{\theta} = -\Delta L_h \cdot [l_h - (x_{cg} - x_{ac})] \tag{11.9}$$

Analysing Equation 11.9 and Figure 11.5, it can be noted that in order to achieve the required pitch acceleration, a negative change in the lift is needed. This entails the assumption that the Kutta condition control on the NACA642015 aerofoil can obtain negative changes in the lift coefficient. This assumption is further addressed in chapter 8, more exactly in subsection 8.6.3.

With the geometric parameters as $x_{cg} - x_{ac}$ and l_h determined in section 11.3, the required ΔL can be determined. Considering the relationship between S_p, the surface area of the horizontal stabiliser and ΔL_h, S_p can be obtained using Equation 11.10. Considering a ΔC_{L_h} of 0.01, the resulted surface area S_p is 0.256 $[m^2]$.

$$S_p = \frac{-\Delta L_h}{\frac{1}{2}\rho V^2 \Delta C_{L_h}} \tag{11.10}$$

Horizontal Tail Preliminary Dimensions

Comparing the results obtained for sizing the horizontal stabiliser for stability with those obtained for control authority, design it is clearly obvious that the control authority is the limiting case. Thus, the surface area S_p will be used and the horizontal stabiliser is trimmed using Equation 11.8. The parameters describing the geometry of the horizontal stabiliser are presented inTable 11.2

Table 11.2: Horizontal stabiliser size and performance

Parameter	Value	Unit
Aerofoil	NACA642015	$[-]$
Surface area	0.256	$[m^2]$
Chord length	0.169	$[m]$
Span	1.52	$[m]$
α_h	0.6	$[^\circ]$
ΔC_l	0.01	$[-]$

It must be noted that the preliminary values are mainly affected by

11.6. Vertical tail sizing

The vertical tail is used in this configuration mainly for lateral stability purposes. Compared to the horizontal stabiliser, only stability requirements can be derived for the vertical stabiliser, as yaw control is not a treated issue due to mission performance requirements.

As the problem of lateral stability is dictated by the aeroplane's ability to counteract a disturbance in the sideslip angle, sizing the vertical stabilisers can be approached heuristically, such as to approximate an appropriate value for C_{n_β} or the 'weathervane stability'.

The approach suggested by Torenbeek [92] is used to approximate the needed vertical tail size as a function of the geometric parameters of the drone's configuration. The following assumptions have been made during the design process:

1. **STB-VTL-01:** The aerofoil considered for the vertical stabiliser is the NACA642015. This is done in consideration of further design changes which might employ the use of plasma actuators for yaw control.
2. **STB-VTL-02:** Torenbeek's approach[92] applies to fuselage-mounted engines. The assumption is valid for the author's configuration, as the engine will be mounted at the aft-most part of the fuselage.
3. **STB-VTL-03:** The fuselage has a rectangular form. This assumption is done in order to simplify the analysis employed by Torenbeek[92].
4. **STB-VTL-04:** The distance between the aerodynamic centre of the main wing and the aerodynamic centre of the vertical stabiliser is the same as l_h. This is a valid assumption as long as a rectangular planform is considered for the vertical stabilisers, with the same chord length as the horizontal one.
5. **STB-VTL-05:** The planform of the vertical stabiliser is rectangular. This is an assumption employed during the calculation and takes the form of a design choice. Therefore it has no effect on the validity of the results.
6. **STB-VTL-06:** The chord length is 0.169m. This assumption is a design choice and is done to match the chord length of the horizontal stabiliser and match the free stream Reynolds number during flight with the Reynolds number reported by Kotsonis M. et al[58].
7. **STB-VTL-07:** Twin vertical stabilisers are considered. This is done in accordance with the choice of an H-tail configuration and is a design choice. The implications of this design choice are carried out accordingly and thus it does not question the validity of the results.
8. **STB-VTL-08:** The vertical stabilisers and the horizontal stabilisers have no effect on each other. This assumption is a non-conservative assumption, as flow separation occurs at the location where the surfaces meet.
9. **STB-VTL-09:** The wake of the propeller is assumed to have no effect. Thus, the ratio V_h/V_∞ is considered to be 1. This assumption is non-conservative, albeit quantifying the effects of the propeller wake lie beyond the available resources.

As no yaw requirements could be identified in chapter 7, sizing the vertical stabiliser will be done for lateral stability.

Following the approach suggested by Torenbeek[92, pp.335-338], sizing the vertical stabilisers is done by estimating the vertical tail volume coefficient. In a similar manner as for the horizontal stabiliser, the surface area needed for lateral stability can be calculated using Equation 11.11.

$$S_v = \frac{C_v S b}{l_h} \tag{11.11}$$

Compared to Equation 11.10, the terms that change are C_v, which will be addressed shortly and b which is the span of the main wings. C_v is approximated empirically using correlated data between C_v and the influences on C_{n_β} of the fuselage $C_{n_{\beta_f}}$, of the propulsion system $C_{n_{\beta_p}}$ and a quantity $\Delta i C_{n_\beta}$ pertaining to the design of twin-vertical stabilisers.

$$C_{n_{\beta_f}} = -K_\beta \frac{S_{fs} l_f}{Sb} (\frac{h_{f_1}}{h_{f_2}})(\frac{b_{f_2}}{b_{f_1}})^{1/3} \tag{11.12}$$

$$K_\beta = 0.3\frac{l_{cg}}{l_f} + 0.75\frac{h_{f_{max}}}{l_f} - 0.105 \tag{11.13}$$

$$C_{n_{\beta_p}} = 0.053 B_p \Sigma \frac{l_p D_p^2}{Sb} \tag{11.14}$$

Equation 11.12 presents the equation used to obtain the contribution of the fuselage to C_{n_β}, where the parameters in the equation are presented in Figure 11.6. For the rectangular fuselage considered, the side surface area is $S_{fs} = 0.15 \cdot 0.7 = 0.105 m^2$, the length of the fuselage is $l_f = 0.7 \quad [m]$, $h_{f_1} = h_{f_2} = h_{b_1} = h_{b_2} = 0.15$m. The surface area and span of the wing are the same as in Table 9.6. K_β is a scaling factor used to account for the fuselage shape and centre of gravity location. Using Equation 11.13, the K_β factor can be estimated using $l_c g = 0.3974$m and $h_{f_m ax} = 0.15$m.

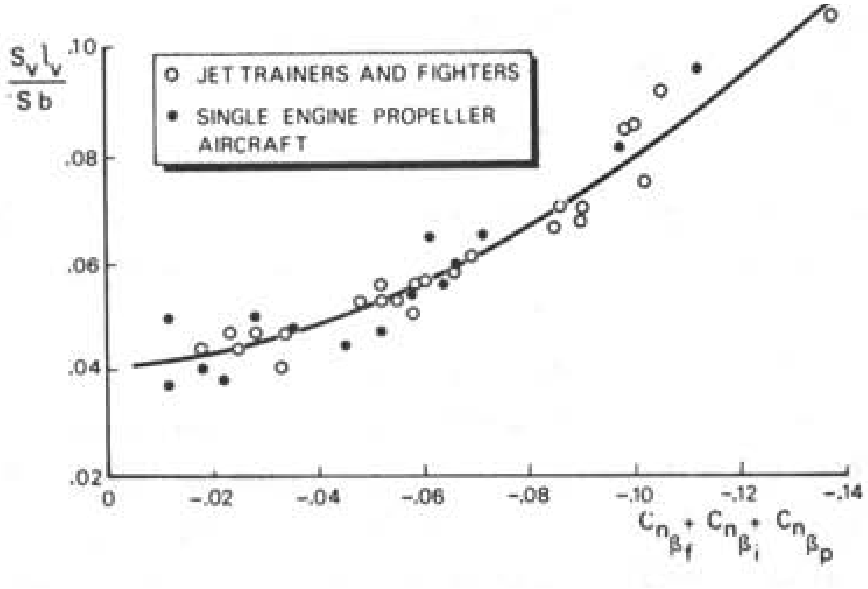

Figure 11.6: Vertical tail volume as a function of ΔC_{n_β}. Statistical data gathered for aircraft with fuselage-mounted engines. Image courtesy of Torenbeek[92]

The contribution due to the propulsion group is calculated using Equation 11.14, which relates the number of blades per propeller, propeller diameter and geometry parameters to a change in $C_{n_{\beta_p}}$. The summation is done for all propellers.

Furthermore, Torenbeek suggests that for high-wing-mounted configurations using two vertical stabilisers, a correction factor $\Delta i C_{n_\beta}$ of -0.017 can be applied[92].

The summation of all these factors results in a value of $C_v = 0.055$. The final dimensions of the vertical stabilisers can be computed using Equation 11.11. Considering two vertical stabilisers, the preliminary parameters are presented in Table 11.3.

Table 11.3: Vertical stabilisers size

Parameter	Value	Unit
Aerofoil	NACA642015	$[-]$
Surface area	2x0.046	$[m^2]$
Chord length	0.169	$[m]$
Span	2x0.274	$[m]$

Empennage layout

With the size of the horizontal stabiliser and the two vertical stabilisers, the problem reduces to finding the optimal layout such that wake effects are minimised or performance is optimised. In the case of the H-tail, two main aspects were taken into consideration: propeller wake effects on the horizontal stabiliser and structural integration with the booms.

First of all, integration with the booms was considered from a complexity point of view, thus it was decided that either integrating the booms at the joint of the horizontal tail with the vertical stabilisers or at the leading edges of the two vertical stabilisers is optimal.

Secondly, it was considered that the horizontal stabiliser should not enter the wake during nominal operations and manoeuvres. Thus it was considered that the horizontal stabiliser must be placed, with respect to the main wings, at a height that would allow a rotation of $8°$ without entering the propeller wake. The assumption that the propeller has a wake the width of the propeller diameter was made. This assumption needs to be further validated. One recommendation for this is employing the estimation of propeller-induced velocities in the wake by G. Dyne[94]. The constant width wake assumption and the geometry of the H-tail are presented in Figure 11.1b. The preliminary geometry describing the H-tail configuration is presented in Table 11.4.

Table 11.4: Empennage layout geometry

Parameter	Value	Unit
Z$_tail$	0.177	$[m]$
Wake angle	8	$[°]$

11.7. Structural design

The empennage was expected to carry a little load compared to the main wing. Therefore it was chosen to take a different design approach after observing that the structure of the main wing was sized partially due to manufacturing limits. The empennage structure will be designed as close to the manufacturing limits of aluminium as possible and after that, it will be checked if the design is strong enough to withstand all the forces and moments.

1. **STB.CTL-ESt-01:** Manufacturing limits will be driving for the design of the empennage.
2. **STB.CTL-ESt-02:** The skin is assumed to not be load carrying.
3. **STB.CTL-ESt-03:** The structure is assumed to carry all the load.
4. **STB.CTL-ESt-04:** Buckling will not occur in the skin of the empennage.

For the layout something was needed that could resist both torsional, bending, and shear forces. A hollow square spar was chosen for both the horizontal and the vertical stabiliser as a compromise between its bending resistance and torsional resistance properties. The spar will be $20mm$ By $20mm$ such that it fits snugly inside the aerofoil. The spar will have a uniform thickness of $0.5mm$.

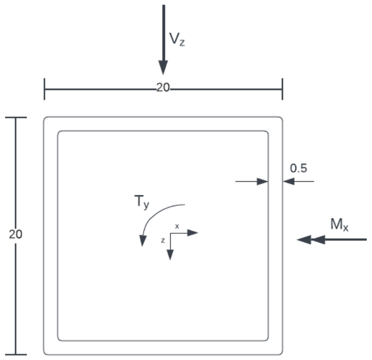

Figure 11.7: Wing box of horizontal and vertical stabilizer

A force analysis was performed on the horizontal stabiliser using the loads that are expected during the maximum pitch rate. The lift force acting on the horizontal stabiliser can be derived from Figure 11.4. It is known from the static stability analysis that the first three terms of the right-hand side of Equation 11.15 equal zero. This leaves Equation 11.16 from which the extra force acting on the wing during pitching can be derived. This extra lift force was added to the lift force calculated by XFLR5 during cruise conditions. The total force and moment distributions were put into the Python code which resulted in a maximum internal bending moment of $3857Nmm$, a torsional moment of $12.1Nmm$, and a shear force of $10.15N$.

$$I_{xx} \cdot q = M_w - L_w \cdot l_w + L_h \cdot l_h + \Delta L_h \cdot l_h \tag{11.15}$$

$$I_{xx} \cdot q = \Delta L_h \cdot l_h \tag{11.16}$$

The maximum normal and shear forces are calculated by using Equation 9.6, Equation 9.7, and Equation 9.8 respectively. The stresses were calculated using a maximum load factor of 3.8. The results and important parameters are shown in Table 11.5.

Table 11.5: Empennage structural parameters

Parameter	**Value**	**Unit**
Spar width	20	$[mm]$
Spar height	20	$[mm]$
Spar thickness	0.5	$[mm]$
Maximum internal bending moment	3857	$[Nmm]$
Maximum internal shear force	10.15	$[N]$
Maximum internal torsional moment	12.1	$[Nmm]$
σ_{max}	90.1	$[MPa]$
τ_{max}	1.05	$[MPa]$
σ_{y-Al}	324	$[MPa]$
τ_{Al}	283	$[MPa]$
τ_{Balsa}	5	$[MPa]$

11.8. Manufacturing

The spar will be made out of Aluminium 2024-T4 by bending it out of a uniform thickness sheet. In the end, a small flange shall be made to which the other end of the spar will adhere. The horizontal spar can be bolted to the vertical spars at the flanges. The ribs, just like the main wing, can be adhered to the spar and the skin can then be adhered to the ribs.

11.9. Final Empennage Design

Horizontal Stabiliser Final Design

Finishing the preliminary design allowed the structural, avionics and propulsion departments to re-estimate the mass budget and provide higher accuracy MMOI values based on the structural layout. Compared to the preliminary design, the MMOI around the y-axis decreased by approximately a factor of 2 from 2.03kgm^2 to 0.98kgm^2. New performance requirements are derived in section 7.4, with the total pitch acceleration requirement decreasing to $9\,°/\mathrm{s}^2$.

Sizing for Longitudinal Static Stability

Similarly to the preliminary design, the final design of the horizontal stabiliser falls under some of the assumptions in section 11.5. The NACA642015 aerofoil is considered as well, while the thin aerofoil theory is still considered. Fuselage effects are neglected, although one recommendation for calculating the destabilising effects of the fuselage is following the method described by N. P. van Hinsberg for estimating aerodynamic characteristics of rectangular prisms[95]. This recommendation is built on the assumption that the fuselage can be approximated as a rectangular prism, which would render such an approach conservative in calculating $\delta C_{m_{fuselage}}$.

A rectangular planform is considered for the final design as well and the chord length of 169mm is used, as the wind tunnel experiment results in subsection 8.6.3 validate the desired efficacy of plasma actuators for a flow field correspondent with this chord length. The same l_h value of 1.03m is considered a design choice for the tail-boom length estimation.

After the preliminary design was concluded, a number of assumptions are removed and the consequent effects are taken into account. Opposed to the preliminary design the final horizontal stabiliser design considers the aerodynamic moment coefficient of the NACA642015 (with a rounded trailing edge) around the mean aerodynamic centre. This produces a destabilising effect, which results in a higher moment to be counteracted by the horizontal tail.

To better approximate the lift performance of the chosen aerofoil, wind tunnel experimental data is used for the lift gradient. The corresponding lift curve gradient curve is presented in Figure 8.19. This will reduce the non-conservative effect of assuming the lift coefficient of the finite horizontal stabiliser to coincide with the higher aerofoil lift coefficient, although three-dimensional effects on the lift are still not quantified. This renders **STB-HTL-06** partially obsolete.

Finally, **STB-HTL-08** is also partially removed, by considering the circulation-induced downwash at the horizontal stabiliser to be constant. Its value was calculated using Equation 11.3, with a new Γ_0 value of 1.99m^2/s, which induces an angle of -0.6°. The downwash gradient is not considered, although the assumption that the downwash angle is constant is only valid for a small range of angles of attack around the trim angle of the aircraft.

For control purposes, the horizontal stability is designed with a -1.8° geometric tilt angle with respect to the main wing. Together with the -0.6° downwash angle, the horizontal stabiliser is thus designed to be trimmed at an angle of -2.4°, for optimal control purposes. The reasoning for this will be discussed under the 'Sizing for Control Authority' part of the final empennage design.

Considering the angle of attack of the horizontal stabiliser, and a moment coefficient around the mean aerodynamic center of the NACA642015 airfoil of -0.06 (corresponding with the values in Figure 8.19 for -2.4°), the new surface area requirement is 0.0989m^2. Considering a safety factor of 1.25, the final surface area needed for stability is 0.123m^2. This results in a total horizontal stabiliser span of 0.732m.

Sizing for Control Authority

The new control requirements derive from the better estimates of MMOI around the y-axis, along with the new pitch acceleration requirement. From wind tunnel experimental data, the change in lift coefficient due to plasma actuation increases from 0.01 to 0.05 in both positive and negative directions of actuation. Due to the fact that the horizontal stabiliser needs to produce a negative lift during static conditions and an even more negative lift to achieve the required pitch acceleration, the angle of attack of the horizontal stabiliser would ideally be -2.4°. This choice is evident by studying Figure 8.19, where it is observed that for an angle of -2.4° a negative change in lift coefficient of 0.05 takes effect upon actuating. Considering a downwash angle of -0.6°, in order to achieve the required -2.4° angle of attack during trim, the horizontal stabiliser is designed with a -1.8° tilt angle.

The required planform area for control authority using plasma actuators is 0.0346m^2. Including a safety factor of 1.25, the final area requirement becomes 0.0433m^2. Thus, it should be noted by comparing with the stability required value that stability will be the limiting case of sizing.

Trimming

In order to better assess the validity of the obtained results, the static stability of the main wing plus the horizontal stabiliser was analysed using XFLR5. Using the ring vortex method (VLM2), the resulting airframe was analysed at different angles of attack. In order to operate at the optimal angle of attack and be statically stable, the condition that $C_m = 0$ for $\alpha = 0$ is imposed.

Initially, trim could only be achieved at a global angle of attack of approximately 3.5°. The quite large trim angle needed would entail that the horizontal stabiliser is producing too much lift than needed for stability, which was attributed to two possible causes. Firstly, it was considered that the surface area of the horizontal stabiliser was overestimated, which would result in a higher magnitude negative lift produced by the tail. Although this is most likely true, the safety factor of 1.25 is considered for averaging the unquantified effects of the assumptions. Thus, it was concluded that the aircraft be rather trimmed by changing the centre of gravity location. This is considered feasible, as the centre of gravity location is constant throughout the flight and thus changing it is a matter of rearranging the internals of the fuselage. The new centre of gravity location was found to be at 23.7% of the mean aerodynamic chord of the main wing, which not only allows the lift of the wing to be contributing to the stabilising effect (as the x_{cg} location is aft of the mean aerodynamic centre) but also places the centre of gravity further away from the neutral point stick-fixed location.

The final parameters pertaining to the horizontal stabiliser are presented in Table 11.6.

Table 11.6: Final horizontal stabiliser parameters and performance

Parameter	Old Value	New Value	Unit
Aerofoil(repeated)	NACA642015	NACA642015 w/ round TE	$[-]$
Surface area(repeated)	0.256	0.123	$[m^2]$
Chord(repeated)	0.169	0.169	$[m]$
Span(repeated)	1.520	0.732	$[m]$
α_h	0.6	-1.8	$[^\circ]$
$x_{cg}/\bar{c}$	31.0	23.7	[%]

Vertical Stabilisers Final Design

The vertical stabilisers were not resized for the final design. This choice is made based on two reasons, one pertaining to the dynamic stability of the aircraft and the other to the resource allocation within the given time-frame. Firstly, changing the size of the vertical stabilisers found using the approach presented in section 11.6 would not have affected the dynamic lateral stability of the system. Secondly, sizing the vertical stabilisers is a process which needs to take place once all other structural and aerodynamic parameters are established. As the required value of C_{n_β} depends heavily on the relative location of the fuselage and vertical stabilisers[92], sizing the vertical stabiliser is a task that comes at the end of one full iteration of all airframe subsystems.

Finally, due to the new required tilt angle of the horizontal stabiliser and new insight into the performance of the rounded TE NACA642015 aerofoil, the location of the horizontal stabiliser is changed. The effective wake angle also changed from 8 to 5.4°, to allow the horizontal tail an angle of attack range of [-2.4, 2.4]° without entering the wake of the propeller. The downwash angle was considered. Moreover, as the fuselage height is modified, the vertical stabilisers will need to be raised with respect to their preliminary position by a value of 3cm.

As a general recommendation, for improving the glide performance of the entire system, the horizontal stabiliser should be designed for positive rather than negative lift. Multiple options are possible, as optimising lift performance and static longitudinal stability is a multi-variable problem, but some general approaches might consider using a different airfoil for the lifting planform with a smaller moment coefficient than the MH115, using a canard instead of an aft-placed tail or placing the centre of gravity more aft of the main wing's centre of lift.

Empennage Structure Final Design

The effective loads on the tail and the cross-sectional dimensions did not change during the resizing of the empennage. Therefore the internal stresses remain the same and the structure of the empennage does not need to be reiterated.

12 Stability and Control

Another essential aspect to take into account when designing an unconventional drone such as the P.U.L.S.E. Drone is stability. While not always required and even hurting the drone's manoeuvrability, a stable aircraft is typically desirable. Whether or not an aerial vehicle is inherently stable, stability goes hand in hand with the manoeuvrability of the aircraft, as a compromise between the two always has to be made. To ensure that the drone fulfils all manoeuvrability requirements and thereby its mission, the UAV is equipped with control surfaces and a control system. This chapter elaborates on the stability characteristics of the P.U.L.S.E. drone as well as the control system that was designed to actuate the plasma control surfaces. For both stability analysis and control system design the underlying assumptions and applied methodology are first described. This is followed by the methods, the results and a discussion regarding their validity and value. Finally, a series of recommendations for future improvements will be given.

12.1. Subsystem Requirements

The requirements for the stability and control subsystem are given in Table 12.1.

Table 12.1: Stability and control subsystem requirements

Identifier	Requirement	Verification	Compliance
SUB-STB-01	The system shall be statically stable in all flight phases.	Analysis	PASS
SUB-STB-02	The system shall be dynamically stable in phugoid motions.	Analysis	PASS
SUB-STB-03	The system shall be dynamically stable in short-period motions.	Analysis	PASS
SUB-STB-04	The system shall be dynamically stable in aperiodic roll motions.	Analysis	PASS
SUB-STB-05	The system shall be dynamically stable in Dutch roll motions.	Analysis	PASS
SUB-PCS-09	The system shall have no moving control surfaces.	Inspection	PASS
SUB-PCS-10	The system shall provide pitch control authority	Analysis	PENDING
SUB-PCS-11	The system shall provide roll control authority	Analysis	PENDING
SUB-PCS-12	The system shall provide yaw control authority	Analysis	PENDING

12.2. Stability analysis

12.2.1. Method

A stability analysis refers to the tendency and response of a vehicle to return to its original state when faced with disturbances. Whereas static stability is only concerned with general tendencies, dynamic stability also investigates the aircraft's response, making it a more thorough approach. As static longitudinal and lateral stability determined the horizontal and vertical tail sizing this was already discussed in section 11.5 and section 11.6 respectively. For dynamic stability analysis, the starting point outlined in succeeding sections is the underlying physical system and the related equations of motion. A series of assumptions are made to simplify and constrain the analysis to a few extreme cases in which stability is most critical:

1. **STB-01:** The governing equations of motion can be decoupled into a set of longitudinal and lateral equations of motion respectively, as the dependencies between the two planes of motion are small and at this stage negligible.
2. **STB-02:** The changes in all state variables are assumed to be small. This assumption is necessary to allow for linearisation around specific flight conditions.
3. **STB-03:** If the system is stable under a series of investigated flight conditions, it will be stable for all reasonable flight conditions.
4. **STB-04:** The system in question is time-invariant. This means that the dynamic properties of the system do not change over time. Especially given that the P.U.L.S.E. Drone is battery-powered and there are no moving control surfaces, this is very realistic.
5. **STB-05:** The OpenVSP software is a linear solver. It is not capable of modelling stall characteristics or any flow separation in general. It should only be used for simple flight conditions with a low angle of attack and sideslip angle. [1].

With these assumptions in place, some of the flight conditions are chosen to be investigated. The stability characteristics of the straight, steady, symmetric flight will be analysed. With the case of interest defined, the equations of motion can now be linearised around them. The linearised equations of motion can be seen in Equation 12.1 and Equation 12.2, where it needs to be emphasised that they are decoupled into symmetric and asymmetric motion as stated in the assumptions. While the left side of the equations is conventional and can often be found in literature [96], the right side with the control derivatives and variables is heavily modified for the plasma actuators used in the P.U.L.S.E. Drone.

$$\begin{bmatrix} C_{x_u} - 2\mu_c D_c & C_{X_\alpha} & C_{Z_0} & C_{X_q} \\ C_{Z_u} & C_{Z_\alpha} + (C_{Z_\alpha} - 2\mu_c) D_c & -C_{X_0} & C_{Z_q} + 2\mu_c \\ 0 & 0 & -D_c & 1 \\ C_{m_u} & C_{m_\alpha} + C_{m_\alpha} D_c & 0 & C_{m_q} - 2\mu_c K_{yy} D_c \end{bmatrix} \begin{bmatrix} \hat{u} \\ \alpha \\ \theta \\ \frac{q\bar{c}}{V} \end{bmatrix} = \begin{bmatrix} C_{X_{dce_{lower}}} & -C_{X_{dce_{lower}}} & -C_{X_T} \\ C_{Z_{dce_{lower}}} & -C_{Z_{dce_{lower}}} & -C_{Z_T} \\ 0 & 0 & 0 \\ C_{m_{dce_{lower}}} & -C_{m_{dce_{lower}}} & -C_{m_T} \end{bmatrix} \begin{bmatrix} dc_{e_{upper}} \\ dc_{e_{lower}} \\ T \end{bmatrix} \tag{12.1}$$

---

[1] openvsp.org (Accessed - 20/6/2023)

$$\begin{bmatrix} C_{Y_\beta} + (C_{Y_{\dot\beta}} - 2\mu_b D_b) & C_L & C_{Y_p} & C_{Y_r} - 4\mu_b \\ 0 & -\frac{1}{2}D_b & 1 & 0 \\ C_{l_\beta} & 0 & C_{l_p} - 4\mu_b K_{xx} D_b & C_{l_r} + 4\mu_b K_{xz} D_b \\ C_{n_\beta} + C_{n_{\dot\beta}} D_b & 0 & C_{n_p} + 4\mu_b K_{xz} D_b & C_{n_r} - 4\mu_b K_{zz} D_b \end{bmatrix} \begin{bmatrix} \beta \\ \phi \\ \frac{pb}{2V} \\ \frac{rb}{2V} \end{bmatrix} =$$

$$\begin{bmatrix} C_{Y_{dca_{right}}} & -C_{Y_{dca_{left}}} & -C_{Y_{dcr_{right}}} & -C_{Y_{dcr_{left}}} \\ 0 & 0 & 0 & 0 \\ C_{l_{dca_{right}}} & -C_{l_{dca_{left}}} & -C_{l_{dcr_{right}}} & -C_{l_{dcr_{left}}} \\ C_{n_{dca_{right}}} & -C_{n_{dca_{left}}} & -C_{n_{dcr_{right}}} & -C_{n_{dcr_{left}}} \end{bmatrix} \begin{bmatrix} dc_{a_{right}} \\ dc_{a_{left}} \\ dc_{r_{right}} \\ dc_{r_{left}} \end{bmatrix} \tag{12.2}$$

As described in [96], the control variables are all assumed to be zero and the state variables instead have non-zero initial conditions. Due to the linearity of the preceding equations, the magnitude of said initial conditions is irrelevant, however, it is important to note that this is not true for a non-linear case, where the magnitude of the initial disturbance can significantly impact the stability characteristics of the system. This is why `STB-02` is required, as the model is only valid for small disturbances due to its linear nature.

Since the control variables are assumed zero and the magnitude of the initial disturbances can be neglected, Equation 12.1 and Equation 12.2 can be simplified to Equation 12.3 and Equation 12.4.

$$\begin{bmatrix} C_{X_u} - 2\mu_c D_c & C_{X_\alpha} & C_{Z_0} & C_{X_q} \\ C_{Z_u} & C_{Z_\alpha} + (C_{Z_{\dot\alpha}} - 2\mu_c) D_c & -C_{X_0} & C_{Z_q} + 2\mu_c \\ 0 & 0 & -D_c & 1 \\ C_{m_u} & C_{m_\alpha} + C_{m_{\dot\alpha}} D_c & 0 & C_{m_q} - 2\mu_c K_{yy} D_c \end{bmatrix} \begin{bmatrix} \hat{u} \\ \alpha \\ \theta \\ \frac{q\bar{c}}{V} \end{bmatrix} = \begin{bmatrix} 0 \\ 0 \\ 0 \\ 0 \end{bmatrix} \tag{12.3}$$

$$\begin{bmatrix} C_{Y_\beta} + (C_{Y_{\dot\beta}} - 2\mu_b D_b) & C_L & C_{Y_p} & C_{Y_r} - 4\mu_b \\ 0 & -\frac{1}{2}D_b & 1 & 0 \\ C_{l_\beta} & 0 & C_{l_p} - 4\mu_b K_{xx} D_b & C_{l_r} + 4\mu_b K_{xz} D_b \\ C_{n_\beta} + C_{n_{\dot\beta}} D_b & 0 & C_{n_p} + 4\mu_b K_{xz} D_b & C_{n_r} - 4\mu_b K_{zz} D_b \end{bmatrix} \begin{bmatrix} \beta \\ \phi \\ \frac{pb}{2V} \\ \frac{rb}{2V} \end{bmatrix} = \begin{bmatrix} 0 \\ 0 \\ 0 \\ 0 \end{bmatrix} \tag{12.4}$$

These homogeneous first-order differential equations have a solution of the form displayed in Equation 12.5. It should be noted that the subscript c refers to the normalisation with the chord and thus indicates the association with the symmetric equations of motion. However, the lateral case is analogous with the subscript b, indicating normalisation with the wingspan. From this point onward, this section will only discuss the symmetric case, as the asymmetric case directly follows. The results of the stability analysis will of course be given for both cases.

$$x = A_x e^{\lambda_c s_c} \tag{12.5}$$

In Equation 12.5 A_x relates to the initial disturbance, while s_c is the dimensionless time, defined as

$$s_c = \frac{V}{\bar{c}} \cdot t \tag{12.6}$$

Continuing with the general solution of the symmetric equations of motion, it is evident that the x-vector for all states should go to zero for a stable aircraft as the time moves to infinity or, mathematically expressed, that,

$$\lim_{s_c \to \infty} x = 0$$

Looking at the general solution, λ_c is left to determine whether or not the aircraft is stable in the equation of interest. To find λ_c, the substitution of the general solution into the equations of motion is required. However, it is useful to first note that,

$$D_c x = \frac{\bar{c}}{V} \frac{d}{dt} (A_x e^{\lambda_c \frac{V}{\bar{c}}} t) = \lambda_c x \tag{12.7}$$

, meaning that the substitution of Equation 12.5 into Equation 12.3 yields the following:

$$\begin{bmatrix} C_{X_u} - 2\mu_c \lambda_c & C_{X_\alpha} & C_{Z_0} & C_{X_q} \\ C_{Z_u} & C_{Z_\alpha} + (C_{Z_{\dot\alpha}} - 2\mu_c) \lambda_c & -C_{X_0} & C_{Z_q} + 2\mu_c \\ 0 & 0 & -\lambda_c & 1 \\ C_{m_u} & C_{m_\alpha} + C_{m_{\dot\alpha}} \lambda_c & 0 & C_{m_q} - 2\mu_c K_{yy} \lambda_c \end{bmatrix} \begin{bmatrix} A_u \\ A_\alpha \\ A_\theta \\ A_q \end{bmatrix} e^{\lambda_c s_c} = \begin{bmatrix} 0 \\ 0 \\ 0 \\ 0 \\ 0 \\ 0 \end{bmatrix} \tag{12.8}$$

In this equation, the A-vector summarises the initial disturbances experienced by the system. While the case in which $A_u = A_\alpha = A_\theta = A_q = 0$, satisfies the equation regardless of λ_c, this is disregarded since it is the trivial solution. As $e^{\lambda_c s_c} \neq 0$, this means that the remaining solutions for Equation 12.8 are found by setting the matrix on the left equal to zero. Since all variables but λ_c in this matrix are stability derivatives, and therefore fixed (due to linearisation), the resulting λ_c values will indicate whether the UAV is stable or not. These are also known as the eigenvalues of the matrix and are found by equating the determinant of the matrix to zero.

However, in order to actually determine the eigenvalues of this matrix and its equivalent in the lateral case, stability derivatives are required. While simple estimation methods do exist, a preliminary CFD analysis was performed to estimate the stability derivatives more accurately. OpenVSP was used to determine all stability derivatives present in the equations of motion. First, the layout of the main wing, horizontal tail and vertical tail was constructed using the Geometry Browser. As these computations are still comparatively preliminary, the fuselage was neglected due to its low impact on the stability derivatives [2]. Then the DegenGeom tool was used to create the geometry that can be read into the VSPAERO tool. The variables used as input in OpenVSP are the values for the designed mission and can be seen in Figure 12.1. With all the stability derivatives filled in, Equation 12.8 can be solved to find a series of λ_c and λ_b for the analogous, lateral case.

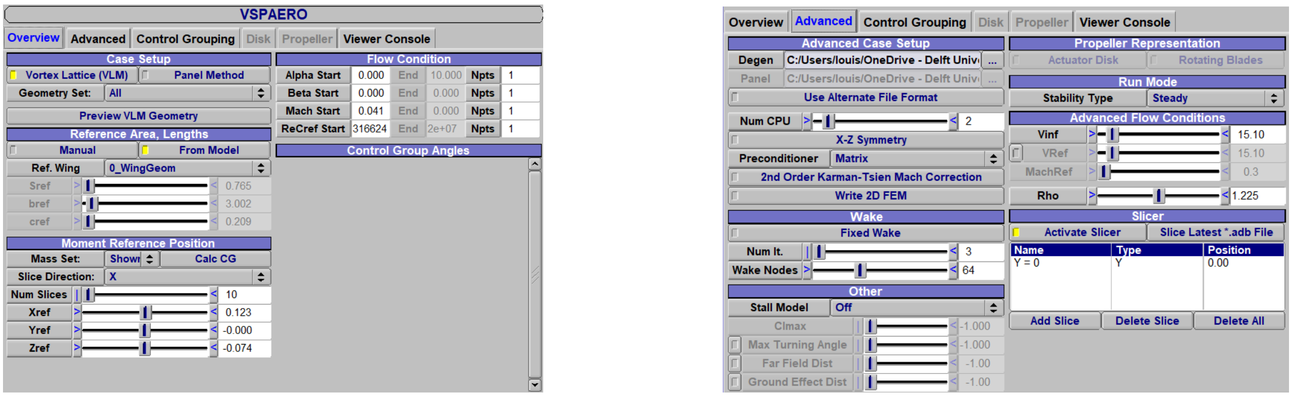

● Vortex Lattice (VLM) ☐ Panel Method
Geometry Set: All
☐ Manual ● From Model
Ref. Wing: 0_WingGeom
Sref 0.765
bref 3.002
cref 0.209
Mass Set: Shown
Slice Direction: X
Num Slices 10
Xref 0.123
Yref -0.000
Zref -0.074
Alpha Start 0.000 End 10.000 Npts 1
Beta Start 0.000 End 0.000 Npts 1
Mach Start 0.041 End 0.000 Npts 1
ReCref Start 316624 End 2e+07 Npts 1

Degen C:/Users/louis/OneDrive - Delft Univ
Panel C:/Users/louis/OneDrive - Delft Univ
☐ Use Alternate File Format
Num CPU 2
☐ X-Z Symmetry
Preconditioner: Matrix
☐ 2nd Order Karman-Tsien Mach Correction
☐ Write 2D FEM
☐ Fixed Wake
Num It. 3
Wake Nodes 64
Stall Model: Off
Clmax -1.000
☐ Max Turning Angle -1.000
☐ Far Field Dist -1.00
☐ Ground Effect Dist -1.00
Stability Type: Steady
Vinf 15.10
☐ VRef 15.10
MachRef 0.3
Rho 1.225
● Activate Slicer

Name	Type	Position
Y = 0	Y	0.00

(a) Overview page

(b) Advanced page

Figure 12.1: OpenVSP settings for stability analysis

12.2.2. Results

The VSPAERO steady stability analysis was run and this resulted in a *.STAB* file which contained all stability derivatives. The ones needed for the equations of motion were extracted and used to create the matrix in Equation 12.8. Using Python, the eigenvalues of this matrix were calculated and plotted as can be seen in Figure 12.2.

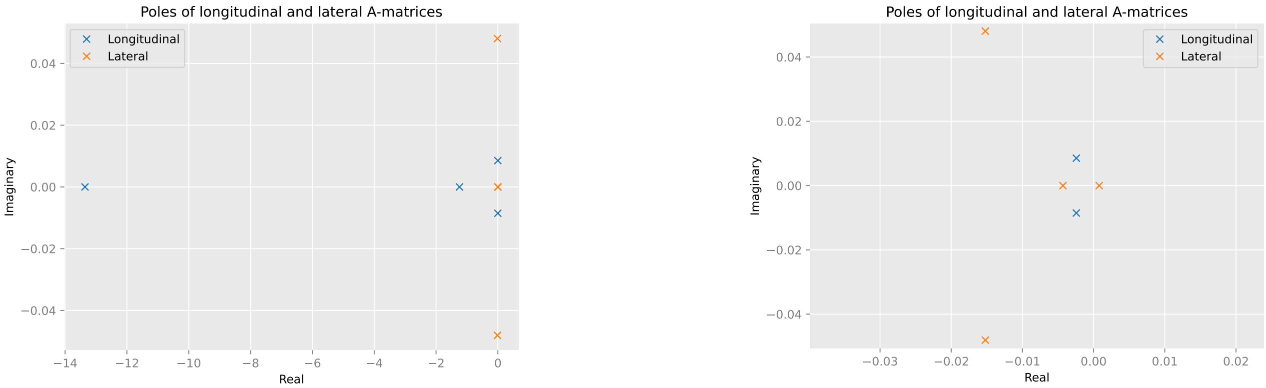

(a) Plotted eigenvalues

(b) Zoomed view of critical region

Figure 12.2: Eigenvalues for longitudinal and lateral case

12.2.3. Discussion

According to Figure 12.2, it can be observed that all eigenvalues, except for one have negative real parts. Inferring from Equation 12.5, it could be concluded that all oscillatory motions are stable since their damping ratios are seemingly positive. In reality, the system is prone to errors and while the resulting eigenvalues are precisely

---

[2] openvsp.org (Accessed - 20/6/2023)

calculated, the results are not necessarily accurate due to errors in the stability derivatives determined by OpenVSP. Although, a magnitude analysis is done on the damping ratios of the Dutch roll and phugoid motions. Their corresponding ratios came out to be 0.30 and 0.27, which indicates that the motions are under-damped. Moreover, since the system is under-damped and the real and imaginary parts of the eigenvalues approach values subject to discretisation and rounding errors, the oscillatory motions cannot be concluded stable with certainty. Thus, in future design steps, emphasis on obtaining an appropriate list of stability derivatives will be of utmost importance and the analysis of the eigenmotions will be addressed on each iteration.

Regarding the non-oscillatory eigenmotions, two are identified in the eigenvalues plots, pertaining to aperiodic roll and spiral. In this case, the aperiodic roll has a positive negative eigenvalue, hence is deemed stable. The positive real eigenvalue belongs to the spiral motion which is deemed slightly unstable. A very slightly unstable spiral motion is easy to correct and thus it was not required for this to be stable [96].

12.2.4. Conclusion & Recommendations

Therefore, from this analysis, it can be concluded that the simplified OpenVSP model is stable. However, it should be noted that this model and the OpenVSP software might contain inconsistencies resulting in errors in the stability derivatives. Therefore more advanced CFD analysis or a full-scale (wind tunnel) test should be performed to observe the stability characteristics of the UAV. Besides this, stability should be checked in all flight phases which might be obtained by linearising multiple times about all flight phases or by using a non-linear model. Lastly, the time response for a different range of inputs can be plotted and checked to observe the UAV's behaviour in different conditions.

12.3. Control system design

12.3.1. Method

The control system design followed a top-down approach starting at top-level functions the system has to fulfil and the different aspects it requires to do so. The main function of the control system is to provide the UAV with the required manoeuvrability and dampen out unexpected disturbances. In addition, it has been decided that the control system will also include an autopilot capable of navigating and guiding the drone according to a path pre-defined by the operator. These main functions result in the high-level architecture that can be seen in Figure 12.3, where the three main blocks are the drone operator, the autopilot, and the physical system which is controlled. In the following, each of these blocks is described in more detail, before the special challenges resulting from the use of plasma actuators are outlined.

The drone operator block can be further split up into three further blocks. Firstly, a joystick represents the direct input from the drone operator, allowing them to steer and fly any mission as desired. Secondly, a mission block defines a pre-programmed flight pattern that the operator can feed into the autopilot, allowing for the UAV to operate completely autonomously. Lastly, the drone operator also has access to a switch in order to switch between autonomous and pilot operations. While the drone operator block is very important in operation it is comparatively simple and therefore not described in further detail in the following sections.

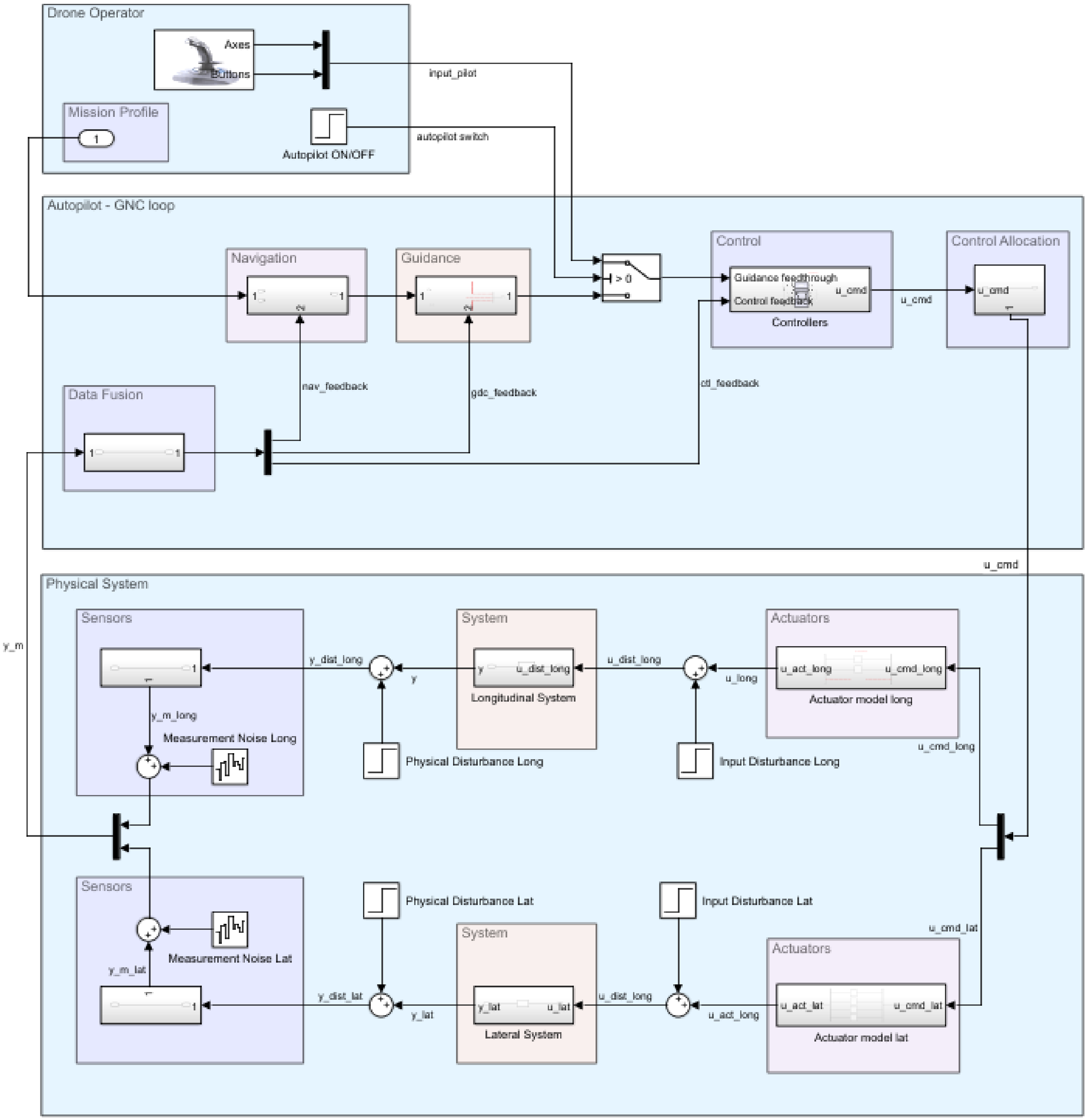

Figure 12.3: High-level software block diagram of the control system

The most important part of the control system is the actual GNC loop (Guidance, Navigation and Control), which is represented in the Autopilot block. The implemented architecture is loosely based on the flight control system in [1], however, major alterations have been made in the control block to accommodate the plasma actuation system. As mentioned before, the control system was designed to not only provide manoeuvrability and disturbance dampening but also navigation and guidance, given a predefined path: This is done in the navigation and guidance blocks. The navigation system takes the mission profile and, with the help of path planning algorithms, defines a target speed, altitude and course in order to follow the path defined in the mission profile. These are fed into the guidance block together with the UAV's current speed, altitude and heading. Based on these inputs the guidance block calculates a desired pitch angle θ_{des} to control the speed, a desired rate of climb $\frac{dh}{dt}_{des}$, which is related to altitude control, and lastly a desired roll angle ϕ_{des} used to control the heading. The navigation and guidance functions of the autopilot have not been worked out in detail due to time constraints and the fact that standard industrial solutions exist for these since they are independent of the plasma actuators.

The desired pitch and roll angles, as well as the desired climb rate, are then fed into the actual control system. However, a distinction has to be made here. As can be seen in Figure 12.3, the control block is preceded by a switch: This switch allows the drone operator to choose between steering the drone themselves or letting it fly on autopilot. In either configuration, the control system takes desired values for the pitch angle, rate of climb and roll angle as inputs. A second set of inputs comes from the sensor model. As the Simulink model is a simulation of the real-life model, the sensor blocks are connected to the output of the state-space systems and have measurement noise artificially added to simulate real-life effects. The sensor model currently simply gives out the state-space output with added noise, as a more sophisticated model would be unreasonable given the current design maturity. The measured data is then fed to the control block via data fusion: This block processes the measured data in real-time to provide feedback to the guidance, navigation and control blocks. In addition to the inputs and outputs of the control system, Figure 12.4 also shows the different controllers for pitch and roll angle as well as the rate of climb. The pitch controller is of the PI-type and includes a pitch damper as well as pitching moment control in case the engine is vertically offset from the centre of gravity. Since this is not the case in the current design, the gain of this proportional controller is set to zero for now. The vertical speed controller is a PID controller, meaning that it also considers future values of the rate of climb to compute the commanded $\frac{dh}{dt}$. The yaw controller is a simple P-type controller to dampen out Dutch roll. Lastly, the roll angle controller is a PID controller with a roll damper.

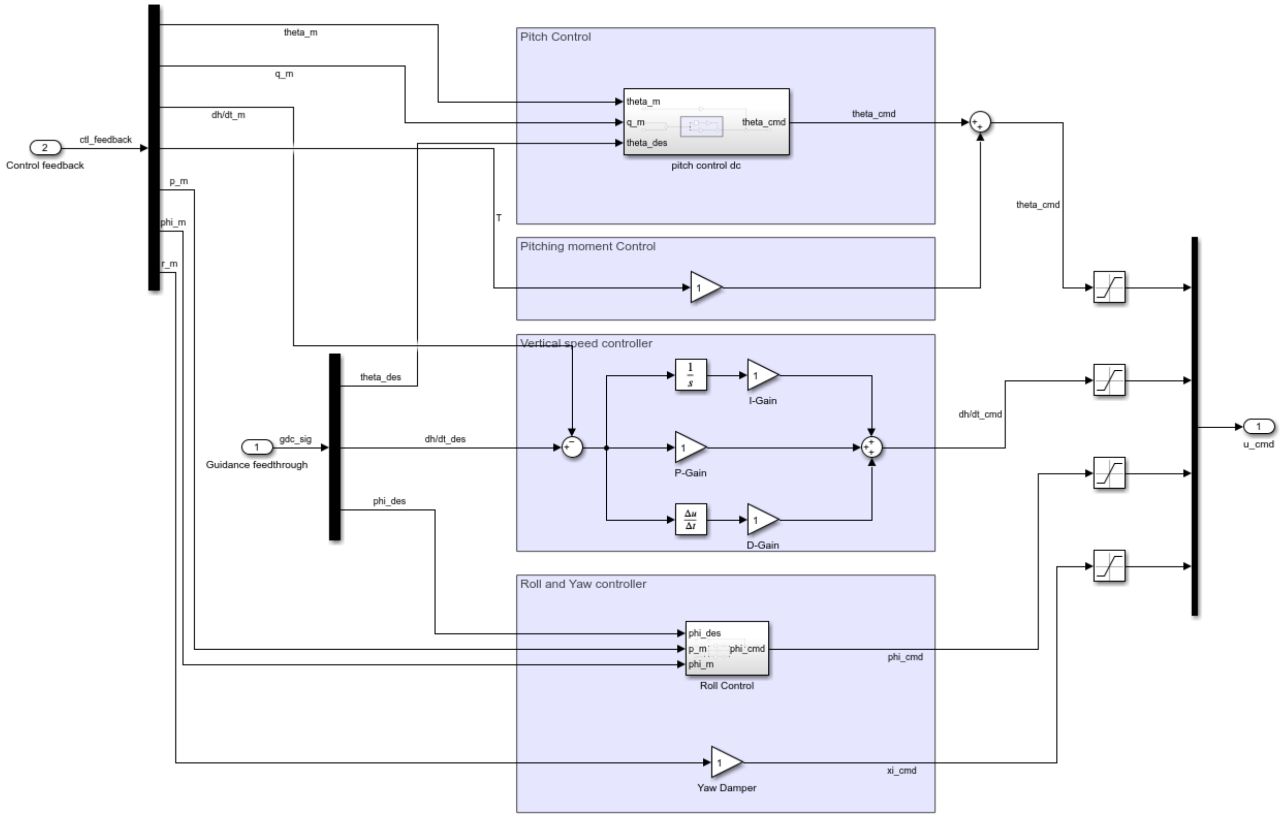

Figure 12.4: Control System of the UAV

In order to produce the states given by the controllers, the plasma actuators need to be operated accordingly. This so-called actuator model is the most crucial deviation the control system of the P.U.L.S.E. drone has when compared to conventional aircraft and control systems. In conventional aircraft, the deflection of the control surfaces has a direct impact on the dynamics of the aircraft, resulting in a comparatively simple actuator model. Applying plasma actuators complicates the actuator models due to a number of factors: As plasma actuators have a low mechanical efficiency [97] and thus rely on efficient use of aerodynamic phenomena, the changes in aerodynamic forces produced by them are highly dependent on environmental conditions. Furthermore, they are characterized by more than one control variable, such as V_{pp}, f_{car} and f_{burst}, adding to the complexity. Last but not least, no reliable and accurate models currently exist to determine the aerodynamic effect a change in the control variables will have.

As the development of such a model is far out of the scope of the project, an experimental approach was taken instead. With a fixed geometry the effect of multiple control variables was tested in a series of wind tunnel experiments explained in chapter 8. As mentioned there, three possible control variables exist: The peak-to-peak voltage V_{pp}, the burst frequency f_{burst}, and the duty cycle dc at which the actuator is fired. V_{pp} was excluded from the start, as continuous voltage changes at such in the high-voltage regime were considered infeasible. In Figure 8.21 the effect of the burst frequency on the aerodynamic coefficients can be seen at different angles of attack and a series of duty cycle settings: However, it is also clear that no relevant gradient and therefore no control authority can be deducted from changes in f_{burst}. These results leave the duty cycle as control variable. In chapter 8, Figure 8.23 shows the measured aerodynamic coefficients against the duty cycle.

It should be noted that again a similar conclusion as for the burst frequency could be drawn, however, when varying the duty cycle at a higher angle of attack, a significant gradient can be seen. While these results cannot be extrapolated to larger angles of attack straightforwardly, placing the control surfaces at a corresponding incidence angle for the required control authority to manoeuver the UAV within the requirements defined by the mission profile. For instance, this means that the ailerons are offset to ensure that they experience $\alpha = 2.6$ required for control. The horizontal tail, hosting the pitch actuator operates at the same incidence angle, while the vertical tailfins have not been redesigned to account for the angular offset due to time constraints.

With the duty cycle being chosen as the control variable and the α assumed in ranges where the duty cycle provides the necessary control authority, the control system can be designed. From the experiments in chapter 8 the lifting coefficient C_l and $\frac{dC_l}{ddc}$ for each duty cycle setting is known. In the following, an explanation is given of how the actuator model and the control derivatives are found from these. As they are different for each actuator, an exemplary actuator model and the related control variables can be found in the following subsection.

12.3.2. Results & Discussion

Looking at Figure 12.3, it was considered infeasible to design the entire control system given the short time frame of the project. Therefore, as a demonstration of how the envisioned control system should work, the pitch controller as can be seen in Figure 12.5 was designed. It has been tuned to control the UAVs' pitch attitude with plasma actuators.

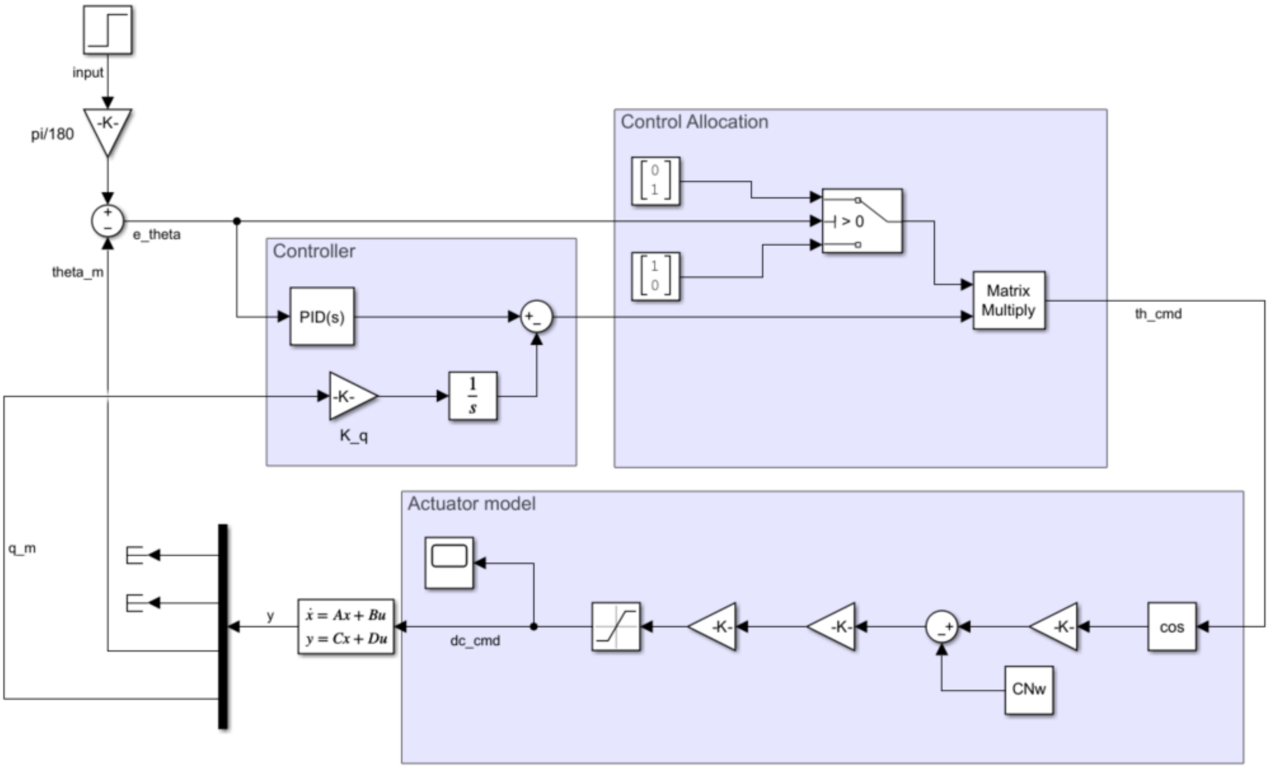

Figure 12.5: Architecture of the pitch controller

In this model, it is assumed that the pitch controller gets an input from the guidance block in the form of a step input. Taking the measured pitch angle and pitch rate into account, the commanded pitch angle is fed into the control allocation, which decides whether the lower or upper actuator should be applied to achieve the commanded pitch angle. The two signals for the upper and lower actuators are then fed to the actuator model used to determine the inputs given by the actuator. In the case of the pitch control of the P.U.L.S.E. Drone, this means that the commanded pitch angle is translated into a duty cycle setting applied to the actuators. The duty cycle setting is fed into the full state-space system, however, only the pitch angle and rate are taken as measured outputs and used as feedback for the control loop. The other outputs are disregarded, and the models used to simulate sensors and data fusion are omitted to simplify the demonstration.

While the control allocation and controller blocks are fairly straightforward, the actuator model and the state-space model are slightly more complicated. The starting point for the actuator model is the following dimensionless version of the equations of motion for pitch motion [96]:

$$C_T = C_{T_w} + C_{T_h}\left(\frac{V_h}{V}\right)^2\frac{S_h}{S} - T_c\frac{2D^2}{S} = \frac{-W}{\frac{1}{2}\rho V^2 S}sin(\theta) \tag{12.9}$$

$$C_N = C_{N_w} + C_{N_h}\left(\frac{V_h}{V}\right)^2\frac{S_h}{S} + T_c\frac{2D^2}{S}sin(i_p) + C_{N_p}\frac{S_p}{S} = \frac{W}{\frac{1}{2}\rho V^2 S}cos(\theta) \tag{12.10}$$

$$\begin{aligned}C_m = C_{m_{ac_w}} + C_{N_w}\frac{x_{cg}-x_w}{\bar{c}} - C_{T_w}\frac{z_{cg}-z_w}{\bar{c}} + C_{m_{ac_h}}\left(\frac{V_h}{V}\right)^2\frac{S_h}{S}\frac{\bar{c}_h}{\bar{c}} + C_{N_h}\left(\frac{V_h}{V}\right)^2\frac{S_h}{S}\frac{x_{cg}-x_h}{\bar{c}}\\ -C_{T_h}\left(\frac{V_h}{V}\right)^2\frac{S_h}{S}\frac{z_{cg}-z_h}{\bar{c}} + \left(T_c\frac{2D^2}{S}sin(i_p) + C_{N_p}\frac{S_p}{S}\right)\frac{x_{cg}-x_p}{\bar{c}} + T_c\frac{2D^2}{S}\frac{z_{cg}-z_p}{\bar{c}} = 0\end{aligned} \tag{12.11}$$

For the actuator model of the pitch motion, a relation between the pitch angle θ and the duty cycle is required. Looking at the preceding equations, Equation 12.11 can be discarded as the pitch angle is not affected by the moment equilibrium. This leaves Equation 12.9 and Equation 12.10, where C_{N_h} is where the duty cycle comes into play. Since only small angles are considered according to the assumptions stated earlier and the initial state assumes $\theta = 0$, Equation 12.9 can also be dropped. As the propulsion system does not have an incidence angle and is therefore assumed to be perfectly in line with the centre of gravity, Equation 12.10 is simplified to Equation 12.12.

$$C_{N_w} + C_{N_h}\left(\frac{V_h}{V}\right)^2\frac{S_h}{S} = \frac{W}{\frac{1}{2}\rho V^2 S}cos(\theta) \tag{12.12}$$

Expanding C_{N_h} to

$$C_{N_h} = \frac{d}{ddc}C_l \cdot \Delta dc$$

yields a full relation between θ and the duty cycle setting as can be seen in Equation 12.13. It is important to realise that this relationship is made possible by the results of the wind tunnel experiments, as $\frac{dC_l}{ddc}$ was found this way.

$$C_{N_w} + \frac{dC_l}{ddc}\cdot\Delta dc\left(\frac{V_h}{V}\right)^2\frac{S_h}{S} = \frac{W}{\frac{1}{2}\rho V^2 S}cos(\theta) \tag{12.13}$$

The implementation of the actuator model can be seen in Figure 12.5. It should be noted that the function is rearranged to give the duty cycle setting as a function of the pitch angle and that the duty cycle is constrained between 0 and 1 with a saturation block. Lastly, preliminary estimation methods [96] as can be seen in the following equations were used to determine the control derivatives required to populate the input matrix B of the state-space system.

$$C_{Z_{dc_{upper}}} = \frac{dCl}{ddc}\left(\frac{V_h}{V}\right)^2\frac{S_h}{S} = 0.03581 \tag{12.14}$$

$$C_{Z_{dc_{lower}}} = -\frac{dCl}{ddc}\left(\frac{V_h}{V}\right)^2\frac{S_h}{S} = -0.03581 \tag{12.15}$$

$$C_{m_{dc_{upper}}} = \frac{dCl}{ddc}\left(\frac{V_h}{V}\right)^2\frac{S_h}{S}\cdot\frac{l_h}{\bar{c}} = 0.1456 \tag{12.16}$$

$$C_{m_{dc_{lower}}} = -\frac{dCl}{ddc}\left(\frac{V_h}{V}\right)^2\frac{S_h}{S}\cdot\frac{l_h}{\bar{c}} = -0.1456 \tag{12.17}$$

With all the values determined in Equation 12.14, Equation 12.15, Equation 12.16 and Equation 12.17, the pitch control system architecture is concluded. However, in order to optimise the pitch controller for a quick response with little oscillation it is necessary to tune the gains K_q, K_p, K_i and K_d in the controller block. This must be done in the next design iteration using the Control System Tuner toolbox in Matlab.

12.3.3. Conclusion & Recommendations

Several recommendations can be made to advance the design in further design phases. The control model created in Simulink should be developed in more detail. Once a fully working simulation has been created, a joystick can be connected and the behaviour of the UAV can be visually assessed using the FlightGear flight simulator. Currently, no filters have been added, filters should be added to reduce the noise in the system. The disturbances and noise that are present in the model should be modelled in more detail. Besides this, the time delay was ignored in the current model. This should be taken into account to improve the system's response time and eliminate any negative effects that can be caused by time delay. Overall, using robust control principles the system should be designed to be able to handle uncertainties and disturbances. This can be done by using the different Add-Ons in Matlab's Simulink. For example, the control system tuner could be used to tune the gains of the system.

The plasma actuators which are part of the *Physical System* could be improved in several ways. As a result of the wind tunnel test explained in section 8.6 it was observed that control authority is present using the duty cycle as the control variable. However, this was only observed in a specific region of angles of attack. As this is not desirable for the final design improvements should be made in this field of the design. Several plasma actuators could be added at different locations along the trailing edge to increase the control authority range. During the test the peak-to-peak voltage was set at a fixed value due to hardware constraints, however, it is known that changing this parameter is a very effective way of achieving control authority [58]. Therefore this effect should be researched in more detail and design changes might have to be made to allow for this in the final design of the UAV. Besides this, more advanced plasma actuators should be used to improve their performance and allow for better controllability. The current design uses DBD plasma actuators, however, as plasma actuation is a relatively new technology, the advancements made in this field will allow for the use of different types of plasma actuators to be explored. The environmental effects on plasma actuators should also be researched in more detail as these might have an impact on the effectiveness and durability of the plasma actuators. Several parameters that should be investigated are the ambient temperature and humidity.

13 Propulsion

This chapter focuses on the sizing of the propulsion subsystem for the project. Its primary objective is to guarantee that the drone possesses sufficient power throughout all phases of flight. The power source and configuration choice were already decided and a trade-off was conducted [33]. Firstly, the subsystem requirements are listed in section 13.1. Then the assumptions are explained for the methodology used in section 13.2. Next, the method is defined in section 13.3 and finally the results and iterations are discussed.

13.1. Subsystem Requirements

In this section, the requirements pertaining to the propulsion subsystem have been listed. This can be seen Table 13.1

Table 13.1: Propulsion subsystem requirements

Identifier	Requirement	Verification	Compliance
SUB-PRP-01	The propeller shall not damage the structure of the UAV	Demonstration	**PASS**
SUB-PRP-02	The propulsion subsystem shall operate at an ambient temperature between 2.3 and 25 Celcius.	Analysis	**PASS**
SUB-PRP-03	The subsystem shall produce noise lower than 30dBA	Testing	**PENDING**
SUB-PRP-04	The subsystem shall help allow the UAV to climb at a rate of 2.8m/s.	Analysis	**PASS**
SUB-PRP-05	The propulsion subsystem shall cost less than 700 euros.	Demonstration	**PASS**
SUB-PRP-06	The propulsion subsystem shall weigh less than 150g	Inspection	**PASS**
SUB-PRP-07	Subsystem shall be operating optimally between 70 and 86% humidity	Testing	**PENDING**
SUB-PRP-08	Subsystem shall not fail under ultimate load consitions	Analysis	**PENDING**
SUB-PRP-09	The subsystem shall be atleast 80% recyclable my mass	Analysis	**PASS**
SUB-PRP-10	The subsystem will have a minimum thrust resolution of 2.6N	Analysis	**PASS**
SUB-PRP-11	Thrust must be provided with an error less than 0.5%	Testing	**PENDING**
SUB-PRP-12	THe propulsion subsystem must be able to produce a thrust of atleast 6N.	Testing	**PASS**

13.2. Assumptions

For the preliminary design of the propulsion subsystem, the problem was simplified by taking the following assumptions:

- **PRP-01:** For the sizing of the propulsion subsystem, it is considered that there is a continuous cruise flight profile. This is considered to be a valid assumption instead of considering only a gliding flight and a climbing turning flight.

- **PRP-02:** An Electronic Speed Controller(ESC) efficiency of 80% is considered [98]. This is a relatively conservative value and it is only expected to be higher. Hence the value of the power consumed by the propulsion system is conservative.
- **PRP-03:** A motor efficiency of 85%[1] is considered. This is a relatively conservative value and it is only expected to be higher. Hence the value of the power consumed by the propulsion system is conservative.
- **PRP-04:** A wiring efficiency of 99%[2] is considered. A high-efficiency copper wire has been used. The length of the wire has been overestimated and hence the efficiency has also been overestimated.

13.3. Method

This chapter talks about the method that was selected to size the propulsion system. When designing the subsystem it had to be kept in mind that dynamic conditions are different, making static measurements invalid for the sizing. This is the reason why the Advance Ratio of the propeller was considered (J). This is defined as the following:

$$J = \frac{V}{n \cdot D} \tag{13.1}$$

Here, *V* is the velocity, *n* is the rotations per second (RPS) and *D* is the diameter of the propeller.
Initially, the thrust coefficient(C_T) was calculated. This was done using the formula:

$$C_T = \frac{T}{\rho \cdot n^2 \cdot D^4} \tag{13.2}$$

To begin the calculation process, an initial value of RPS is selected, which is used to determine the thrust coefficient. Using the obtained thrust coefficient, we refer to a given figure, labelled as Figure 13.2, to find the corresponding value of a parameter called J. Subsequently, this value of J is utilized in an equation, referred to as Equation 13.1, to calculate a new value for RPS. The process is then repeated iteratively by using the newly calculated RPS value until the RPS falls within a predetermined margin of 2% accuracy. Once the desired accuracy level is achieved for the RPS value, the next step involves determining the efficiency of the propeller using the Advance Ratio. This efficiency is determined by referencing another figure, denoted as Figure 13.2, and extracting the appropriate value based on the Advance Ratio. Finally, we find the required power using Equation 13.3, where P is the power, T is the thrust and V is the Velocity.

$$P = T \cdot V \tag{13.3}$$

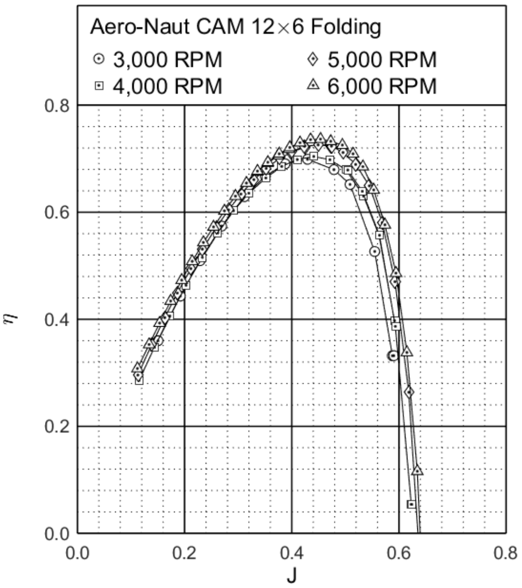

Figure 13.1: Efficiency vs Advance Ratio

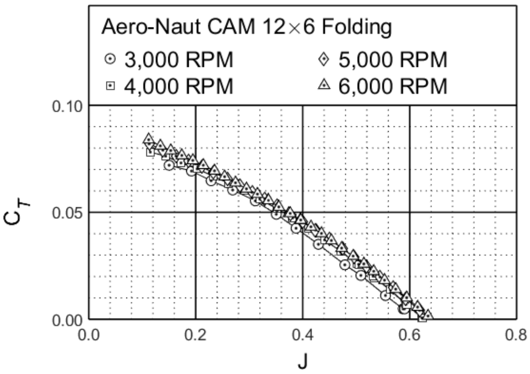

Figure 13.2: Thrust Coefficient vs Advance Ratio

---

[1] tytorobotics.com (Accessed - 14/6/2023)

[2] copper.org (Accessed - 14/6/2023)

In summary, the iterative process involves selecting an initial RPS, calculating the thrust coefficient, finding the corresponding J value, determining a new RPS using the J value, and repeating this process until the RPS value converges within a 2% margin. Once the convergence is achieved, the Advance Ratio is utilized to obtain the efficiency of the propeller from Figure 13.2. A summary of the methodology can be seen in Figure 13.3

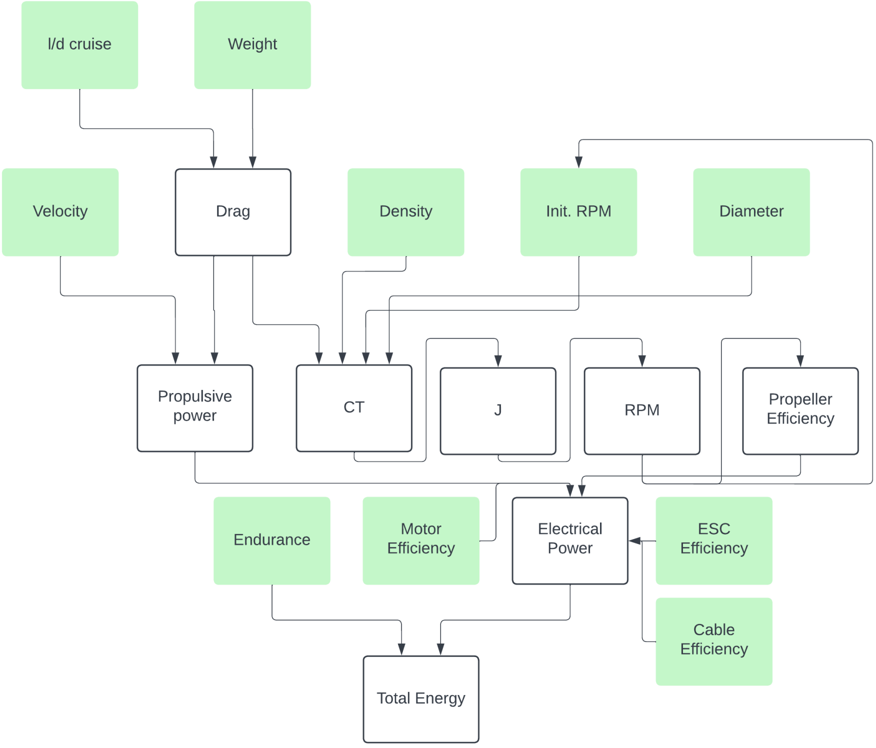

Figure 13.3: Propulsion Subsystem Methodology

13.4. Results and Selection

This section talks about the final values of the propulsion parameters and the selection of the propellers and the motors.

13.4.1. Result

Using the flow described in the previous section, the results of the propulsion system are summarized in Table 13.2

Table 13.2: Propulsion Parameters

Parameter	Value
Thrust(N)	6.86
RPM	7700
Diameter(m)	0.305
J	0.38
CT	0.045
Propeller Efficiency	0.72
Required Power(W)	103.6
Total Energy (Wh)	446.8

13.4.2. Motor and Propeller Selection

Based on the sizing results, an appropriate motor and corresponding propeller are selected. The chosen motor is the SunnySky X3520 V3[3], which aligns with the desired specifications. For this motor, a folding propeller was selected, specifically the Reely Electric Motors Airplane Propeller with dimensions of 12 x 6 inches. A folding propeller is selected such that during the cruise phase of the flight, the propellers can fold in making the structure more aerodynamically efficient. The folding propeller chosen would look something like Figure 13.4.

---

[3] sunnyskyusa.com (Accessed - 14/6/2023)

Figure 13.4: Folding Propeller Example

Overall, the selected motor and propeller combination is well-suited to meet the requirements identified during the sizing process.

13.5. Final Iteration

Following the initial parameters determined in the previous iteration. One final iteration is conducted. In this step, it is seen that the required thrust goes down. This is mainly because of the fact that the L/D during the cruise changed from 14.1 to 19.1 as seen in subsection 7.4.2. The final propulsion parameters can be found in Table 13.3

Table 13.3: Final Propulsion Parameters

Parameter	**Value**
Thrust Cruise(N)	4.354
RPM	7249
Diameter(m)	0.305
J	0.41
CT	0.0285
Propeller Efficiency	0.689
Required Power(W)	65.61
Total energy(Wh)	283.02

Following this, an iteration of the selection procedure is also done. Here it is seen that the motor and propeller combination selected is definitely good enough for the new requirements. Additionally, a lower battery energy capacity is required which is why the size of the battery changes. This can be seen in chapter 15.

14 Avionics

The avionics subsystem deals with the flight controller and additional sensors as well as the telecommunication equipment. First, the subsystem requirements will be listed. Then, the different options for different components such as the telecommunication solution will be created and a final component choice will be made. Finally, the final layout will be presented and discussed.

14.1. Subsystem Requirements

The most important requirements that the subsystem has to fulfil can be seen in Table 14.1. The design options will then be chosen such that they comply with these requirements.

Table 14.1: Avionics subsystem requirements

Identifier	Requirement	Verification	Compliance
SUB-AVC-01	The Avionics system shall be able to transmit all required data over a range of at least 10km	Analysis	PASS
SUB-AVC-02	The Avionics system shall be able to record navigation video	Inspection	PASS
SUB-AVC-03	The Avionics system shall be able to transmit navigation video	Analysis	PASS
SUB-AVC-04	The Avionics system shall be able to transmit telemetry data during nominal operation.	Analysis	PASS
SUB-AVC-05	The Avionics system shall be able to operate between external temperature of 2.5C and 40C	Testing	PENDING
SUB-AVC-06	The Avionics system shall be able to maintain an internal temperature between 0 and 45 Celsius.	Testing	PENDING
SUB-AVC-07	The Avionics system shall be fully compliant with electromagnetic emissions (European EMC standards)	Analysis	PASS
SUB-AVC-08	The Avionics system shall reserve 7 Mb/s for the payload subsystem.	Analysis	PASS
SUB-AVC-09	The Avionics system shall provide a data interface for the payload subsystem.	Inspection	PASS
SUB-AVC-10	The Avionics system shall be able to measure the position in a global frame.	Inspection	PASS
SUB-AVC-11	The Avionics system shall be able to measure the internal temperature	Inspection	PASS
SUB-AVC-12	The Avionics system shall be able to measure the indicated airspeed	Inspection	PASS
SUB-AVC-13	The Avionics system shall be able to measure the pitch angle	Inspection	PASS
SUB-AVC-14	The Avionics system shall be able to measure the roll angle	Inspection	PASS
SUB-AVC-15	The Avionics system shall be able to measure the yaw angle	Inspection	PASS
SUB-AVC-16	The Avionics system shall be able to measure the pitch rate	Inspection	PASS
SUB-AVC-17	The Avionics system shall be able to measure the roll rate	Inspection	PASS
SUB-AVC-18	The Avionics system shall be able to measure the yaw rate	Inspection	PASS
SUB-AVC-19	The system shall be able to estimate its heading in a global frame.	Inspection	PASS
SUB-AVC-20	The system shall be able to estimate its horizontal distance to the operator.	Analysis	PASS
SUB-AVC-21	The Avionics system shall be able to generate a $5\,\mathrm{V}$ burst frequency control signal for the plasma actuators.	Analysis	PASS

14.2. Telecommunications

One of the primary components of the Avionics subsystem is telecommunications. A large number of options are available on the market at vastly different price points and capabilities. Therefore a trade-off has been performed to obtain a suitable communication link that fulfils the stakeholder's needs and requirements at a low cost-, weight- and energy budget impact.

This trade-off is done by first listing the options in a Design option tree and infeasible options are eliminated. Then, these options are combined into three concepts which are then traded off. Finally, a sensitivity analysis is performed in order to investigate the sensitivity of the choice of weights.

14.2.1. Design Options

First, relevant design options have been gathered and visualized in a design option tree which is shown in Figure 14.1. The main requirements from Table 14.1 are the requirement for a communication range of $10\,\mathrm{km}$ from the customer, the data rate for video and payload, and the compliance with the electromagnetic-emission standards of the European Union [99].

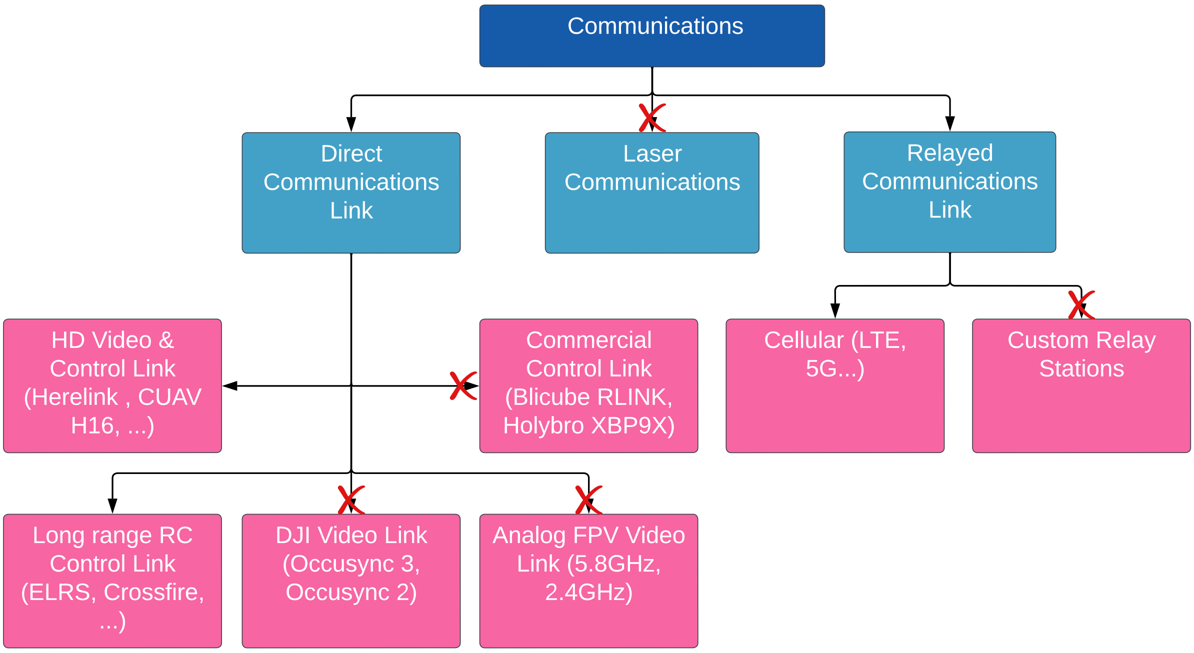

Figure 14.1: Design option tree for the telecommunications system. The crossed-out arrows indicate options that are deemed sub-optimal or unfeasible.

Next, based on these requirements and other factors, the elimination of concepts from the design option tree will be explained.

- **Laser communications**: There are no commercial options available and big problems such as extremely fast and accurate tracking are required on both ground and in the air.
- **Custom Relay Stations**: These are considered infeasible to design and would have to be placed in the flight area before each flight which would increase operational complexity significantly.
- **DJI Video Link**: The maximum range when complying to the EU regulations is 8 km [100] which does not satisfy requirement SUB-AVC-01.
- **Commercial Control Link**: These systems have significantly higher cost over hobby-grade options and are therefore not considered.
- **Analog FPV System**: Analog FPV systems have realtively low quality, and due to EU emmission regulations that limit the power to 25 mW at 5.8 GHz [99] have small ranges in the order of a maximum of an absolute maximum of a low single-digit kilometers with quasi-isentropic antennas.

14.2.2. Concept Generation

From these design options, three concepts are created. These will now be described in detail and later trade-off. All three concepts satisfy the relevant subsystem requirements and void electromagnetic interference due to the plasma since the highest frequency of electromagnetic interference is 50 MHz [1].

Concept 1 - Long range RC Control Link + Cellular

This concept consists of a long-range low data-rate RC telemetry radio and, to provide high data-rate capability for payload and video, an additional cellular connection. The cellular connection alone is considered too low reliability and high latency to be used as a standalone communications link.

The RC radio link was chosen as a TBS-Crossfire since it provides the possibility of telemetry pass-through to the ground station running on a laptop or tablet for data visualization. This makes it possible to monitor things such as UAV position in areas with an unreliable cellular connection. The radio link then connects to Radiomaster TX16s MK2 to allow pilot control. For the cellular connection, an open source project called UAV-cast [1] at 160.9€ was chosen over commercial options such as XB-Link [2] at 646.4€ as the price is significantly lower for similar capability. Additionally, The RaspberryPi companion computer included in this concept also gives a convenient payload interface with USB3 or Ethernet which allows storing of data or other payload control

---

[1] docs.uavmatrix.com

[2] store.xbstation.com (Accessed - 15/6/2023)

tasks by running programs in its Linux operating system. In Table 14.2 an overview of all the components is shown. The cost relates to the cost of telecommunications for two UAVs and a ground station.

Table 14.2: Component breakdown of concept 1 for telecommunications.

Components	**Weight** [kg]	**Cost (Total)** [€]	**Energy** [W h]
RasbPi 4B	0.046	150	6
Crossifre RX	0.003	55.66	0.8
Huwaei E3372h-153	0.05	159	7
TX16S MK2	-	230	-
Crossifre TX	-	193.91	-
Arducam 12MP	0.004	55.8	2.5
Cellular Contract	-	150	-
Total	**0.103**	**994.37**	**16.3**

Concept 2 - HD Video & Control Link

This concept consists of a long-range, high data-rate link which includes a video transmission system and a ground controller usually running the Android operating system. The chosen system is Herelink which has a range of 12 km [**herelink**] and an Ethernet interface for the payload. In Table 14.3 an overview of all the components is shown.

Table 14.3: Component breakdown of concept 2 for telecommunications.

Components	**Weight** [kg]	**Cost (Total)** [€]	**Energy** [W h]
Herelink	0.098	1685	8
Hawkeye - Herelink Cam 4k	0.04	373.72	6
Total	**0.138**	**2058.72**	**14**

Concept 3 - HD Video & Control Link + Cellular

This concept consists of the same HD Video & Control Link as described in section 2. In addition, to increase the range to virtually unlimited range and provide a convenient payload interface, a Cellular connection in the form of a UAVCast is included. In Table 14.4 an overview of all the components is shown.

Table 14.4: Component breakdown of concept 3 for telecommunications.

Components	**Weight** [kg]	**Cost (Total)** [€]	**Energy** [W h]
RasbPi 4B	0.046	150	6
Huawei E3372h-153	0.05	106	7
Herelink	0.098	1685	8
Hawkeye - Herelink Cam 4k	0.04	373.72	6
Total	**0.234**	**2314.72**	**27**

14.2.3. Trade-off

Finally, the trade-off can be performed. In Table 14.5 the five chosen criteria can be seen. The weight of these components will later be varied in the sensitivity analysis. Then, the options are scored and the result is computed. This results in concept 1 being chosen as can be seen in Table 14.6.

Table 14.5: Telecommunication trade-off criteria weight and justification

Criterion	**Weight**	**Explanation**	**Weight Justification**
Mass	10	The total weight of the telecommunication system on the UAV.	The relative mass of the communication system is small.
Cost	25	The total cost of the system, including the ground station.	The budget is constraining and the cost of the telecommunication system can be a significant part.
Range	15	How much range is the most limiting aspect the telecommunication system provides.	All options satisfy the range requirement of 10km, therefore the range would only be additional capability.
Energy	15	The total power drawn by the telecommunication system on the aircraft.	The power draw of the communication system is comparatively small.
Reliability	35	How reliably the link keeps connection, includes things such as cellular coverage gaps and obstruction by buildings.	High importance as continuous radio communication is important for safety and navigation

Table 14.6: Trade-off summary table for the telecommunication trade-off

Concept	Telecommunication					Result
	Mass	Cost	Range	Energy	Reliability	
	10	25	15	20	30	100
Concept 1	8	6	10	8	6	72.0
Concept 2	7	3	6	8	9	66.5
Concept 3	5	2	10	5	9	62.0

Additionally, a trade-off analysis was performed. This was done by varying the weights 10%, 20% and 30%. This resulted in no changes in the selected option and thus the trade-off is concluded to be non-sensitive and concept 1 will be used.

14.2.4. Remote-ID

From the 1st of January of 2024 remote-ID is required for the operation of drones [101]. This allows ground personnel to identify the operator of drones aiding law enforcement officers. As the drone would most likely be operated after this date, this system is deemed essential to be implemented to allow operations. Thus a Remote-ID module has to be integrated on the Drone. For this the DroneBeacon Db203can[3] is chosen. It is an ESP32 based system and connects via DroneCAN to the Pixhawk6X. It consumes about 0.5 W of power, weighs5 g and is fully certified for Remote-ID regulations in the European Union.

14.3. Flight Controller

The flight controller is one of the most crucial components of the UAV. It has to process sensor data and execute the GNC algorithm. As a total flight controller failure almost certainly leads to mission failure and thus reliability is very important.

A number of options were considered for the flight controller. These are using a Commercial Off-The-Shelf (COTS) controller, using a general-purpose computer such as a Rasberry Pi, or a self-designed flight controller. Of these options, only the COTS solution is considered favourable and feasible in the timeframe of the project.

Thus, reliable and well-established in the consumer range to limit cost were explored. There are a huge number of autopilot options in both closed- and open-source available. For a wide range of them, data availability is scarce and information on reliability even more so. Thus a well-established autopilot, the Standard Set of the Pixhawk 6X by Holybro was chosen[4], as it fulfils the requirements, is situated in the more professional side of the consumer market at 500€ and is a well-known brand with a good reputation. Other options that were considered were more hobby-oriented flight controllers at around 100€, but ultimately it was decided against them due to reliability concerns, as the flight controller is one the most critical components.

---

[3] dronescout.co (Accessed - 15/6/2023)

[4] holybro.com (Accessed - 15/6/2023)

The Pixhawk6X can run both Ardupilot[5] aswell as PX4[6] which are popular ope source autopilots. These can satisfy all the requirements set by the customer and have extensive documentation available online.

14.4. Sensors

The last set of components that have to be selected for the Avionics system are sensors. A number of requirements deal with the environmental aspects that the sensor system has to measure. Subsystem requirements SUB-AVC-13 to SUB-AVC-18 are all satisfied by the redundant Inertial Measurement Units (IMU) in the Pixhawk 6X. Additionally, the Pixhawk 6X possesses internal temperature sensors and thus SUB-AVC-11 is satisfied as well.

Four relevant requirements remain that have to be measured by dedicated components, these are SUB-AVC 2, 10, 12, and 19, requiring a video camera, GPS, a pitot tube, and a compass respectively.

- **SUB-AVC-02 - Camera:** It was decided that for navigation and safety purposes the UAV shall have a navigation camera, especially for optional BVLOS operation. Considering our chosen Cellular communication system which will transmit the video via UAV-cast [7]. The project recommends Logitech USB cameras or a Raspberry Pi camera module. To give good situational awareness, a high field of view RasberryPi camera module with a fixed focus, the Arducam 12MP IMX708 $102°$[8], has been chosen.
- **SUB-AVC-10 & SUB-AVC-19 - GPS:** This requirement originates directly from the customer. A large number of GPS modules are available for UAV applications. The DroneCAN M8N GPS[9] has been chosen as the manufacturer Holybro is well established and the module includes a UBlox NEO M8N and communicates over a special CAN bus protocol called DroneCAN. The module also allows simultaneous communication with up to 3 GNSS Constellations choosing from GPS, Galileo, Glonass, and BeiDou for additional reliability and accuracy. This module also includes a compass satisfying an additional requirement.
- **SUB-AVC-12 - Pitot-Tube:** This requirement originates from the control system. Again, a well-established manufacturer (Mateksys) component ASDP-4525[10] has been chosen. The sensor communicates over I2C as this version is significantly cheaper than the DroneCAN version.

14.5. Description of Final Design

In the previous sections, all relevant components have been selected. A completed list of components can be seen in Table 14.7. Additionally, for future system budgeting, 100 g of wiring is also included as a conservative estimate.

Table 14.7: A list of the selected Avionics components.

Component	**Function**	**Mass** [g]	**Power** [W]	**Energy** [W h]	**Cost** [€]
Pixhawk 6X	Flight Controller	74	3	6	391.35
ASPD-4525	Pitot Tube	25	0.025	0.05	6
M8N GPS	GNSS + Compass	36	1	2	42.98
TBS Crossfire Micro V2	RC Receiver	3.23	0.095	0.8	32.43
Rasberry Pi 4B	LTE Communication	46	3	6	75
E3372h-153	LTE Modem	50	3.5	7	53
Arducam 12MP	Navigation Camera	4	1.25	2.5	30
DroneBeacon Db203can	Remote-ID	5	0.5	1	64
Avionics Wiring	Connect Components	100	0	0	30
Total		**343.23**	**12.37**	**25.35**	**724.76**

All the components are only required once for each UAV and the budgets shown here are thus the numbers for a single UAV. To visualize how these components are connected, a block diagram has been created which is shown in Figure 14.2. The GPS port identifier signifies a proprietary Holybro connector that includes power and data transfer over UART. The MAVLink telemetry is an open source messaging protocol both for communicating with drones but also for communication between onboard drone components[11].

---

[5] ardupilot.org (Accessed - 20/6/2023)

[6] px4.io (Accessed - 20/6/2023)

[7] github.com (Accessed - 15/6/2023)

[8] arducam.com (Accessed - 15/6/2023)

[9] holybro.com (Accessed - 15/6/2023)

[10] mateksys.com (Accessed - 15/6/2023)

[11] mavlink.io - (Accessed - 15/6/2023)

The diagram also includes the two servos used to actuate the parachute and airbag latches, as it was deemed unnecessary to include a stand-alone diagram for such a small system. The layout for the complete electrical system including the Electrical Power System and the HV PLasma generation system can be seen in chapter 17.

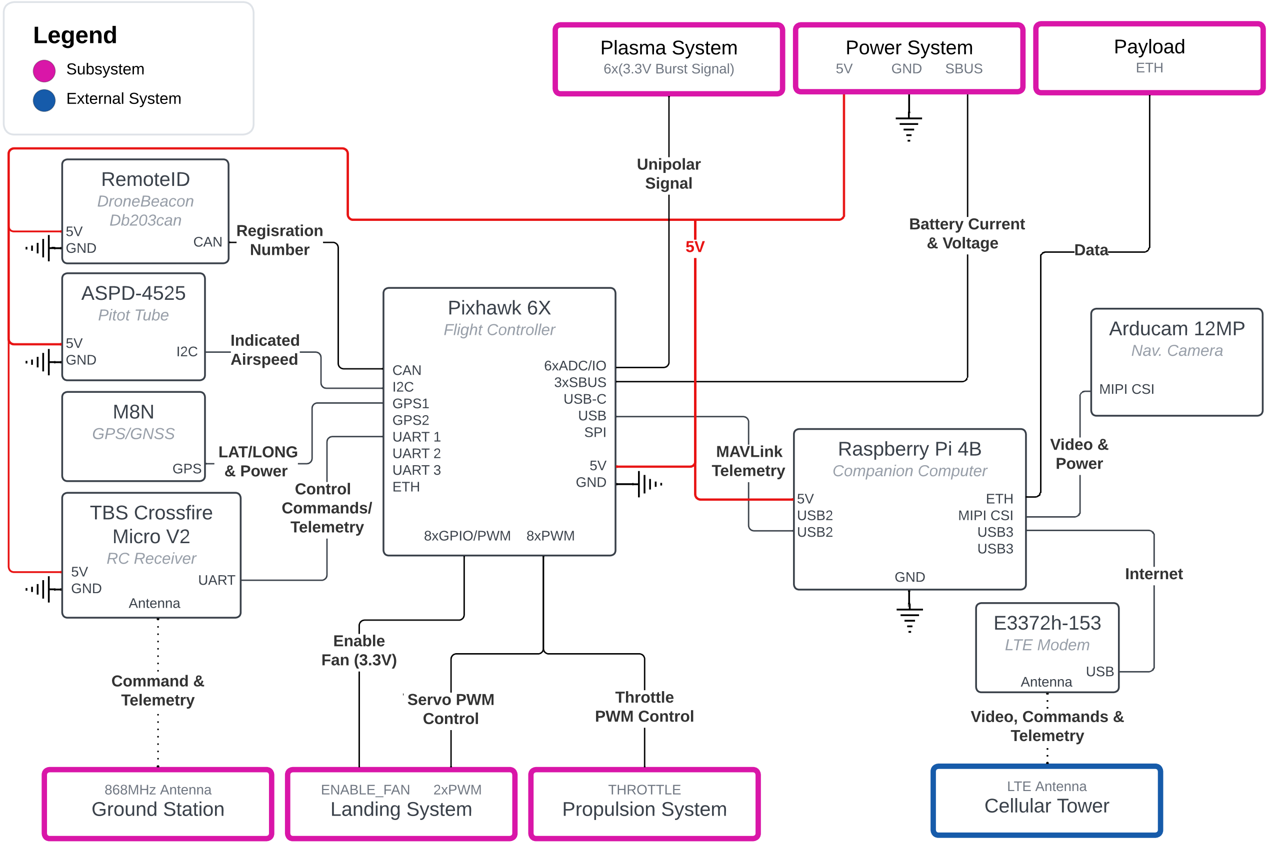

Figure 14.2: Electrical Block Diagram for the Avionics Sub System

14.6. Conclusion and Recommendations

The presented system layout is expected to satisfy all the requirements that the customer imposed on it. In addition to that, it also provides a navigation vide- feed and future-proofing items such as the RemoteID component. Additionally, the RaspberryPi companion computer gives a convenient payload interface with USB3 or Ethernet which allows for storing data and other payload administration tasks. The design of the telecommunications system, especially the cellular component, might require a relatively high amount of effort to configure but should perform similarly to much more expensive COTS systems.

In this class of UAV, a large amount of avionics components are available commercially. This presents certain challenges in selecting ideal components but also means prices are low and information availability is high. As all components are chosen from reputable companies, the reliability is expected to be high.

As with any system that requires multiple components, an integrated system test should be performed to verify that all components work together well. This is especially important for interference, to which GPS Receiver can be susceptible, as it is hard to predict.

Additionally, in the preliminary fuselage internal configuration seen in chapter 17, the Avionics component layout can be seen. An important thing to verify for this is, that this provides ample cooling through NACA airducts and the components are not too closely packed. However, as this is a complex interdisciplinary problem, this should be tested by monitoring the UAVs internal temperature during initial flights.

15 Electrical Power System

The Electrical Power System (EPS) subsystem deals with providing the components of the aircraft with the necessary power and energy to complete their function over the two-hour flight time. In the initial trade-offs, it was determined that the main power source will be a battery. In this chapter, the components will be chosen and the architecture of the subsystem presented. First, the subsystem requirements will be listed. Then, the different options for the battery chemistry will be selected and a final component choice will be made. Next, the power distribution board will be selected and then the final layout will be presented and discussed.

15.1. Subsystem Requirements

The most important requirements that the subsystem has to fulfil can be seen in Table 15.1. The design options will then be chosen such that they comply with these requirements.

Table 15.1: EPS subsystem requirements

Identifier	Requirement	Verification	Compliance
SUB-EPS-01	The EPS shall provide sufficient power for the system's peak power condition.	Analysis	PASS
SUB-EPS-02	The EPS shall provide a 12 V, 3 A connection for the payload.	Analysis	PASS
SUB-EPS-03	The EPS shall provide 5 V at sufficient amperage for the avionics.	Analysis	PASS
SUB-EPS-04	The EPS shall provide sufficient energy capacity for the systems 2 hour endurance.	Analysis	PASS
SUB-EPS-05	The battery capacity shall have 10% margin to allow for unusable capacity.	Analysis	PASS
SUB-EPS-06	The battery capacity shall have 10% margin to allow for power consumption prediction uncertanties.	Analysis	PASS
SUB-EPS-07	The EPS shall not overheat or catch fire.	Test	PENDING
SUB-EPS-08	The EPS shall provide sufficient amperage at the desired voltage to the HV Plasma system.	Analysis	PASS
SUB-EPS-09	The EPS shall be able to measure its total power consumption.	Test	PENDING
SUB-EPS-10	The EPS shall be able to measure the battery voltage.	Inspection	PASS

15.2. Battery

The battery is the primary component of the UAV's power system. It has to provide energy for the two-hour endurance and be able to satisfy the system's peak power draw during all flight phases. It is also one of the heaviest components of the UAV at about a quarter of the weight. Therefore reducing the weight by selecting a suitable battery chemistry is paramount.

15.2.1. Battery Chemistry

A large number of different battery chemistries are available with different advantages and disadvantages. Unsurprisingly, for aircraft the power density $\frac{\text{W h}}{\text{kg}}$ plays the most pivotal role. The highest energy density battery chemistries from Townsend et al. [102] are shown in the following list and their viability is discussed. As is common with battery technology, there are also a lot of not yet commercially available options that promise power densities of $500\,\frac{\text{W h}}{\text{kg}}$[1] and more. However, these options are not yet commercially available and are thus not considered viable.

- **Li-Ion** - 100-265$\frac{\text{W h}}{\text{kg}}$ - Li-Ion Batteries have a long cycle-life, relatively high energy and power density and are able to deliver at a relatively high price. [102]
- **Li-Po** - 100-265$\frac{\text{W h}}{\text{kg}}$ - These are similar to Li-Ion batteries but have a polymer electrolyte instead of a liquid. Typically they have lower energy densities but higher discharge ratings[2]. [102]
- **Zn-O$_2$** - 442$\frac{\text{W h}}{\text{kg}}$ - These have low cell voltages at 1.4 V and the high energy densities are mostly achieved for non-rechargeable versions. Additionally, these batteries are not yet available on the market. [102]
- **Li-Air** - 11140$\frac{\text{W h}}{\text{kg}}$ - These batteries can offer drastically higher energy densities than Li-ion but have several disadvantages. These are very limited charging cycles, poor safety, and no commercial availability. [102]
- **Li-SOCl** - 500-700$\frac{\text{W h}}{\text{kg}}$ - Very low power density at $18\,\frac{\text{W}}{\text{kg}}$ and poor market availability. [102]

---

[1] catl.com (Accessed - 19/6/2023)

[2] makeuseof.com (Accessed - 20/6/2023)

15.2.2. Component Selection

This essentially only leaves two realistic options at this scale of UAV, Li-Ion and Li-Po. These are readily available commercially in multiple different capacities. In this case, the choice is made simply on a battery that can satisfy the requirements at the lightest weight. The relevant requirements for the batteries are listed below.

- Minimum Rated Capacity = $\frac{390.6\,\mathrm{W\,h}}{90\%\cdot 90\%} = 482.22\,\mathrm{W\,h}$
- Minimum Power = $1866\,\mathrm{W}$

Additionally, if the battery is chosen between $15\,\mathrm{V}$-$35\,\mathrm{V}$ no additional switching converter is needed. This conveniently allows for a six cells in series (6S) Li-Ion battery at a nominal voltage of $22.2\,\mathrm{V}$ resulting in a required capacity of $\frac{482.22\,\mathrm{W\,h}}{22.2\,\mathrm{V}} = 21.72\,\mathrm{A\,h}$ which can be reached by a commonly available $22\,\mathrm{A\,h}$ 6S battery. For multi-copters, Li-Po batteries are often chosen since they are dependent on the high discharge rating to satisfy the power draw of multiple motors. However, the required power is easily achievable by Li-Ion batteries which typically offer higher energy densities.

The highest energy density Li-Ion candidate that could be identified was the TDrone Ares 6S $22\,\mathrm{A\,h}$ at a price of 640€, a mass of $1940\,\mathrm{g}$, energy of $488.4\,\mathrm{W\,h}$, full capacity for 300+ charge cycles, and a C-Rating of 5[3]. This battery uses a relatively new semi-solid state electrolyte, allowing for the energy density of $250\,\frac{\mathrm{W\,h}}{\mathrm{kg}}$ to approach the maximum stated by Townsend et al. of $260\,\frac{\mathrm{W\,h}}{\mathrm{kg}}$ [102], which is significantly higher than other Li-Po drone batteries available. As it satisfies all the requirements, this battery is chosen in this stage of design. If the weight increases in later stages of design, this choice might have to be revisited and a different battery such as the $27\,\mathrm{A\,h}$ of the same battery might have to be chosen.

15.3. Power Distribution Board

The Electrical power system has to satisfy a number of requirements which can not be satisfied by the battery alone. These are listed below.

- A $12\,\mathrm{V}$, $3\,\mathrm{A}$ output for the payload.
- A $5\,\mathrm{V}$, $2.6\,\mathrm{A}$ out for the Avionics.
- The EPS has to measure its total power consumption.
- The EPS has to measure the battery voltage.

The $5\,\mathrm{V}$ and $12\,\mathrm{V}$ outputs require voltage regulation from the battery voltage of $22.2\,\mathrm{V}$. This should be done by switching (buck) converters as simple voltage regulators would waste large amounts of energy.

15.3.1. Component Selection

In conjunction with the component choice of the Pixhawk6X in chapter 14 the power distribution board Holybro PM03D[4] is chosen as it satisfies all the requirements imposed on it. It has integrated $5\,\mathrm{V}$, $3\,\mathrm{A}$ and $12\,\mathrm{V}$, $3\,\mathrm{A}$ switching converters and a battery voltage and current sensing capability which can be connected to the Pixhawk6X over I2C.

15.3.2. Estimated power consumption

Switching converters are significantly more efficient than simple voltage regulators and be often over 90% efficient [5]. In this case, they are assumed 90% efficient. Using this the power consumption of the PM03D can be calculated. The power consumption of the payload system is known to be $17\,\mathrm{W}$ at $12\,\mathrm{V}$ and for the avionics $12.37\,\mathrm{W}$ $5\,\mathrm{V}$ as seen in Table 14.7. Therefore, using Equation 15.1, the power losses for the PM03D are estimated to be $3.26\,\mathrm{W}$.

$$P_{dissipated} = P_{out} \cdot \left(\frac{1}{\eta_{\text{conversion}}} - 1 \right) \tag{15.1}$$

15.4. Description of Final Design

In the previous sections, all relevant components have been selected. A completed list of components can be seen in Table 15.2. Additionally, for mass budgeting, $100\,\mathrm{g}$ of high current 12AWG wiring, mainly for the wiring to the ESC and motor, is also included.

---

[3] 3dxr.co.uk (Accessed - 20/6/2023)

[4] holybro.com (Accessed - 20/6/2023)

[5] en.wikipedia.org (Accessed - 20/06/2023)

Table 15.2: A list of the complete list of selected Electrical Power System components.

Component	**Function**	**Mass** [g]	**Power** [W]	**Energy** [W h]	**Cost** [€]
TDrones Ares 22Ah 6S	Battery	1940	-	-	641.38
PM03D	Power Management PCB	59	3.21	6.42	48.07
12AWG Silicon Wire	High Current Wiring	100	-	-	20
Total		**2099**	**3.21**	**6.42**	**709.45**

It should be noted that the efficiency losses of the wiring, which are expected to be very low, are included in the propulsion system design. Finally, an electrical block diagram is shown in Figure 15.1. The battery is connected to the power management board, which measures the battery voltage and the total current usage through a sense resistor. Together with the known capacity of the battery the remaining flight time of the battery can be estimated from this data.

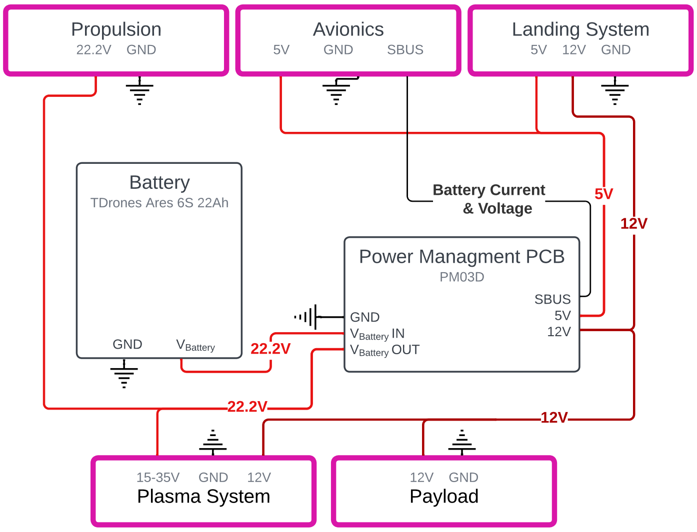

Figure 15.1: Electrical Block Diagram for the Power Sub System

16 Landing and Ground Support systems

In phase C[33], it was determined that conventional runway take-off and landing are not viable for the P.U.L.S.E. Drone design. As such, the designs of alternative landing and take-off methods are explored in this chapter. The landing system consists of a parachute and an airbag and is designed in section 16.1, whilst the catapult used for the take-off is chosen in section 16.2. Lastly, the ground station design is covered in section 16.3.

16.1. Landing

The landing system is essential to the function of the system. A reliable and safe landing system is required for the operation of the UAV. This becomes especially important when considering operations over urban areas. As the UAV has a considerable weight of ≈ 8.5 kg, reducing the speed during a system failure is essential. Thus a parachute system has been chosen in the preliminary trade-off.

16.1.1. Subsystem Requirements

The most important requirements that the subsystem has to fulfil can be seen in Table 16.1. The design options will then be chosen such that they comply with these requirements.

Table 16.1: Landing system Requirements

Identifier	Requirement	Verification	Compliance
SUB-LND-01	The Parachute shall be able to decelerate the aircraft to 5 m/s or lower on touchdown.	Analysis	PASS
SUB-LND-02	The system shall be able to be forced to perform an emergency landing by the operator during all flight phases.	Testing	PENDING
SUB-LND-03	The system shall be able to land within the designated test area.	Testing	PENDING
SUB-LND-04	The system shall be able to perform emergency landings autonomously.	Analysis	PASS
SUB-LND-05	The system shall be able to land without causing any subsystem failures.	Testing	PENDING
SUB-LND-06	The parachute system shall not interfere with the UAVs mission.	Inspection	PASS
SUB-LND-07	The aircraft shall land horizontally.	Analysis	PASS
SUB-LND-08	The parachute ejection mechanism shall not use consumables.	Inspection	PASS
SUB-LND-09	The minimum height at which the system shall be able to safely land is 50m.	Testing	PENDING
SUB-LND-10	The landing system shall enable safe landing during operations over an urban area.	Inspection	PASS

16.1.2. Parachute Selection

To reduce design effort, it has been decided to select a COTS solution for the parachute system. There are few parachute systems for fixed-wing aircraft available that are rated for weights close to the MTOW of ≈ 8.5 kg. The only suitable system that could be identified has been selected, a ready-made system rated for a ≈ 10 kg UAV by the company FruityChutes[1] has been selected. The parachute bundle includes a pilot parachute for ejection, has a total mass of 650 g, a drag coefficient C_D of 2.2, and has a diameter of 2.13 m.

A parachute's effectiveness significantly decreases the slower the descent speed is. Thus, most parachute landing systems still have considerable speeds of $5\,\frac{\text{m}}{\text{s}}$-$10\,\frac{\text{m}}{\text{s}}$ during touchdown [103].

Using Equation 16.1 a descent speed of $4.36\,\frac{\text{m}}{\text{s}}$ can be calculated. This results in impact energy of 81.8 J. These values are considered too high to be absorbed by the structure during landing impact repeatedly. Thus an impact energy-absorbing system has to be included. This is commonly an airbag system [104, 105, 106, 107]. A simple servo-actuated hatch is chosen. The opening of this hatch will lead to the pilot parachute being pulled out by the airflow which is the intended design for this product.

$$V_{descent} = \sqrt{\frac{m \cdot g}{0.5 \cdot C_D \cdot \rho \cdot S}} \tag{16.1}$$

16.1.3. Airbag Sizing

As mentioned in the previous section, the descent speed has been identified as too high to be absorbed by the structure during landing impacts. Thus the design of an airbag has been conducted that reduces the landing acceleration to the maximum load factor the UAV is designed for during normal operation. This eliminates the need for any additional structural considerations resulting from the ground impact. This airbag consists of a ripstop nylon skin which is inflated by a fan during descent. There are multiple theoretical design resources [107, 108] as well as simulation approaches in ANSYS LSDYNA [109] available to model landing accelerations. Due to the computational resources required, during this stage of design, a theoretical approach has been chosen to allow rapid design iteration.

The approach described in Zhou et al. [107] has been followed. This approach follows theoretical work outlined by Browning [108] where a number of assumptions are listed.

- **AIRB-01:** The UAV is oriented lands vertically.
- **AIRB-02:** The parachute list is neglected.
- **AIRB-03:** No heat transfer during compression.
- **AIRB-04:** The cross-sectional area along the horizontal plane is constant during compression.
- **AIRB-05:** The change of shape of the airbag can be neglected.

---

[1] shop.fruitychutes.com (Accessed 21/06/2023)

The airbag will be situated in the fuselage alone, and the primary force transfer during landing will be through the bottom skin of the fuselage. Thus a rectangular cross-section has been chosen to effectively decelerate the UAV during impact.

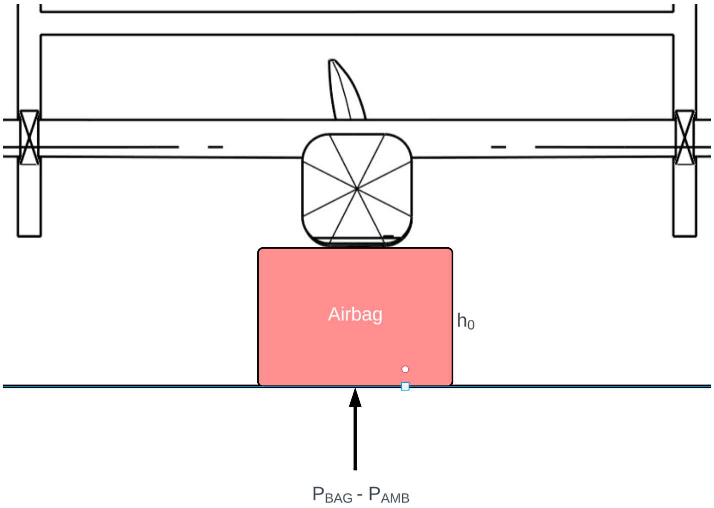

Figure 16.1: Schematic illustration of the UAV Airbag

Using trial and error design and the analysis method described in Zhou et al. [107]. The main design parameters where the airbag height and orifice area. This resulted in the values shown in Table 16.2. The packing density airbag was estimated at $224.9\,\frac{\text{kg}}{\text{m}^3}$ based on FruityChutes[2]. The resulting acceleration can be seen in Figure 16.2. As can be seen, the final velocity is $2.3\,\frac{\text{m}}{\text{s}}$, which is still a 72% reduction in impact energy.

Table 16.2: Airbag Dimensions

Description	**Identifier**	**Value**
Airbag Length	L	0.8 m
Airbag Initial height	h_0	0.5 m
Airbag Width Top	B_1	0.18 m
Airbag Width Bottom	B_1	0.18 m
Orifice Area	A_O	0.016 m^2
Airbag Volume	V_t	0.072 m^2
Airbag Surface Area	S_a	1.27 m^2
Packing Volume	V_p	338.29 cm^2

---

[2] https://fruitychutes.com/files/help/NARCON-2013-Rocketry-Recovery-Technology-Slides.pdf (Accessed 21/06/2023)

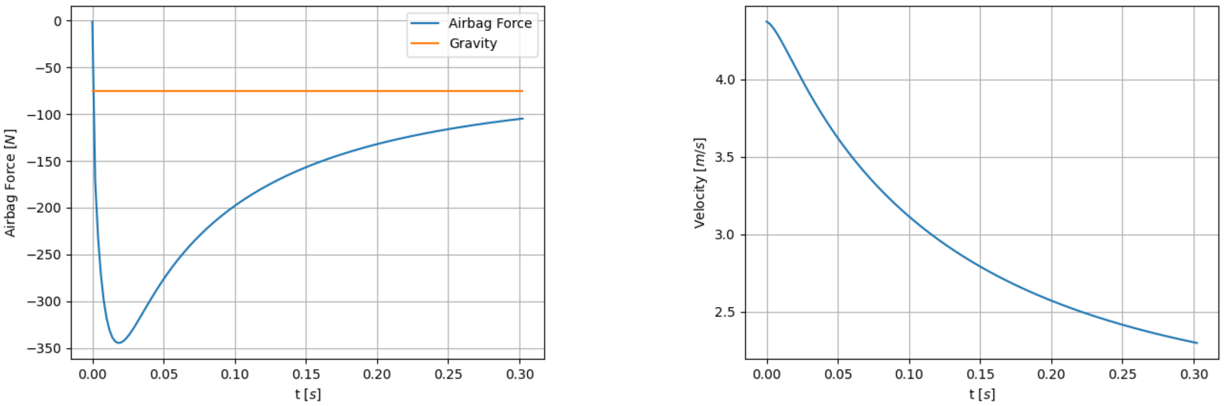

(a) Force exerted on the UAV by the airbag.

(b) Vertical velocity of the UAV after touchdown

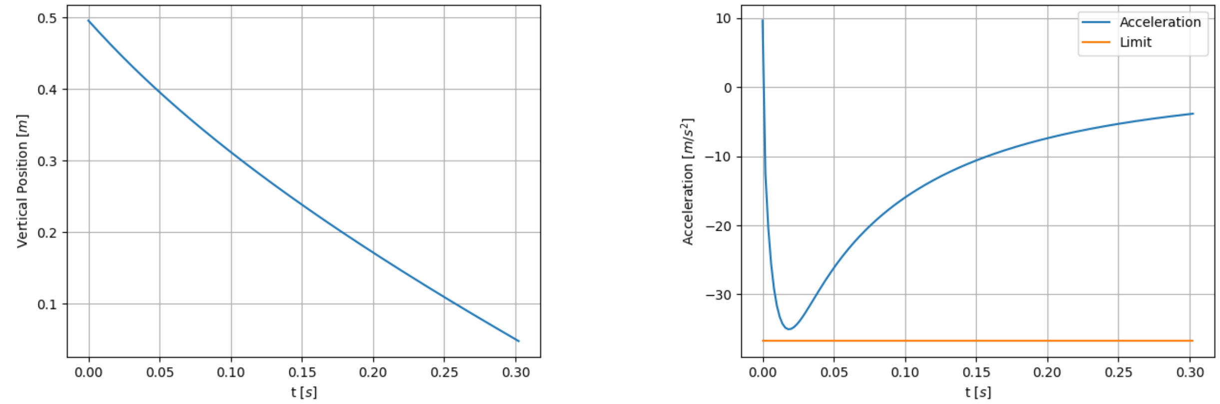

(c) Vertical position of the UAV after touchdown

(d) Vertical acceleration of the UAV after touchdown

Figure 16.2: Various parameters of the UAV during touchdown with the airbag deployed

The airbag deployment is controlled by a fan and servo. Therefore a fan has to be selected. The requirement for this fan is that it inflates the airbag during descent. Assuming that the parachute has decelerated the aircraft to descent velocity at 25 meters, the fan has 5.7 s to inflate the airbag. Thus a fan with a mass-flow of at least $0.013\ \frac{\mathrm{m}^3}{\mathrm{s}}$ is required. For this the EBMPapst 8452/2 H4P is chosen [3]. This fan has a $0.033\ \frac{\mathrm{m}^3}{\mathrm{s}}$ and thus is easily able to inflate the airbag in the required time, allowing a large safety margin should the parachute deploy slowly.

16.1.4. Description of Final Design

A list of components can be seen in Table 16.3. The electrical diagram for the system can be seen in Figure 16.3.

Table 16.3: A complete list of the components of the landing system

Quantity	**Component**	**Function**	**Mass** [g]	**Power** [W]	**Energy** [W h]	**Cost** [€]
1	FWRB-84-S-2P-OB	Parachute	0.65	0	0	566.02
2	9G Servo	Hatch Latches	0.024	2.88	0.088	28
1	Ripstop Nylon 66	Airbag	0.076	0	0	23.8
1	HBm Papst 8452 HP	Airbag Fan	0.105	6.8	0.057	75.44
1	Other Components	Fan transistor etc	0.002	0	0	10
Total			**0.85708**	**9.68**	**0.14**	**703.26**

---

[3] https://www.ebmpapst.com/de/en/products/axial-fans/p/84522H4P.html (Accessed 21/06/2023)

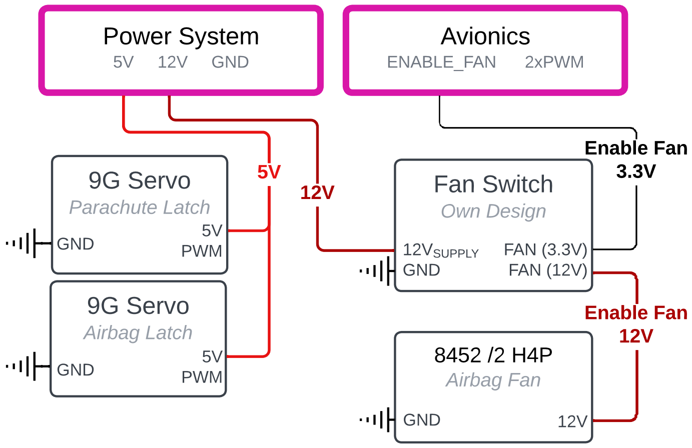

Figure 16.3: Electrial Block Diagram for the Landing System

16.1.5. Conclusion and Recommendations

As a part of this section, the landing system of the P.U.L.S.E. Drone is designed, consisting of two main components - a parachute and an airbag. While the analysis performed in this section resulted in applicable parachute and airbag design, there are several further analysis and design steps that could not be implemented and are instead presented as recommendations.

Firstly, parachute sizing was based entirely on static loads during the descent. However, the deployment of the parachute is expected to produce substantial shock loads. These shock loads should be determined and the supporting structure reinforced appropriately to ensure that the UAV structure can land without damaging the structure or severing parachute cables. Several methods exist for parachute shock estimation, such as the one presented in [110].

Additionally, there is a possibility that wind gusts will drag the parachute along the ground after landing, possibly leading to critical damage to the drone. As such, a mechanism to remotely disconnect the parachute after landing should be designed and implemented.

Moreover, the airbag analysis performed in this section assumed a perfectly vertical landing. It is clear that such a landing can not be feasibly replicated in real-life environments, and as such it is recommended that airbag-drone stability is analysed. This would provide a range of angles at which the UAV can land safely, and would further affect the landing system and structural design.

Lastly, an extensive testing series for the landing system, utilising equivalent weights and accelerometers, is recommended to validate assumptions and design choices made.

16.2. Take-Off

This section discusses the Take-Off subsystem of the P.U.L.S.E. drone specifically designed for the chosen mission. After careful consideration and trade-offs evaluated in the conceptual trade-off, it became evident that a catapult launch was the optimal choice. The primary reason for selecting this launch method is its superior reliability and accuracy. Catapults can either be bought off the shelf or be built in-house. Due to simplicity and the constraints of the DSE, it was decided to buy it off the shelf.

16.2.1. Requirements

Table 16.4 is a table that summarises the subsystem requirements of the take-off subsystem.

Table 16.4: Launcher Requirement

Identifier	Requirement	Verification	Compliance
SUB-TO-01	The Launcher shall launch the drone at a velocity higher than the stall speed	Analysis	PASS
SUB-TO-02	The Launcher shall cuz any damage to the structure of the drone	Demonstration	PENDING
SUB-TO-03	The Launcher shall be lighter than 35 kilograms	Inspection	PASS
SUB-TO-04	The Launcher shall be at least 90% reliable	Testing	PASS
SUB-TO-05	The Launcher shall be cheaper than €10000.	Inspection	PASS

16.2.2. Launcher Selection

Based on the subsystem requirements explained in Table 16.4, a catapult was chosen. The chosen catapult was the Elevon X [4]. This launcher has a maximum launcher energy of 1000 J. Using this, the maximum take-off velocity of the drone can be calculated.

$$V = \sqrt{\frac{LE}{0.5 \cdot m}} \tag{16.2}$$

Using Equation 16.2, where LE is the launcher energy, m is the mass of the drone and V is the launch velocity, the launch velocity of the drone due to the launcher can be calculated. This turns out to be 15.375 m/s. This value is just greater than the cruise velocity which implies that this catapult is perfectly optimised for the mission. The catapult also has a track length of 2.4 m. Finally, the catapult costs €5760 which fits the budget.

16.3. Ground Station

To facilitate control of the aircraft, a ground control station is needed as the aircraft is unmanned. This is closely related to the choices made in the Avionics chapter 14 and the component selections have been made in this section already. In addition to the components selected in this section, two options for the ground control software are introduced.

16.3.1. Subsystem Requirements

The most important requirements that the subsystem has to fulfil can be seen in Table 16.5.

Table 16.5: Ground Station Requirements

Identifier	Requirement	Verification	Compliance
SUB-GSS-01	The Ground Station shall be able to transmit commands over a range of at least 10km	Analysis	PASS
SUB-GSS-02	The ground station shall be able to transmit relevant pilot commands at a sufficient update rate.	Testing	PENDING
SUB-GSS-03	The ground station shall be fully compliant with electromagnetic emissions (European EMC standards)	Analysis	PASS
SUB-GSS-04	The ground station shall be able to display all required telemtery data	Inspection	PASS
SUB-GSS-05	The ground station shall be able to display aircraft position	Inspection	PASS
SUB-GSS-06	The ground station shall have a standard RC pilot control interface with at least 2 joysticks	Inspection	PASS
SUB-GSS-07	The ground station software shall allow mission planning using waypoints	Inspection	PASS
SUB-GSS-08	The pilot control interface shall be able to operate without external power for at least 2.5 hours	Testing	PENDING

16.3.2. Components and Electrical Layout

In chapter 14 component choices for the selected telecommunications system have been made. These are considered sufficient for the current design stage. A completed list of components can be seen in Table 16.6. In this case, power, energy and mass are not included, since these are only relevant for UAV system budgeting, which the ground station does not affect. The laptop or tablet has to be supplied by the operator and thus their cost is not included.

Table 16.6: A list of the selected Ground Station components.

Component	Function	Cost [€]
E3372h-153	LTE Modem	53
TX16S MK2	Remote Control	230
Crossfire TX	Transmitter Ground	193.91
Laptop/Tablet	Run Ground Control Software	-
Total **12.37**	**25.35**	**476.91**

As ground station software, two commonly available ground control software are available that satisfy the requirements. These are two open source software packages, MissionPlanner[5], which runs on laptops, or

---

[4] elevonx.com (Accessed - 21/6/2023)

[5] https://ardupilot.org/planner/ (Accessed - 21/06/2023)

QGroundControl[6] which can run on both tablets and laptops. Both these options can plan UAV missions via waypoints, display the current UAV position, show the navigation video and have many additional capabilities.

Finally, an electrical block diagram is shown in Figure 16.4. As can be seen, the crossfire radio receiver has the capability of sharing MAVLink telemetry over WiFi with the ground station computer. This allows redundant mission monitoring of the UAV.

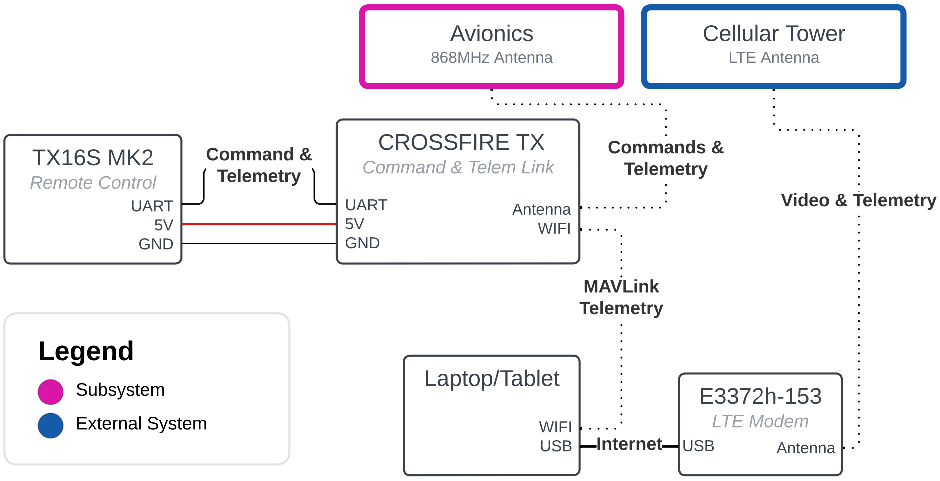

Figure 16.4: Electrical Block Diagram for the Ground Station System

17 Final Design

This chapter aims to give a general overview of the final design that flows from the designed subsystems in previous chapters. The layouts of the different structural and electrical components are briefly discussed. Furthermore, overall geometry is shown and a final design impression is depicted.

17.1. External design

The final design consists of a high-wing double boom configuration. The fuselage adopted a square cross-section with circular edges including a nose and tail cone. Regarding the wing, a segmented design was carried out. The root part consists of a rectangular planform extending to the middle part of the wing where the tapered section is situated. The wingtip, the third section of the wing, contains the control surfaces. The main wing is connected to the empennage with a set of rectangular booms. The overall dimensions of the UAV are depicted in figure 17.1.

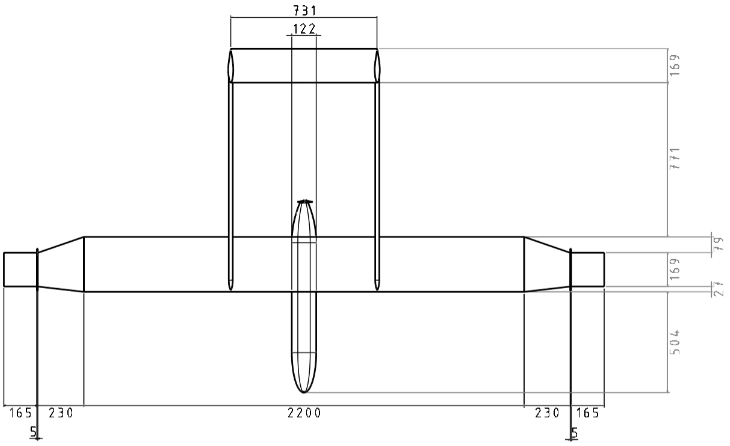

Figure 17.1: Design dimensions

---

[6] http://qgroundcontrol.com/ (Accessed - 21/06/2023)

An impression of the UAV operating in its designated environment is shown in figure 17.2

Figure 17.2: Final design impression

17.2. Internal design

Regarding the internal design of the fuselage, the configuration can be summarised as is done in figure 17.3. The different numbered components are listed in table 17.1.

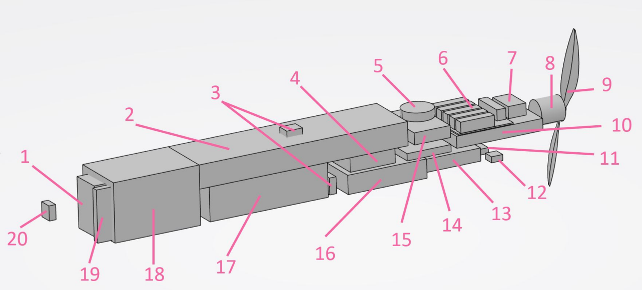

Figure 17.3: Fuselage internal layout

Table 17.1: Fuselage components

Component	Name	Function
1	Rasberry Pi 4B	LTE Communication & Payload Interface
2	FWRB-84-S-2P-OB	Parachute
3	9G Servo	Parachute and airbag Hatch Latch
4	8452 /2 H4P	Airbag Fan
5	M8N GPS	GNSS + Compass
6	DAR70575-HR (x6)	HV Relay
7	Turnigy Plush-32 80A	Control power to motor
8	SunnySky X3520 V3 KV560	Motor
9	12x6 folding AEROnaut CAM	Provide thrust
10	Minipuls RM10	HV Cascade
11	TBS Crossfire Micro V2	RC Receiver
12	ASPD-4525	Pitot Tube
13	Pixhawk 6X	Flight Controller
14	PM03D	Power Management PCB
15	Minipuls Control	HV Control Board
16	Riptop Nylon 66	Airbag
17	UnmannedRC 22Ah 6S	Battery
18	Payload	Payload space
19	E3372h-153	LTE Modem
20	Arducam 12MP	Navigation Camera

17.3. Aerodynamic analysis

To validate the use of the PULSE drone with the mission description, the advantages of the drone using plasma technology have to be verified. For this, CFD analysis using Ansys Fluent was used. The solution shown in Figure 17.4 is a time-averaged model using k-omega SST viscous model and broadband noise sources acoustic model, note that this simulation had to be completed without the control sections since it returned to be a problematic geometry (this will be reanalysed for the final submission). This results in a final lift drag ratio of 14.6 and source noise of 56 dB. These values should be used in the next design iterations. Propagating this noise 55 m leads to a receiver noise level of 22dB. The plasma actuators will generate noise as well, which cannot be simulated, however, the frequency domain on which it occurs is limited to the carrier frequency and thus the noise can be removed in post-processing. Therefore the design meets the low noise requirements and the lift-drag ratio ensures efficient operations.

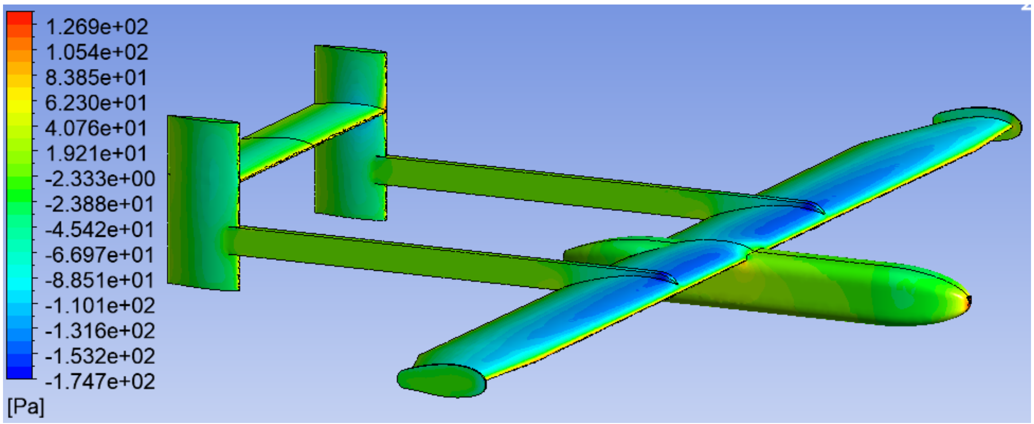

Figure 17.4: Pressure distribution of the final design using k-omega sst model

17.4. Hardware Block Diagram

Multiple different sections integrate various hardware components. These are the ground system, avionics, landing system, propulsion, and plasma system. Each of these sections has displayed its respective diagram and subsystem interfaces. In this section, these separate hardware diagrams are combined and shown in Figure 17.5. As every subsystem connects to power, a power bus has been implemented for visualisation purposes. This is simply a distribution network, where the power system provides various different voltages which various subsystems use.

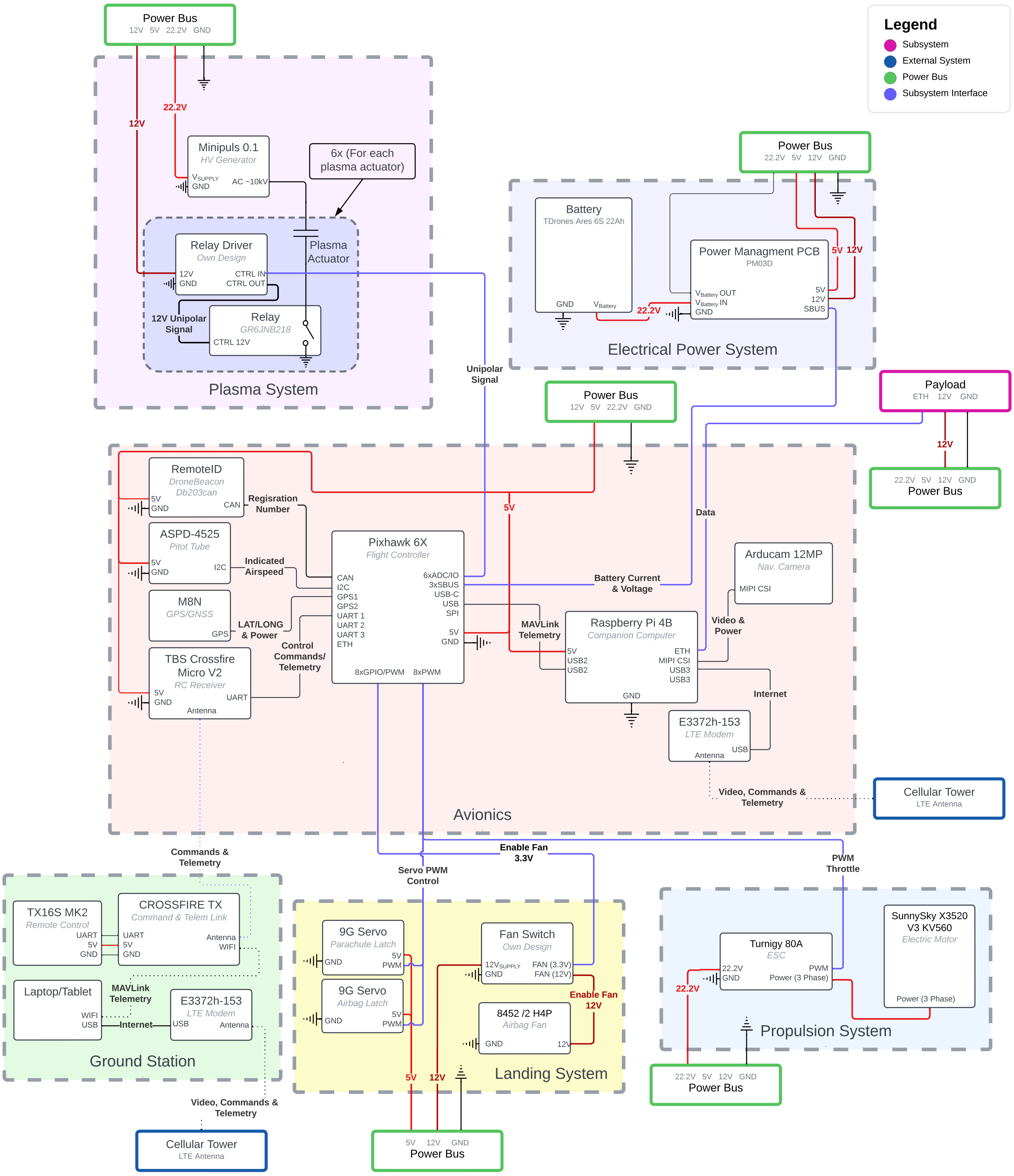

Figure 17.5: Hardware Block Diagram

17.5. Electrical Block Diagram

In Figure 17.8 the electrical block diagram of the UAV is shown. The typical value shows the average value over the UAV usage time of 2 hours.

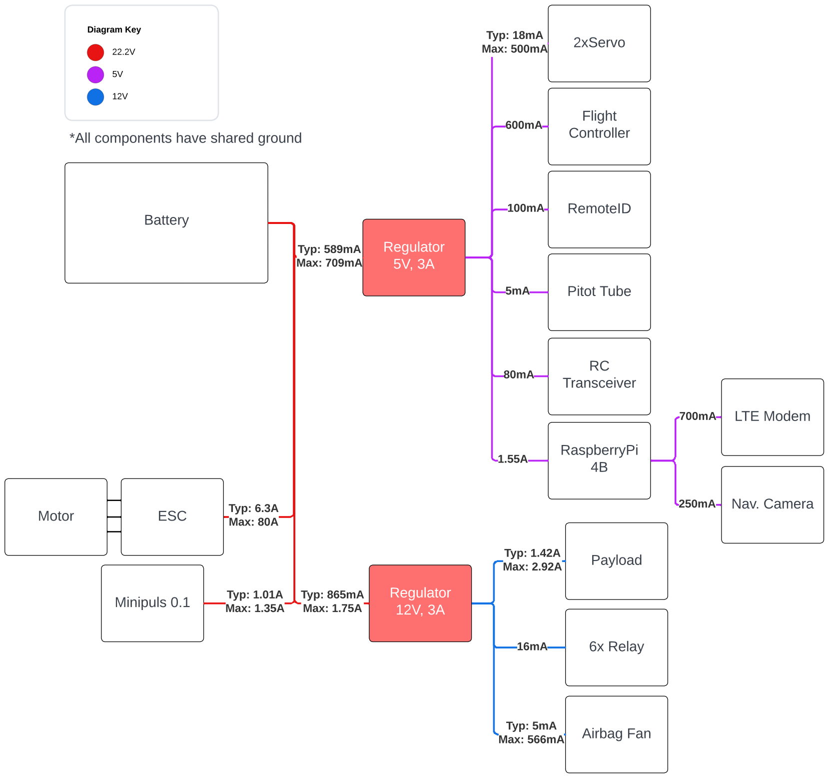

Figure 17.6: Electrical Block Diagram

17.6. Software Block Diagram

The Pixhawk 6X is expected to run an open-source autopilot called Ardupilot which has extensive capabilities. As this is not developed by this group, no software diagram is included for this system. However, both the ground station and the companion computer execute mission-critical software. Their interrelations are shown in Figure 17.7. A custom GNC algorithm is expected to be run in Ardupilot whose architecture is detailed in chapter 12.

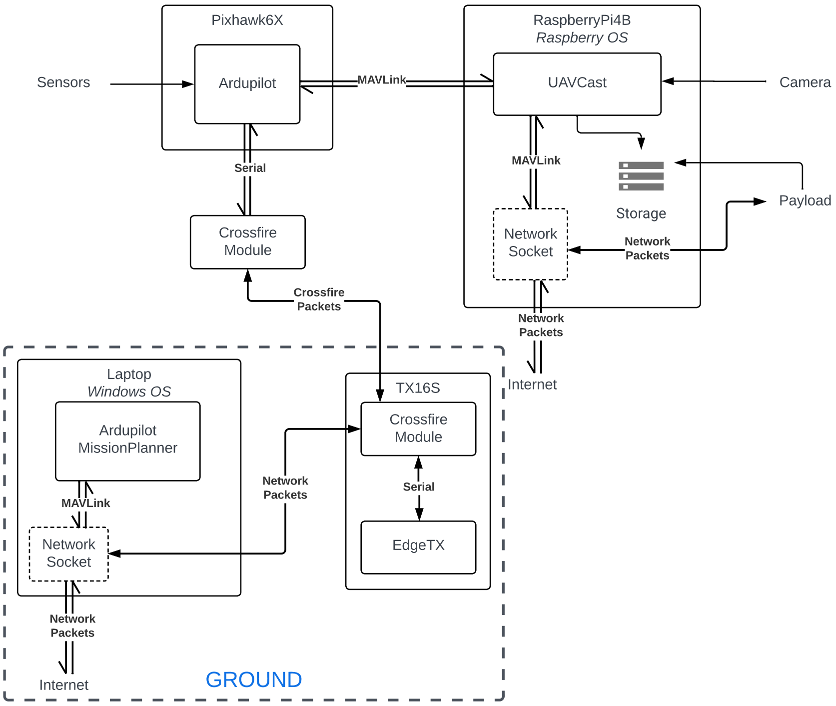

Figure 17.7: Software Block Diagram for the Flight Controller

17.7. Data handling and Communication Flow Diagram

In Figure 17.8 a communication and Data handling flow diagram is shown. Data quantities not specified by the manufacturer have been estimated conservatively. Should cellular coverage not be available all data is stored on the Raspberry Pi 4B. As the handling of data and the flow of communication go hand in hand, the diagram is presented in a combined version.

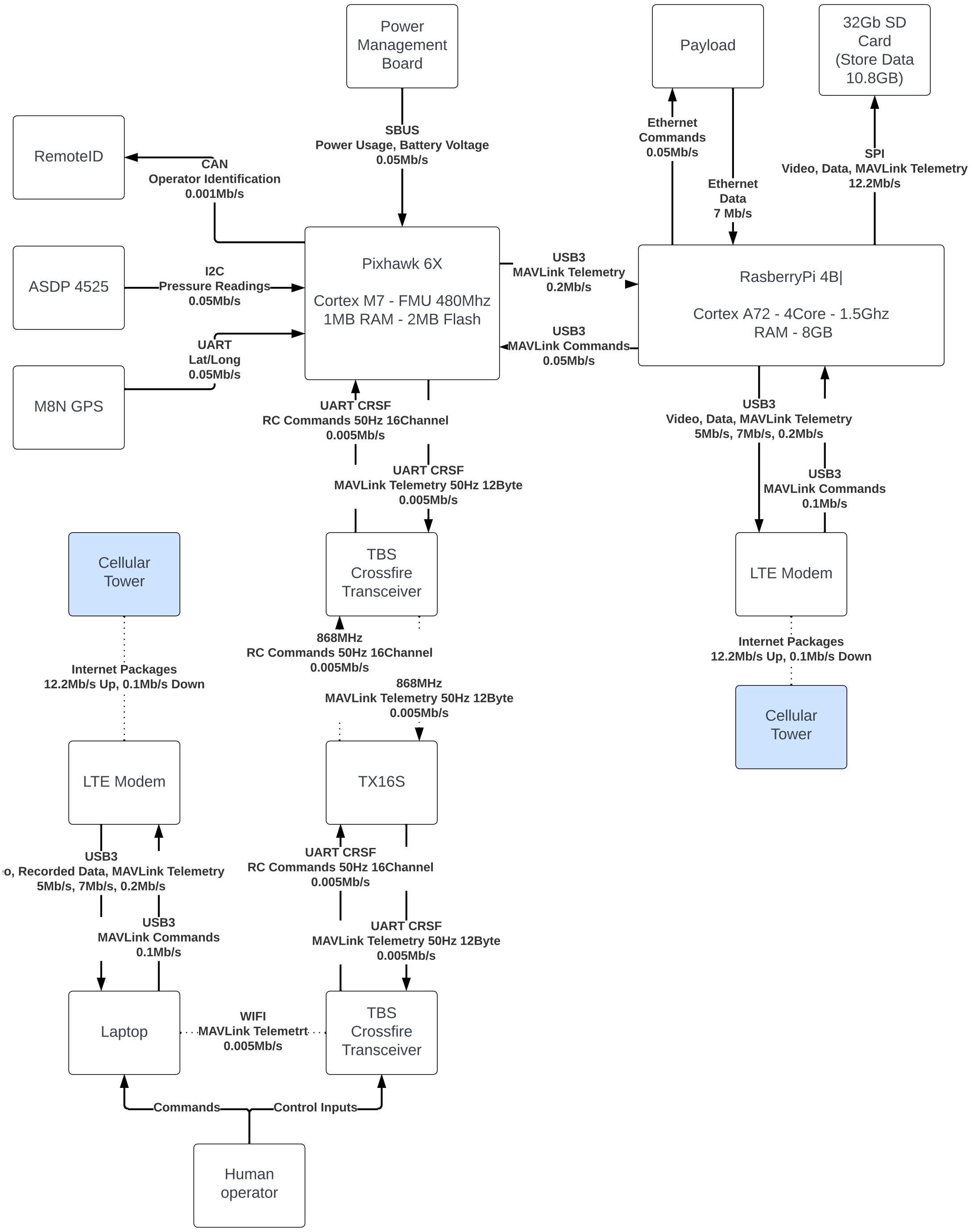

Figure 17.8: Data Handling and Communication Flow Diagram

18 Budget

This focuses on crucial aspects of drone design and operation, including the power, energy, weight, and cost budgets. These budgets directly impact the drone’s performance, endurance, efficiency, and feasibility. By analyzing power allocation, energy sources, weight distribution, and costs, we aim to provide insights into optimizing drone performance and ensuring economic viability. These budget considerations are vital for successful drone development and deployment.

18.1. Power and Energy Budget

The power budget is an essential aspect of the project. It describes the peak power required during the peak loads. It allows the design team to choose a power source that provides power to all of the subsystems at a particular time. On the other hand, the energy budget does not focus on the peak. Instead, it dictates the endurance of the mission. It is about the total energy in the battery and how it is to be distributed. Figure 18.1 gives the subsystems of the drone that require power and energy.

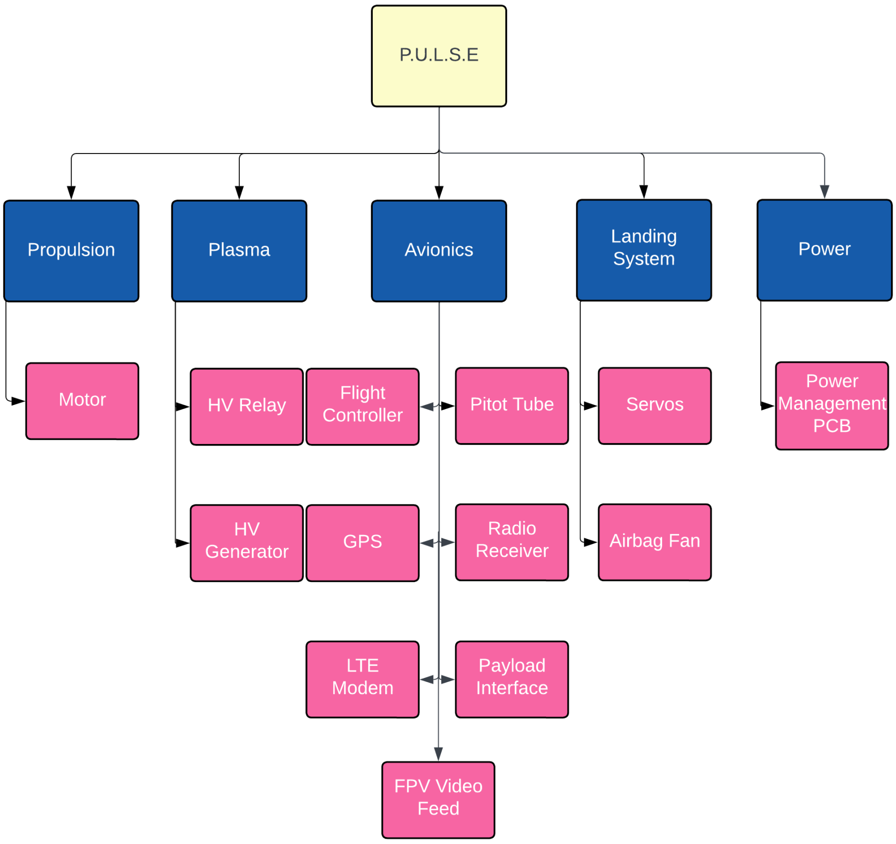

Figure 18.1: Power and Energy Distribution

Table 18.1 gives an overview of the actual peak power rating and maximum required energy for each of the components. As can be seen, the maximum required power at any moment in time is 1866.6 W. The available power provided by the battery is 2997W. Similarly, for the energy required, the maximum energy required at full performance would be 390.56 Wh whereas the battery capacity is 395Wh.

Table 18.1: Power and Energy Budget

Subsystem	Peak Power(W)
Propulsion	1776
Plasma	30.29
Power	3.26
Avionics	12.37
Landing System	9.68
Payload	35

Subsystem	Max. Energy(Wh)
Propulsion	278.95
Plasma	45.57
Power	6.52
Avionics	25.35
Landing System	0.145
Payload	34

18.2. Mass Budget

The mass budget explores the crucial task of allocating mass within a drone system. Proper weight management is essential for optimal performance, stability, and payload capacity. This section examines weight distribution to get the most out of the flight capabilities and operational efficiency. Figure 18.2 gives a summary of the mass of the various components of the drone.

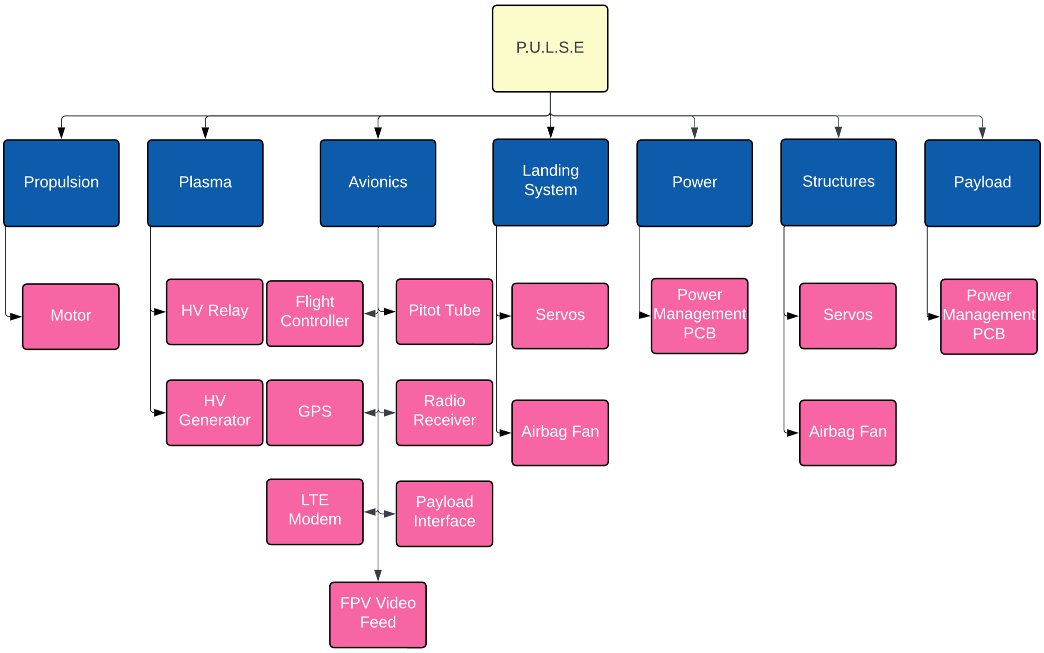

Figure 18.2: Mass Budget

Table 18.2 gives an overview of the mass of the different components in the drone for the first iteration. As can be seen, the mass of the entire system adds up to 8.65kg. The constraint due to legal requirements of the drone being below 15kg is hence met.

Table 18.2: Mass Budget

Subsystem	Mass[kg]
Propulsion	0.306
Plasma	0.889
Power	2.099
Avionics	0.34
Landing System	0.88
Payload	1
Structures	3.135

Subsystem	Mass[kg]
Propulsion	0.305
Plasma	0.39
Power	2.993
Avionics	0.34
Landing System	0.8786
Payload	1
Structures	3.3

These values were then used as new design parameters for the second iteration. For this iteration, a 5% margin was taken into account over the previous iteration. The final values of the masses can be seen in the table on the right. The total weight of the drone turns out to be 8.63kg

18.3. Cost Budget

Cost management plays a crucial role in the development process of the project. One of the stakeholder requirements (REQ-CUS-15) set by the customer emphasizes the significance of cost control. According to this requirement, the total expenses for developing and constructing 2 drones must not surpass 30,000 EUR. This chapter provides an insightful breakdown of the cost distribution among the different subsystems involved in the project, aiding in a comprehensive understanding and efficient management of expenses. It also explains the predicted return on investment of the product. Figure 18.3 shows the cost breakdown structure of the project.

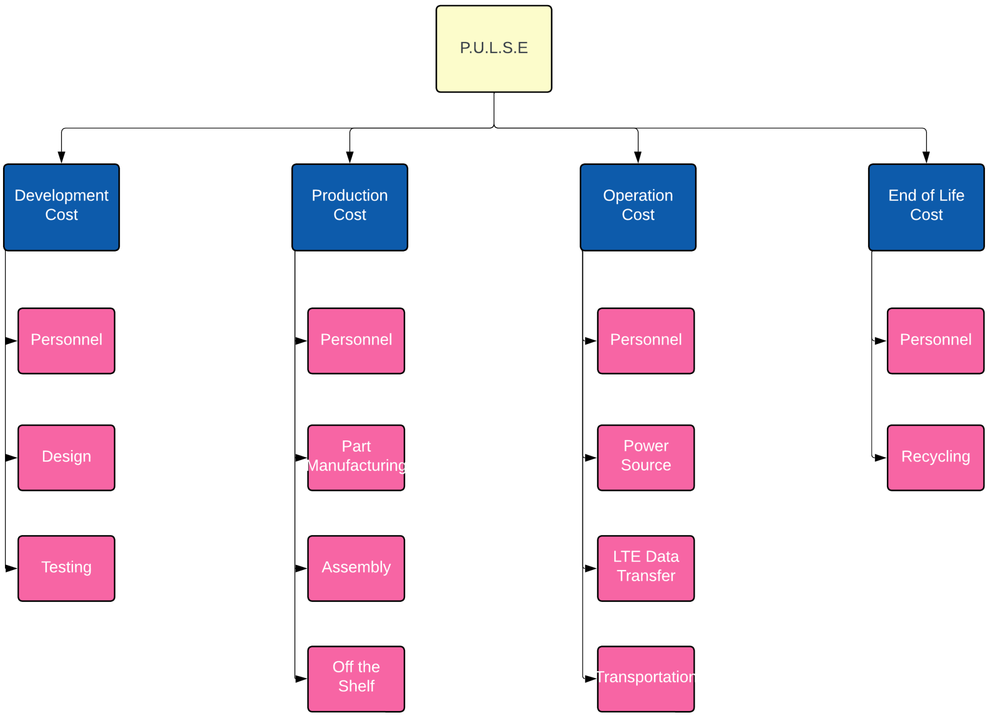

Figure 18.3: Cost Breakdown Structure

18.3.1. Off the shelf Components

To largely minimize production hassles. Many off-the-shelf components were chosen. The cost of these components has been summarised below.

Avionics

The avionics subsystem is one of the major places where the budget is spent. This is mainly because most of the parts chosen are all off-the-shelf. The list of products with individual costs is summarised in Table 18.3. It should be kept in mind that this is for the cost of components for 1 aircraft. The total cost will become double.

Table 18.3: Avionics Cost Breakdown

Component	Function	Cost [€]
Pixhawk 6X	Flight Controller	391.35
ASPD-4525	Pitot Tube	6
M8N GPS	GPS + Compass	43
TBS Crossfire Micro V2	Radio Receiver	32
Raspberry Pi 4B	LTE Communication & Payload Interface	75
E3372h-153	LTE Modem	53
Raspberry Pi Camera 3	FPV Video Feed	30
Avionics Wiring	Connect Components	30
DroneBeacon Db203can	Remote-ID	64

Ground Station

The ground station comprises several components, including the LTE Modem, Remote Controller, and joystick. It is important to note that the laptop, which is an integral part of the ground station, is assumed to be provided by the user and is therefore not considered in the cost budget. Table 18.4 is a summarised list of items and its respective costs.

Table 18.4: Ground Station Cost Breakdown

Component	Function	Cost [€]
E3372h-153	LTE Modem	53
TX16S MK2	Remote Controller, Joysticks	230
Crossfire	Transmitter Ground	193.91

Plasma

The plasma subsystem consists of the high-voltage relays, the power source for the plasma actuators and the wiring. The plasma itself has a negligible cost and hence has not been taken into consideration. Table 18.5 gives an overview of all the components and the costs of each of them.

Table 18.5: Plasma Cost Breakdown

Component	Function	Cost [€]
Copper + Dielectric	Ailerons	100
Copper + Dielectric	Elevators	100
Copper + Dielectric	Rudder	100
Belden Wire & Cable 8890 002100	HV Wire	81
Minipuls 0.1	HV Generator	2148
DAR70575-HR	HV Relay	254.7
Other Components	PCB, Diodes	40

Power

The power subsystem is responsible for supplying energy to all the components of the UAV, ensuring their proper functioning. It encompasses the power supply for the motor and the plasma. Table 18.6 gives a summary of the cost breakdown for the power systems.

Table 18.6: Power Cost Breakdown

Component	Function	Cost [€]
UnmannedRC 27AH 6S	Battery	641.38
PM03D	Power Management PCB	48.07
12AWG Silicon	High Current Wiring	20

Propulsion

The propulsion system consists of the Electronic Speed Controller(ESC), motor and propeller. All of these parts are chosen off-the-shelf for simplicity. Table 18.7 gives an overview of the cost breakdown of the propulsion system.

Table 18.7: Propulsion Cost Breakdown

Component	Function	Cost [€]
12x6 folding AEROnaut CAM	Provide thrust	9.5
SunnySky X3520 V3 KV560	Motor	55.69
Turnigy Plush-32 80A	Control power to motor	36.48

Landing and Take-Off

The Landing and Take-Off systems have been considered separate systems of the UAV as they are all external products being used to simplify these processes. This includes the catapult launching system and the parachute-airbag landing system. Table 18.8 gives the cost distribution of different subsystems.

Table 18.8: Take-Off and Landing Cost Breakdown

Component	Function	Cost [€]
FWRB-84-S-2P-OB	Parachute	566.02
9G Servo	Parachute and airbag Hatch Latch	28
Riptop Nylon 66	Airbag	23.8
8452 /2 H4P	Airbag Fan	75.44
Elevon X	Catapult	5760

Overall Cost Off the Shelf

This chapter presents a summary of the cost analysis for off-the-shelf components required to build two drone prototypes. With the inclusion of a second prototype, the prices of subsystems have doubled. The cost of the take-off system and ground station were considered, as a single catapult can launch both drones and one ground control system is necessary at a time. The total cost for the off-the-shelf components of both prototypes amounts to €17962.6. This analysis focuses solely on off-the-shelf components and does not include custom-built or specialized parts, or other expenses like software development or maintenance. Understanding these costs aids in assessing the economic feasibility and scalability of the drone project.

Table 18.9: Overall Cost

Subsystem	Cost €
Propulsion	203.34
Plasma	5647.4
Power	1418.9
Avionics	1449.52
Landing System	1406.52
Structures	1600
Launching System	5760
Ground Station	476.91
Total	17962

18.3.2. Testing

According to the user requirements, the product should be developed with a maximum testing time of 30 hours. This costs money. The car for transportation, the sim cards for communication and the manpower needed were considered in the analysis. The breakdown of the testing process has been described in Table 18.10

Table 18.10: Testing Cost Breakdown

Component	Function	Cost€
Car	Transportation	450
3 x Sim Cards	Connection	150
Personnel	Overall Control	900
	Total	1500

18.3.3. Manufacturing

Finally, the cost of the manufacturing process is budgeted. This includes the manpower required, the machines and the workspace required and the cost of raw materials. The cost of the materials is considered negligible compared to the manufacturing costs, as they are relatively common and readily available. Regarding manufacturing, it is estimated that the production of 2 UAVs costs roughly € 5000. The fuselage, wing, booms and empennage are investigated separately, taking into consideration recurring costs such as materials and manufacturing operations, as well as non-recurring costs, such as custom dies.

18.4. Sustainability

In this section, the overall sustainability of the product is considered. The stakeholder provided a requirement stating that the product was to be at least 80% sustainable. This was kept in mind throughout the design phase. Table 18.11 gives an overview of the sustainability budget of the project.

Table 18.11: Sustainability Budget

Subsystem	Sutainability(%)	Rationale
Propulsion	85	The motor is 100% recyclable, The ESC is 30% recyclable and the propeller has a very high recyclability. The overall weighted sustainability is then calculated from this.
Structures	100	Since the structure is made of aluminium and balsa and both materials are completely recyclable or reusable.
Plasma	50	The copper tape used is a 100% recyclable. The silicon-coated wire used is 50%. The PCBs used are 30%. Finally, the high-voltage relays used are 10% recyclable. The weighted average is calculated for the final sustainability of the subsystem
Power	95	The battery which is the main weight of the subsystem is a 100% recyclable
Avionics	30	Consists of PCBs and all of them are 30% recyclable
Landing	90	The servos and the fan are reusable but not recyclable. But the nylon which is the main weight of the drone is completely recyclable

It can be seen that the final design is 88% recyclable. This is higher than the requirement stated by the consumer of 80%.

19 Operations and Logistics

To aid in project development and to familiarise stakeholders with the operational profile of the drone, the concept of operations and logistics is developed in this chapter. Firstly, the various key elements of the operation are described in section 19.1, while a visual representation of the interaction of these elements is presented in section 19.2. Lastly, section 19.3 discusses the logistical aspect of the operation.

19.1. Elements of Operations

Major elements of the operational concept are the plasma-controlled UAV itself, the human operator, a ground control station, a launcher, the measurement environment, a charging station, a satellite navigation system and transportation. A detailed explanation of these elements is presented in this section.

19.1.1. Unmanned Aerial Vehicle

The central element in the mission is a fixed-wing drone which utilises plasma actuators for attitude control. The UAV is equipped with payloads (microphones and/or cameras) to measure scientific data over the measurement environment and communicates data and status to and receives commands from the ground station. The UAV has been designed to be modular, such that it can be taken apart easily. A launcher/catapult will be used to launch the UAV, and it shall land in a specified area using a parachute.

Once the designated launch and landing locations, as well as measurement area and pattern, have been specified, the UAV shall perform its flight fully autonomously, relying on an array of flight instruments and satnav data for navigation and control. Nevertheless, the operator has the capability to fully take over the control of the UAV at any point of the flight. As such, the UAV shall have sufficient communication capabilities for live data transmission and control.

19.1.2. Operator

The operator is responsible for the (dis)assembly of the UAV, ground control station and launcher, selection of launch/measurement/landing area, inspection and pre-flight checks, monitoring of the flight and control of the UAV when necessary. The operation is designed to be performed by a single person. Moreover, the operator must have the necessary certifications and training before operating the UAV.

19.1.3. Ground Control Station

The ground control station, or GCS, serves as the main interface between the operator and the UAV in flight. The GCS must ensure sufficient uplink and downlink capabilities to receive live measurement, flight and health data at maximum UAV range, as well as transmit commands to the UAV. Moreover, the GCS shall have one or more screens to present clear information to the operator, as well as necessary peripherals for command and manual control of the UAV.

The GCS shall additionally have an interface with the launcher, as well as Internet and satellite navigation capabilities for localisation and weather data. The ground control station shall be powered by a battery, with a longer battery life than the maximum endurance of the UAV.

19.1.4. Launcher/Catapult

In the trade-off performed during the conceptual trade-off[33], it was decided that the UAV shall be launched using a dedicated launcher. The launcher will be controlled by the GCS and is responsible to provide the necessary airspeed and climb angle to the UAV required for clearing obstacles. At this stage, it is yet unclear whether the launcher shall be acquired from a third party or designed and built in-house.

19.1.5. Measurement Environment

The measurement environment is the primary object of the operation. In chapter 3, an example measurement mission and areas are provided, namely, noise mapping over nature reserves and small-to-medium urban areas on the Dutch coast. The UAV will be designed to cover an area of $1000\,\mathrm{m} \times 2000\,\mathrm{m}$ in a single flight. The specific measurement area is selected by the operator before each mission through the GCS.

19.1.6. Satellite Navigation System

To ensure proper position determination, both the UAV and the GCS shall be equipped with a satellite navigation system receiver. At this stage, it is unknown which of the four core satellite systems will be used.

19.1.7. Charging Station

Since both the UAV and the GCS are powered by batteries, charging stations for both systems must be designed or acquired. Adequate over-current and over-voltage protection must be included within the charging stations.

19.1.8. Transport

Due to measurement areas being relatively remote and both flight and communication ranges of the UAV being limited, all systems (the UAV, GCS and launcher) are designed to be transportable. A cargo van was chosen as the base mode of transportation from which transportability requirements were defined, however, any vehicle with equal or larger cargo space could be used.

19.2. Concept of Operations Diagram

To help visualise operational elements within the environment, as well as relations between said elements, a concept of operations diagram is presented in Figure 19.1. It must be noted that the elements are for visual representation only and are not accurate to the final design.

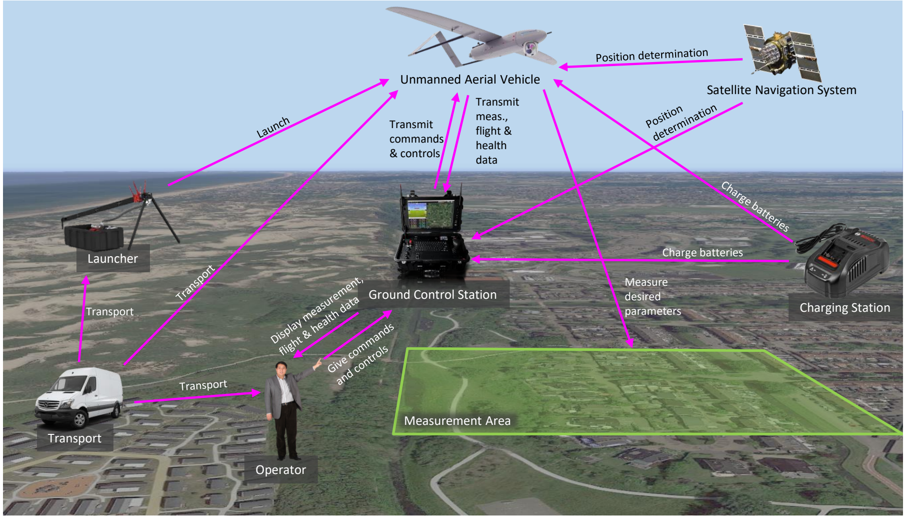

Figure 19.1: Concept of Operations Diagram[1]

[1] Image sources: Background - Google Maps. UAV - [111]. Operator - Microsoft Powerpoint Stock Images. Satellite Navigation - [112]. GCS - [113]. Charging Station - [114]. Launcher - [115]. Transport Van - Evox Images.

19.3. Operation Logistics

The logistics have been broken down into four main parts. These are production, storage, transportation and end-of-life logistics.

19.3.1. Production

The project is expected to entail the production of two prototypes. Due to the limited budget, these should be built with limited specialised tools. Production is expected to take place at the TU-Delft, thus a wide variety of tools such as various 3D printers, CNC-milling machines and other tools are available at low cost. Additionally, a UAV protection and transportation crate shall be either procured and customised with foam inlays or built entirely. Similarly, a catapult shall be bought off the shelf.

19.3.2. Storage

Since the UAV is a TU-Delft project the storage is expected to be at TU-Delft facilities. The UAV can simply be stored in the transportation crate. Current battery technology, however, presents safety challenges as they might catch fire. To avoid them causing damage to other property these should be stored in a battery safety storage box. Special care and observation should be taken during battery charging since this phase presents an increased fire risk.

19.3.3. Transportation

The transportation of the UAV and launcher will be done with a cargo van. To reach the intended launch site, public roads will be used. The final journey to the launch site can then be done on foot with wheels on the catapult and UAV crate that allow for easy transportation. This allows for economic transportation over large distances and a large area that can be accessed.

An option that is not considered likely which would present challenges, is transportation over oceans. EASA only allows up to $100\,\mathrm{W\,h}$ batteries on planes [116], which means the batteries can not be transported by plane, so these would have to be transported separately or new batteries would have to be acquired at the destination. The alternatives of cargo ships would be slow and would have to be planned far in advance.

The UAV design should allow for easy assembly and disassembly in the field which should allow for quick setup times during operation. Additionally, to protect the UAV during transportation the design should allow for transportation in a protecting crate to avoid damage during transport.

19.3.4. End-Of-Life

Since the UAV is designed to be recyclable, special care should be taken at the end of life. Once the UAV is deemed unneeded, unusable or not economically usable the UAV should be disassembled into its major components. The major components that should be recycled are the battery, parachute, some of the avionics and the structure. These should be brought to appropriate sites or reused. Other smaller components should also be recycled or reused at an appropriate waste recycling plant.

20 Sustainability

Over the last decade, the engineering sector has taken up the responsibility of creating new technologies in a way that minimises the damage it causes to the planet. The following chapter will focus on the aspects of this project that have an environmental impact and details ways this impact can be minimised. Its results are taken into account next to the requirements defined.

20.1. Circular Economy & Material Considerations

Circular economy (CE) is a school of thought that originated in the 1960s and has been refined over the years. It proposes an economy that works with closed material loops [117]. A product is created, used, reused and repaired before it is eventually recycled. The system promotes the usage of recyclable material, treats resources as scarce, and reduces the production of waste. *The Ellen MacArthur Foundation* is an organisation that connects academia, institutions, business, and policymakers to implement the ideas of CE globally [118]. They have collaborated with *Granta Design* to create The Material Circularity Index (MCI) tool. It quantifies the recyclability of a material and can also mitigate risks by integrating price volatility as well as regulatory and supply chain analysis. This tool will be used to choose the materials that will be used to build the UAV to satisfy the recyclability requirement of 80%.

20.2. Sustainability During Product Phases

In order to address the sustainability of the author's work, four key instances must be identified as being most important to the circular economy aspect of the project. These relate to the development, production, testing and operation of the product. The phases are addressed chronologically and correspond to a certain extent to the established workflow diagram. Note, however, that sustainability is a design philosophy and thus should be applied constantly through all phases of the design. The extent of this section is not to provide unreasonable or fictional strategies, but rather the actual steps that were taken and will be taken in order to ensure a sustainable design. The sustainability of third parties will not be addressed, although the sustainability of third-party interactions and the usage of energy and materials during these interactions will be analysed.

The first and most broad key instance is the conceptual design of the product. This includes in different proportions Phases A to D, with an emphasis on the activities that directly relate to designing the product, such as establishing the key requirements, performing concept trade-offs and assessing the risks to be encountered during the project. This phase unfolds at the drawing table and the process entails mostly intellectual resources. Due to this reason, the sustainability strategy for the design phase is restricted to the set of practices that each team member takes to ensure the process is sustainable. These mainly include drinking and eating habits during work hours and the use of energy during the workday. Regarding drinking and eating habits, all team members use reusable/ recyclable water bottles to ensure proper hydration and most food is brought in reusable plastic/ glass containers, limiting the use of disposable cutlery and dishes. Other resources used during this phase are electrical energy, the use of which is limited by making use of the available daylight. Lastly, all team members use sustainable transportation such as public transport, or cycling. Although exact numbers are not available to assess the sustainability of the specified methods of transportation and the energy generation of the Fellowship, these aspects are considered beyond the scope of the present work.

Secondly, the production phase is a prospective phase that is not expected to occur during the DSE. Although a production plan will be handed in during Phase D, thus sustainable development strategies for production can be explored to be included in the production plan. The assembly process is largely determined by the design. Complex designs result in a longer and more extensive assembly process. Therefore designing in a way that simplifies the assembly process will result in a lower environmental impact. This process is called Design For Assembly (DFA) [119]. The DFA guidelines are as follows. Minimising the part count will vastly simplify the design process and therefore decrease the assembly time. Making a design modular will increase the repairability and therefore increase the lifetime of the product. The manufacturing process impacts the environment in two ways, by use of energy and by generation of waste. Lean Manufacturing is a practice that aims to reduce both [120]. Material waste and actions that do not create value are treated as unnecessary squandering by lean manufacturing, therefore it should be a practice of the manufacturing body, to avoid unnecessary waste.

Testing is a phase that normally runs in parallel to the design process, but time constraints will most likely not allow this during the DSE. Technically, since testing will not occur during the DSE it is sustainable by default, but pun aside the testing phase will be addressed as a non-fictional phase occurring after the DSE. The testing phase can entail wind tunnel usage, testing communications, or full-flight tests. Throughout these processes, sustainability and technical performance will be traded off due to resource constraints. For example, the sustainability of using a wind tunnel will be restricted to reducing energy consumption and devising experiments in the most time-efficient way to ensure no energy is wasted. Full flight tests must ensure no emissions are created by the product during testing and transportation to the testing site/ facility must be done in the most sustainable way possible. Since the size of the product has not yet been established, the most sustainable method of transportation can vary from public transport to high-consumption vans. The testing site shall also not be polluted and the testing author shall ensure energy generation from sustainable resources, thus the use of on-site gas electricity generators will be prohibited. The testing should also not interfere with local economical activities on/near the testing site by impeding local production and economy.

During the operational phase of the product, no emissions shall be produced by the aircraft directly as per the sustainability requirements mentioned in [33]. Furthermore, the operation of the aircraft should not impede the local landscape during all possible operational phases including the unlikely event of a crash. However, the transportation of the UAV may still produce emissions, these can be reduced by using electric vehicles for transport to and from the launch site.

Finally, in the End-Of-Life phase, careful consideration must be taken to dispose off the drone in the most environmentally friendly manner. The procedure follows the flowchart seen in chapter 20.

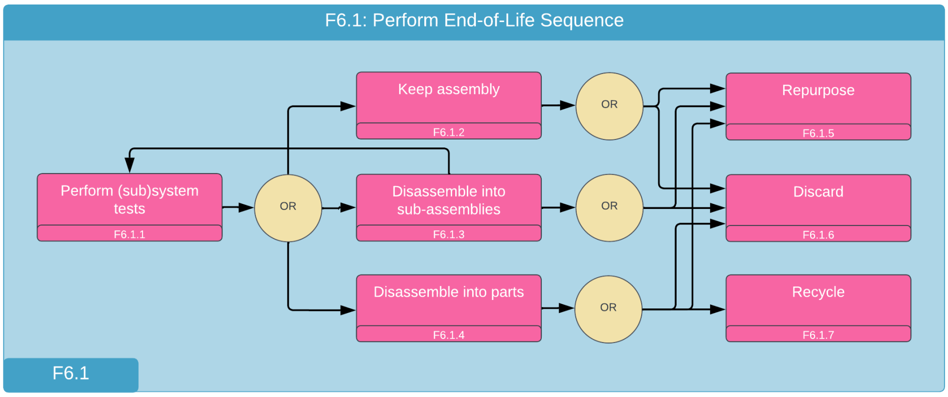

Figure 20.1: Sustainability Plan

- Comprehensive Testing: Firstly, the entire system undergoes rigorous testing to determine if any parts can be repurposed or reused.
- Breakdown into Subsystems: If repurposing or reusing the entire system is not feasible, the drone is dismantled into its subsystems.
- Subsystem Testing: Each subsystem is then subjected to the same battery of tests as performed on the whole system to identify any salvageable components.
- By adhering to this methodical approach, we ensure that every effort is made to maximize the utilization of the drone's components and minimize waste.

20.3. Sustainability Assessment and Conclusions

The methods presented in section 20.2 and their implementation within the design process need to be assessed throughout all phases. A number of indicators will be used differently in each phase. To summarise, a breakdown of the indicators and checks is presented below:

1. Development phase: no quantifiable indicators, but all throughout the ten weeks of DSE, the energy consumption shall be kept at a minimum
2. Production: used materials will be assessed on their Material Circularity Index. This will be constructed on the *Whole Product Approach* presented in the methodology of the Material Circularity Index documentation[118]
3. Testing: no quantifiable indicators, but the environmental impact of testing shall be kept to a minimum
4. Operation: assessed on MCI, energy usage and carbon footprint

In conclusion, the sustainable development strategy of the author's project entails a combination of quantifiable indicators, in order to ensure the product's sustainability compared to regulations and other competitors and a number of internal practices enforced by each team member.

21 Verification and Validation

21.1. Verification

Verification is essential to ensure the credibility of the model. It consists of the confirmation to check that the code is correct and that the outputs provided by the code are the values according to the model that has been used. This process is divided into two types, Code Verification and Calculation Verification

21.1.1. Code Verification

Code verification is the process of checking the code itself. It is to ensure that the program does not have any programming errors. This however does not necessarily check if the calculations have been done correctly. There are 2 types of code verification:

Static Testing and Debugging

Static testing is the process of verifying code without actually running it. The main goal of this is to enforce traditional coding techniques and standards into the code written. A tool such as PyLint can be chosen if most of the code is written in Python.

Debugging is the process of correcting the code being tested in case of any mistakes. There are two types of debugging: Static debugging is the process where the reader just reads the code and potential mistakes are fixed. On the other hand, dynamic debugging involves running the code and fixing the issues based on the errors in the output.

Dynamic Verification

Dynamic testing is a crucial type of software testing that involves the execution of the code being tested. Unlike static testing, which focuses on analyzing the code without actually running it, dynamic testing aims to identify and address any issues that may arise during program execution. Dynamic testing can be further classified into two sub-categories: unit testing and system testing.

UNIT TESTING

This focuses on testing individual components or modules of the code to ensure their behaviour aligns with the expected functionality. This type of testing allows for early detection and resolution of bugs and helps maintain code quality and reliability. Following is a table consisting of the unit tests that were performed:

Table 21.1: Unit Tests

Test ID	Test	Rationale	Output
VER-UT-1	Input/Output Formatting	Checking the shape and size of the data. Does not check the data itself	True/False
VER-UT-2	Input/Output Conversions	Checks that all of the calculation parameters are in SI units.	True/False
VER-UT-3	Extreme Condition Test	Inputting extreme values in the code. The maximum errors can be found at these values allowing for easier identification of systematic errors.	Accuracy
VER-UT-4	Equation Implementation	Visually inspecting and hand calculating the equations to verify that the equations have been typed in correctly.	Accuracy

SYSTEM TESTING

This involves evaluating the entire system. This comprehensive testing approach encompasses all components and subsystems, ensuring they function effectively together and meet the desired specifications. System testing helps uncover issues related to integration, interoperability, performance, and overall system behaviour, providing valuable insights into the system's performance in a real-world environment.

21.1.2. Calculation Verification

Calculation verification is the process of checking and validating the accuracy of mathematical calculations performed within a software system. It involves comparing expected results with the actual results produced by the software to ensure correctness. It is crucial for ensuring accurate calculations in complex mathematical operations.

One of the to perform calculation verification is by Reference Solution Test. Here, the entire model is run and the final value of the code is then compared to an analytical solution. This analytical solution could be calculated by hand or any third-party software, such as Wolfram Alpha [1]. Additionally, during the implementation of more complicated concepts in code, simplified versions of the code were used to compare the complicated code to. This was frequently done during the process of the second iteration, comparing the result of the code from the first iteration with that of the second. Through this, it could be verified that the model is correct and makes sense.

---

[1] https://www.wolframalpha.com/

21.2. Product Verification

Product verification entails the process of checking if a product complies with all of the requirements. There are numerous methods to conduct his verification process. These are namely Analysis, Demonstration, Testing and Inspection. A short explanation for each of these methods can be found below.

- Analysis: This method involves examining data, information, or processes to identify patterns, trends, or inconsistencies. Analysis can be performed through statistical analysis, data mining, or reviewing documents to uncover insights and validate the information.
- Demonstration: In this method, the verification is carried out by observing a product, system, or process in action. It involves showcasing the functionality or performance of a product or system to confirm that it meets the specified requirements or standards. For example, a software developer may demonstrate the features of a new application to ensure its functionality.
- Testing: Testing is a common method used to verify the performance, functionality, or reliability of a product, system, or software. It involves executing a series of predefined test cases to check whether the item being tested behaves as expected. Testing can include unit testing, integration testing, system testing, performance testing, and more, depending on the context.
- Inspection: Inspection involves a detailed examination or evaluation of a product, process, or system to ensure compliance with standards, specifications, or requirements. It typically involves a visual examination, measurement, or comparison against defined criteria. Inspections can be done on physical objects, documents, or procedures.

21.2.1. Compliance Matrix

This section gives a summary of all of the system requirements and an overview of the compliance of each of these requirements. The compliance has been divided into 3 categories: Pass, Fail and Pending.

Table 21.2: Compliance Matrix

Requirement ID	Requirement	Verification	Compliance
SYS-BDG-01	The development, production and 30 hours of test flight for two systems shall cost less than 30,000 Euros.	Analysis	**PASS**
SYS-BDG-02	The system shall be designed in detail in 4000 man hours.	Analysis	**PASS**
SYS-COM-01	The system shall be able to transmit all data at a range of at least 10 km.	Demonstration	**PASS**
SYS-COM-03	The system shall be able to transmit its geographical location during nominal operation.	Analysis	**PASS**
SYS-COM-04	The system shall be able to encrypt all transmitted data	Demonstration	**PASS**
SYS-COM-06	The system shall be able to transmit a live video feed during nominal operation.	Analysis	**PASS**
SYS-CTL-01	The system shall be able to fly remote controlled.	Demonstration	**PASS**
SYS-CTL-02	The system shall require only a single operator.	Demonstration	**PASS**
SYS-CTL-05	The system shall save all flight data locally during operation.	Analysis	**PASS**
SYS-CTL-06	The system shall warn the operator in case of critical or dangerous situations.	Testing	**PENDING**
SYS-CTL-07	The system shall be able to complete one operational cycle autonomously, excluding take-off and landing.	Demonstration	**PASS**
SYS-CTL-08	The system shall return to the mission start position if contact with the operator is lost.	Analysis	**PASS**
SYS-CTL-10	The system shall be able to be forced to perform an emergency landing by the operator during all flight phases.	Demonstration	**PASS**
SYS-ENV-01	The system shall be able to operate at an ambient temperature between 2.5 and 40 Celsius.	Testing	**PENDING**
SYS-ENV-02	The system shall be able to maintain an internal temperature between 0 and 50 Celsius.	Testing	**PENDING**
SYS-ENV-04	The system shall be able to operate at an ambient humidity range below 86 percent.	Testing	**PASS**
SYS-LAN-01	The system shall be able to land within the designated test area.	Testing	**PASS**
SYS-LFT-02	The system shall not use any mechanical high lift devices.	Inspection	**PASS**
SYS-LGL-03	The system shall operate below 120 m.	Analysis	**PASS**

SYS-LGL-05	The system shall not operate within 30m of people not involved.	Inspection	**PASS**
SYS-LGL-06	The system shall weigh less than 15kg.	Inspection	**PASS**
SYS-LGL-09	The system shall produce noise that is lower than 30 dBA when it propagates to the target measurement area.	Testing	**PENDING**
SYS-PAY-01	The system shall be able to carry at least 1.0 kg of payload.	Inspection	**PASS**
SYS-PAY-02	The system shall be able to carry a payload with 99.6x99.6x152.1 mm dimensions.	Inspection	**PASS**
SYS-PAY-09	The system shall reserve 35 W for the payload subsystem's peak power condition.	Inspection	**PASS**
SYS-PER-06	The system shall have a range of at least 10 kilometres.	Analysis	**PASS**
SYS-PER-07	The system shall have an endurance of at least 2 hours.	Analysis	**PASS**
SYS-REL-02	The system's catastrophic failure rate shall be lower than 7.5 per 100,000 flight hours.	Analysis	**PENDING**
SYS-REL-03	The system's critical failure rate shall be lower than 37.5 per 100,000 flight hours.	Analysis	**PENDING**
SYS-REL-05	The system's marginal failure rate shall be lower than 105 per 100,000 flight hours.	Analysis	**PENDING**
SYS-STR-01	The system shall not experience any destructive resonance during any part of the mission.	Testing	**PENDING**
SYS-STR-02	The system shall house all subsystems required to fulfill the mission.	Inspection	**PASS**
SYS-STR-03	The system shall provide access for maintenance of the subsystems	Analysis	**PASS**
SYS-STR-04	The system shall be able to withstand a maximum load factor of 3.75 and -1.5.	Analysis	**PASS**
SYS-STR-06	The system shall protect all susceptible subsystems from the environment.	Analysis	**PASS**
SYS-STR-07	The system shall be able to withstand ultimate load factors.	Testing	**PASS**
SYS-SUP-01	The support personnel shall be at most 2 people.	Inspection	**PASS**
SYS-SUP-02	The support personnel shall be able to lift at least 35 kg.	Demonstration	**PENDING**
SYS-SUS-01	The system shall be at least 80 percent recyclable by mass.	Analysis	**PASS**
SYS-SUS-07	The system shall not contaminate bodies of water during nominal operation.	Analysis	**PASS**
SYS-SUS-08	The system shall not contaminate the ground during nominal operation.	Analysis	**PASS**
SYS-TEC-01	The system shall be unmanned.	Demonstration	**PASS**
SYS-TEC-02	The system shall have no moving control surfaces.	Inspection	**PASS**
SYS-TEC-03	The system shall be manufacturable by accessible manufacturing processes.	Analysis	**PASS**
SYS-TEC-04	The system shall provide simple access to all subsystems and parts.	Inspection	**PENDING**
SYS-TEC-05	The system shall incorporate plasma actuators.	Analysis	**PASS**
SYS-THR-02	The system shall be able stay aloft in case of an engine failure.	Analysis	**PASS**
SYS-MFD-16	The system shall be able to measure all of its critical parameters	Testing	**PASS**
SYS-COM-07	The system shall have data interfaces for all subsystems	Demonstration	**PASS**

21.3. Product Validation

The process of product validation aims to check if the customer's needs are met[2]. Regarding the specific project, it validates the satisfactory accomplishment of the mission. Such validation procedures could be mission scenario tests, operation readiness tests etc. In this section, a list of validation techniques is given in Table 21.3, to be used as a guide for future V&V procedures.

---

[2] nasa.gov - (Accessed - 16-06-2023)

Table 21.3: Suggested validation tests

ID	Validation procedure	Rationale
VLD-TST-01	Nominal operations simulation	Showcase that all nominal operations are executed according to the operations and mission plans.
VLD-TST-02	Nominal flight test	Showcase that the mission is accomplished to the customer.
VLD-TST-03	Adverse conditions test	Investigate if the UAV can operate in extreme environmental conditions, as close as possible to the required values.
VLD-TST-04	Emergency landing test	Showcase the emergency procedures to the customer
VLD-TST-05	Stress failure test	Investigate how the system behaves before and during failure.
VLD-TST-06	End-to-end communications test	Check if the ground segment and UAV data interfaces work correctly.
VLD-SIM-01	Transportation demonstration	Demonstrate that all related systems can be transported.

Based on the illustrated table, multiple procedures can be planned during the testing phases. Specifically, the descriptions can be elaborated into test plans and can accordingly be performed, following the procedures of Figure 5.4 and Figure 5.5. It is worth mentioning that in case more appropriate validation tests or simulations are found in later project phases, they should be added in Table 21.3. For the execution of such tests, close communication with the stakeholders, such as the customer, is required, as they directly relate to their needs.

22 Conclusions and Recommendations

This final report shows the progress made in the past 10 weeks regarding the design of an Unmanned Aerial Vehicle without moving control surfaces with the aim to explore the implementation and application of plasma actuators. The report covers the full design spectrum from initial project management and design trade-offs to detailed subsystem design and finalized overall design. In this chapter the conclusions found during the design process are discussed per subsystem, including their respective recommendations.

In order to determine important performance parameters, relations between wing surface area and velocity were used to obtain a cruise speed of 15.1m/s. During the glide phases of the missions the aircraft will glide at an angle of $sin(1/19)$ and for turning performance a 540° angle was considered taking into account roll dampening. Pitching motions of the aircraft are initiated by increasing flight velocity and were set to be a result of angular acceleration rather than a change in the angle of attack. This was done to simplify the design, but it is recommended to investigate using a change in angle of attack for movements.

The final step of the current iteration was to assess the aerodynamic performance of the drone within the mission profile of gliding to reduce noise. Using a time-averaged method, the glide ratio was finally estimated to be within the region of 14.6. Note that this value was not used for performance calculations, but the previously estimated value of 19. Moreover, the noise footprint of the drone was analysed using time averages CFD methods which resulted in 56dB at the source and after propagating 55m results in 22dB. The plasma actuating will noise as well, which cannot be simulated, however, the frequency domain on which it occurs is limited to the carrier frequency and thus the noise can be removed in post-processing.

In order to obtain accurate aircraft control, plasma-actuated circulation control over a rounded trailing edge aerofoil was chosen. For bidirectional control, three-electrode (2x grounded, 1x exposed) AC-DBD plasma actuators are used. The viability of the chosen method is proven through analysis and wind tunnel testing. Plasma control surfaces using this method were therefore used incorporated in the horizontal and vertical stabiliser as well as the wing tips of the main wing. We recommend that more extensive wind tunnel experiments should be done. The effect of the trailing edge geometry and actuator placement can be analysed. The effect of atmospheric conditions on the actuators as well as the noise produced by the actuators can be analysed. Finally, the local velocity fields can be measured with a PIV which could give more insight into the local effect of the actuators.

The wing, presented in Figure 22.1 is divided into two parts with different functionalities. The main part consists of a rectangular and tapered part with an aspect ratio of 12 that acts as the lifting body of the UAV. And an outer rectangular part that acts as the control section. The aerofoil of the lifting body was chosen mainly for its

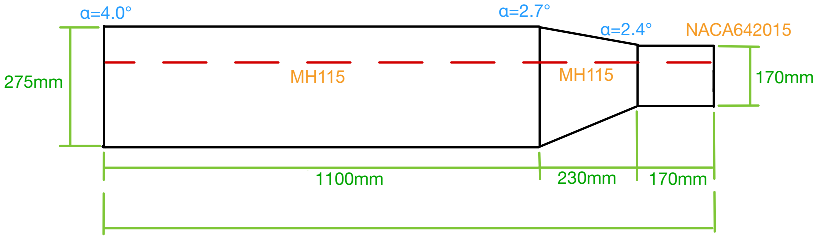

Figure 22.1: Current design iteration of the main wing. Drawn to scale

lifting characteristics which resulted in the MH115 propeller aerofoil. The NACA642015 with a rounded trailing edge was chosen for the aileron. To integrate these two bodies an interplate was used such that the sudden change in geometry and pressures do not cause any three-dimensional effects. We recommend reconsidering the aerofoil design decision since propeller aerofoils have a high moment coefficient and thus the tail is larger than alternative aerofoils may be. Furthermore, winglets should be integrated into the design to mitigate the 3D effects near the wingtips. A Computational Fluid Dynamics (CFD) analysis with a turbulence model such as K-epsilon should be performed to analyse the interactions between aerodynamic interfaces between various structures, for example, the wing and fuselage sections. Using this CFD analysis, the effect of connecting the two surfaces by blending them gradually can also be investigated.

For sizing the fuselage, internal components were the driving factor. A semi-monocoque shape was used in order to combine structural and aerodynamic benefits. Using the obtained dimensions, stress studies were performed regarding yielding, crippling, hole stress concentrations, and buckling. Using the findings of these studies a structure was obtained consisting of a set of six formers connected by four stringers situated in the corners. This main fuselage skeleton was chosen to be made out of Aluminium 2024 alloy. The yellow poplar wood skin surrounding this structure includes two access holes required for parachute and airbag deployment. The nose and tail cone were designed to be removable to access payload and electrical components. It is recommended that numerical methods are used to analyse the loads and stresses in the structure during landing and that tests that simulate the flight loads are performed before the flight test.

For the tail design, stability turned out to be the limiting factor. The H-tail configuration carries integrated plasma surfaces for longitudinal control and is furthermore situated such that the propeller wake is avoided. The vertical tails are sized to counteract destabilizing effects of the fuselage, propeller and effective dihedral. Vertically, they are positioned to provide enough ground clearance with respect to the fuselage bottom upon landing. For structural integrity of the empennage rectangular wing boxes are used in the horizontal and vertical stabilizers. The wing boxes in the vertical stabilizers are directly attached to the two booms, connecting the empennage to the main wing. For further studies, it is recommended to reiterate the destabilising effects of the fuselage as its geometry changed and is expected to change over iterations, this will change the vertical tail sizing. Additionally, after the iteration of including a yaw requirement for performance, a control section of the vertical stabiliser can be defined. After this is done, taper and sweep can be considered for the non-control sections of the tail such that the vertical tail is reduced in size.

After the wind tunnel test, it can be concluded that the angle of attack range at which the actuators work is dependent on their placement with respect to the trailing edge. Therefore multiple actuators are needed in order to gain full control authority over the aircraft at every angle of attack. The control derivatives of plasma actuators would also need to be researched further to determine how the system reacts to all control inputs such that a working control model can be created.

For design decisions regarding propulsion, the flight profile was considered to be cruise only. Although this is not the case, it is still a valid assumption since the continuous cruise is more demanding than the determined flight profile consisting of climb and glide phases. The motor battery combination that was eventually chosen can provide a peak thrust that is higher than the thrust required during the climbing stage of the flight. The final propeller-motor-combination chosen is the SunnySky X3520 V3, a 12-inch folding pusher propeller.

An important consideration throughout the design process is the sustainability of the project. This does not only cover the sustainability of the final product but also the economic, operational and social sustainability. The first step for this is to define a school of thought that allows the implementation of sustainable principles. Circular Economy proposes an economy that works with closed material loops. A product is created, used, reused and repaired before it is finally recycled. This reduces the overall waste of a mission. However, this is just a general idea that has to be converted into a specific analysis for the particular project. The sustainability aspects of this project have been split into different phases: The conceptual phase, the production phase (using lean manufacturing), the testing phase, the operational phase and the end-of-life phase. Sustainability must be maintained in all of these phases for the whole project to be environmentally friendly.

References

[1] Wilm Friedrichs. “Unmanned Aerial Vehicle for Flow Control Experiments with Dielectric Barrier Discharge Plasma Actuators”. Thesis. 2014.

[2] Dick Simons et al. “Comparative assessment of measured and modelled aircraft noise around Amsterdam Airport Schiphol”. In: *Elsevier* (2022).

[3] Macrotrends. *Airbus Group Research and Development Expenses 2012-2022 | EADSY*. URL: https://www.macrotrends.net/stocks/charts/EADSY/airbus-group/research-development-expenses (visited on 01/05/2023).

[4] Macrotrends. *Boeing Research and Development Expenses 2010-2023 | BA*. URL: https://www.macrotrends.net/stocks/charts/BA/boeing/research-development-expenses (visited on 01/05/2023).

[5] Electrofluidsystems. *Unmanned Systems Overview*. URL: https://www.electrofluidsystems.com/Systems/Unmanned-Systems (visited on 05/02/2023).

[6] MarketsandMarkets. *UAV Market by Point of Sale, Systems, Platform (Civil Commercial, and Defense Government), Function, End Use, Application, Type (Fixed Wing, Rotary Wing, Hybrid), Mode of Operation, Mtow, Range Region - Global Forecast to 2027*. 2022. URL: https://www.marketsandmarkets.com/Market-Reports/unmanned-aerial-vehicles-uav-market-662.html (visited on 05/01/2023).

[7] FactMR. *Fixed Wing Drone Market*. Nov. 2022. URL: https://www.factmr.com/report/fixed-wing-drone-market (visited on 01/05/2023).

[8] H. Yokoyama. “Simulation of acoustic oscillatory flows around a curvature controlled by a plasma actuator”. In: *Applied Acoustics* 205 (2022).

[9] Chuan He. “Plasma Slats and Flaps: An Application of Plasma Actuators for Hingeless Aerodynamic Control”. PhD thesis. 2008.

[10] Flint Thomas, Alexey Kozlov, and Thomas Corke. “Plasma actuators for bluff body flow control”. In: (2006), p. 2845.

[11] Thomas C Corke. *Design of aircraft*. Pearson, 2003.

[12] Dr. Jochen Kriegseis. *Towards turbulent drag reduction via discharge-based virtual wall oscillations – experimental strategies and flow diagnostics*. Seminar. 2023.

[13] Cheng Zhang et al. “Atmospheric-pressure pulsed plasma actuators for flow control: shock wave and vortex characteristics”. In: *Plasma sources science and technology* 28.6 (2019), p. 064001.

[14] Applied Aeronautics. *ALBATROSS-US*. Web Page. URL: https://store.appliedaeronautics.com/albatross-us/.

[15] Edge Autonomy. *Penguin C: Integrated SUAS*. Web Page. URL: https://edgeautonomy.io/solutions/penguin-c/.

[16] Unmanned Systems Technologies. *XV – Long-Range VTOL Hybrid Drone*. URL: https://www.unmannedsystemstechnology.com/company/plymouth-rock-technologies/xv-long-range-vtol-hybrid-drone/ (visited on 05/01/2023).

[17] EOS Technologie. *STRIX 300 MINI UAV*. Web Page. URL: https://www.eos-technologie.com/en/mini-UAV-Strix-300.htm.

[18] C-Astral. *Unmanned Aircraft Systems*. 2018. URL: https://www.c-astral.com/en/unmanned-systems/bramor-c4eye (visited on 05/01/2023).

[19] Black Swift. *Black Swift S2 UAS*. Web Page. URL: https://bst.aero/black-swift-s2-uas/#more.

[20] Tekever. *AR4 - Model Overview*. URL: https://www.tekever.com/models/ar4/ (visited on 05/01/2023).

[21] Event38. *E400 Mapping Drone*. Web Page. URL: https://event38.com/fixed-wing/e400-vtol-drone/.

[22] European commission. *Useful PLASMa for AEROdynamic control*. URL: https://cordis.europa.eu/project/id/234201 (visited on 02/05/2023).

[23] Sekimoto Satoshi et al. “Inflight Demonstration of Stall Improvement Using a Plasma Actuator for a Small Unmanned Aerial Vehicle”. In: *aerospace* ().

[24] Volantex. *Volantex RC Ranger EX Long Range FPV / UAV platform Unibody big weight carrier*. URL: https://www.volantexrc.eu/volantex-rc-ranger-ex-long-range-fpv-uav-platform-unibody-big-weight-carrier-v757-3-pnp-p-224.html (visited on 05/02/2023).

[25] Elizabeth Howell PhD at Spaceflight.com. *This wild DARPA CRANE X-plane could be a giant leap in aircraft design*. URL: https://www.space.com/darpa-crane-x-plane-active-flow-control (visited on 05/02/2023).

[26] Jie Jiang et al. “Combining UAV and Sentinel-2 satellite multi-spectral images to diagnose crop growth and N status in winter wheat at the county scale”. In: *Field Crops Research* 294 (2022).

[27] Mahmood A. Al-Shareeda Et al. “Unmanned aerial vehicle: a review and future directions”. In: *Indonesian Journal of Electrical Engineering and Computer Science* 30.2 (2000), pp. 123–456.

[28] Janet Mayowa Nwaogu et al. “Application of drones in the architecture, engineering, and construction (AEC) industry”. In: *Automation in Construction* 150 (2023).

[29] Enkhsaikhan Boldsaikhan Hossein Eskandaripour. “Last-Mile Drone Delivery: Past, Present, and Future”. In: *The Application of Drones in Logistics* 7 (2023).

[30] Routescene. *Using UAV LiDAR mapping to monitor landslides safely*. 2020. URL: https://www.routescene.com/case-studies/uav-lidar-mapping-landslides-safely/ (visited on 05/01/2023).

[31] Debolina Nath et al. “A Novel Drone-Station Matching model in Smart Cities based on Strict Preferences”. In: *Unmanned Systems* 11 (2023).

[32] Hannes Braßel et al. “Optimal UAV Hangar Locations for Emergency Services Considering Restricted Areas”. In: *Drones* 7 (2023).

[33] Archisman Acharya et al. “The Ionic Drone: A plasma-assisted UAV with no moving control surfaces - Midterm Report”. 2023.

[34] Government of the Netherlands. *GoDrone*. URL: https://map.godrone.nl/ (visited on 05/17/2023).

[35] URL: `https://en-gb.topographic-map.com/map-rzf8cz/Coepelduynen/`.

[36] C. Li, S. Li, and Y. Liu. “The model research on boustrophedon pattern of risk elements transmission between the same structure micro-grids”. In: 10 (Feb. 2016), pp. 377–384.

[37] Taua Cabreira, Lisane Brisolara, and Paulo Ferreira Jr. “Survey on Coverage Path Planning with Unmanned Aerial Vehicles”. In: *Drones* 3 (Jan. 2019), p. 4. DOI: `10.3390/drones3010004`.

[38] Lauren Nagel. *A Guide to Lithium Polymer Batteries for Drones*. URL: `https://www.tytorobotics.com/blogs/articles/a-guide-to-lithium-polymer-batteries-for-drones` (visited on 12/13/2021).

[39] Archisman Acharya et al. “The Ionic Drone: A plasma-assisted UAV with no moving control surfaces - Baseline Report”. 2023.

[40] Daniel P Raymer. *Aircraft design: A conceptual approach*. AIAA education series. Reston, Va.: American Institute of Aeronautics and Astronautics. ISBN: 1563478293.

[41] Fabrizio Nicolosi et al. “Fuselage aerodynamic prediction methods”. In: *Aerospace Science and Technology* 55 (2016), pp. 332–343. ISSN: 1270-9638. DOI: `https://doi.org/10.1016/j.ast.2016.06.012`. URL: `https://www.sciencedirect.com/science/article/pii/S1270963816302218`.

[42] Dries Verstraete, Jennifer L. Palmer, and Mirko Hornung. “Preliminary Sizing Correlations for Fixed-Wing Unmanned Aerial Vehicle Characteristics”. In: *Journal of Aircraft* 55.2 (2018), pp. 715–726. DOI: `10.2514/1.C034199`. URL: `https://arc.aiaa.org/doi/abs/10.2514/1.C034199`.

[43] Justin Winslow, Vikram Hrishikeshavan, and Inderjit Chopra. “Design Methodology for Small-Scale Unmanned Quadrotors”. In: *Journal of Aircraft* 55.3 (2018), pp. 1062–1070. DOI: `10.2514/1.C034483`. eprint: `https://doi.org/10.2514/1.C034483`. URL: `https://doi.org/10.2514/1.C034483`.

[44] Jay Gundlach. “Designing Unmanned Aircraft Systems: A Comprehensive Approach”. In: (2012).

[45] Chuan He, Thomas C. Corke, and Mehul P. Patel. “Plasma Flaps and Slats: An Application of Weakly Ionized Plasma Actuators”. In: *Journal of Aircraft* 46.3 (May 2009), pp. 864–873. DOI: `10.2514/1.38232`. URL: `https://doi.org/10.2514/1.38232`.

[46] Xin Gu et al. “Plasma Gurney Flap Flight Control at Low Angle of Attack”. In: *Journal of Aircraft* 60.1 (Jan. 2023), pp. 172–189. DOI: `10.2514/1.c036702`. URL: `https://doi.org/10.2514/1.c036702`.

[47] Shinya Ueno. “Investigation of a Plasma Gurney Flap for Lift Enhancement”. MA thesis. École Polytechnique de Montréal, May 2010. URL: `https://publications.polymtl.ca/320/`.

[48] Massachusetts Institute of Technology. *Rocket aims for cheaper nudges in space; plasma thruster is small, runs on inexpensive gases*. 2009. URL: `https://www.sciencedaily.com/releases/2009/02/090223221524.htm`.

[49] J. Reece Roth. “Aerodynamic flow acceleration using paraelectric and peristaltic electrohydrodynamic effects of a One Atmosphere Uniform Glow Discharge Plasma”. In: *Physics of Plasmas* 10.5 (May 2003), pp. 2117–2126. DOI: `10.1063/1.1564823`. URL: `https://doi.org/10.1063/1.1564823`.

[50] A. Seifert et al. “Roll Contrial via Active Flow Control: From Concept to Flight”. In: *Journal of Aircraft* 47.3 (May 2010), pp. 864–874. DOI: `10.2514/1.45910`. URL: `https://doi.org/10.2514/1.45910`.

[51] Andrey A. Sidorenko et al. “Plasma control of vortex flow on a delta wing at high angles of attack”. In: *Experiments in Fluids* 54.8 (Aug. 2013). DOI: `10.1007/s00348-013-1585-4`. URL: `https://doi.org/10.1007/s00348-013-1585-4`.

[52] Marc T. Hehner et al. “Virtual wall oscillations forced by a DBD plasma actuator operating under beat frequency - a concept for turbulent drag reduction”. In: *AIAA AVIATION 2020 FORUM*. American Institute of Aeronautics and Astronautics, June 2020. DOI: `10.2514/6.2020-2956`. URL: `https://doi.org/10.2514/6.2020-2956`.

[53] O. Mahfoze and S. Laizet. “Skin-friction drag reduction in a channel flow with streamwise-aligned plasma actuators”. In: *International Journal of Heat and Fluid Flow* 66 (Aug. 2017), pp. 83–94. DOI: `10.1016/j.ijheatfluidflow.2017.05.013`. URL: `https://doi.org/10.1016/j.ijheatfluidflow.2017.05.013`.

[54] Armin Kurz et al. “Boundary Layer Transition Control using DBD Plasma Actuators”. In: *AerospaceLab Journal* 6 (June 2013), pp. 1–8.

[55] Marios Kotsonis. “Plasma-based control for laminar-turbulent transition: past experience and future directions”. In: *APS Annual Gaseous Electronics Meeting Abstracts*. APS Meeting Abstracts. Jan. 2021, BM23.005, BM23.005.

[56] Gilles Boesch et al. “Flight Control Using Wing-Tip Plasma Actuation”. In: *Journal of Aircraft* 47.6 (Nov. 2010), pp. 1836–1846. DOI: `10.2514/1.44003`. URL: `https://doi.org/10.2514/1.44003`.

[57] Ernest C. Batlle, Ricardo Pereira, and Marios Kotsonis. “Airfoil Stall Hysteresis Control with DBD Plasma actuation”. In: *55th AIAA Aerospace Sciences Meeting*. American Institute of Aeronautics and Astronautics, Jan. 2017. DOI: `10.2514/6.2017-1803`. URL: `https://doi.org/10.2514/6.2017-1803`.

[58] Marios Kotsonis, Robin Pul, and Leo Veldhuis. “Influence of circulation on a rounded-trailing-edge airfoil using plasma actuators”. In: *Experiments in Fluids* 55.7 (June 2014). DOI: `10.1007/s00348-014-1772-y`. URL: `https://doi.org/10.1007/s00348-014-1772-y`.

[59] P. F. Zhang et al. “Numerical Simulation on Plasma Circulation Control Airfoil”. In: *AIAA Journal* 48.10 (Oct. 2010), pp. 2213–2226. DOI: `10.2514/1.j050133`. URL: `https://doi.org/10.2514/1.j050133`.

[60] Thomas C. Corke, C. Lon Enloe, and Stephen P. Wilkinson. “Dielectric Barrier Discharge Plasma Actuators for Flow Control”. In: *Annual Review of Fluid Mechanics* 42.1 (Jan. 2010), pp. 505–529. DOI: `10.1146/annurev-fluid-121108-145550`. URL: `https://doi.org/10.1146/annurev-fluid-121108-145550`.

[61] W. Shyy, B. Jayaraman, and A. Andersson. “Modeling of glow discharge-induced fluid dynamics”. In: *Journal of Applied Physics* 92.11 (Dec. 2002), pp. 6434–6443. DOI: `10.1063/1.1515103`. URL: `https://doi.org/10.1063/1.1515103`.

[62] Yildirim Suzen, George Huang, and David Ashpis. “Numerical Simulations of Flow Separation Control in Low-Pressure Turbines Using Plasma Actuators”. In: *45th AIAA Aerospace Sciences Meeting and Exhibit*. American Institute of Aeronautics and Astronautics, Jan. 2007. DOI: `10.2514/6.2007-937`. URL: `https://doi.org/10.2514/6.2007-937`.

[63] P C Dörr and M J Kloker. “Numerical investigation of plasma-actuator force-term estimations from flow experiments”. In: *Journal of Physics D: Applied Physics* 48.39 (Sept. 2015), p. 395203. DOI: `10.1088/0022-3727/48/39/395203`. URL: `https://doi.org/10.1088/0022-3727/48/39/395203`.

[64] John Murphy and Philippe Lavoie. “Characterization of DBD Plasma Actuators via PIV Measurements”. In: *51st AIAA Aerospace Sciences Meeting including the New Horizons Forum and Aerospace Exposition*. American Institute of Aeronautics and Astronautics, Jan. 2013. DOI: `10.2514/6.2013-346`. URL: `https://doi.org/10.2514/6.2013-346`.

[65] Anthony Tang et al. “Empirical relations for discharge current and momentum injection in dielectric barrier discharge plasma actuators”. In: *Journal of Physics D: Applied Physics* 54.24 (Mar. 2021), p. 245204. DOI: `10.1088/1361-6463/abec0b`. URL: `https://doi.org/10.1088/1361-6463/abec0b`.

[66] R. Swanson and Christopher Rumsey. “Numerical Issues for Circulation Control Calculations”. In: *3rd AIAA Flow Control Conference*. American Institute of Aeronautics and Astronautics, June 2006. DOI: `10.2514/6.2006-3008`. URL: `https://doi.org/10.2514/6.2006-3008`.

[67] Gregory Jones. “Pneumatic Flap Performance for a 2D Circulation Control Airfoil, Steady and Pulsed”. In: (July 2005).

[68] C. L. Enloe et al. “Mechanisms and Responses of a Dielectric Barrier Plasma Actuator: Geometric Effects”. In: *AIAA Journal* 42.3 (Mar. 2004), pp. 595–604. DOI: `10.2514/1.3884`. URL: `https://doi.org/10.2514/1.3884`.

[69] M.T. HEHNER et al. “On the fabrication of durable dielectric-barrier discharge plasma actuators”. In: (2022). DOI: `10.13009/EUCASS2022-4898`. URL: `https://www.eucass.eu/doi/EUCASS2022-4898.pdf`.

[70] F. F. Rodrigues et al. “Influence of Exposed Electrode Thickness on Plasma Actuators Performance for Coupled Deicing and Flow Control Applications”. In: *Volume 3: Fluid Mechanics Micro and Nano Fluid Dynamics Multiphase Flow*. American Society of Mechanical Engineers, Aug. 2021. DOI: `10.1115/fedsm2021-65728`. URL: `https://doi.org/10.1115/fedsm2021-65728`.

[71] S. A. Saleh et al. “Multistage and Multilevel Power Electronic Converter-Based Power Supply for Plasma DBD Devices”. In: *IEEE Transactions on Industrial Electronics* 65.7 (2018), pp. 5466–5475. ISSN: 1557-9948. DOI: `10.1109/TIE.2017.2777379`.

[72] Sven Grundmann, Michael Frey, and Cameron Tropea. “Unmanned Aerial Vehicle (UAV) with Plasma Actuators for Separation Control”. In: *47th AIAA Aerospace Sciences Meeting including The New Horizons Forum and Aerospace Exposition*. 2009. DOI: `10.2514/6.2009-698`. URL: `https://arc.aiaa.org/doi/abs/10.2514/6.2009-698`.

[73] Kento Suzuki et al. “Development of small high-voltage AC power supply for a dielectric barrier discharge plasma actuator”. In: *Review of Scientific Instruments* 92.2 (2021). ISSN: 0034-6748. DOI: `10.1063/5.0015377`. URL: `https://doi.org/10.1063/5.0015377`.

[74] Jörg Brutscher. *Minipuls 0.1*. 2012. URL: `https://www.gbs-elektronik.de/media/download_gallery/minipuls01e.pdf` (visited on 06/16/2023).

[75] Satoshi Sekimoto et al. “Flow-control capability of electronic-substrate-sized power supply for a plasma actuator”. In: *Sensors and Actuators A: Physical* 306 (2020), p. 111951. ISSN: 0924-4247. DOI: `https://doi.org/10.1016/j.sna.2020.111951`. URL: `https://www.sciencedirect.com/science/article/pii/S0924424719320965`.

[76] Mame Andallah Diop, Antoine Belinger, and Hubert Piquet. “10 kV SiC MOSFET Evaluation for Dielectric Barrier Discharge Transformerless Power Supply”. In: *Plasma* 3.3 (2020), pp. 103–116. ISSN: 2571-6182. URL: `https://www.mdpi.com/2571-6182/3/3/9`.

[77] GIGAVAC. *Product Specifications - GR6JNB218*. URL: `https://dc-components.com/wp-content/uploads/GIGAVAC-GR6JNB218-HV-Relay.pdf` (visited on 06/16/2023).

[78] Akinlolu Ponnle. “Development of a Low Cost Micro controller based Under and Over Voltage Protection Device”. In: 3 (Sept. 2014), pp. 1225–1229.

[79] ON Semiconductor. *NPN transistor - 2N4401 - Specifications*. URL: `https://www.farnell.com/datasheets/661741.pdf` (visited on 06/16/2023).

[80] Airfoil Tools. *NACA 642-015 AIRFOIL (n64015-il)*. 2023. URL: `http://airfoiltools.com/airfoil/details?airfoil=n64015-il`.

[81] Harinaldi et al. “Flow Control with Multi-DBD Plasma Actuator on a Delta Wing”. In: *Evergreen* 7.4 (Dec. 2020), pp. 602–608. DOI: `10.5109/4150513`. URL: `https://doi.org/10.5109/4150513`.

[82] Kun Chen et al. “Experimental investigation of influence of sliding discharge DBD plasma on low-speed boundary layer”. In: *AIP Advances* 10.3 (Mar. 2020), p. 035108. DOI: `10.1063/1.5134848`. URL: `https://doi.org/10.1063/1.5134848`.

[83] Nicolas Benard et al. “Nanosecond Pulsed Plasma Actuators”. In: *ERCOFTAC Bulletin* 94 (Mar. 2013), pp. 11–16.

[84] Mame Andallah Diop, Antoine Belinger, and Hubert Piquet. “10 kV SiC MOSFET Evaluation for Dielectric Barrier Discharge Transformerless Power Supply”. In: *Plasma* 3.3 (Aug. 2020), pp. 103–116. DOI: `10.3390/plasma3030009`. URL: `https://doi.org/10.3390/plasma3030009`.

[85] Michael Wicks and Flint O. Thomas. “Effect of Relative Humidity on Dielectric Barrier Discharge Plasma Actuator Body Force”. In: *AIAA Journal* 53.9 (Sept. 2015), pp. 2801–2805. DOI: `10.2514/1.j053810`. URL: `https://doi.org/10.2514/1.j053810`.

[86] John David Anderson. “Introduction to Boundary Layer”. In: *Fundamentals of aerodynamics*. McGraw-Hill Education, 2017, pp. 974–980.

[87] Mark D Maughmer. “Design of Winglets fr High-Performance Sailplanes”. In: *Journal of Aircraft* (Nov. 2003). DOI: `http://dx.doi.org/10.2514/1.10817`.

[88] Walter Pilkey, Deborah Pilkey, and Zhuming Bi. *Peterson’s Stress Concentration Factors (4th Edition)*. 2020. URL: `https://app.knovel.com/hotlink/khtml/id:kt012EDEA1/petersons-stress-concentration/holes-notation`.

[89] H.D. Curtis. *Fundamentals of aircraft structural analysis*. 1997.

[90] “Aircraft Wood Information”. In: *Light Aircraft Association* (). URL: `http://www.lightaircraftassociation.co.uk/engineering/TechnicalLeaflets/Building,%5C%20Buying%5C%20or%5C%20Importing/TL%5C%201.14%5C%20Wood%5C%20Information.pdf`.

[91] R. Jones, D. J. Cleaver, and I. Gursul. “Aerodynamics of biplane and Tandem Wings at low Reynolds numbers”. In: *Experiments in Fluids* 56.6 (2015). DOI: `10.1007/s00348-015-1998-3`.

[92] Egbert Torenbeek. *Synthesis of subsonic airplane design: An introduction to the preliminary design, of subsonic general aviation and transport aircraft, with emphasis on layout, aerodynamic design, propulsion, and performance*. Kluwer Academic Publishers, 1996.

[93] URL: http://airfoiltools.com/airfoil/details?airfoil=n64015-il.

[94] Gilbert Dyne. “Symposium on Advances in Propeller Research and Design”. In: 91st ed. MEDDELANDEN FRAN STATENS SKEPPSPROVNINGSANSTALT, 1981.

[95] Nils Paul van Hinsberg. “Aerodynamics of smooth and rough square-section prisms at incidence in very high Reynolds-number cross-flows”. In: *Experiments in Fluids* 62.3 (2021), p. 50.

[96] J.A. Mulder et al. *Flight Dynamics Lecture Notes*. 2023rd ed. TU Delft. Mar. 2013.

[97] Jochen Kriegseis et al. “Comprehensive effectiveness and efficiency evaluation of dielectric barrier discharge plasma actuators”. In: *51st AIAA Aerospace Sciences Meeting including the New Horizons Forum and Aerospace Exposition*. 2013, p. 898.

[98] Andrew Gong and Dries Verstraete. “Development of a dynamic propulsion model for electric UAVs”. In: Nov. 2015.

[99] European Commission. *Radio equipment directive 2014/53/EU*. Legal Rule or Regulation. 2014. URL: https://eur-lex.europa.eu/legal-content/EN/TXT/?uri=CELEX:32014L0053.

[100] DJI. *Specs - Video Transmission*. URL: https://www.dji.com/nl/rc/specs (visited on 06/15/2023).

[101] European Commission. “Commission Delegated Regulation (EU) 2019/945 of 12 March 2019 on unmanned aircraft systems and on third-country operators of unmanned aircraft systems”. In: *Official Journal of the European Union* (2019).

[102] Ashleigh Townsend et al. “A comprehensive review of energy sources for unmanned aerial vehicles, their shortfalls and opportunities for improvements”. In: *Heliyon* 6.11 (2020), e05285. ISSN: 2405-8440. DOI: https://doi.org/10.1016/j.heliyon.2020.e05285. URL: https://www.sciencedirect.com/science/article/pii/S2405844020321289.

[103] Masoud Alizadeh, Ahmad Sedaghat, and Ebrahim Kargar. “Shape and Orifice Optimization of Airbag Systems for UAV Parachute Landing”. In: *Int'l J. of Aeronautical Space Sci.* 15 (2014), pp. 112–121. DOI: 10.5139/IJASS.2014.15.3.335.

[104] Basem Al-Madani et al. “Design of Fully Automatic Drone Parachute System with Temperature Compensation Mechanism for Civilian and Military Applications”. In: *Journal of Advanced Transportation* 2018 (2018). ISSN: 0197-6729. DOI: 10.1155/2018/2964583. URL: https://doi.org/10.1155/2018/2964583.

[105] Kashif I. B. H. Ansari et al. “Design and development of an auto-inflatable airbag as the failsafe system of unmanned aerial vehicle”. In: *Materials Today: Proceedings* 77 (2023). ISSN: 2214-7853. DOI: https://doi.org/10.1016/j.matpr.2022.12.103. URL: https://www.sciencedirect.com/science/article/pii/S2214785322074752.

[106] Piotr Bartkowski and Robert Zalewski. “Passive safety system for small unmanned aerial vehicles”. In: *MATEC Web Conf.* 157 (2018), p. 03001. URL: https://doi.org/10.1051/matecconf/201815703001.

[107] X. Zhou, S. M. Zhou, and D. K. Li. “Optimal Design of Airbag Landing System without Rebound”. In: *IOP Conference Series: Materials Science and Engineering* 531.1 (2019). ISSN: 1757-899X 1757-8981. DOI: 10.1088/1757-899X/531/1/012001. URL: https://dx.doi.org/10.1088/1757-899X/531/1/012001.

[108] A. C. Browning. “A theoretical approach to air bag shock absorber design”. In: 1963.

[109] Masoud Alizadeh, Ahmad Sedaghat, and Ebrahim Kargar. “Shape and Orifice Optimization of Airbag Systems for UAV Parachute Landing”. In: *Int'l J. of Aeronautical Space Sci.* 15 (2014), pp. 112–121. DOI: 10.5139/IJASS.2014.15.3.335.

[110] H. G. Heinrich and David P. Saari. “Parachute Opening Shock Calculations with Experimentally Established Input Functions”. In: *Journal of Aircraft* 15.2 (Feb. 1978), pp. 100–105. DOI: 10.2514/3.58321. URL: https://doi.org/10.2514/3.58321.

[111] sUAS News. *UAV factory Penguin C Mk2*. 2020. URL: https://www.suasnews.com/2020/11/uav-factory-penguin-c-mk2/ (visited on 05/17/2023).

[112] Global Positioning System Directorate. *Global Positioning System satellite achieves 20 years on-orbit*. 2010. URL: https://www.afspc.af.mil/News/Article-Display/Article/250062/global-positioning-system-satellite-achieves-20-years-on-orbit/.

[113] Oz Robotics. *Ground control system for unmanned vehicles*. URL: https://ozrobotics.com/shop/ground-control-station-for-uav-ugv-drones-and-robotics-19in-hdw-intel-i3/ (visited on 05/17/2023).

[114] Bosch. *18 V lithium-ion battery fast charger*. URL: https://www.boschtools.com/us/en/boschtools-ocs/batteries-chargers-starter-kits-bc1880-146184-p/ (visited on 05/17/2023).

[115] Edge Autonomy. *16 kj - pneumatic drone launcher by UAV Factory Ltd.. Europe: Aeroexpo*. URL: https://www.aeroexpo.online/prod/uav-factory-ltd-europe/product-174156-63525.html (visited on 05/17/2023).

[116] EASA. *Lithium Batteries - Frequently Asked Questions*. URL: https://www.easa.europa.eu/en/the-agency/faqs/lithium-batteries (visited on 05/17/2023).

[117] Thibaut Wautelet. “The Concept of Circular Economy: its Origins and its Evolution”. 2018. DOI: 10.13140/RG.2.2.17021.87523.

[118] Ellen Macarthur Foundation. *Circularity Indicators*. URL: https://emf.thirdlight.com/link/3jtevhlkbukz-9of4s4/@/preview/1?o (visited on 05/17/2023).

[119] Fractory. URL: https://fractory.com/design-for-assembly-dfa/#:~:text=III%5C%20Conclusion-,What%5C%20Is%5C%20Design%5C%20for%5C%20Assembly%5C%3F,more%5C%20consistent%5C%2C%5C%20therefore%5C%20more%5C%20productive. (visited on 05/17/2023).

[120] United States Environmental Protection Agency. URL: https://www.epa.gov/sustainability/lean-thinking-and-methods-introduction (visited on 05/17/2023).